### SATELLITE RADAR IMAGERY ANALYSIS FOR GROUND HAZARD RISK MONITORING IN RAILWAY TRACKS AND SLOPES

By

Sumanth Varma Byrraju

Bachelor of Engineering Vasavi College of Engineering, 2012

Master of Science (MSc) University of South Carolina, 2018

Submitted in Partial Fulfillment of the Requirements

For the Degree of Doctor of Philosophy in

Civil Engineering

Molinaroli College of Engineering and Computing

University of South Carolina

2025

Accepted by:

Dimitris Rizos, Major Professor

Robert L Mullen, Committee Member

Yu Qian, Committee Member

Mike Sutton, Committee Member

Ann Vail, Dean of the Graduate School

© Copyright by Sumanth Varma Byrraju, 2025

All Rights Reserved.

## **DEDICATION**

Dedicated to my family and friends, who helped me see the end of the tunnel when I no longer could.

#### **ACKNOWLEDGMENTS**

First and foremost, I would like to express my deepest gratitude to Dr. Dimitris Rizos, my advisor and Chair of the committee, for their continuous guidance, support, and encouragement throughout this research journey. Their invaluable insights and unwavering patience have been instrumental in shaping this research. I am also incredibly grateful to my committee members, Dr. Mullen, Dr. Sutton, and Dr. Qian. Their thoughtful feedback and expertise have significantly enhanced the quality of this work, providing direction and clarity during critical moments of my research.

This research would not have been possible without the funding and support of the Federal Railroad Administration (FRA) and the Department of Civil and Environmental Engineering at the University of South Carolina. Their support enabled me to explore the potential of satellite radar imagery for ground hazard risk monitoring along railway tracks and slopes.

Thank you to my colleagues and fellow researchers, especially Brennan Gedney, Reza Naseri, Brittney Stinson, and Dr. Ning, for your contributions.

I am deeply indebted to my family for their endless love and encouragement. To my parents, your belief in me has been my anchor throughout this journey. To my partner, Madhuri, and our daughter, Nithara, the newest member of our family, your patience, understanding, and constant support have meant more than words can express.

Finally, I am grateful to all the friends and mentors I have met. This journey has been challenging yet rewarding, and each of you has made a lasting impact on my personal and professional life.

Thank you all for your part in this achievement.

#### **ABSTRACT**

Railway transportation is essential to national economies globally, and disruptions from geohazards can result in significant operational delays and considerable economic consequences. Satellite radar technologies, including Interferometric Synthetic Aperture Radar (InSAR), offer an effective means to monitor geohazard risks across extensive railway networks. This thesis employs Multi-Temporal InSAR (MTInSAR) techniques, including Persistent Scatterer InSAR (PSInSAR) and Small Baseline Subset (SBAS), to identify high-risk areas along railway rights of way (ROW) prior to geohazard occurrences. However, the efficiency of these MT-InSAR and, consequently, the caliber of the data generated may be restricted by elements like topographical profile, vegetation, and surface soil properties. This thesis presents first a detailed site categorization approach to define areas according to site-specific characteristics, improving radar processing precision.

Next, this thesis adapted two Multi-Temporal InSAR techniques, i.e., PSInSAR and SBAS, to improve the detection of scatterers in the broader region of interest by introducing the new concept of a "Rolling SAR Image Stack." Furthermore, three post-processing techniques were developed, i.e., "Thresholding," "Accumulation," and "Clustering Timeline," that successfully detected the critical locations where geohazard failures may initiate. The thesis also demonstrates that these techniques, when used with Coherence Change Detection (CCD), a SAR method that is demonstrated to identify regions with high soil saturation can improve hazard detection. The proposed approach

demonstrates that modern SAR-based analysis provides useful tools for railway operators to detect critical locations prone to geohazards, which enhances safety and reduces interruptions by prompting immediate actions. This research underlines the relevance of combining data from soil and environmental sources with satellite observations to conduct complete hazard monitoring. Additionally, it underscores the necessity of future satellite technology developments to improve coverage and dependability.

# TABLE OF CONTENTS

Dedication	iii
Acknowledgement	iv
Abstract	vi
List of Tables	xiii
List of Figures	XV
List of Symbols	xxiii
List of Abbreviations	xxiv
Chapter 1: Introduction	1
1.1 Background	1
1.2 Research Problem	5
1.3 Research Objectives	7
1.4 Organization of the Thesis	8
Chapter 2: Literature Review	11
2.1 Overview of Geohazards in Railway Infrastructure	11
2.2 Methods of Geohazard Detection and Monitoring	14

	2.3 Geohazard Risk Prediction	. 16
	2.4 Satellite Fundamentals	. 18
	2.5 Multi-Temporal SAR Techniques	. 22
Chap	eter 3: Methodology	35
	3.1 Research Approach	. 35
	3.2 Factors Influencing Data Quality	. 38
	3.3 Data Quality Based Classification	. 44
	3.4 Selected Sites	. 48
	3.5 Data Acquisition and Tools Used	. 52
	3.6 Employed Methods	. 55
	3.7 Limitation of Conventional MTInSAR	. 69
Chap	oter 4: Proposed Method for Identifying Regions with Geohazard Potential	70
	4.1 Rolling Stack MTInSAR (RS-InSAR)	. 71
	4.2 Thresholding	. 71
	4.3 Scatter Accumulation	. 75
	4.4 Clustering Timeline	. 75
Chap	eter 5: Validation Study	77
	5.1 Event	. 77
	5.2 Data Availability	. 77
	5.3 Site Description	. 79

5.4 MTInSAR Analysis	81
5.5 Discussion	86
Chapter 6: Results and Discussion	88
6.1 Detection of Geohazard Prone Area Using InSAR	88
6.2 Performance of Proposed Framework	90
Chapter 7: Conclusion.	93
7.1 Summary of Key Findings	93
7.2 Contribution to Research and Practice	94
7.3 Limitation of Study	96
7.4 Future Research Direction	96
References	98
Appendix A: Site Mobilization Monitoring	110
A.1 Lincoln, NE	110
A.2 Birmingham, AL	121
A.3 Maupin, OR	128
A.4 Atlanta, GA	136
A.4 Burlington, ND	141
A.5 Shiner, TX	150
A.6 Yellowstone, MT	155
A.7 Santa Clemente, CA	163

	A.8 Sandstone, WV	167
	A.9 Raymond, MN	175
	A.10 Quinn's, MT	181
	A.11 Pueblo, CO	182
Appe	endix B: Coherence and Soil Moisture Model	189
	B.1 Blackville, SC	189
	B.2 Yosemite, CA	192
	B.3 Bodega, CA	196
	B.4 Santa Barbara, CA	200
	B.5 Cortez, CO	204
	B.6 Chatham, MI	211
	B.7 Sandstone, MN	212
	B.8 Columbia, SC	213
Appe	endix C: Mathematical Background	218
	C.1 Data Preparation of Sentinel-1 (TOPS data type)	219
	C.2 SAR Interferogram	226
	C.3 CCD	235
	C.4 Multi-Temporal SAR	237
	C.5 PSInSAR	259
	C 6 SBAS	241

C.7 Pro	posed Post-Processing	Methods	5
C., 110	posed i ost i rocessing	1410410410410410410410410410410410410410	$\sim$

# LIST OF TABLES

Table 3.1 Sites where InSAR techniques are applied for mobilization monitoring.	51
Table 3.2 Shows the Acquisition periods for the CCD timeline analysis used for developing the coherence and soil moisture model.	53
Table 4.1 Shows the theoretical precision and suggested threshold values for coherence.	74
Table 5.1 Data used for Wayanad analysis	80
Table A.1 Data Availability of Sentinel-1A covering the city of Lincoln, Nebraska	114
Table A.2 Satellite Data Acquisition Periods for Birmingham, Alabama	124
Table A.3 Satellite Data Acquisition Periods for Maupin, OR	131
Table A.4 Satellite Data Acquisition Periods for Dekalb County, Georgia	139
Table A.5 Satellite Data Acquisition Periods for Burlington, ND	144
Table A.6 Satellite Data Acquisition Periods for Shiner, Texas.	153
Table A.7: Shows the Sentinel-1A data used for analysis.	158
Table A.8: Satellite data for acquisition periods for San Clemente, California	166
Table A.9 Sandstone WV Analysis Datasets	171
Table A.10 Shows the data acquired for conducting PSInSAR from Sentinel-1A	180

Table B.1 Sentinel-1 Data used for Blackville CCD analysis	191
Table B.2 Sentinel-1 Data used for Yosemite CCD analysis	195
Table B.3 Sentinel-1 Data used for Bodega CCD analysis	199
Table B.4 Sentinel-1 Data used for Santa Barbara CCD analysis	203
Table B.5 Sentinel-1 Data used for Cortez CCD analysis	207
Table B.6 Shows the coordinates of sensor	217
Table C.1 Recommended Threshold Values	249

# LIST OF FIGURES

Figure 1.1 Recent derailment events due to landslides: (a) TGV derailment Ingenheim, France, 3/5/2020; (b) CSX derailment Draffin, Kentucky, 2/13/2020[3][4]	1
Figure 2.1 This image shows multiple monitoring instruments used to monitor a geohazard	15
Figure 2.2 The electromagnetic spectrum is shown here	19
Figure 2.3 The effect of orbit baselines on the phase change is illustrated	23
Figure 2.4 PSInSAR and SBAS analysis of the same representative site:  (a) PSInSAR image connection graph; (b) PSInSAR computed deformation map; (c) SBAS image connection graph; (d) SBAS computed deformation map.	28
Figure 2.5 Example of CCD image analysis and correlation with water content: (a) Visual image of site with a railroad track between point A and B; (b) A typical coherence image of the site showing high coherence along the track; (c) Coherence along the track is changing due to increasing soil moisture; (d) Coherence along the track is lost due to high soil moisture content.	34
Figure 3.1 Effects of Slope Alignment on Deformation Measurements - Maupin OR Site: (a) Sentinel 1B LOS is in the direction of the slope and causes maximum sensitivity to SAR measurement of ground movement; (b) Sentinel-1B LOS is perpendicular to slope causes low SAR sensitivity to SAR measurement of ground movement	41
Figure 3.2 Site Classification Decision Tree	46
Figure 3.3 Examples of the four site categories	49
Figure 3.4 Shows the pre-processing workflow	34
Figure 3.5 Shows the workflow for first stage of processing stage.	59

Figure 3.6: Shows the workflow chart for coherence generation.	61
Figure 3.7 Shows PS processing chain workflow chart	63
Figure 3.8 Shows the processing chain for SBAS analysis.	65
Figure 3.9 Shows the post processing workflow for InSAR processing chain.	68
Figure 4.1 Rolling Stack MTInSAR (RS-MTInSAR) analysis concept	72
Figure 5.1 Shows the origin point of the landslide with the regions affected highlighted. (b)Shows the rescue efforts underway for the landslide event. (c) Shows satellite coverage of the region and its path.	78
Figure 5.2 (a) Shows the different areas of interest. (b) Shows the deformation overtime of the scatterer highlighted in (c). (c) Shows the large deformation scatterers before the landslide took place highlighted by white box in (a)	82
Figure 5.3 (a) Shows low activity in the region using the data till February 08, 2024. (b)Shows the region experiencing some deformations. (c) Shows the increasing deformations in the region (d) Shows the activity in the region before the landslide took place	84
Figure 5.4 (a) Show the start of activity in the region where the landslide initiated. (b) Shows the constant activity in the region where the landslide initiated. (c) Shows low presence of activity in the region where the landslide was initiated. (d) Graph shows the number of displacement points over each analysis.	85
Figure 5.5 Shows the crown of the landslide in the same region as the activity map shown by Scatter accumulation	87
Figure A.1 (a) Shows the derailment; (b) Shows the location where the derailment took place; (c) The coverage of Sentinel-1A covering the area of the accident	111
Figure A.2 Shows the soil profile of the region.	112
Figure A.3 (a) the displacement map superimposed on the optical image. (b) PS analysis results with high displacement (c) shows the	

derailment site with high subsidence in the region highlighted (d) Shows the progress of the displacement over time of one PS point	116
Figure A.4 (a) the post event displacement map superimposed on the optical image. (b) PS analysis results with high displacement with red-highlighted region showing consistently high subsidence and red-highlighted region showing a derailment event which took place 2 months after the analysis.	116
Figure A.5 (a) Coherence from 05/11 to 05/23/2021 (b) Coherence from 05/23 to 06/04/2022 (c) Coherence from 06/04 to 06/16/2022	118
Figure A.6 (a) Coherence from 06/16 to 06/28/2021 (b) Coherence from 06/28 to 07/22/202 (c) Coherence from 07/22 to 08/03/2021	118
Figure A.7 Coherence from 08/03 to 08/15/2021	120
Figure A.8 (a) Shows the location of concern for the instability analysis; (b) Shows the mine region and the area under observation; (c) The coverage of Sentinel-1A covering the city of Birmingham, Alabama	122
Figure A.9 The soil profile map of the Village Creek mine in Birmingham, Alabama	124
Figure A.10 (a) Shows the total PS in the area under observation. (b) Stable PS has been removed, and high displacement PS are only shown. (c) Shows the total PS in the region of concern (d) Shows only the PS which have experienced high displacement in the region	126
Figure A.11 (a) Shows the high displacement PS on the railway track east of the site. 2 PS are highlighted to observe the progress of displacement. (b) Shows the displacement over time for the highlighted displacement.	126
Figure A.12 (a) Shows the high displacement PS on the railway track close to the mine cliff. 2 PS are highlighted to observe the progress of displacement. (b) Shows the displacement over time for the highlighted displacement.	127
Figure A.13 Oregon Maupin Site: (a) Location on the map; (b) Street view of rockfall site; (c) Sentinel 1-B coverage for primary and alternate orbits; (d) Sentinel 1-A coverage	129

Figure A.14 (a) The displacement map superimposed on the optical image.  (b) PS analysis results with displacement (c) Shows the progress of the displacement over time of one PS point.	131
Figure A.15 Post-Event Analysis Total deformation map of Persistent Scatterers. No significant position change noted.	133
Figure A.16 (a) Coherence from 9/17 to 9/29/2019. (b) Rainfall during September 2019. (c) Displacement progress of a PS point near the rockfall event.	133
Figure A.17 Coherence maps: (a) 12-day period right before the event; (b)  Coherence during the event	135
Figure A.18 (a) Shows the location of the sinkhole near Atlanta; (b) Sentinel 1-A coverage of the region; (c) Closer view of the region where the sinkhole took place; (d) The sinkhole affecting the driveway of the resident.	137
Figure A.19 The soil profile map of the region in Dekalb County	137
Figure A.20 (a) The displacement map superimposed on the optical image; (b) PS analysis results with high subsidence highlighted;(c) Show the progress of the displacement over time of one PS point.	139
Figure A.21 Burlington, North Dakota (a) Location on the map; (b) Sentinel 1-B coverage for primary and alternate orbits; (c) Sentinel 1-A coverage of the region	142
Figure A.22: The soil profile map of the region in Burlington, ND	142
Figure A.23(a) The displacement map superimposed on the optical image; (b) PS analysis results with high displacement; (c) Shows the progress of the displacement over time of one PS point.	146
Figure A.24 (a) Coherence from 03/24 to 04/05/2022 (b) Coherence from 04/05 to 04/17/2022 (c) Coherence from 04/17 to 04/29/2022	146
Figure A.25(a) Coherence from 04/29 to 05/11/2022 (b) Coherence from 05/011 to 05/23/2022 (c) Coherence from 05/23 to 06/05/2022	148
Figure A.26 (a) Shows the location of the derailment near the center of the town shiner: (b) shows the derailment: (c) The coverage of Sentinel-	

1A's Ascending orbit; (d) the coverage of Sentinel-1A's descending orbit.	151
Figure A.27 The soil profile map of the region in Shiner Texas	153
Figure A.28 (a) shows the PSInSAR analysis combining both satellite orbits. (b) shows PS with high displacement. (c) shows the near the great crossing where the train derailment took place. (d) shows the displacement over time of the PS near the great crossing	154
Figure A.29 (a) Shows the locations where significant damage to infrastructure took place; (b) Shows the flooding event near Gardiner River; (c) The coverage of Sentinel-1A covering Yellowstone Park and cities surrounding it	156
Figure A.30: Shows the region under observation.	158
Figure A.31 (a) Shows the PSInSAR deformation points; (b) Shows the area of instability in the area under observation	160
Figure A.32 (a) Shows the Yellowstone monitoring region and the railway track connecting Cody and Ralston; (b) Shows the BNSF rail network in the region.	160
Figure A.33 (a) Shows the results from PSInSAR analysis over the region; (b) Shows the stable points of analysis being removed with only high subsidence PS; (c) Shows the high PS surrounding railway right of way near the railway track connecting the city of Cody and Ralston; (d) Shows the average displacement over time of PS points with high subsidence.	162
Figure A.34 (a) Shows the location of the railway line facing disruption; (b) Shows the area under observation; (c) Shows the Sentinel-1A Ascending orbit with the area under observation being highlighted; (d) Shows the Sentinel-1A Descending orbit with the area under observation being highlighted.	164
Figure A.35 Soil map of the region	164
Figure A.36: (a) shows the high displacement PS for the region using Sentinel-1A Ascending orbit; (b) shows the high displacement PS for the region using Sentinel-1A Descending orbit	166

Figure A.37 Show the high displacement PS near Oceanside with (a) showing the Sentinel-1A Ascending orbit and (b) showing the Sentinel-1A Descending orbit	168
Figure A.38: Shows the high displacement PS between Oceanside and San Clemente (a)(c)(e) shows the PS analysis from Sentinel-1A Ascending orbit (b)(d)(f) shows the PS analysis from Sentinel-1A Descending orbit.	168
Figure A.39 (a) Incident site; (b) Derailment; (c) Locomotive view of rockfall; (d) Two distinct slope failures ~100 m apart	169
Figure A.40 Shows the site classification for the derailment study	171
Figure A.41 DS Accumulation at (a) 6 months; (b) 5 months; (c) 4 months; (d) 3 months; (e) 2 months; (f) 1 months; (g) 19 days; and (h) 7 days before the rockfall event and derailment	173
Figure A.42 (a) Clustering and critical area identification; (b) DS Clustering timeline shows the DS cluster density in the critical subset and the timeline of the change	174
Figure A.43 (a) The train derailment; (b) The accident on the world map; (c) The location of the derailment in the town of Raymond, MN; (d) The data path of Sentinel-1A covering the region with the accident highlighted.	176
Figure A.44 The soil profile map of the region in Raymond, MN	178
Figure A.45 (a) shows the total PS over the observation area. (b) Shows high displacement PS with stationary points removed. (c) Shows the area where the derailment took place. (d) Shows the average subsidence monitored in the region	180
Figure A.46 Quinn's Hot Springs Resort, Montana, Derailment Site: (a) Location; (b) Derailment	183
Figure A.47 Data availability for Site: (a) Sentinel-1B original overage; (b) Sentinel-1A inadequate coverage	183
Figure A 48 Shows the railway derailment taking place	185

Shows the location of the accident; (c) Highlights the optical image of the cracks in the region; (d) Shows the deformation over time of
the high PS
Figure B.1 The relationship between normalized moisture changes and normalized coherence
Figure B.2 The relationship between normalized moisture changes, coherence, and rainfall for Yosemite Sentinel-1A orbit-1 data
Figure B.3 The relationship between normalized moisture changes, coherence, and rainfall for Yosemite Sentinel-1A orbit-2 data
Figure B.4 The relationship between normalized moisture changes, coherence, and rainfall for Bodega Sentinel-1A orbit-1 data
Figure B.5 The relationship between normalized moisture changes, coherence, and rainfall for Bodega Sentinel-1A orbit-2 data
Figure B.6 Santa Barbara site: Normalized soil moisture, rainfall, relative humidity and signal coherence as a function of time
Figure B.7 The relationship between normalized moisture changes, coherence, and rainfall for Cortez Sentinel-1A orbit-1 data
Figure B.8 The relationship between normalized moisture changes, coherence, and rainfall for Cortez Sentinel-1B orbit-1 data
Figure B.9 The relationship between normalized moisture changes, coherence, and rainfall for Cortez Sentinel-1B orbit-2 data
Figure B.10 The equipment deployed in the site (a) Remote Sensing Station (b) Solar panel (c) Leaf wetness smart sensor (d) Repeater (e) Modulator (f) Light Sensor (g) Soil moisture sensor (h) Soil moisture sensor (i) Solar Radiation Shield (j) Runtime Smart Sensor (h) Soil moisture (l) Davis Angementar (m) Rein Cause
(k) Soil moisture (l) Davis Anemometer (m) Rain Gauge
Figure B.11 The moisture content sensors are denoted by the black boxed numbers, and the middle red triangle represents the main sensor
Figure B.12 Shows the relationship between normalized coherence,
rainfall and soil moisture

Figure C.1 Show the three sub-swaths in TOPSAR acquisition	220
Figure C.2 Shows part of the unprocessed SAR image of the city Columbia, SC. The image shows a distinct salt and pepper look separated by multiple swaths	223
Figure C.3 (a) Shows the SAR image that is not multi-looked. (b) Shows the multilooked image (a) to a factor of 5:20[1]	225
Figure C.4 Shows the workflow of MT-InSAR process	238
Figure C.5: Rolling Stack MTInSAR analysis concept	247

# LIST OF SYMBOLS

$arphi$ or $\delta\phi_{int}$	Interferometric Phase
γ	Coherence component.
$h_{rms}$	Root mean square height.
$\theta$	Incident angle.
Α	Amplitude.
σ	Radar reflectivity.
I	Intensity.
R	Radar Range.
μ	Theoretical precision
λ	Wavelength of radar signal
B <sub>perp</sub>	Critical baseline in perpendicular direction.
Н	Satellite altitude.
f	frequency of the radar.
$BW_r$	Range bandwidth.

Interferometric Phase

## LIST OF ABBREVIATIONS

ROW Right of Way	ROV
InSARInterferometric Synthetic Aperture Radar	InSA
PSInSAR Persistent Scatterer InSAR	PSI
CCD	CCI
SBAS	SBA
FBG Fiber Bracket Grating	FBC
E.M Electro. Magnetic	E.M
DEMDigital Elevation Model	DEN
DS	DS.
LOS Line of Sight	LOS
MTInSAR	MT]
SVD	
USCRN	
ESA European Space Agency	ESA
ASF	ASF
GEE	GEF
USGS	USC
SLC Single Look Complex	
GCP	
RSRolling Stack	

### **CHAPTER 1: INTRODUCTION**

Geohazards are critical geologic conditions with a high potential to cause significant damage to infrastructure, property, and even loss of life. Shallow geohazards occur in the upper layer of the earth's crust and directly affect infrastructure [2]. These geohazards progress slowly over long periods of time, and they are relatively stable until triggered by external events such as rainfall, mining, and construction [3]. Railway right of way often traverses natural or constructed slopes susceptible to shallow geohazards such as landslides and subsidence [4]. Failures associated with these hazards cause derailments, significant damage to railway infrastructure, and transportation service disruption, resulting in economic losses and potential safety risks. The early detection of shallow geohazards relies on identifying and monitoring their underlying causes. Using satellite radar data to detect precursors of shallow geohazards in railway right of way is an innovative approach that can significantly improve early warning and mitigation strategies [5]. Interferometric Synthetic Aperture Radar (InSAR) techniques have been widely used in displacement monitoring [6] of areas that have already been identified as critical. InSAR provides a unique combination of high-resolution, wide-area coverage, and non-invasive monitoring, making it an ideal tool for this work's objectives.

### 1.1 Background

Railway transportation is an essential element in modern economies [7], as it is a sustainable [8], reliable [9], and efficient mode of transportation for passengers and

freight across extensive networks. Rail networks play an important role in economic growth [8] because they facilitate trade, connect industries, and ensure the movement of goods over vast distances, often at less expensive costs and with less environmental impact than other modes of transportation [9].

Furthermore, railway infrastructure is becoming an increasingly critical asset as it expands to accommodate the demand for freight and passenger services [8]. This expansion demonstrates the railway industry's responsiveness to contemporary commercial demands and the growing focus on sustainable transportation solutions [10]. Rail travel utilizes considerably less fuel per ton-mile than road transport and has a reduced carbon footprint, rendering it a favored option for sustainable infrastructure [9]. Moreover, the dependability of rail systems, less influenced by meteorological and traffic variables than road or air transport, highlights their significance in preserving supply chain stability and service continuity [11].

The extensive breadth of railway networks from the expanding use of railways sometimes leads them to navigate difficult terrains, making them susceptible to environmental hazards such as landslides, subsidence, and erosion. These geohazards threaten infrastructure integrity and safety, as they may result in interruptions, delays, and, in extreme instances, derailments. The economic ramifications of these hazards surpass infrastructure maintenance expenses, encompassing wider effects such as delays in commodities transportation, diminished productivity, and possible human fatalities [12]. Thus, the efficient oversight and upkeep of railway infrastructure are essential to mitigate these risks and preserve rail transit's economic and social advantages [13].

One of the most common of these geohazards is landslides, caused by multiple natural and man-made factors or a combination [14]. They occur when rocks, loose soil, and debris move downhill due to excessive moisture or site mobilization [15]. Landslides present a significant hazard as they potentially obscure pathways hindering train operations. A landslide affecting a railway line suspends operations and necessitates extensive clearance activities, potentially resulting in service disruptions lasting days or weeks. This research began with identifying mudslide-inducing factors using a radar satellite in the TGV derailment near Ingenheim, France, on March 5, 2020 [2] (Figure 1.1a) and the CSX derailment near Draffin, Kentucky, on February 13, 2020 [3] (Figure 1.1b). These landslides blocked the railway track, leading to service disruption and loss of lives. The slow sinking or settling of the ground is called subsidence. It can make the foundation of a railroad unstable, leading to uneven tracks that need to be fixed and maintained all the time [16]. Subsidence can result in uneven settling of railway tracks, causing track deformation and misalignment. Over time, these deformations undermine track stability, necessitating frequent repairs and increasing the risk of derailment [17]. Subsidence along the railway Right of Way (ROW) typically progresses gradually but intensifies after precipitation and compromises soil stability. The economic impact of subsidence includes not only the costs of repairs but also the long-term effects on track upkeep, which raises costs and shortens the life of the infrastructure. Erosion, frequently induced by water runoff, undermines embankments and track foundations, heightening the risk of slope failures that impede railway lines or result in track washouts [15]. Erosion of embankments comprises, endangering the track base and necessitating immediate action to prevent breakdowns [18]. These hazards are generally slow-moving



Figure 1.1 Recent derailment events due to landslides: (a) TGV derailment Ingenheim, France, 3/5/2020; (b) CSX derailment Draffin, Kentucky, 2/13/2020[3][4].

but can accelerate swiftly under specific circumstances, such as after intense rainfall, soil saturation, or seismic activity.

passengers and goods, railway operators can take preventive actions when they can detect early conditions of probable ground movement or soil instability. This is made possible by effective monitoring. By implementing sophisticated geohazard monitoring systems, railway operators can diminish the frequency and severity of service disruptions, minimize maintenance expenses, and prolong the lifespan of essential infrastructure. Geohazard monitoring is essential for risk management in railway infrastructure, protecting the network from the unpredictable and often catastrophic effects of natural and human-induced ground hazards. By implementing thorough monitoring, rail operators can improve operational resilience, maintain safety standards, and reduce the economic impact of geohazard-related disruptions. Monitoring systems based on satellite radar imaging, such as Interferometric Synthetic Aperture Radar (InSAR), offer continuous data across broad and remote areas for early detection and analysis of ground deformation and soil moisture changes.

#### 1.2 Research Problem

Geological hazards are complicated processes caused by man-made (such as urbanization and deforestation) and natural (such as earthquakes and tsunamis) elements. Thus, geohazard susceptibility maps that consider multiple factors are crucial to detect and mitigate their effects on railway infrastructure effectively [19]. The risk prediction models for monitoring geohazards use data categorized as static and time-varying, respectively. Static data encompasses a wide range of information, including topography,

soil profiles, historical activity, and land use. On the other hand, time-varying data is collected at regular intervals through specialized sensors tailored to specific objectives such as weather and rainfall patterns, soil moisture levels, seismic activity, and site movements. Models like the rainfall threshold models predict landslides by utilizing rainfall intensity data with historical landslide occurrences [20]. These models use static data like terrain characteristics, historical occurrences, and soil types with time-varying data from weather and soil moisture sensors near the regions most likely to experience geohazards [21]. When high-risk regions experience intense rainfall exceeding the threshold, landslide warnings are triggered [22]. Hydrological models stimulate water flow through topography to assess the potential for slope failure. These models utilize real-time soil moisture, groundwater levels, and streamflow measurements and are integrated to assess the potential for slope instability [23] [24]. On the other hand, geotechnical models concentrate on the soil and rock properties to detect slope stability and utilize active sensors to monitor slope deformation [25]. Existing models have two important needs to be addressed in order to increase the precision and predictive power of geohazard models. Initially, it is essential to identify specific locations—rather than merely general areas—that are at heightened danger. This localized identification offers a targeted strategy for monitoring and mitigation initiatives. Secondly, installing sensors that can gather time-varying information, including ground movement, soil moisture, or seismic activity, is important. These sensors deliver real-time data that can monitor the fluctuating conditions leading to geohazards, facilitating more precise and prompt predictions. Although planning and risk mitigation benefits greatly from these broad evaluations, the inability to identify precise monitoring locations and the resourcedemanding characteristics of instrumentation highlights the necessity for progress in geohazard prediction tools [21]. Integrating InSAR-based remote sensing data and developing cost-effective, scalable sensor technology will be essential. By resolving the deficiencies of existing geohazard models, they can evolve from general regional evaluations to specific, actionable insights, increasing their effectiveness in safeguarding lives and infrastructure.

### 1.3 Research Objectives

The dissertation focuses on establishing an innovative framework that utilizes satellite radar imagery and other data sources to monitor and identify high-risk zones for geohazards. The proposed technique is developed based on the InSAR family of satellite radar signal processing techniques and monitors for earth surface mobilization and soil moisture changes. This methodology fills a major gap in current geohazard monitoring methods, which lack the scalability required for continuous, non-invasive observation of broad areas like railway corridors. To bridge this gap, this research addresses key questions related to geohazard monitoring and InSAR analysis.

First, the region being monitored is classified. The classification system has been developed and implemented to determine the effective InSAR technique. Based on the site class, the dissertation also investigates the adaptation and optimization of Multi-Temporal InSAR techniques, including Persistent Scatterer InSAR (PSInSAR), Small Baseline Subset (SBAS), and Coherence Change Detection (CCD), for regional-scale geohazard monitoring.

Second, this research examines the detection and quantification of surface

mobilization preceding collapse using InSAR techniques. The hypothesis underpinning this inquiry is that areas near geohazard-prone zones exhibit measurable subsidence, frequently occurring weeks or months before failure. The study then looks into the relationship between changes in soil moisture content and changes in radar signal coherence. The hypothesis is that considerable variations in soil water content increase failure risk, and this phenomenon is assessed by studying coherence changes in radar imaging.

Finally, this research introduces three new postprocessing techniques to enhance risk potential identification over large regions. When used in tandem, these techniques display regions experiencing significant activity and locations most susceptible to failure.

The proposed system's efficacy is confirmed by real-world studies of recognized geohazard events, demonstrating the framework's robustness, reliability, and applicability to various scenarios. This dissertation addresses research topics to develop a scalable, non-invasive monitoring system for the early detection and risk assessment of geohazard-prone areas, offering actionable insights for railway safety and maintenance.

## 1.4 Organization of the Thesis

This thesis is structured comprehensively to guide the reader through the study of geohazards and the use of satellite radar imagery as a monitoring tool. It covers foundational concepts and introduces new monitoring methods, ensuring a thorough understanding of the topic.

In Chapter 2 we review the types of geohazards affecting railway infrastructure and evaluate traditional monitoring approaches such as geotechnical sensors and LiDAR.

We then introduce the principles of Interferometric SAR (InSAR), highlighting how radar phase differences can be used to detect ground movement. The chapter explores advanced multi-temporal InSAR techniques—PSInSAR, SBAS, and Coherence Change Detection (CCD)—and discusses their advantages and limitations in monitoring deformation and soil moisture changes in vulnerable areas.

Chapter 3 presents the framework for geohazard monitoring using MTInSAR techniques. It begins by introducing a site classification based on terrain, vegetation, and data availability. The chapter details key geometric and surface parameters affecting SAR data quality. The chapter outlines a multi-stage analysis workflow, including SAR data acquisition, preprocessing, and processing using PSInSAR, SBAS, and CCD. It concludes by describing limitations of these methods and the need for overcoming them.

Chapter 4 discusses the three post-processing techniques introduced to enhance geohazard detection: Thresholding, Accumulation, and Clustering Timeline. The Accumulation method is used to identify progressive deformation patterns, while the Clustering Timeline highlights consistent spatial anomalies indicative of potential hazard zones. These methods are applied are shown to improve early warning capabilities and geospatial data interpretation.

In Chapter 5 a comprehensive analysis of Wayanad landslide is conducted, the results of multi-site analyses using MTInSAR techniques are presented, demonstrating the capability of satellite radar imagery to detect early-stage ground movement and geohazard activity confirmed the framework's ability to detect subtle pre-failure activity, providing critical insights into deformation dynamics and improving early hazard identification across diverse terrains.

In Chapter 6 presents the results of the InSAR analysis. It is divided into two key sections: the first deals with site mobilization, and the second focuses on the development of soil moisture models based on the satellite data collected in known sensor locations.

Finally, Chapter 7 concludes the thesis, summarizing the findings and offering recommendations for future research. Potential avenues for further exploration in automation are discussed, aiming to refine and expand the use of SAR technology for geohazard monitoring.

#### **CHAPTER 2: LITERATURE REVIEW**

Geohazards, which include natural events like landslides, earthquakes, and volcanic outbursts, are very dangerous to people, buildings, and the environment.

Advanced monitoring and analytical techniques are necessary to mitigate these threats.

This chapter gives an overview of the geohazards that have been monitored in this work, focusing on their effects and existing monitoring strategies. Furthermore, this chapter introduces the fundamentals of Synthetic Aperture Radar (SAR) remote sensing, which is an effective method for monitoring and assessing geohazards.

### 2.1 Overview of Geohazards in Railway Infrastructure

Geohazards consist of diverse natural disasters, frequently originating from complex interactions between geological formations, hydrological systems, and other natural phenomena. Some of the common examples of geohazards are landslides, rockfalls, earthquakes, volcanic eruptions, and tsunamis. Earthquakes and tsunamis are geohazards that cannot be monitored as they are caused due to tectonic activity. These geohazards trigger other geohazards due to their location, creating a cascading effect.

Landslides, being an increasingly frequent geohazard, possess the potential to inflict severe repercussions upon both populations and infrastructure. Various sources can initiate landslides; however, water is predominantly a triggering agent and, in some cases, the cause for the landslide, like in the case of mudslides, which trigger due to a sudden

increase in soil moisture. Intense precipitation has the potential to saturate the soil [26], leading to the occurrence of debris flow and mudslides that descend slopes, causing great harm [27]. The process of deforestation worsens the porous nature of the soil, rendering it increasingly vulnerable to the occurrence of landslides [28]. Moreover, the presence of water has the potential to elevate pore pressure in the subsurface, substantially compromising the cohesive properties of soil. Comprehending these causal elements is crucial in formulating efficient monitoring and mitigation approaches [29] [30].

Rockfalls fall under the landslide category. They occur when rocks detach from a steep slope with minimal or nonexistent lateral movement before the event. This phenomenon occurs swiftly, with the detached particles subsequently rolling down the slope [31]. The main forces that induce the fall of unstable rocks include triggering mechanisms such as water, ice, earthquakes, and vegetation development. Water infiltration into fissures within the underlying rock strata can lead to the accumulation of pressure exerted on hazardous rock formations. Water may penetrate fissures in the rock and undergo freezing, leading to the expansion of these fissures. The process, known as "frost wedging" or "freeze-thaw," gradually dislodges loose boulders from cliff slopes. Recent studies indicate that fluctuations in daily temperatures and the occurrence of intense heat can also lead to the destabilization of rock slabs [15].

Debris flows are landslides that are rapid, gravity-driven movements of water-saturated debris, such as rocks, dirt, and organic material, that occur mostly in mountainous environments. These flows are extremely destructive because of their high velocities, huge impact forces, and ability to transport massive amounts of debris across great distances. Heavy rainfall is a common cause of debris flows because it quickly

saturates loose sediments, reducing stability [32]. Rainfall-induced landslides can transform into debris flows as the landslide material gets fluidized, a phenomenon that is heavily impacted by early soil moisture levels, which govern the initiation mechanisms. Furthermore, channel degradation and sediment mobilization play an important role in debris flow development. Surface runoff in mountainous places concentrates in channels, eroding and mobilizing silt, especially in areas with plentiful loose material at the base of high cliffs. As a result, silt is constantly added to the flow, increasing its size and capacity for destruction. This is known as the progressive bulking effect [33].

Sinkholes are depressions or holes in the ground formed by the collapse of a surface layer. They can occur naturally, owing to the dissolution of soluble rocks such as limestone, gypsum, and salt, or they can be caused by human activity [34]. These geological characteristics represent substantial infrastructure and human safety dangers, needing further investigation and management. Sinkholes are classified into three types: collapse sinkholes, which are large, sudden depressions caused by the collapse of ground into voids created by dissolving rocks; subsidence sinkholes, which are shallow, expansive depressions caused by gradual ground settling over dissolving beds of halite, gypsum, or glauberite; and cover-collapse sinkholes, which are smaller features often induced by human activity and formed by sediment migration into dissolution voids [35].

The geohazards described above commonly exhibit subtle indications of an approaching failure, gradually manifesting before a catastrophic disaster. Identifying these initial indicators is important in mitigating the risk of casualties and asset damage [36]. Small-scale landslides or minor ground movements can be precursors to larger, more devastating landslides. Identifying these indicators and promptly implementing

appropriate actions are integral to efficient landslide mitigation strategies [37].

# 2.2 Methods of Geohazard Detection and Monitoring

Effective geohazard detection and monitoring requires various sensors for early warning purposes, and are critical for reducing the threats these disasters cause. These sensors are used to identify initiation mechanisms and failure dynamics. Each sensor has unique constraints that must be understood to optimize its application. Conventional geotechnical assessments involve intrusive drilling and excavation to discover and map soil and rock structures, features, and engineering properties. These methodologies are essential for comprehending local subsurface geological and geotechnical conditions and critical for evaluating geohazards such as slope failures and earthquake damage [38](Figure 2.1). Even though they are crucial, conventional geotechnical sensors frequently have high precision, but poor durability, and high sensitivity to external interferences, which might restrict their usefulness in early warning systems and real-time monitoring [39]. Recent advances in fiber optics have shown that specific sensors like Fiber Bracket Grating (FBG) sensors transmit all light wavelengths and reflect specific Bragg wavelengths. The shift in response of this wavelength is attributed to changes in temperature strain or pressure, allowing for precise measurements of these parameters [39]. Despite being widely used for real-time monitoring, FBG sensors have drawbacks when used in the field, including sensitivity to environmental changes and the requirement for reliable installation methods [39]. Lidar technology has significantly transformed landslide monitoring by utilizing laser pulses to generate topographical maps of exceptional detail [40]. The capacity to infiltrate vegetation cover offers vital insights into the topographical conditions and stability of slopes [41] [42]. Studies have shown

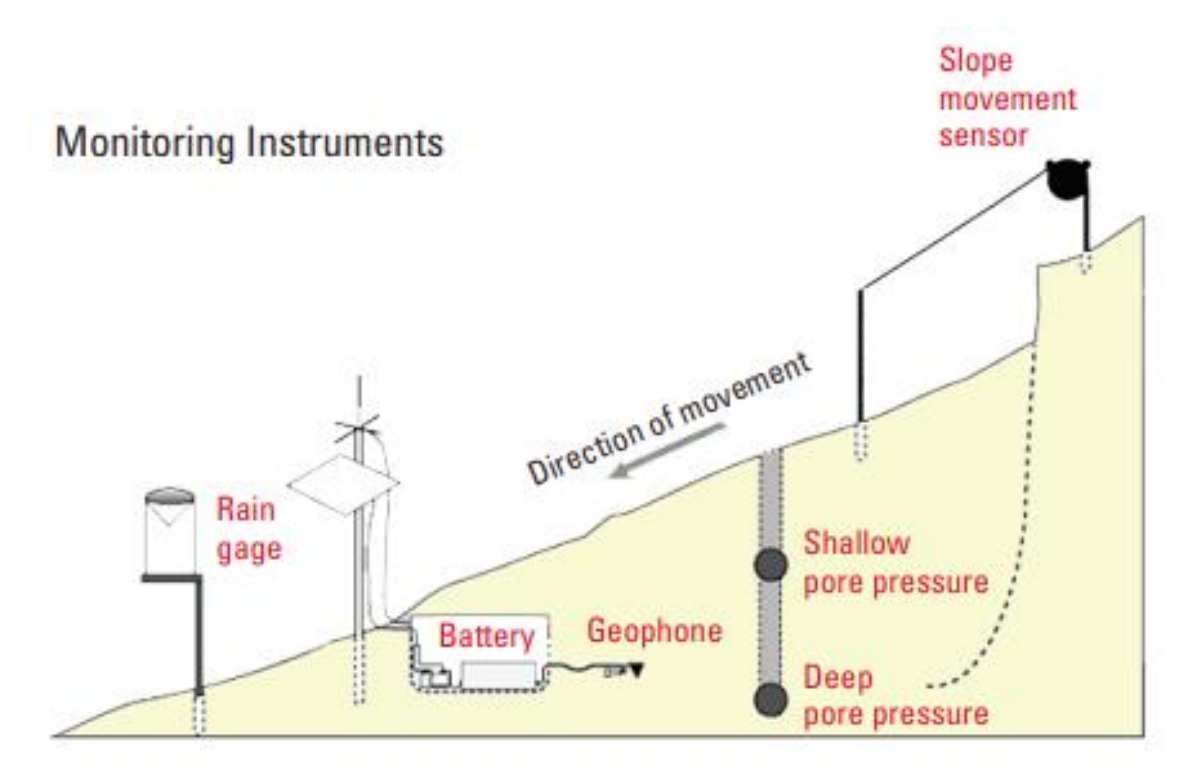


Figure 2.1 This image shows multiple monitoring instruments used to monitor a geohazard

LIDAR is efficient in the seasonal mapping of landslide activities and measuring their mobilization [43]. Nevertheless, LIDAR has limitations, such as reduced operational effectiveness during adverse weather conditions, infrequent data collection intervals, and reliance on aerial platforms, primarily airplanes, as opposed to satellites, albeit with limited exceptions. The utilization of LIDAR is accompanied by significant financial implications due to its inherent disadvantages [44].

Some common sensor types, like rain gauges, soil moisture sensors, and pore-water pressure sensors, monitor the influence of water and how it may induce geohazards. Meanwhile, flow stage sensors, ground vibration sensors, and video cameras monitor the surface change itself. Data from these sensors is varied, and data interpretation is crucial to analyzing information derived from these monitoring systems. This process allows specialists to evaluate the stability of slopes and detect any potential anomalies or risk factors that may be present [45] [16]. Every sensor category employed for geohazard monitoring possesses distinct limitations, including environmental sensitivity, data integration difficulties, and operational constraints. Different sensor technologies are commonly combined to overcome these constraints to improve geohazard detection and management capabilities. Integrating data from diverse sources and enhancing sensor technology can result in more efficient geohazard monitoring and risk reduction measures [46].

# 2.3 Geohazard Risk Prediction

Geohazard risk prediction or susceptibility mapping is a crucial area of study focused on comprehending and mitigating the effects of geohazards. The field uses many

approaches and technologies to evaluate, forecast, and mitigate risks. Geohazard risk prediction is done by mapping or modeling the hazards. The maps show geohazard zonation and the probability of geohazard occurrence given a set of environmental conditions. This statistical assessment of geohazard susceptibility assumes that future geohazards would occur under conditions similar to previous ones [47].

Parameters that make the region vulnerable to movement and triggering processes that initiate the movement are considered to model geohazard susceptibility and hazard [48]. These parameters are monitored based on existing static data, and discreet sensors are used to monitor real-time data. Geological and geotechnical factors significantly influence risk prediction, including fault lines, granite formations, soil mineralogy, and slope stability. This information is frequently obtained from digital elevation models, surveys, and historical maps, which fall into the static data categories as they stay relatively constant throughout the year [49]. Geohazards are triggered greatly by environmental and climatic factors, such as precipitation and temperature, such as permafrost thawing. These factors are monitored using discreet time-varying sensors that provide reliable data for specific regions. Although time-varying sensors are accurate in most cases, they have limitations related to accessibility and disruptions due to environmental factors like flooding. Some remote sensing technologies like LIDAR and GIS have been shown to mitigate these limitations and are being integrated into current risk prediction approaches [47].

In the literature, risk prediction models are based on various data sources and parameter combinations [50] [51]. This is because each geohazard has unique characteristics, and factors influencing it differ based on site characteristics [52]. When

all available parameters are utilized, correlated and redundant information is probably considered, which may result in a map with a lower degree of accuracy [53]. An explanation for this phenomenon is the Hughes effect or the curse of dimensionality. However, some common parameters in most models are the site mobilization and soil moisture content [50] [54]. In this work, satellite radar techniques are shown to be effective alternatives to monitor these parameters compared to discreet time-varying sensors. This work also shows a new way of identifying geohazard susceptible regions based on radar signal processing techniques.

## 2.4 Satellite Fundamentals

#### 2.4.1 Satellite Radars

Radar satellite sensors have been valuable sources for monitoring change detection. These sensors capture target parameters different from optical sensors by providing unique information. A radar sensor operates within the microwave range of the electromagnetic (EM) spectrum (Figure 2.2). The band has a wavelength in the centimeter range. This results in radio waves penetrating substances such as heavy cloud cover, fog, and rain. Most radar sensors are active sensors, meaning they do not rely on the sun to illuminate their targets and are not influenced by the day-night cycle [6]. Finally, the most important property of radar sensors is that they are coherent sensors. A coherent sensor can generate an electromagnetic field that maintains a consistent phase relationship between the electric field value, location, and time. This enables the radar sensor to precisely capture every ground target's amplitude and phase information.

Amplitude values correspond to the radar backscatter, where a brighter pixel on the radar

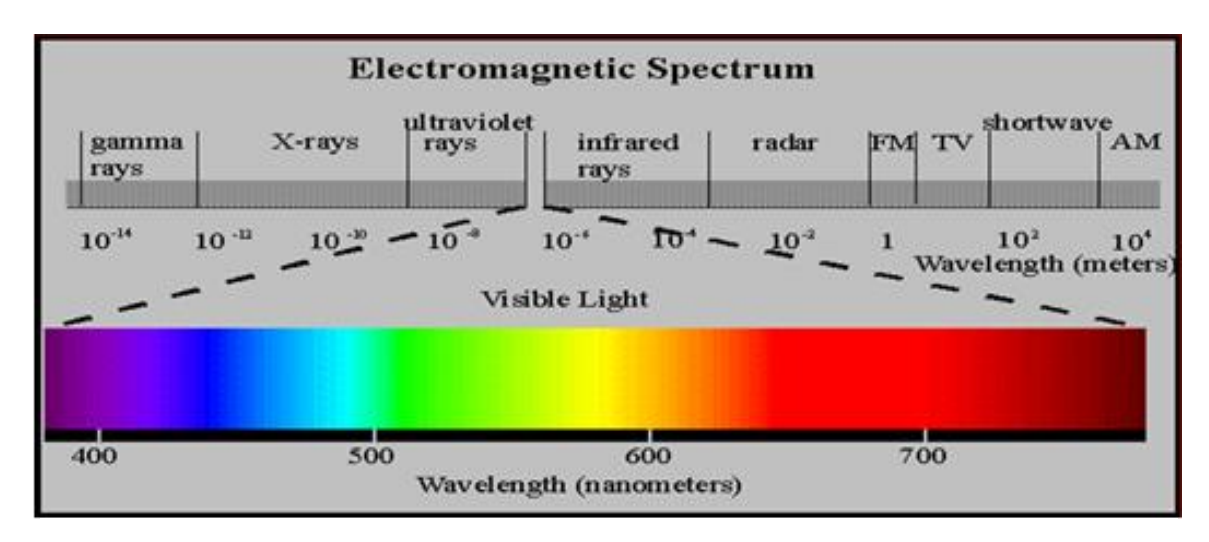


Figure 2.2 The electromagnetic spectrum is shown here.

image of the target indicates a higher backscatter signal intensity at the corresponding point of the target. The phase value is determined by the distance between the sensor and the target and the interaction between the electromagnetic signal and the ground surface. Radar signals exhibit different interactions with the surface compared to other sensing systems, providing interesting new information about the observed environment [55].

SAR interferometry, commonly known as Interferometric SAR or InSAR, relies on the coherent fusion of complex SAR images. The phase of a single Synthetic Aperture Radar (SAR) image is predominantly random, lacking any discernible pattern, and hence does not provide valuable insights into the target. Nevertheless, the cohesive combination of the phase of two or more SAR images does contain valuable target data, and the utilization of these phase serves as the foundation of SAR interferometry.

Multiple methods exist for constructing an interferogram. For the interferogram to be beneficial, the SAR images must be distinguished from one another, typically in terms of their imaging geometry, imaging time, or both.

This research works with satellite images captured at separate points in time and from the same or slightly varied spatial positions. The two cross-correlated images are called an interferometric pair, and their cross-correlation produces a SAR interferogram. The term used to refer to the phase of a SAR interferogram is the interferometric phase. InSAR also measures the interferometric coherence, quantifying the similarity in SAR images.

To describe the phase components of an interferogram, it is assumed that the scattering mechanism is identical in both images, i.e., the only difference between the two

SAR acquisitions is the time delay. Then, the interferometric phase between two acquisitions can be estimated as

$$\varphi = \varphi_{topo} + \Delta \varphi_{prop} + \Delta \varphi_{scat} + \Delta \varphi_{\delta R} \tag{1}$$

Where " $\varphi$ " is the interferometric phase between two acquisitions; " $\varphi_{topo}$ " is the topographic phase component; " $\Delta\varphi_{prop}$ " is the delay difference in phase activity due to atmospheric conditions like the presence of water vapor; " $\Delta\varphi_{scat}$ " is the change in scattering behavior. This component can be due to surface characteristics like changes in dielectric constant or other phase contributions like temporal decorrelation; and " $\Delta\varphi_{\delta R}$ " is the displacement of the reflected scatterers between the two acquisitions in the satellite line of sight direction.

Each component of the interferometric phase has a different application. For Digital Elevation Model (DEM) generation  $\varphi_{\text{topo}}$  is isolated. For coherence estimation,  $\Delta \varphi_{\text{scat}}$  is measured. Finally, for DInSAR application,  $\Delta \varphi_{\delta R}$  is obtained by removing the topographic phase obtained from external DEM. The atmospheric phase component is always present when trying to compute any of the interferometric components. It is only mitigated when large stacks of data are used [55].

# 2.4.2 Limitations of InSAR

InSAR analysis is widely utilized in ground deformation monitoring; however, it assumes that both SAR images share the same scattering mechanism, which is often not true in real-world scenarios due to factors such as satellite positioning and time delays that introduce errors in the interferometric phase. Common limitations in InSAR displacement measurement include temporal decorrelation, spatial decorrelation, and

noise during phase processing [56]. Temporal decorrelation arises from long intervals between radar image acquisitions, leading to changes in vegetation and topography, as well as phase delays caused by atmospheric effects in the ionosphere and troposphere. Spatial decorrelation occurs when the distance between radar acquisitions is large, resulting in significant variations in radar look angles and coherence loss due to differing pulse phases [57]. This is influenced by the satellite's baseline, defined by its position during acquisition, and is expressed through parallel and perpendicular baselines [56](Figure 2.3). Noise during phase processing stems from factors like the flat-earth effect, topographic variations, orbital errors, and atmospheric delays, all of which compromise the accuracy of ground deformation results. Advanced multi-temporal SAR techniques address these limitations by utilizing extensive SAR data stacks specifically designed to mitigate phase decorrelation and atmospheric effects [57]. Research in the late 1990s led to two primary approaches: one focusing on coherent, point-wise radar targets known as permanent or persistent scatterers (PS) and the other exploring distributed scatterers (DS) through techniques like Small Baseline Subset (SBAS).

# 2.5 Multi-Temporal SAR Techniques

The image pairs referred to as interferograms were used in early studies to identify changes between the acquisitions and obtain displacement in satellite lines of sight (LOS). Subsequently, the method was modified to incorporate a multi-temporal approach (MTInSAR) to reduce displacement measurement errors and enable tracking of surface changes over time. In contrast to the early InSAR analysis process that considers a single pair of SAR images, MTInSAR techniques combine interferograms derived from an extensive series of Synthetic Aperture Radar (SAR) images (stack of images) acquired

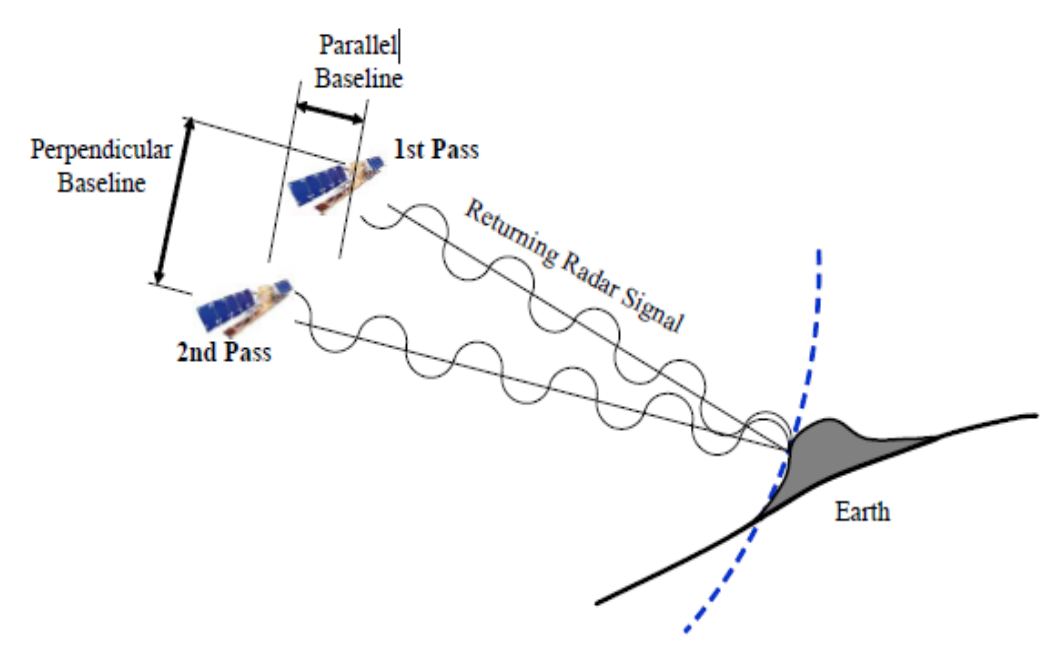


Figure 2.3 The effect of orbit baselines on the phase change is illustrated.

within the observation period. One of MTInSAR's key features is its ability to identify small surface changes over time. But during the analysis period, if there is a sudden large change (>30mm deformation, etc.) between any two acquisitions in the interferogram or the scatterer loses coherence due to other factors, MTInSAR analysis fails to monitor the change even if the surface is experiencing the deformation. The main difference among the multi-temporal methods lies in how SAR image pairs are created. The criteria for an image pair to be able to generate an interferogram depends on the baseline between them. The baseline is the distance or time between two acquisitions. If it is distance, it's called the spatial baseline, and the temporal baseline is time. For an interferogram to be viable, we need to first obtain a critical baseline in a perpendicular direction. In interferometry, there exists a critical baseline over which the generated interferogram will be pure noise. Interferometry becomes impossible as the difference in viewing angle becomes too great to prevent the overlapping of the imaged ground spectra. This critical baseline is based on the ground resolution cell, the radar frequency, and the sensor-to-target distance. The critical baseline for Sentinel-1 interferometry is approximately 5 Km, as determined by equation Eq. (6). In practice, anything more than 3/4 of the critical baseline produces significant noise. Interferometry can only be used for point-like targets when the baseline is more significant than this [1].

$$B_{perp}^{crit} = \frac{H.BW_r}{f} \frac{\sin \theta}{\cos^2 \theta} \tag{2}$$

Where,  $B_{perp}^{crit}$  is the critical baseline in the perpendicular direction; H is the satellite altitude;  $BW_r$  is the range bandwidth or inverse of the duration of the pulse; f is the frequency of the radar.

Once the baseline between two images is within the limit, we can use the image pair in MTInSAR. The Persistent Scatterer (PSInSAR) and Small Baseline Subset (SBAS) approaches are two MTInSAR techniques used for displacement measurements. The coherence change detection timeline (CCD) method is an alternate multi-temporal technique that observes changes to surface properties. The PSInSAR, SBAS, and CCD techniques are discussed below.

### 2.5.1 PSInSAR

The Persistent Scatterer Interferometric Synthetic Aperture Radar (PSInSAR) technique is one of the first developed MTInSAR [58] that employs fundamental InSAR principles over an extensive sequence of images to achieve highly accurate displacement measurements. The initial stage of the PSINSAR stacking technique involves constructing a connection graph. This step establishes a network connecting the master and slave pairs based on their baseline values, ultimately generating differential interferograms. The images in the network have a common master image based on a minimum temporal baseline for the most extreme pair. The maximum number of possible connections is equal to N-1, where N is the number of acquisitions. The image pairs are depicted graphically through connection graphs, which use the satellite acquisition date on the x-axis and the relative satellite position on the y-axis [59]. The displacement estimation begins with identifying "Persistent Scatterers" (PS) in the observation area, and they can encompass a range of objects, including urban infrastructure like buildings, windows, roofs, and railway lines, as well as natural features like rocks and roads. The PS are identified as individual pixels, or group of pixels, exhibiting consistent high coherence in all the image pairs throughout the analysis period [58].

To reduce processing time, the PS are first identified using amplitude dispersion MuSigma. In the time frame under consideration, the amplitude dispersion index is calculated as the ratio of the mean intensity value to the standard deviation  $\sigma A$  of the image intensity.

$$MuSigma = \frac{mA}{\sigma A} \tag{3}$$

A PS is present when backscattering intensity shows little temporal variability. The amplitude dispersion index calculation enables the selection of candidates for PSC (Permanent Scatterers Candidates) points at the outset without the need for phase coherence analysis. High dispersion index pixels (MuSigma=0.60%), which have comparable values throughout time and relatively high amplitude values in most conditions, make them suitable candidates for persistent scatterers. After identifying these targets, a phase history analysis is conducted to identify potential PS candidates based on their coherence. MuSigma should always be less than the threshold for coherence, as a larger MuSigma will reduce the number of PS in the identification stage. A threshold of 0.7 coherence is chosen to identify PS targets. A higher threshold for coherence would reduce the number of PS but increase the accuracy of the measured displacement. However, due to a large temporal baseline for a 25-image SAR stack, a 0.7 coherence threshold is preferable; a higher threshold reduces the presence of PS in the active monitoring region.

To obtain the deformation over time, the PS technique employs a linear model to obtain residual height and displacement velocity. Residual height is the phase error

present in the interferometric phase after the topographic component is removed. The linear model can be described by the Equation 4

$$\phi(M) = (H \times K) + (V \times T \times \frac{4\pi}{\lambda})$$
(4)

Where, " $\phi(M)$ " is the displacement phase for the M<sup>th</sup> interferogram pair; "V" is the mean displacement velocity of the observation time period; "T" is the temporal baseline between the two acquisitions in the interferogram; " $\lambda$ " is the wavelength of the radar signal used; "H" is the residual height error due to the reference DEM used; "K" is the geometric parameter which depends on the baseline and incidence angle

Equation 4 is solved using a brute force approach to obtain the displacement velocity and residual height [59]. The displacement velocity from Equation 4 is used to calculate deformation over time. An implementation example of the PSInSAR is shown in Figure 2.4 The connection graph is shown in Figure 2.4 (a), and the computed deformation map is shown in Figure 2.4 (b). Blue deformation points indicate subsidence, and red deformation points indicate the raising of the surface in the direction of the satellite's line of sight (LOS). Figure 2.4 (c) shows the connection graph for SBAS analysis with a large number of master files. The deformation analysis from the SBAS connection graph is shown in Figure 2.4 (d). The SBAS analysis is further explored in the following section

#### 2.5.2 SBAS

The Small Baseline Subset (SBAS) technique is a variant of MTInSAR analysis, which shares some similarities with PSInSAR. In contrast to PSInSAR, which primarily concentrates on observing deformation in coherent targets, SBAS analysis is primarily

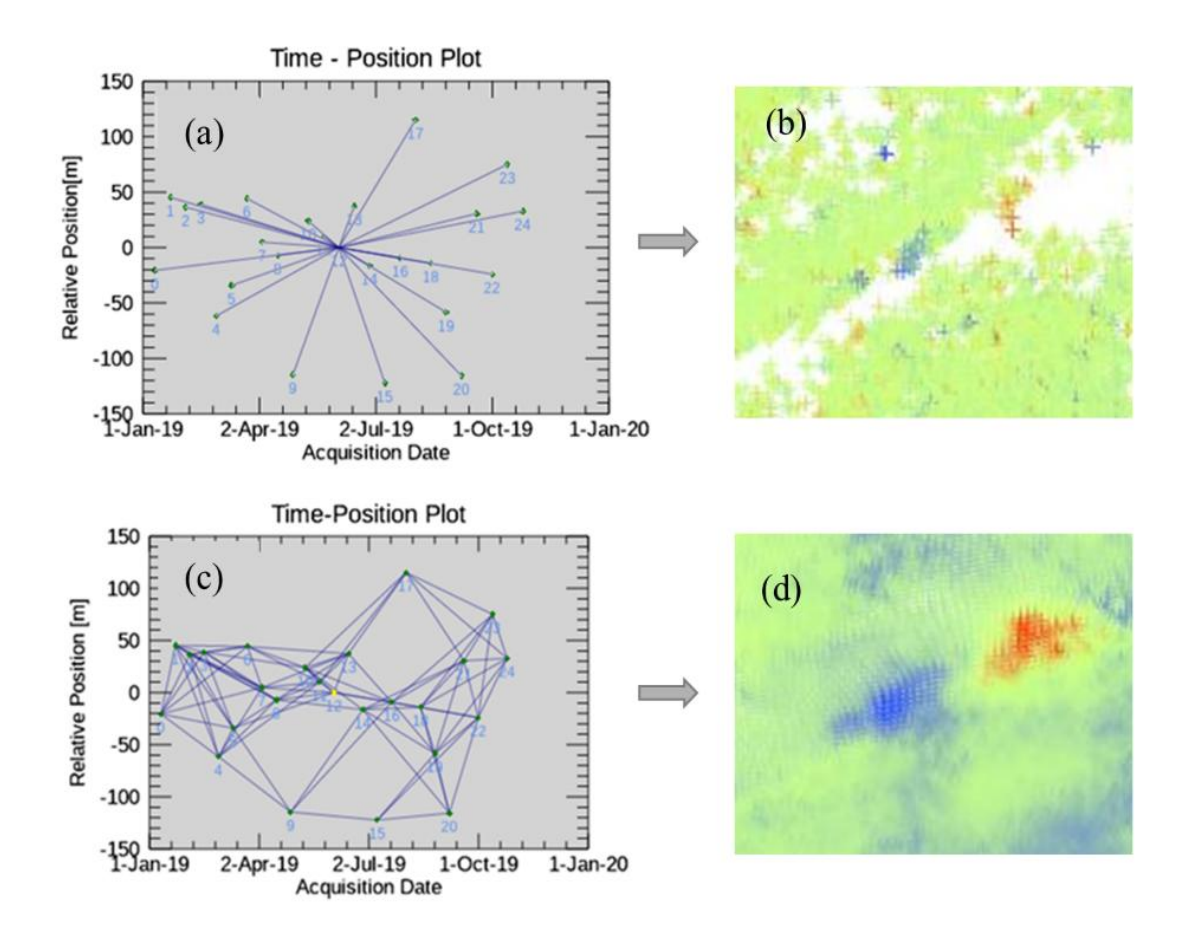


Figure 2.4 PSInSAR and SBAS analysis of the same representative site: (a) PSInSAR image connection graph; (b) PSInSAR computed deformation map; (c) SBAS image connection graph; (d) SBAS computed deformation map.

concerned with monitoring the progression of deformation in diffused radar targets known as Distributed, or Dispersed, Scatterers, (DS) [58]. The processing methodology of the SBAS technique exhibits numerous notable distinctions compared to PSInSAR. One prominent distinction is the use of multiple master images in the connection graph stage of the SBAS approach and is employed to mitigate the deterioration of coherence in InSAR pairs of PSInSAR as the temporal baseline expands in extreme pairs. The maximum number of connections in the connection graph can be described by Equation 5 where given N acquisitions, and the most significant number of viable connections M between all of the acquisitions is given by

$$\frac{N+1}{2} \le M \le N(\frac{N+1}{2}) \tag{5}$$

The criteria for interferogram pairs are generated based on the spatial baseline being shorter than 2% of the critical baseline and a temporal baseline in the 90 to 180-day range. An additional criterion based on the maximum connections for each master file is set at 10. Increasing the maximum connections increases the processing time as the number of interferograms increases, but the improvement in accuracy falls significantly after 10. Reducing the number of connections to less than 5 increases the atmospheric errors as the number of redundant interferograms decreases substantially [60].

The interferogram pairs from the connection graph are arranged in a matrix form due to the number of interferograms being larger than the number of acquisitions. The matrix is formed based on the steps described below. The interferometric phase for each pair can be described by the equation

$$\delta\phi_{int}(r,a) = \phi(t_B, r, a) - \phi(t_A, r, a)$$

$$\approx \Delta\phi_{disp} + \Delta\phi_{topo} + \Delta\phi_{atm} + \Delta\phi_{orb} + \Delta\phi_{noise}$$
(6)

Equation 6 represents the DInSAR interferogram where " $\phi_{int}(r,a)$ " is the interferometric phase for range (r) and azimuth(a) coordinates, with  $\delta$  denoting the differential interferogram i.e, interferometric phase without the topographic phase component; " $t_A \& t_B$ " represent the time of acquisition of the SAR images with  $t_A < t_B$ ; " $\Delta \phi_{disp}$ " is the deformation phase along the line of sight direction between  $t_A \& t_B$ ; " $\Delta \phi_{topo}$ " is the residual topographic phase caused by DEM inaccuracy; " $\Delta \phi_{atm}$ " is the atmospheric phase error; " $\Delta \phi_{orb}$ " is the phase error caused by the orbit; " $\Delta \phi_{noise}$ " is the random phase noise error;

The set of M interferograms from the connection graph can be represented by a system of M equations with N unknowns, which can be defined as

$$A\phi = \delta\phi \tag{7}$$

Where, A is the M X N matrix;  $\phi = (\phi(t_1), \phi(t_1), \phi(t_2), \phi(t_3), \dots, \phi(t_N))^T$  is the deformation phase N X 1 vector; The vector for the differential interferogram phase  $\delta \phi$  can be expressed as

$$\delta\phi = (\delta\phi(t_1), \delta\phi(t_1), \delta\phi(t_2), \delta\phi(t_3), \dots, \delta\phi(t_N))^T$$
 (8)

Based on the Equation 7 the deformation velocity can be described by

$$Bv = \delta \phi \tag{9}$$

Where B is M X N matrix and v is the mean phase velocity and is described as

$$v = [v_1, v_2, v_3, \dots, v_N]^T$$

$$= \left[\frac{\phi_1}{t_1 - t_0}, \frac{\phi_2 - \phi_1}{t_2 - t_1}, \frac{\phi_3 - \phi_2}{t_3 - t_2}, \dots, \frac{\phi_N - \phi_{N-1}}{t_N - t_{N-1}}\right]^T$$
(10)

The matrix Equation 9 is processed using Single Value Decomposition (SVD) and is further explored in [60]. The SBAS method utilizes a linear model similar to PSInSAR to generate deformation over time from the SVD results. An implementation example of the SBAS is also shown in Figure 2.4 The connection graph is shown in Figure 2.4 (c) and the computed deformation map is shown in Figure 2.4 (d).

This difference in processing makes SBAS analysis particularly effective in areas with low concentrations of coherent targets due to temporal factors like seasonal vegetation growth, etc. [58]. The ability of SBAS to measure deformations even when PS points are scarce, or completely absent, makes it suitable for measuring deformations in rural regions. Unlike PSInSAR, where the deformation measurements approach the actual deformations, SBAS readings have a lower level of precision due to the low coherence threshold used in the development of deformation maps [61]. In view of the deformation maps shown in Figure 2.4 (b) and (d) it is noted that PSInSAR produces a lower density of deformation points than the SBAS at the same site using the same dataset. Furthermore, the SBAS deformation map shows a larger activity region, while the PSInSAR analysis shows the exact region where the event occurred.

## 2.5.3 Coherence Change Detection Timeline

The Coherence Change Detection (CCD) approach utilizes radar waves obtained from SAR imagery to identify changes that have taken place between two consecutive images. The sensitivity of the SAR sensor to changes allows the technique to detect

subtle changes not visible in other methods. The coherence between the two images is evaluated by the sum of the spatial and temporal decorrelation of the signals, ranging from 0 to 1 [62]. The total coherence,  $\gamma_{total}$ , can then be expressed as the product of the independent terms representing different effects as.

 $\gamma_{total} = \gamma_{Geometric} \times \gamma_{DC} \times \gamma_{Vol} \times \gamma_{Thermal} \times \gamma_{Temporal} \times \gamma_{Processing}$  (11) Where,  $\gamma_{Geometric}$  represents the effects of the difference in the incidence angles between the two acquisitions;  $\gamma_{DC}$  is due to the differences in the Doppler centroids between the two acquisitions;  $\gamma_{Vol}$  represents the effects of penetration of the radar wave in the scattering medium;  $\gamma_{Thermal}$  captures the characteristics of the system, including gain factors and antenna characteristics;  $\gamma_{Temporal}$  captures the effects of the physical changes in the terrain on the scattering characteristics of the surface; and  $\gamma_{Processing}$  depends on the choice of the signal processing algorithm.

When coherence is obtained for two SAR images, which use similar geometry, the coherence contribution from  $\gamma_{Geometric} \times \gamma_{DC} \times \gamma_{Thermal} \cong 1$ . Then, the computed coherence primarily arises due to the disturbances detected on the surface of the target area [63]. The  $\gamma_{Vol}$  component of coherence is directly influenced by the extent of the radar wave. This penetration of the radar wave is dependent on the dielectric constant of the soil [64], which is directly related to the soil moisture content [65]. An area with 0 coherence has changed drastically between the image acquisitions, attributed mainly to moisture change, surface roughness, or a long time elapsed between acquisitions. While a single CCD analysis can identify critical surface and subsurface features, processing individual pairs of images is inadequate for monitoring a region over an extended period. Using a large stack of SAR images, the timeline method creates image pairs for CCD

analysis based on the chronological order of the SAR images. [65]. An example of a CCD analysis is shown in Figure 2.5. Figure 2.5 (a) shows the visual image of a site with a railroad track segment between points A and B clearly visible. Figure 2.5(b) shows a typical coherence image of the site showing high coherence along the track that is attributed to low moisture content in the track. Figure 2.5(c) shows decreasing coherence due to increasing soil moisture associated with a rainfall event. Figure 2.5(d) shows the coherence along the track being completely lost due to very high soil moisture content resulting from prolonged intensive rainfall.

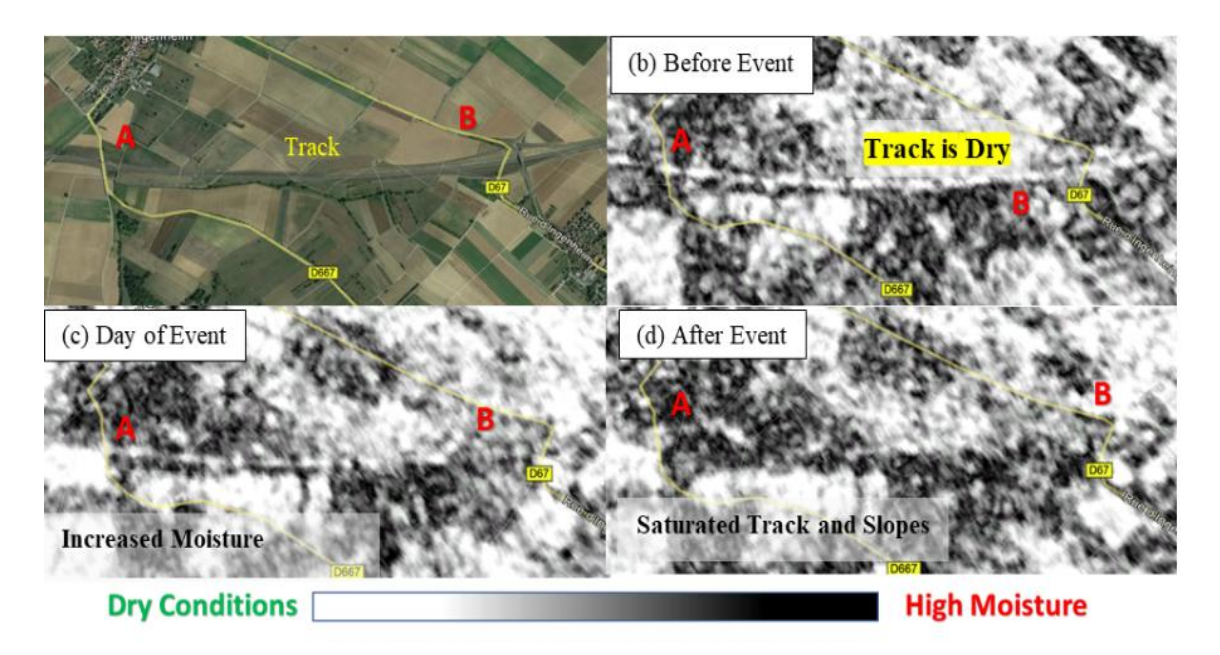


Figure 2.5 Example of CCD image analysis and correlation with water content: (a) Visual image of site with a railroad track between point A and B; (b) A typical coherence image of the site showing high coherence along the track; (c) Coherence along the track is changing due to increasing soil moisture; (d) Coherence along the track is lost due to high soil moisture content.

## **CHAPTER 3: METHODOLOGY**

Developing the technique that monitors the railway ROW for identifying critical locations exhibiting high risk for geohazard initiation is based on the study of nineteen sites with a history of geohazard events and/or availability of soil moisture measurements. The sites were studied for at least twelve months before an event date using archived and current satellite SAR data. The MTInSAR processing techniques reported by the authors [66] are implemented on these sites, and the findings are assessed based on the data quality, availability, and site characteristics. The following sections discuss the parameters affecting the quality of the results.

# 3.1 Research Approach

A systematic approach consists of two major stages to demonstrate the validity of the two research hypotheses and develop a process for geohazard monitoring along the railway ROW. The first stage conducts extensive studies on many sites where known events have taken place to develop a methodology. These studies provided key observations related to radar interaction and site conditions used in the development of the proposed technique. The technique was then used to validate and qualify the proposed procedures on a second set of geohazards. The second stage focuses on developing a workflow that integrates the procedures formulated in the first stage. The following sections discuss the research approach in detail.

### 3.1.1 Site Selection

First, several sites are identified in coordination with Class I railroads. The preliminary selection of sites is conducted based on the event type and the need for site data collection for model development and validation. The events considered in this study are:

- Landslides
- Rockfalls
- Track Settlement
- Embankment Failure
- Slope Failure
- Derailment
- Slope Stability Risk
- No event (for site data collection and/or routine satellite monitoring)

Once the sites are identified, the availability of satellite data is investigated in regard to:

- Number of satellites monitoring the site
- Number of orbits of each satellite
- Availability and length of historic data for at least 12 months before the event

Subsequently, the diverse site conditions that may affect the quality of the acquired satellite data are considered when evaluating the site. Such conditions include:

• Vegetation including seasonal variation and vegetation coverage level classified

as (i) no vegetation, (ii) Low/sparse growth, (e.g. grass typically < 5 inch), (iii) Medium growth, and (iv) Tall/dense growth (e.g. tree canopy)

- Soil condition (per OSHA classification [67])
- Main soil type (Silt/Clay/Sand)
- Topography and terrain
- Climate (e.g., rainfall, snow fall and snow cover, extreme weather conditions within a year)
- Seismicity
- Human-induced vibrations (e.g. blasts)

Subsequently, the selected sites are classified based on the quality of the gathered satellite data. This classification incorporates various factors, including vegetation coverage, soil composition, topographical attributes, proximity to significant water bodies, prevalent weather patterns, data accessibility, and data reliability.

Site classification serves as a practical guide to determine effective monitoring techniques based on site conditions. The precision and quality of ground monitoring techniques change based on these site conditions. Some monitoring techniques, like SBAS analysis, are computationally expensive. However, the precision of these techniques is lower than that of PSInSAR, and they can be applied to a broader range of site characteristics. The classification facilitates the selection of suitable InSAR methodologies. Urban locations and regions with low vegetation are optimal for Persistent Scatterer Interferometry (PSI), whereas vegetated regions with low coherence are suited for SBAS.

Site classification enhances long-term monitoring tactics, as diverse monitoring techniques are required for rapidly changing site conditions. For example, rapidly deforming areas require changing data stack size, while stable zones can be monitored with large stack sizes. This guarantees that monitoring corresponds with the specific dynamics of each location. In conclusion, site classification is an efficient guide for InSAR monitoring, as it aligns methodology, analyses, and computational resources with the changing conditions of each region, leading to more precise and actionable results.

# 3.2 Factors Influencing Data Quality

Within this thesis's scope, several site parameters that influence the effectiveness of the MTInSAR methodology are identified, and their effect on SAR data is discussed. The parameters are classified into two categories: geometric parameters and surface parameters. The following sections provide further discussion on the topic.

#### 3.2.1 Geometric Parameters

Geometric parameters are influenced by topographic features like slope grade and the alignment of the said slope. SAR sensors are side-looking sensors that monitor a region with an angle of incidence. The side-looking influences the quality of data as some regions will not be illuminated by the sensor, and others will be partially illuminated. The illumination of these regions is dependent on the topographic features, which are geological parameters, and they affect the SAR sensor measurements through geometric interactions [68]. These parameters are:

<u>Slope Grade:</u> The region under monitoring can be flat or have slope terrain. Regions that are flat reflect backscatter based on surface properties like roughness, dielectric constant,

and vegetation. However, regions with slopes are influenced by additional topographic characteristics like the steepness of the slope and its alignment. Monitoring steep slopes using SAR can be challenging due to the geometric alignment of the topographic features. In cases of steep slopes, a phenomenon called layover occurs where the imaging shows the top part of the slope being laid over the lower section of the slope. The other effect of a steep slope is shadowing, where the SAR signal does not illuminate part of the region due to the intervening slope [62]. Furthermore, these complex topographic conditions make it challenging to eliminate errors in deformation measurements. By taking into account the "local incidence angle," or the angle between the SAR look direction and the slope, a more sensible monitoring limit can be established. This range can be used as a rough guideline for the local incidence angle. As most SAR satellites have incidence angles between 20° and 50° this establishes the slope limit at approximately 50° [69].

Slope Alignment: Slope alignment is a topographic feature that affects the backscatter of SAR satellites. Current SAR satellites are polar orbiting, i.e., they orbit around the poles for each revolution and monitor Earth's surface [70]. Since the direction of the satellite is constant, when the SAR line of sight (LOS) direction is in the same direction as the slope, the SAR's sensitivity to movement along the slope is maximum. In conditions where the slopes will be directly facing the satellite, the sensitivity to slope movement is reduced since the displacement should cross a threshold in the satellite line of sight before it can be detected [57]. This phenomenon can be seen in the case of a rockfall event in Maupin, OR, where SBAS analysis was used to perform deformation analysis. The alignment of the slope in this case limited the visibility of pre-failure motion in the satellite LOS. As a

result, the event was only partially captured, highlighting the importance of considering slope geometry in InSAR-based hazard assessments as seen in Figure 3.1.

Due to the regional properties like rocky terrain, this region has high backscatter. Although the surface properties of the region were supposed to generate large backscatter the look angle contributed the most in monitoring the region. The region was monitored using Sentinel-1B, with the LOS in the same direction as the slope movement. The region showed high sensitivity to displacement measurement, and the displacement progression was noticed eight months before the rockfall event, as seen in Figure 3.1 (a). However, when the same region was observed using Sentinel-1A, where the slope is facing the satellite, the sensitivity to deformations was low, and the deformations were not observed until one month before the event took place, as seen in Figure 3.1 (b). The region where the rockfall event took place is highlighted in red. The high deformation in the surrounding region was caused by a different event. The direction of the deformation is opposite in the two images due to the one-dimensional monitoring, and the actual deformation is in the perpendicular direction of both readings. This implementation example is further explored in [71].

#### 3.2.2 Surface Parameters

Surface characteristics like surface roughness, soil moisture, vegetation, and soil type influence surface scattering. These parameters influence the amount of radar signal reflected back to the sensor and thereby affect the quality of the monitoring process [72]. This study uses a C-band radar wave, and its interactions with surface parameters are discussed below.

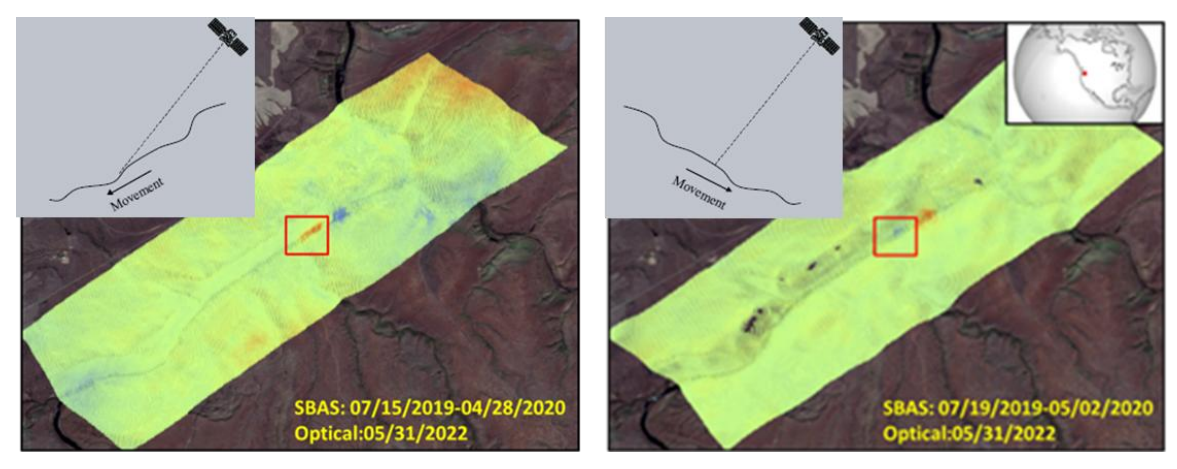


Figure 3.1 Effects of Slope Alignment on Deformation Measurements - Maupin OR Site: (a) Sentinel-1B LOS is in the direction of the slope and causes maximum sensitivity to SAR measurement of ground movement; (b) Sentinel-1B LOS is perpendicular to slope causes low SAR sensitivity to SAR measurement of ground movement.

<u>Surface Roughness:</u> The main factor controlling how radar signals bounce back from a surface is its roughness and the target's dielectric constant. A smooth and flat surface will reflect the incident radar wave away from the radar and is known as specular scattering. In these conditions there will be no scattering of energy back toward the radar unless the surface is facing the radar. Because the majority of natural surfaces are not perfectly smooth, the scattering of the incident radar wave is diffused in a variety of directions, including back again toward the radar [73]. Surfaces with a higher degree of roughness disperse more energy in all directions, including the direction towards the radar. For the purpose of better illumination, a surface should be "rougher," which means the height variations of the surface should be large [74]. Surface roughness can be quantified based on the root mean square height,  $h_{rms}$ , of the mean height of the surface into three categories, i.e., smooth, intermediate and rough as:

Smooth: 
$$h_{rms} < \frac{\lambda}{25\cos\theta}$$

Intermediate:  $\frac{\lambda}{25\cos\theta} < h_{rms} < \frac{\lambda}{4\cos\theta}$  (12)

Rough:  $h_{rms} > \frac{\lambda}{4\cos\theta}$ 

The surface roughness is directly related to satellite wavelength  $\lambda$  and inversely related to the cosine of the incident angle  $\theta$  [75]. The area for surface roughness measurement is the resolution cell, which is the smallest distinguishable area that a radar system can differentiate [76]. This study does not directly measure surface roughness for the purpose of site classification. Instead, it uses an existing database that categorizes surface roughness according to the soil type [77] [78] [79].

Dielectric Constant: A material's dielectric constant indicates how it affects the transmission of electromagnetic waves. The dielectric constant of the majority of natural materials falls somewhere in the range of 3 to 8 when the material is dry. However, the dielectric constant of liquid water is approximately 80. Hence, the quantity of water present in the target, regardless of its form (such as soil moisture or vegetation water content), significantly affects the radar backscattering [80]. A higher percentage of liquid water raises the dielectric constant and decreases the radar wave's ability to penetrate the target. The amount of liquid water in the target can change as a result of environmental conditions, and this change can be easily observed in SAR images and their multitemporal interferometric combinations [70]. It should also be important to consider that the presence of soil moisture has minimal effect on the quantitative error in deformation studies; it mainly affects the signal strength [81]. Although the dielectric constant greatly influences the backscatter of a region, it is not considered a factor for site classification for deformation measurements since it changes rapidly and requires accurate site readings that are difficult to track. However, it's utilized as a factor in CCD, which depends on the change in backscatter as an indicator of soil moisture change [82]. Vegetation: There are intricate and varied relationships between the various types of vegetation and the scattering processes that result due to big differences in their geometric shape and density of plants. Leaves, tree trunks, grass blades, and shrubs in a variety of forms can all be considered scattering elements. The dielectric changes that are brought about by variations in the amount of water present in the soil and canopy have a significant impact on the backscattered intensity that is measured in agricultural areas. Similarly, the forests also exhibit significant variations in forest backscatter due to

fluctuations in soil and canopy water content. The scattering coefficient of such radar targets is defined by the scattering characteristics of the individual items, their spatial distribution within the layer, and the medium's dielectric constant [70]. As a general rule, a C-band radar sensor cannot penetrate deep and is more sensitive to the structure of the canopy. The backscattering signal, in most cases, gets trapped within the canopy, and low backscattering occurs. The backscattering increases in dry and fall conditions when there is low leaf cover [83]. C-band SAR sensors can be used for short (less than 12cm in height) and, in some cases, medium vegetation (12-45cm). Areas with large vegetation are difficult to monitor for deformations due to complex factors involved in the backscattering mechanism [84].

Surface wetness: Flooded regions alter significantly the backscattered signal signature. The backscatter in regions with low-forest canopy will increase suddenly because the radar signal will bounce with the forest and reflect back to the sensor ("double bounce"). In contrast, if the region has no forest and the plain surface is flooded, the region will lose its backscatter as the radar signal bounces away from the sensor ("specular reflection") [70]. The sudden change in the scattering principle is due to water covering the surface roughness and making the surface completely smooth.

# 3.3 Data Quality Based Classification

<u>SAR Data Availability:</u> Sites should have access to extensive stacks of satellite data (over 12 months) to effectively monitor the region. Regions with less than 7 months of data are automatically classified as "C" class. The low classification is given due to the inability to perform multi-temporal SAR analysis. If the region has access to multiple satellites,

the classification system is applied for each satellite, and the highest classification is chosen as the site classification. In many cases, if an area is inaccessible or classified as a lower tier by one satellite, its classification improves when viewed from an alternate angle or through an additional satellite.

The site parameters directly influencing the proposed site classification in order of priority are: (i) slope grade, (ii) slope alignment, (iii) vegetation, (iv) surface roughness, and (v) surface wetness. The classification process is captured in a decision tree shown in Figure 3.2. The decision tree begins the classification process by identifying the slope grade and potential slope alignment. These are prioritized because the sensor covers a large area (250 km x 250 km), and topographic features are the most significant influences on the classification. Next, the workflow considers surface parameters that can affect classification on a more regional level.

<u>Slope grade</u>: The slope grade is classified into three categories based on the incidence angle of the observing satellite. Regions with slope values more than 50 have a higher chance of geometric distortions like layover, shadowing, and overlaying effects. Flat terrain has additional influences like surface wetness, which do not influence regions with slopes [69].

<u>Slope alignment</u>: The slope alignment is classified into two categories: (i) slope aligned with the line of sight, and (ii) slope directly faces the satellite, i.e. perpendicular to LOS. Large-scale deformations are still detected in case (ii), and conventional InSAR can still be used for monitoring and early warning systems. Finally, regions with large slopes not facing the satellite cannot be monitored due to the shadowing effect.

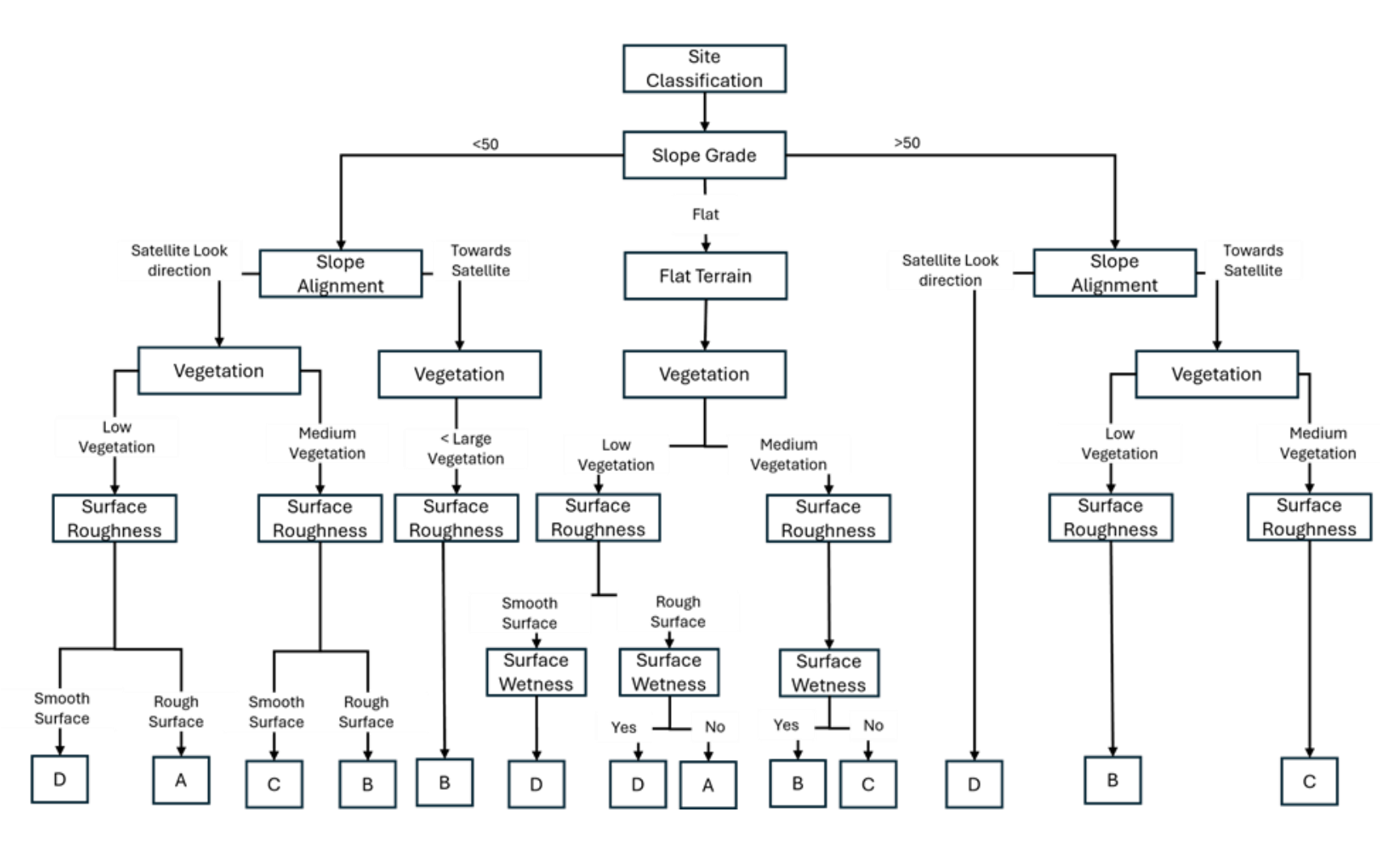


Figure 3.2 Site Classification Decision Tree

<u>Vegetation:</u> - After slope alignment, the radar signal first interacts with vegetation before it interacts with the surface. Two cases are considered: (i) Low vegetation (<12 cm) and (ii) medium vegetation (12-45 cm). The proposed system does not consider data from sites with large vegetation(>45cm) as no backscatter is available from these conditions and the site should be classified as D.

<u>Surface roughness</u>: Since this study does not measure the exact surface roughness of the region, the monitoring is divided into only two categories: smooth and rough. Regions with slope in the look direction of the SAR sensor require surface roughness for backscattering. When the region is smooth, the signal gets reflected away; this signal loss leads to a classification of D. The presence of vegetation helps in some smooth terrains where the radar signal gets reflected due to the vegetation acting like a rough surface. In conditions where the surface is facing toward the sensor, the surface roughness does not influence to the degree as it would other terrain conditions.

<u>Surface wetness</u>: - Surface wetness causes the surface roughness of the region to be converted to a smooth surface, causing the specular reflection to the radar signal, i.e., the signal gets reflected away. The only conditions where the surface wetness can improve the results would be when additional elements like vegetation or man-made structures cause the reflected radar signal to go back to the sensor [84].

A descriptive characterization of each site class is presented next:

Class A – Ideal: Examples include flat terrain and hilly/mountainous terrain (when slopes follow the satellite line of sight), minimal vegetation coverage without significant seasonal variation, multiple satellites and/or orbits,

and at least 24-month satellite historical data are available with multiple orbit directions.

Class B – Normal: Examples include open terrain, rolling hills, short escarpments, minimal vegetation coverage without significant seasonal variation, and at least 12-month satellite historical data available.

Class C – Noisy: Examples include hilly/mountainous terrain (when slopes face away from satellite line of sight) with medium to dense and tall vegetation with significant seasonal variation, escarpments, less than 12-month satellite historical data available, or intermittent data availability.

Class D – Dark: These are sites that are not visible to the satellite, and there is no line of sight. Examples include mountainous terrains, gorges with dense and tall vegetation, tall escarpments, and dense vegetation coverage without significant seasonal variation. In some conditions, these sites may be ideal in terrain profile but be located in satellite blind spots.

Examples of the four categories are shown in Figure 3.3

## 3.4 Selected Sites

Two groups of sites are identified. The first group comprises sites where a known event has occurred and is associated with monitoring sites for mobilization prior to an event, and the second group consists of instrumented sites where soil moisture records are available and is associated with monitoring sites for changes in the soil moisture content through the satellite coherence of the signal.



Figure 3.3 Examples of the four site categories

#### 3.4.1 Sites for Mobilization Monitoring

An initial set of thirteen sites have been selected for data collection and processing. These sites are identified and recommended by our industry partners due to reported recent events. The sites were used to develop the methodology for geo-hazard monitoring and to identify the limitations of existing methods. Based on the deformation analysis using PSInSAR and SBAS methods, threshold values for filtering noise were developed. In sites with vegetation elements, two post-processing methods were developed to overcome its influence. The post-processing methods were developed with Site ID #9 and tested in other rockfall events to validate the method. The selected sites satisfy the selection criteria consistent with classes A, B, or C with one exception being classified as D. The site classified as D is done due to lack of data available to monitor the region before the derailment event took place. The coordinates in the table cover roughly 1km<sup>2</sup> of area; even though the event's exact location is known in several sites, the surrounding areas are also included to show relative activity. In some cases, like Site ID #7 and #8, the monitoring region covers large areas, with the center located in the coordinates provided. Table 3.1 shows the events monitored for site mobilization. These events are further discussed in Appendix A

#### 3.4.2 Sites for Monitoring Soil Moisture Content Change

The relationship between soil saturation and signal coherence has been investigated to develop models that link changes in soil saturation to coherence. These models aim to define threshold values for triggering events and quantify associated risks, providing a foundation for future studies. Instrumented sites, such as those monitored by NOAA's U.S. Climate Reference Network (USCRN) [85], offer valuable data for this

Table 3.1 Sites where InSAR techniques are applied for mobilization monitoring.

ID	Site location	Coordinates (Lat/Long)	Event	<b>Event Date</b>	Analysis period	Site Class
1	Lincoln, NE	40.70, -96.53	Derailment	6/25/2021	10/31/20 - 9/20/20	В
2	Birmingham, AL	33.47, -86.95	Stability	Continuous	10/22/20 - 10/12/22	В
3	Maupin, OR	45.17, -121.10	Rockfall	5/7/2020	5/21/19 - 12/05/21	A
4	Atlanta, GA	33.83, -84.30	Sinkhole	12/2021	6/26/21- 5/04/22	В-С
5	Burlington, ND	48.25, -101.46	Derailment	5/1/2022	5/11/21 - 10/14/22	A
6	Shiner, Texas	29.43, -97.18	Derailment	6/3/2022	7/10/21 - 6/10/22	A
7	Yellowstone, MT	43.64, -111.36	Landslide	6/16/2022	1/10/21 - 9/1/22	A
8	Santa Clemente, CA	33.25, -117.37	Soil Erosion	10/1/2022	1/10/21 - 10/01/22	A
9	Sandstone, WV	37.76, -80.89	Rockfall	3/9/2023	7/3/22 - 3/2/23	В-С
10	Raymond, MN	45.01, -95.23	Derailment	3/30/2023	2/18/22-3/9/23	В
11	Quinn's MT	47.33, -114.78	Derailment	4/2/2023	04/14/22-03/28/23	D
12	Pueblo, CO	38.38, -104.61	Derailment	10/15/2023	12/16/22-10/12/23	A
13	Wayanad, India	11.46, 76.13	Debris flow	07/30/2024	08/05/22-07/24/24	В-С

research. USCRN sensors across the country measure soil moisture, relative humidity, precipitation, and soil temperature, contributing to comprehensive environmental monitoring. For this study, eight sites (listed in Table 3.2) were selected to perform Coherence Change Detection (CCD) analysis. Since the soil moisture change is correlated to signal coherence as computed from satellite SAR images, the sites are also selected based on site classes A and B defined in the previous section, with the exception of two sites that experienced large season vegetation and are classified as C. NOAA sensor coordinates encompass an area of approximately 1 km², indicating a significant level of uncertainty compared to the SAR sensor's resolution(15m²). The mean and standard deviation of coherence readings over the 1 km² were calculated based on the sensor coordinates to obtain a reliable interpretation of coherence over the sensor's coverage area. Since the C-band sensor has low penetration power, only the top 5cm of soil layer data was used for the soil moisture analysis. These sites are further discussed in Appendix B

# 3.5 Data Acquisition and Tools Used

To efficiently monitor ground hazards and estimate risk, this thesis uses a combination of MTInSAR within the framework of existing data sources. Prominent satellite systems are Sentinel-1 constellation for SAR data and Sentinel-2 and Landsat for satellite optical imagery. Sentinel-1, operated by the European Space Agency (ESA), is a radar imaging satellite that delivers high-resolution C-band Synthetic Aperture Radar (SAR) data. It is suitable for tracking ground deformation and surface properties over time, even when clouds are present or at night. The optical sensors are used to identify the locations of radar data. Landsat has high resolution, but high revisit time as compared

Table 3.2 Shows the Acquisition periods for the CCD timeline analysis used for developing the coherence and soil moisture model

ID	Site location	Coordinates (Lat/Long)	Analysis period	Site Class
1	Blackville, SC	33.36, -81.33	01/03/2019- 06/18/2022	В
2	Yosemite, CA	37.76, -119.82	01/10/2019-07/29/2022	A
3	Bodega, CA	38.32,-123.07	01/03/2019-05/03/2022	A
4	Santa Barbara, CA	34.41,-119.88	01/10/2019-09/15/2022	A
5	Cortez, Co	37.26, -108.50	01/10/2019-12/31/2022	A
6	Chatham, MI	46.33, -86.92	-	С
7	Sandstone, MN	46.11, -92.99	-	С
8	Columbia, SC	33.93, -81.02	03/26/2023-03/12/2024	В

to Sentinel-2 with low revisit time but low resolution. Sentinel-2, a series of Earth observation satellites operated by ESA, provides optical, which is especially beneficial for assessing land cover and vegetation. The supplementary datasets thoroughly comprehend ground conditions, with radar data from Sentinel-1 offering deformation insights and optical data from Sentinel-2 augmenting environmental context.

Supplementary data sources are essential for enhancing analysis. Meteorological databases yield data on precipitation patterns and temperature fluctuations, which affect soil moisture and deformation processes. Soil profiles, encompassing information on soil type, permeability, and compaction, provide insights into subsurface characteristics that may influence ground stability. Satellite data is investigated within the framework of the other data sources.

Various software tools and platforms are utilized to process radar data and perform the studies. The SARSCAPE is used as a toolbox within L3Harris software and is extensively utilized for processing Sentinel-1 data, encompassing activities like interferometric processing and coherence analysis. Google Earth Engine (GEE) is a robust cloud-based platform for analyzing extensive geospatial datasets, facilitating the swift integration of radar and optical imagery. The Copernicus Open Access Hub of ESA facilitates access to Sentinel data, whilst the USGS Earth Explorer portal is utilized to obtain Landsat imagery and additional geographic data.

Some Python codes were developed to integrate and process the vast satellite data. Integrating these tools facilitates a comprehensive method for monitoring ground hazards and evaluating risks in railway corridors and other essential infrastructure zones.

## 3.6 Employed Methods

The MTInSAR methodology workflow used for geohazard analysis is described below. The workflow is divided into three stages: pre-processing, which deals with data acquisition and data sorting; processing, which deals with InSAR technique application; and finally, post-processing, which involves the data filtration steps to identify regions most likely to experience geohazards. The CCD analysis from the methodology is used to develop coherence and soil saturation models and is currently used for qualitative geohazard monitoring. The mathematical background of the individual steps and the available options for each step are explored in detail in Appendix B. The guidelines to automate this workflow are currently under development and beyond the scope of this thesis.

## 3.6.1 Pre-Processing

This stage involves identifying the site for monitoring and preparing the data for multi-temporal analysis. This stage follows the steps in Figure 3.4:

<u>Input:</u> This step obtains the coordinates of the monitoring region or area of interest in latitude and longitude. To prevent map projection errors, the coordinates must be in a constant datum throughout the analysis period.

<u>Shapefile creation:</u> This step creates a shapefile polygon using Google Earth with a minimum dimension of 7.5km x 7.5km. To reduce approximation errors in the processing stage, the area of interest must be placed in the center of the polygon.

<u>Data download:</u> Single Look Complex (SLC) SAR images are acquired using the shape file from the previous step. Alaskan Space Facility (ASF) and European Space Agency

(ESA) datahubs are used to download the data. SLC images are minimally processed by satellite and have full complex radar signals. This data type has both phase and amplitude, and the pixels are spaced equally in azimuth and range direction. The data is restricted to the observation period and covers the complete polygon. If no data is available, the shapefile polygon is recreated with the area of interest away from the center of the polygon to incorporate the data acquisition.

<u>Data sorting:</u> Some areas of interest have access to data from several orbits (ascending and descending) and satellites (Sentinel-1A and Sentinel-1B). The data from multiple orbits cannot be used in the same analysis stack, as that would increase the spatial decorrelation in the processing stage. To prevent errors in the analysis, the data from these orbits and satellites are sorted so that all the SAR images are grouped according to their respective look angle. The sorting is done based on two factors: the first is that each satellite passes over the same region every 12 days, and the second is the path and frame metadata remain constant for data with the same look angles.

Output: Output from the pre-processing step are Single Look Complex (SLC) images sorted according to their respective satellite direction and look angle. Single Look Complex (SLC)images have focused SAR data, and the pixels are spaced equally in azimuth direction and slant range. The data is represented as complex numbers containing both phase and amplitude.

#### 3.6.2 Processing

Figure 3.5 illustrates the initial workflow for preprocessing analysis stage. In this phase, the pre-processed data is used to derive coherence using the CCD algorithm, as

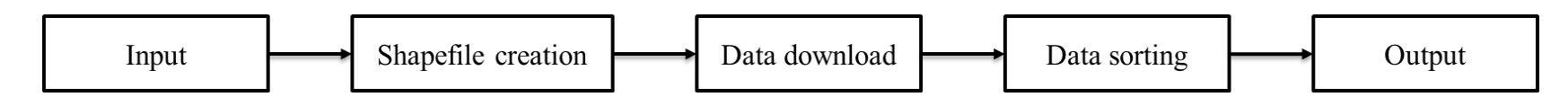


Figure 3.4 Shows the pre-processing workflow.

well as displacement from the PSInSAR analysis and displacement trend information from SBAS techniques.

<u>Input:</u> Input for the processing stage is the SLC data grouped according to their respective look angle.

<u>Data preparation:</u> The 250km x 250km input SLC file is reduced to contain only the Area of Interest, and the image's polarization is chosen in this step. All SAR analyses in this study use VV polarization as this type of polarization has maximum penetration ability. VH polarization is used for polarimetry analysis, which is not part of this study. This step is performed to reduce the computational time of the investigation.

Connection graph: A connection graph refers to the visual representation of InSAR image pairs. Each SAR image in a data stack is systematically paired for InSAR analysis. Two types of connection graphs exist: Time-Position plot and Time-Baseline plot. The x-axis in the Time-Position plots represents the date the image was acquired, while the y-axis represents the baseline in meters relative to the master image. The x-axis in the Time-Baseline represents the date when the image was acquired, while the y-axis represents the normal baseline between the two images, measured in meters. The Time-Position plot is commonly employed to illustrate the correlation between pairs of images, as demonstrated in Figure 3.5 and Figure 2.4 for PSInSAR and SBAS connection graphs.

The processing stage deviates in this step. The data from the previous step is paired based on the processing requirement for each analysis. For CCD, the SAR data is paired based on a timeline approach, i.e., for the first CCD analysis, image one is paired with image two; for the second analysis, image two is paired with image three, and so on.

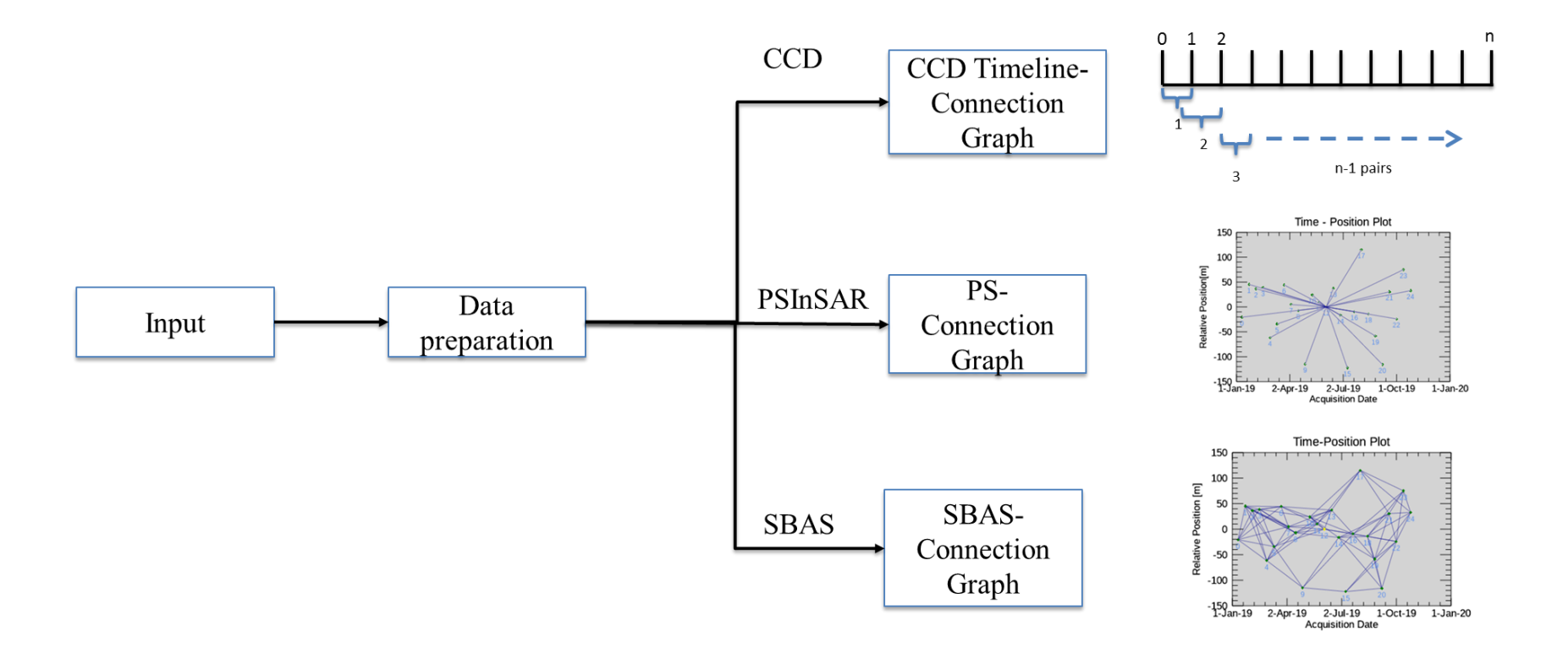


Figure 3.5 Shows the workflow chart for first stage of processing stage.

PSInSAR utilizes a collection of 25 or more images that possess similar polarity and geometry. A singular master image serves as a point of reference, and all other images in the stack are paired with it. The master image is based on the temporal baseline being equidistant for the first and last images from it. i.e. it's the middle image of the data stack.

SBAS utilizes a collection of 25 or more images that possess similar polarity and geometry. SAR pairs are created based on low temporal and spatial baselines to ensure low coherence loss in the generated interferograms. SBAS analysis uses multiple master images, with each image having multiple pairs. The number of SAR pairs for each master file is based on the temporal baseline, which is set between 90 and 180 days, and the spatial baseline is set as 2% of the critical baseline. A critical baseline is the maximum viable baseline for the satellite platform. For SBAS connection graph a super master file exists which is the middle image of the data stack and is used to obtain the relative spatial baseline for the complete stack.

Figure 3.5 shows the connection graph for all three types of analysis.

## 3.6.2.1 Coherence Change Detection

The steps for obtaining coherence between each connection pair from the connection graph are shown in Figure 3.6. The process of obtaining coherence is called coherence change detection.

<u>Interferometric processing and coherence generation:</u> Coherence is generated as a byproduct of InSAR processing. In InSAR processing, the image pairs obtained from the connection graph are co-registered, meaning that the resolution cells of two SAR images

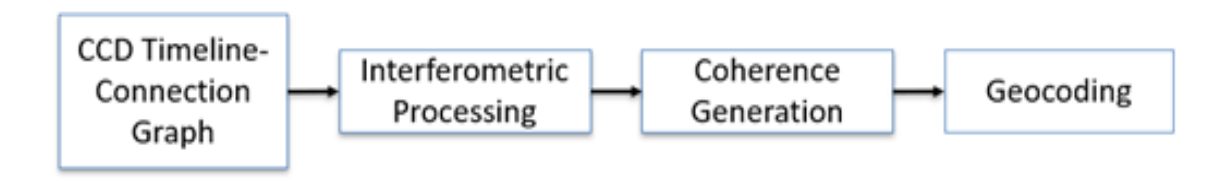


Figure 3.6: Shows the workflow chart for coherence generation.

are aligned. An interferogram is developed by removing the phase components of the slave image from the master image. Additional phase components due to satellite tilt and irregular ellipsoidal shape of earth called flat earth phase are removed. Coherence between the image is calculated following the removal of flat earth phase, the math for the process is described in [31].

<u>Geocoding:</u> The coherence data from the analysis is in satellite coordinate system i.e. each resolution cell is arranged at slant geometry along the satellite flight direction.

Geocoding step is conducted to convert the data from satellite geometry to cartographic reference system of choice by aligning the satellite path with a reference DEM.

#### 3.6.2.2 PSInSAR

To obtain the displacement component from PS in satellite line of sight, the analysis follows the steps in Figure 3.7

Interferometric Process: This step performs DInSAR analysis on all the pairs generated in the connection graph stage. It follows InSAR processing steps seen in coherence generation with additional topographic phase filtering carried out on the image pair [31]. This analysis produces an unwrapped phase depicting the displacement between the two acquisitions.

<u>Coherence-based PS selection:</u> During the computation of an interferogram, the coherence between the two image pairs is obtained. A coherence threshold of 0.7 is used to identify PS. A 0.7 coherence threshold indicated the loss of coherence in most cases is due to either displacement or minor atmospheric effects. The stable PS or high-coherence pixels in the time series are selected based on amplitude dispersion value, which is the

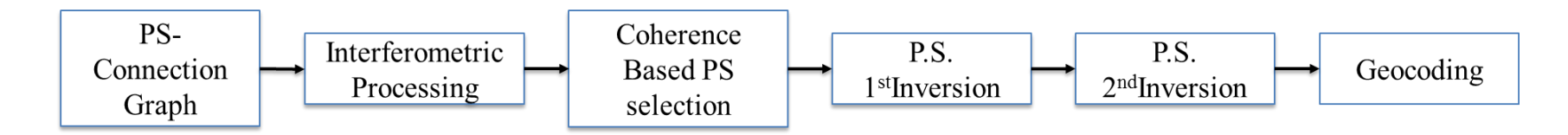


Figure 3.7 Shows PS processing chain workflow chart.

amplitude standard deviation divided by the mean amplitude. Using PS for displacement estimation generates displacement data that is effective qualitatively. The influence of amplitude dispersion field is further explored in [59].

<u>PS 1st Inversion:</u> The amplitude dispersion value is utilized to quantify the extent of displacement velocity, specifically the displacement over time data of each PS. This is done by tracking the displacement of each PS through all image pairs, by progressively subtracting the displacement of consecutive image pairs. The displacement over time data obtained still has the presence of atmospheric components in this step.

<u>PS 2<sup>nd</sup> inversion:</u> In this step, the atmospheric component is filtered from the displacement rate obtained in the first inversion. This step uses a Low-Pass spatial filter and a High-Pass temporal filter to get a displacement rate without atmospheric contributions. The parameters for the atmospheric filtering in the second inversion step are described further in [86] [87] [88]

<u>Geocoding:</u> The displacement data obtained from the above steps are geocoded to the preferred coordinate system for more straightforward extrapolation of results in post-processing steps. The process is similar to geocoding done for CCD analysis.

#### 3.6.2.3 SBAS

To obtain the displacement trend in satellite line of sight the analysis follows the steps in Figure 3.8

<u>Interferometric Process:</u> This step performs DInSAR analysis on all the pairs generated in the connection graph stage. It follows a traditional DInSAR analysis described in [1] and produces an unwrapped phase from which displacement can be obtained.

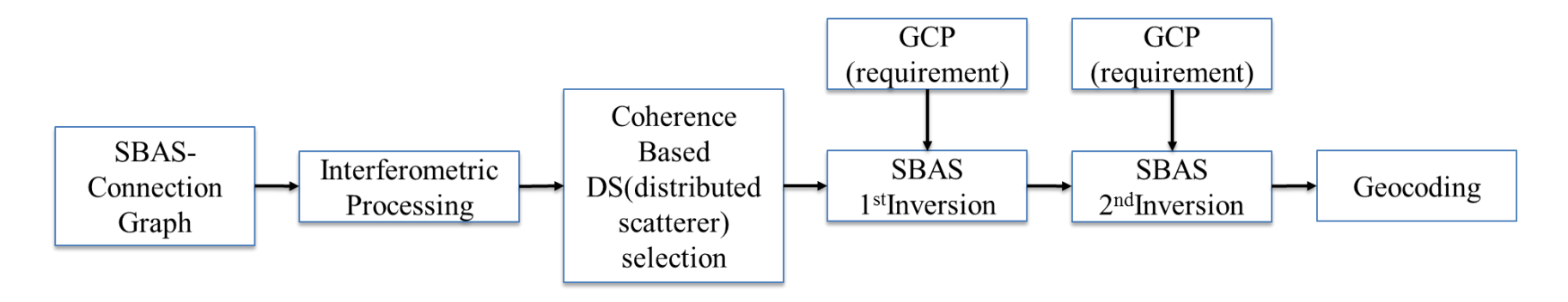


Figure 3.8 Shows the processing chain for SBAS analysis.

<u>Coherence based DS selection:</u> During the computation of an interferogram the coherence between the two image pairs is obtained. A coherence threshold of 0.3 is used to identify distributed scatters. Using DS for displacement estimation generates displacement trend data that is effective quantitatively instead of qualitatively.

First Inversion: The unwrapped interferograms are refined and re-flattened (terrain-induced variations are removed) to be used as an input for the Single Value

Decomposition (SVD) matrix inversion technique. The SVD inversion is employed to solve equations that characterize the stack of unwrapped interferograms, yielding the displacement solution for each acquisition date. The displacement time series values are referenced to the oldest date as zero, and the displacement over time from this point is considered.

Ground Control Points: Ground Control Points (GCP) are stable reference points used to improve the displacement rate output [89]. The phase change occurring over these points are considered accurate and assumed to describe the displacement of actual ground region. The GCP points are selected away from region to be monitored as placing them on the region experiencing displacement would affect the results.

<u>Second Inversion:</u> In this step, the atmospheric component is filtered from the displacement rate obtained in the first inversion. This step uses a Low-Pass spatial filter and a High-Pass temporal filter to get a displacement rate without atmospheric contributions. The parameters for the atmospheric filtering in the second inversion step are described further in [86] [87] [88]

Geocode: The displacement trend data obtained from the above steps are geocoded to the

preferred coordinate system for more straightforward extrapolation of results in postprocessing steps. The process is similar to geocoding done for CCD analysis.

## 3.6.3 Post-Processing

The post processing is performed on the individual output of InSAR analysis and follow the workflow from Figure 3.9

Coherence data: Coherence data are processed in two ways based on their application. First, when the data is used for monitoring geohazards, rainfall data is correlated with coherence to observe locations with consistently low coherence after the rainfall event. This is done to identify regions with high soil saturation. The second is to use the coherence data obtained near the USCRN NOAA locations to understand the relationship between coherence and soil saturation. The coherence data over the sensor location is converted from a monochromatic photo to excel data. The sensor's coordinates are over an area of approximately 1 km², which is larger than each resolution cell of coherence (15 m²). To get a reliable interpretation, the mean and standard deviation of coherence reading covering the approximate sensor area used for correlation. This data is used for model development.

MTInSAR Displacement data: The displacement from MTInSAR analysis is filtered based on the magnitude of the displacement, and displacement in the range of -10 mm to 10 mm is removed from observation data. The resultant image shows the site mobilization map of the region. The filtering is done for two reasons. The first is based on the assumption that phase components due to atmosphere and topography are only

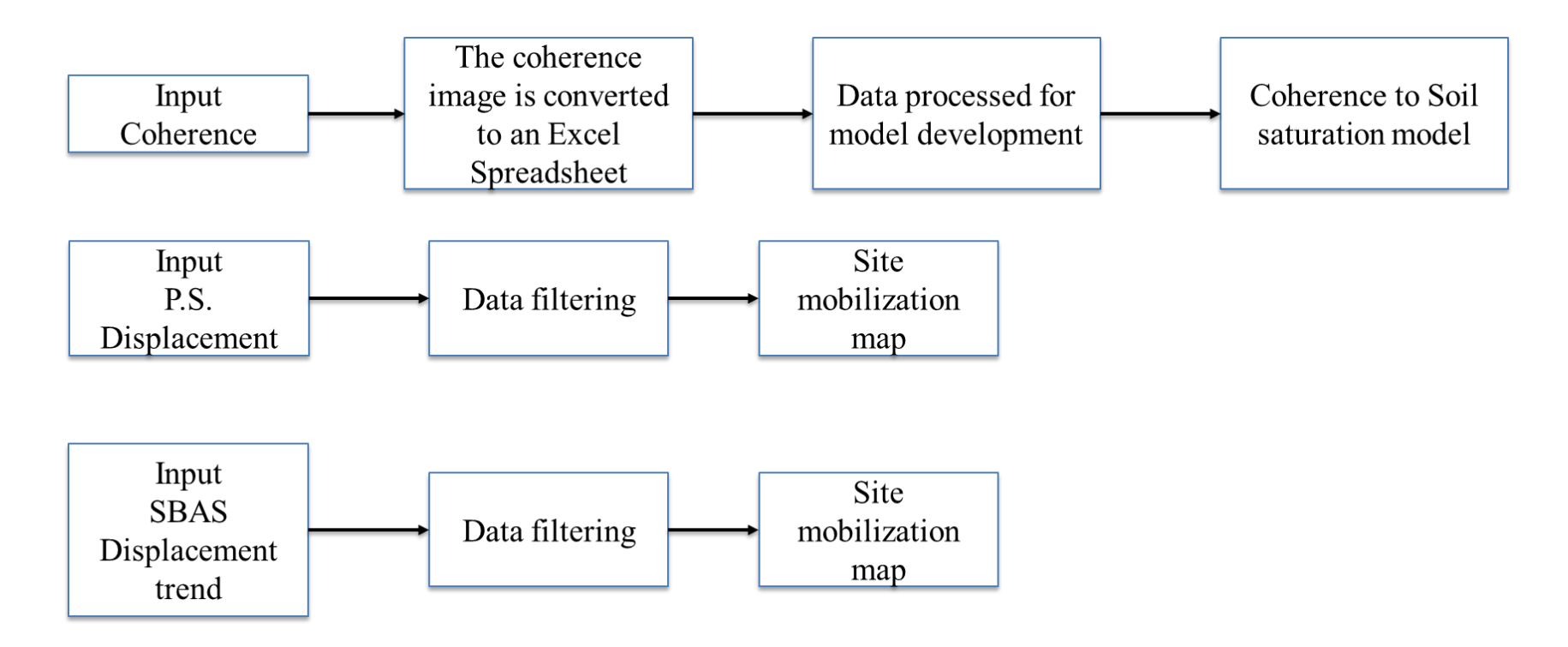


Figure 3.9 Shows the post processing workflow for InSAR processing chain.

partially eliminated. The second is the displacement data crossing the threshold, representing the actual movement of the surface, whether the magnitude is accurate or not.

## 3.7 Limitation of Conventional MTInSAR

One of MTInSAR's key features is its ability to accurately identify small surface changes over time. To do this, the analysis uses large stacks of data, and an increase in stack size increases the accuracy by reducing the contributions of residual height and atmospheric influence. However, using large data stacks negatively influences the region being monitored. If significant changes occur during the analysis period in an interferometric pair, such as movement exceeding 30mm, or if the region loses coherence due to external factors, the region stops being a scatter, and monitoring it becomes unfeasible even if the area continues to experience deformation. This condition is prevalent in PSInSAR but is also experienced in SBAS analysis. To mitigate this condition, two post processing methods were developed and are discussed in chapter 4

# CHAPTER 4: PROPOSED METHOD FOR IDENTIFYING REGIONS WITH GEOHAZARD POTENTIAL

As discussed in Section 3.8, one of MTInSAR's key features is its ability to accurately identify small surface changes over long periods. However, during the analysis period, if there is a significant change (e.g., movement > 30mm) between two acquisitions or if the scatterer loses coherence for other reasons, the change cannot be monitored even if the surface is undergoing deformation. In geohazard monitoring, areas classified as A or B have been identified as suitable candidates for monitoring. These regions are characterized by low vegetation and high radar backscatter coverage, allowing conventional MTInSAR to be applied for monitoring deformations over the time span covered by the SAR image stack. However, as the analysis time frame increases, seasonal vegetation coverage and errors resulting from a larger satellite spatial baseline make the detection of both PS and DS scatterers infrequent, due to the loss of continuity in the observable scatterers. Therefore, detecting critical areas through deformation monitoring using conventional MTInSAR is not feasible. The proposed approach implements MTInSAR techniques using a "Rolling Stack" (RS) concept to detect scatterers over extended time periods, in conjunction with three post-processing operations, namely, "Thresholding," "Scatterer Accumulation," and "Clustering Timeline." These methods were initially presented as Threshold stacking and Timeline in [66] [71], these methods have been refined in this thesis and are called rolling stack

scatter accumulation and clustering timeline.

# 4.1 Rolling Stack MTInSAR (RS-MTInSAR)

The proposed RS-MTInSAR limits the size of the stack of SAR images in its conventional implementation to a number of images necessary for maintaining accuracy and controlling noise, typically between 20 and 25, depending on site class and the specific MTInSAR method. Subsequently, site monitoring for a duration exceeding the time spanned by the stack is achieved through a series of MTInSAR analyses. Each analysis employs an updated SAR image stack, where the first SAR image is removed from the front of the stack, and a new SAR image is added to the end, creating a "rolling stack" effect.

Figure 4.1 demonstrates the concept, assuming a monitoring period of one year, and a temporal image acquisition baseline of 12 days, yielding a total number of 30 SAR images. For demonstration purposes only, assuming a stack size of 20 SAR images, 12 MTInSAR analyses need to be performed. Each analysis provides the geolocation of the PS or DS scatterers within the analysis stack, as well as the time history of movement at each point. This information is considered in the post-processing steps of the proposed method method.

# 4.2 Thresholding

MTInSAR methods implement filters to treat temporal and spatial decorrelation of the signals in order to improve the quality of the deformation results, but only to a certain extent. Loss of coherence due to atmospheric contributions results to higher noise in the deformation measurements derived from the MTInSAR and hinders the detection

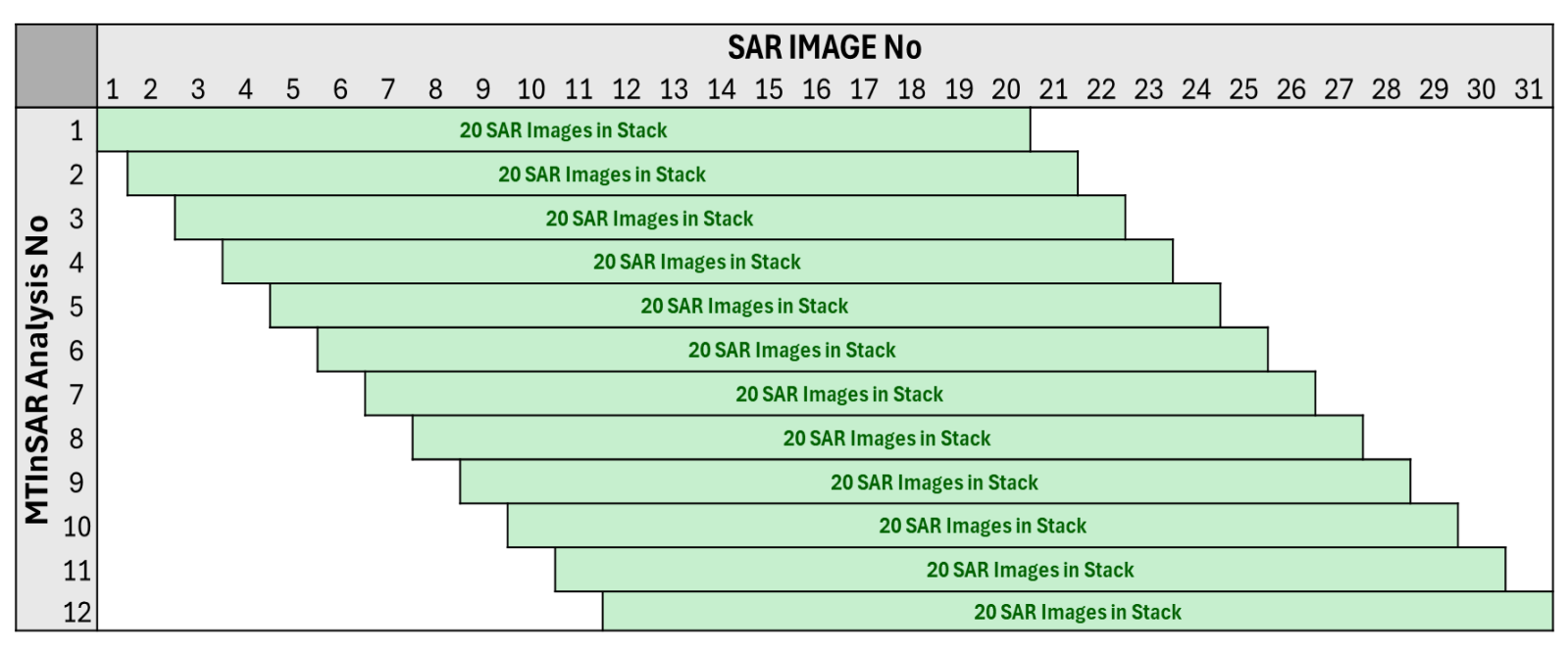


Figure 4.1 Rolling Stack MTInSAR (RS-MTInSAR) analysis concept

of critical areas. The proposed *Thresholding* is a post-processing filtering method implemented to all deformation analyses from the proposed RS-MTInSAR. The objective of the proposed filtering is to identify and remove the scatterers from the solutions that are formed by residual coherence losses from decorrelations, or represent points that, although they are properly identified, the exhibit small movement and are of no interest in the identification of the critical areas.

The criterion for the threshold is based on the coherence threshold used in the PS and DS identification process. In the case of PSInSAR, a coherence threshold of 0.7 is used as an indicator of PS, while in the case of SBAS, a coherence threshold of 0.3 is used as an indicator for DS points. The magnitude of the filter is determined by the theoretical precision of SAR deformation data as reported in [90] [91]. The precision depends on the wavelength of the SAR sensor and the measured coherence. For example, for a C-band sensor and a scatterer with 0.7 coherence, the theoretical precision is 20 mm and any deformation above the theoretical is considered the true deformation. However, any deformation below the theoretical value may be masked by noise. In the proposed RS-MTInSAR, the theoretical precision should not be used as the threshold criterion because the coherence fluctuates in each SAR image pair in the stack. Thus, to prevent active deformation points from being filtered, conservative threshold values are recommended as shown in 4.1. These conservative thresholds serve to balance false positives and false negatives in geohazard detection. This approach ensures that the methodology remains adaptable across varied terrain and environmental conditions.

Table 4.1 Shows the theoretical precision and suggested threshold values for coherence

Coherence	Theoretical Precision (mm)	Threshold Value +/- (mm)
0.9	8	6
0.8	14	8
0.7	20	10
0.65	23	11
0.6	26	12
0.55	30	14
0.5	35	16
0.45	41	18
< 0.4	> 50	20

## 4.3 Scatter Accumulation

The identification of the critical areas in the region of interest starts with establishing the *Landsat* optical image of the region to geolocate the scatterers. Landsat is publicly available through Google Earth. At the end of each RS-MTInSAR analysis the identified set of scatterers are filtered as discussed in the "Thresholding" section and superimposed on the optical image of the region. For both event investigation and active monitoring, it is recommended that the monitoring period starts at least one year before the date of the event, or before the active monitoring commences. The scatterer accumulation will result in a continuously updated deformation map with the location of all scatterers appearing on the optical image. At this step, the critical locations can be identified by visual inspection, as areas where the density of accumulated scatterers increases over time. The detection of the critical locations, however, is implemented in a structured manner in the last post-processing tool, i.e. Clustering Timeline, discussed next.

# 4.4 Clustering Timeline

The last step in the proposed process for identifying the critical location within a larger monitoring region pertains to identifying the formation and progression of cluster of scatterers every time a new set of RS-MTInSAR analysis data becomes available. To this end, a grid is overlayed on the optical image with a subset size dependent on a combination of the desired resolution of the critical areas and the average number of the detected scatterers in the region. Higher risk areas are identified as those subsets, or group of subsets, that exhibit higher density of the clustered scatterers compared to their

surrounding subsets. At this stage, although regions with a high potential for geohazard failure are identified, the imminency of the failure is not evident. A timeline analysis showing the rate at which the clusters are formed between any two successive data sets is used as an indication that a geohazard event failure is imminent. The timeline method is based on the geohazard observation that before the triggering event there is a rapid increase in the density of the cluster in the geohazard vicinity.

## **CHAPTER 5: IMPLEMENTATION STUDY**

The RS-MTInSAR with Thresholding, Scatterer Accumulation and Clustering Timeline analysis were first validated through implementation to Site ID 3 using both SBAS and PSInSAR analyses and have been reported in [92]. This section presents a case study that considers Site ID 13 for the validation of the method that is based on the RS-SBAS analysis.

## 5.1 Event

On July 30, 2024, the Wayanad district in Kerala, India, was hit by a massive landslide due to heavy rainfall affecting the region. This was a debris flow with the origin of the landslide shown in Figure 5.1(a) [93]. The mud from this region followed the path through the village of Mundakkai and Chooralmala. The landslides caused over 100 confirmed dead and many more missing. The rescue efforts were challenged by heavy rain and difficult terrain Figure 5.1(b) [93].

# 5.2 Data Availability

The region under investigation is in southern India, where Sentinel-1A provided coverage. This region is covered by Sentinel-1A satellite once every 12 days, the satellite path is shown in Figure 1(c). The region is located in rural areas with access to radar signals from the satellite in orbit; the region has vegetation in it, and based on these site conditions, the region is classified as "B".

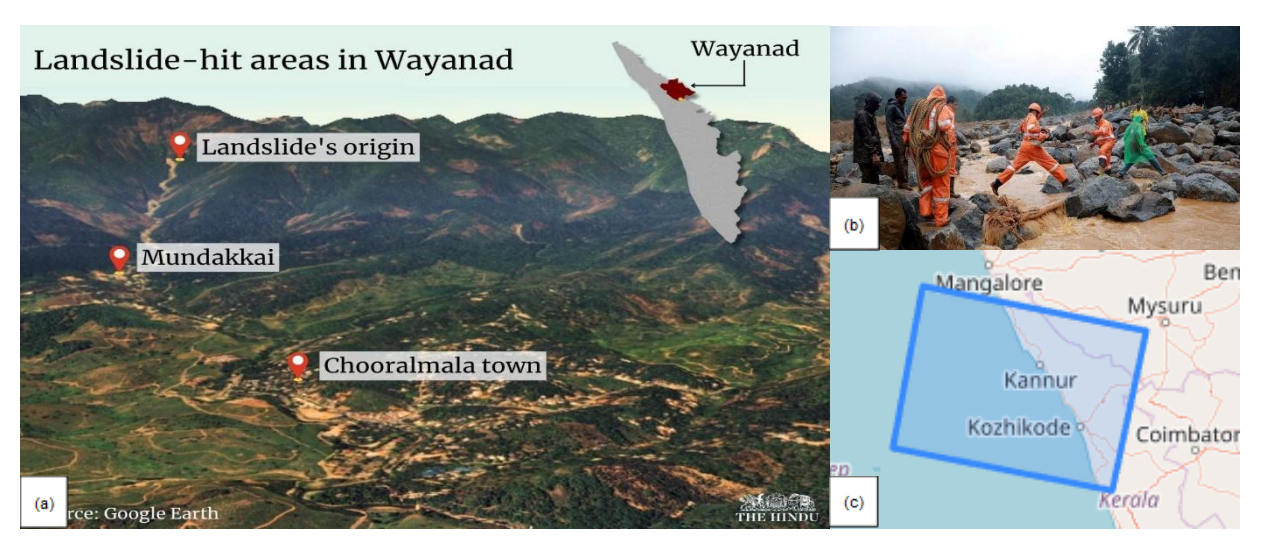


Figure 5.1 Shows the origin point of the landslide with the regions affected highlighted. (b)Shows the rescue efforts underway for the landslide event. (c) Shows the satellite coverage of the region and its path.

The dataset for this study is obtained from the Sentinel constellation, and the satellite images are downloaded from the Sentinel-1 EU datahub and Alaska Satellite Facility (ASF). The analysis employs SBAS techniques with post-processing methods, scattering accumulation, and timeline methods using archived satellite radar images spanning 36 months; the final data acquisition is taken five days before the disaster. The acquisition periods are detailed in Table 1. The region also has a cloud presence, reducing the number of optical images available from Sentinel-2. Since this is a recent event, post-event analysis is not available at this time.

The region under investigation is in southern India, where Sentinel-1A provided coverage. This region is covered by Sentinel-1A satellite once every 12 days. The region is located in rural areas with access to radar signals from the satellite in orbit; the region has vegetation in it, and based on these site conditions, the region is classified as "B". The dataset for this study is obtained from the Sentinel constellation, and the satellite images are downloaded from the Sentinel-1 EU datahub and Alaska Satellite Facility (ASF). Fig 1(c) shows the path taken by the Sentinel1-A satellite. The analysis employs SBAS techniques with post-processing methods, scatter accumulation, and timeline methods using archived satellite radar images spanning 36 months; the final data acquisition is taken five days before the disaster. The acquisition periods are detailed in Table 1. The region also has a cloud presence, reducing the number of optical images available from Sentinel-2. Since this is a recent event, post-event analysis is not available at this time.

## 5.3 Site Description

The region under investigation is located in Kerala, India, at latitude/longitude (11.54/76.14). The analysis covers roughly 140 mi<sup>2</sup> and analyzes the multiple landslide events occurring around the same time due to the same rainfall events. This region experienced frequent rainfall

Table 5.1 Data used for Wayanad analysis

Data Set	Sentinel 1-A (Ascending)
Pre-event	08/17/2022 to 25/07/2024

events with annual rainfall of 157 inch [94]. The day before the landslide the region experienced a rainfall of 22.519 inches. This region is classified as a mountain slope with 35 to 70 percent slopes [93]. The soil profile for the site is unavailable due to the size of the analysis area and the lack of access to soil records in India.

## 5.4 MTInSAR Analysis

#### 5.4.1 SBAS

The SBAS analysis was conducted using a 25-image stack. The deformation map is superimposed on an optical image taken on April 10, 2024. The optical image close to the event date showed high cloud cover. The displacement observed is in mm and plotted on the color-coded SBAS images that show the total displacement over the entire analysis region. The deformation map in Figure 5.2(a) is highlighted in three regions with the red box being the point of origin of the landslide, the white box showing the largest cluster of deformation and the yellow box showing the village on path of the landslide. Large deformations taking place on the region on the path of landslide flow. Figure 5.2(c) image shows the concentration of high displacement points in the path of landslide event near the point of origin.

The deformation over time seen in Figure 5.2(b) shows the region having low displacement until February 20, 2024 followed by sudden increase in deformations. The region had minimal precipitation during this period [95]

#### 5.4.2 Scatter Accumulation

The SBAS analysis was able to identify displacement taking place in the path of the landslide, but it fails to show any deformations in the region where the landslide originated. Scatter accumulation method is used in this region to identify large activity areas. The

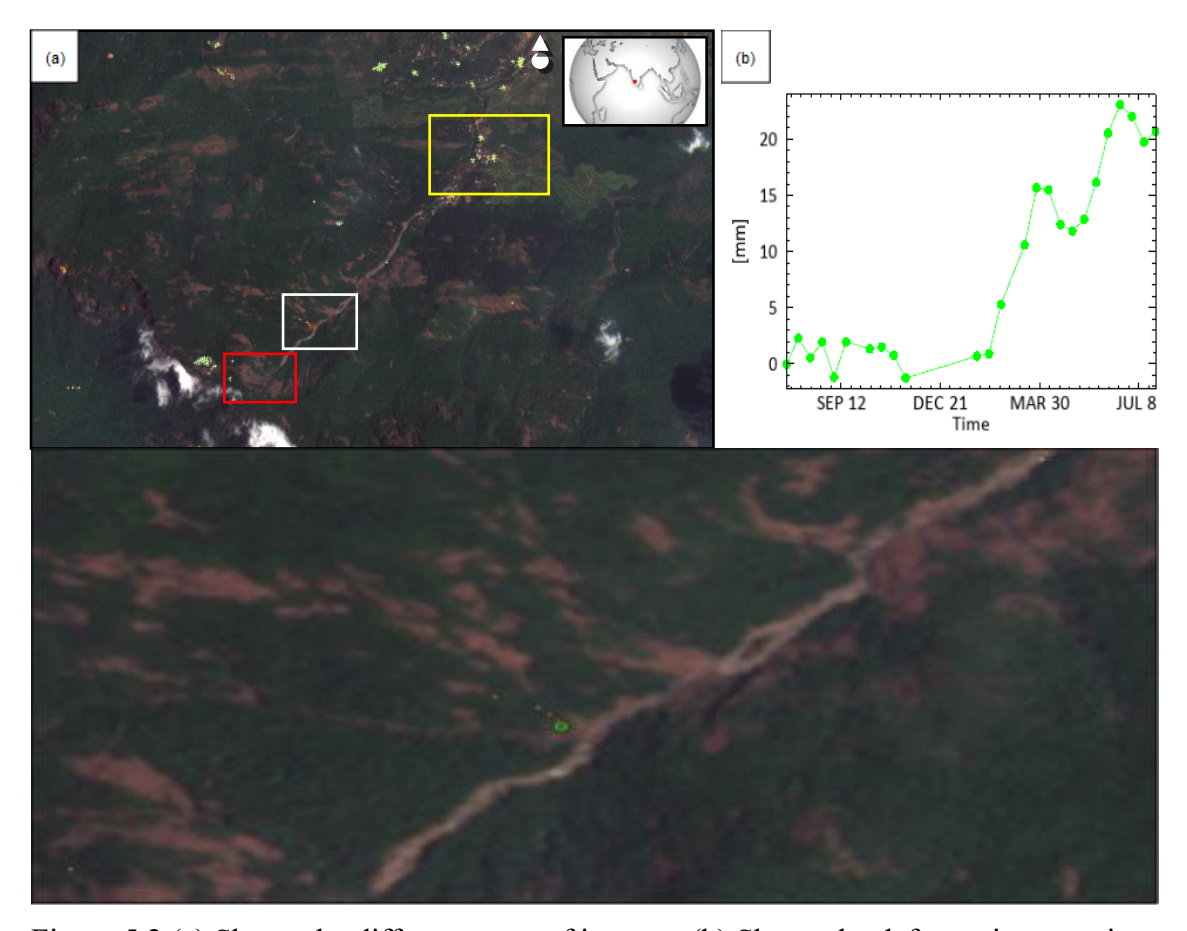


Figure 5.2 (a) Shows the different areas of interest. (b) Shows the deformation overtime of the scatterer highlighted in (c). (c) Shows the large deformation scatterers before the landslide took place highlighted by white box in (a)

analysis used 25 images with new images being cycled as per [96]. A total of 24 analysis are conducted out of which 3 analysis produced invalid results due to no connection graph being formed from the available data due to large spatial baseline. These are covered by analysis periods April 26, 2023, to May 14, 2024; 01/08/2023 to March 27, 2024; September 22, 2022, to September 17, 2023. The results from scatter accumulation show the activity in the region began in the analysis period covering December 15, 2022, to February 20, 2024, Figure 5.3(b) highlighted by red square, before which the region was relatively calm Figure 5.3(a). The region showed progressively increasing activity until the landslide event when the region has significantly high activity compared to surrounding regions Figure 5.3(c)(d).

## 5.4.3 Clustering Timeline

The timeline analysis of the region reveals a general increase in activity leading up to the landslide, with a notable drop in the final observation before the event. Figure 5.4(a) highlights the initiation zone of the landslide, covering a two-month period prior to its occurrence. Figure 5.4(b) shows consistent activity in the region 17 days before the event, while Figure 5.4(c) illustrates a sharp decline in displacement five days prior. Figure 5.4(d) summarizes the number of displacement points detected throughout the analysis period, revealing heightened activity 3–4 months before the event, followed by a significant reduction shortly before it occurred. This trend suggests that the landslide-triggering mechanism was likely activated after the final data acquisition.

## 5.5 Discussion

The region exhibits moderate vegetation cover, allowing radar signals to penetrate but limiting the presence of strong Persistent Scatterers (PS). Prior to the event, a cluster of

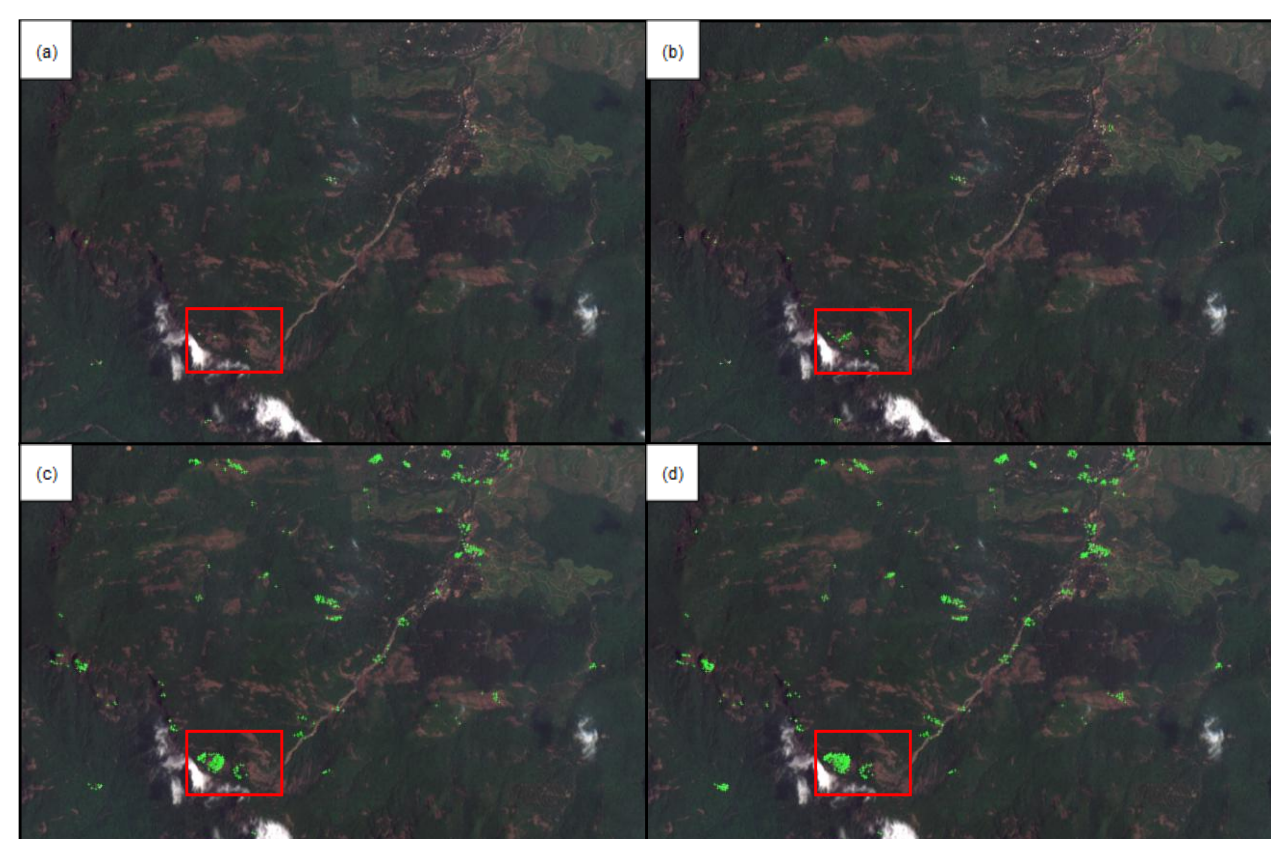


Figure 5.3 (a) Shows low activity in the region using the data till February 08, 2024. (b) Shows the region experiencing some deformations. (c) Shows the increasing deformations in the region (d) Shows the activity in the region before the landslide took place.

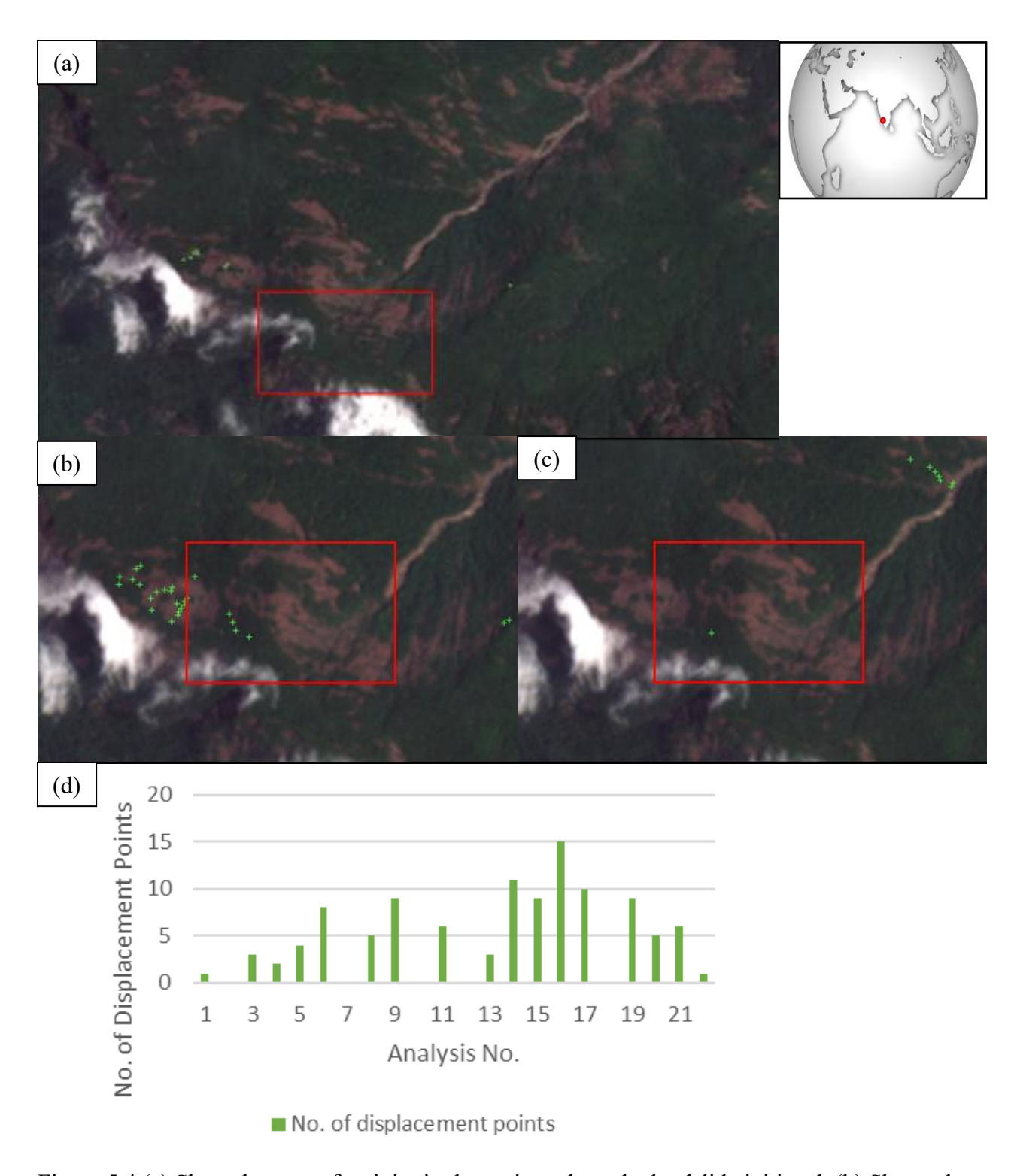


Figure 5.4 (a) Show the start of activity in the region where the landslide initiated. (b) Shows the constant activity in the region where the landslide initiated. (c) Shows low presence of activity in the region where the landslide was initiated. (d) Graph shows the number of displacement points over each analysis.

deformation-related scatterers was detected along the eventual landslide path; however, this cluster did not coincide with the actual initiation point of the slide. The origin point showed significant pre-event activity, evident through the accumulation of scatterers. When this scatter accumulation data is compared with post-event imagery obtained from the NRSC(National Remote Sensing Center) [93] [97], it aligns with the location of the landslide crown, as shown in Figure 5.5. Notably, signs of activity were present before the onset of rainfall in the region. Although the initial activity may not have been directly caused by rainfall, the severe precipitation event that followed the final analysis period is likely to have served as the primary trigger. The scatter accumulation method demonstrated strong potential for identifying regions highly susceptible to landslide activity. In contrast, certain limitations were observed in other methods: the timeline analysis was constrained by adverse weather conditions taking place after the final acquisition, while the conventional SBAS approach failed to detect the landslide origin due to coherence loss in one of the radar images.

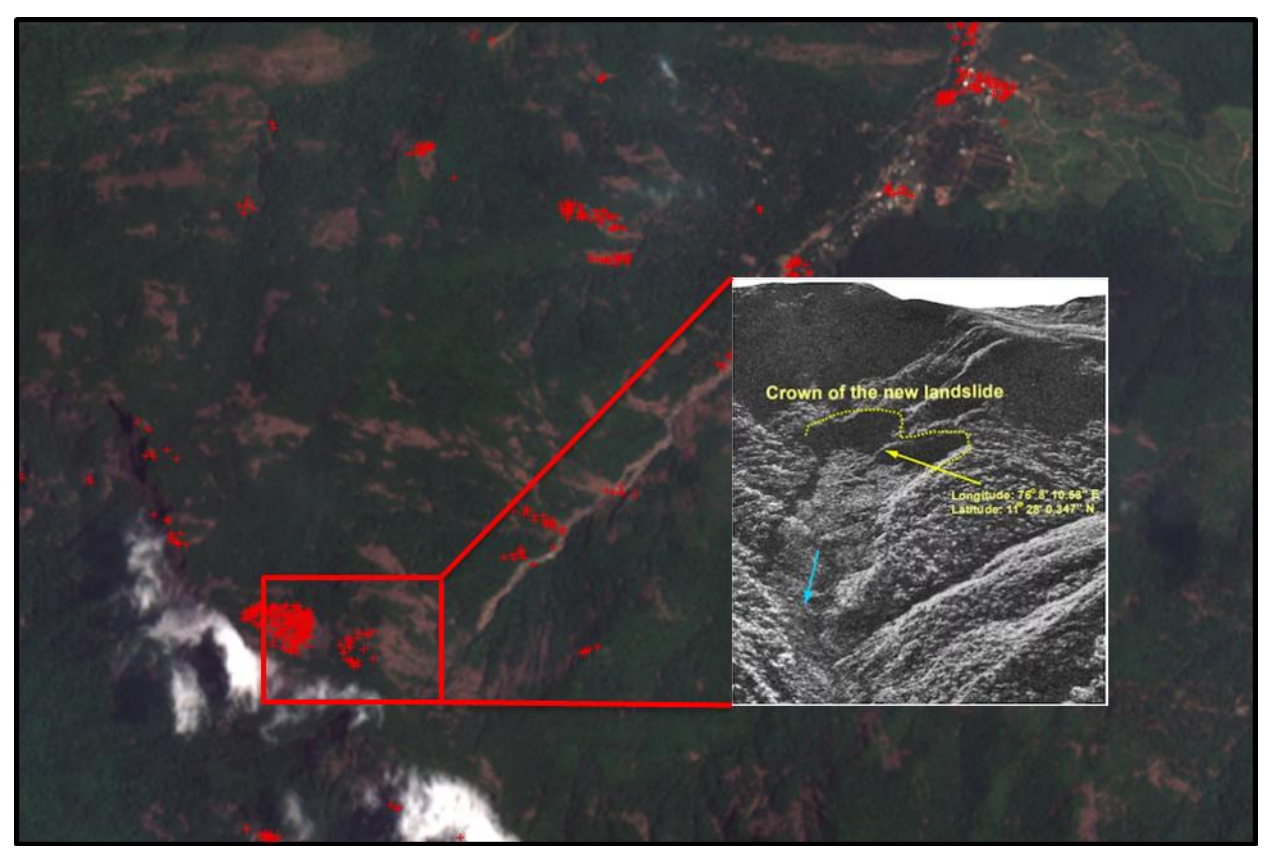


Figure 5.5 Shows the crown of the landslide in the same region as the activity map shown by Scatter accumulation [97]

#### **CHAPTER 6: RESULTS AND DISCUSSION**

The study's results indicated the efficacy of satellite radar methods such as MTInSAR in detecting geohazard risks along railway systems. PSInSAR effectively identified ground subsidence and surface displacement in derailment incidents, notably in Burlington, North Dakota, and Cody, Wyoming, where considerable subsidence occurred near railway lines. These deformation monitoring systems highlight the possibility of anticipating and reducing future dangers. In contrast, CCD analysis was helpful for spotting moisture-related instability because it could detect shifts in soil moisture, which frequently occurred before geohazard. In Lincoln, Nebraska, and Maupin, Oregon, coherence loss from rainfall was associated with heightened soil moisture, potentially inducing soil instability and resulting derailments. The research indicated that geological and environmental elements, including soil composition, topography, and vegetation, substantially affected the accuracy of radar data. The classification system incorporating these factors has facilitated the selection of specialized monitoring strategies across diverse terrains.

# 6.1 Detection of Geohazard Prone Area Using InSAR

The findings provide evidence in support of the hypothesis that subtle ground movements frequently preceded failure events. Subsidence trends were consistently detected months prior to derailments and rockfalls in the pre-event MTInSAR analysis conducted at several locations (e.g., Lincoln, NE; Maupin, OR). These trends highlight

how well InSAR can provide early warning indicators for possible hazards. For instance, the Maupin site analysis underscored the value of MTInSAR in predictive geohazard assessment by demonstrating incremental mobilization over eight months before a rockfall event.

The research also highlights the limitations of MTInSAR in lower-class sites (e.g., Sandstone, WV, classified below Class B), where sudden loss of coherence often results in the exclusion of active deformation points. To address these challenges, a remote monitoring framework was developed and implemented, effectively overcoming the constraints of conventional MTInSAR. This framework successfully identified subtle ground movements preceding geohazard events, which were not identified by conventional methods.

The Wayanad, India case demonstrated how conventional MTInSAR failed to detect the early signs of deformation leading to a debris flow event. Applying the newly developed framework captured these subtle pre-event movements, demonstrating its capability to enhance hazard detection in challenging environments.

#### 6.1.1 Role of Soil Moisture in Hazard Initiation:

CCD analysis revealed a significant relationship between lower radar coherence and higher soil moisture, especially following rainfall events. This relationship was readily apparent at locations such as Burlington, ND, Lincoln, NE, and Maupin, OR, where a substantial loss of coherence was caused by excessive rainfall or snowfall. The results highlight the importance of soil moisture in the onset of hazards. These findings suggest a direct relationship between soil saturation and coherence.

The relationship between soil moisture and other environmental conditions on coherence was explored by correlating coherence from CCD with data from USCRN sensors. Results from several sensors around the country suggest that in conditions of no vegetation to low vegetation, there is a direct relationship between coherence, soil moisture and precipitation. This was seen in Bodega, CA, and Santa Barbara, CA. In the presence of low vegetation to medium vegetation, like in Blackville, SC and Cortez, CO, the correlation was present during the summer months, which can be attributed to low vegetation during this season. Regions with high vegetation, like Chatham, MI, and Sandstone, MN, showed consistently low coherence irrespective of moisture content, which led to the suspension of research efforts in these sites. Finally, a floodplain site in Columbia, SC was set up with extensive environmental parameter monitoring systems. This site was chosen because it didn't have ambiguity related to the sensor's location as in other USCRN sensors. The results from this site showed a direct relationship between soil moisture and coherence during the no vegetation period and also when the vegetation was in medium height, suggesting coherence can be used in such conditions. However, the correlation falls sharply as the vegetation increases.

This study suggests that regions immediately surrounding railway tracks have low vegetation, and the coherence change detection can be used to identify sudden soil saturation.

# 6.2 Performance of Proposed Framework

## 6.2.1 Comparison with The Current State of Practice

The proposed framework outperformed conventional MTInSAR in regions

Classified lower than B, where environmental conditions prevent the detection of scatterers or the deformations scatterers are lost due to sudden large deformation.

Sandstone, West Virginia, is an example of a tough environment in which the Rolling Stack MTInSAR approach shows its capacity to outperform conventional MTInSAR. With a rolling stack of 25 photos, the RS-SBAS analysis, in this instance, found two key clusters of displacement that were compatible with the slope failures that ultimately caused the accident. The sensitivity and accuracy of the suggested framework are demonstrated by its capacity to identify growing deformation activity in the failure site cluster several months before the rockfall event. Conventional MTInSAR approaches have missed subtle changes because of susceptibility to noise in vegetated or low-radar-reflectivity zones.

In Wayanad, India, the conventional MTInSAR could not identify deformations in the debris flow's origin point. At the same time, the proposed framework in the form of "scatterer accumulation" showed significant activity in the form of high-deformation scatterers in the origin point region. The framework also identified the crown of the landslide months before the disaster. Its capacity to identify early displacement in such conditions demonstrates the framework's superiority.

The framework is validated by demonstrating its effectiveness in higher site classifications, like in Maupin, OR, where both MTInSAR and the proposed framework successfully identified the origin point of the rockfall. The start of the deformation activity in both methods coincided roughly with the same period (8 months before the event).

6.2.2 Advantages of Early Identification Using The Proposed Framework.

The suggested frameworks show early detection capabilities by highlighting regions with hazard potential. In Sandstone, WV, two clusters of activity were identified when "Scatterer Accumulation" was used along with RS-MTInSAR, out of which one of the clusters failed and resulted in derailment. At the same time, mitigation efforts were employed in the form of retaining walls to the second cluster. Although the mitigation efforts were done proactively with no input from this research, a similar strategy can be applied to stop additional events highlighted by this framework. The clustering timeline also identified the cluster would experience imminent failure four days before the event.

The framework identified high-risk areas in regions surrounding the town of Wayanad, India, which later experienced other landslide events. Due to low access to insitu data, the origin point of these landslides cannot be correlated with the high-risk areas identified using the "Scatterer Accumulation".

The combination of displacement trends and soil moisture data can provide comprehensive knowledge of the threat in future applications. The suggested framework's incorporation of multi-temporal satellite data provides spatial and temporal coverage in contrast to conventional monitoring techniques, which frequently rely solely on single-stack MTInSAR.

## **CHAPTER 7: CONCLUSION**

This dissertation presents a comprehensive framework for identifying and monitoring geohazard-prone areas along railway tracks and slopes using advanced satellite radar imagery techniques. The research successfully demonstrates the efficacy of the proposed methodology in addressing key challenges in geohazard monitoring and mitigation.

# 7.1 Summary of Key Findings

- MTInSAR can identify small deformations preceding a geohazard event.
- The effectiveness of MTInSAR techniques depends on geometric properties and site conditions
- A classification system is developed based on the factors influencing SAR data acquisitions.
- The classification system divided into four levels (A to D) is used to guide the application of MTInSAR
- Sites classified as A have the best radar reflections, and PSInSAR can be used to measure deformations accurately
- Sites classified as B have relatively low radar reflections and require SBAS to measure deformation trends.

- Sites classified as C are challenging for conventional MTInSAR due to low radar returns due to season vegetation or other factors.
- Sites classified as D are unsuitable for SAR monitoring due to lack of line of sight from SAR sensors.
- Sites classified as C and some B are challenging to measure due to the loss of coherence of the scatterers midway through the analysis period, leading to the loss of observation scatterers.
- Soil moisture change, a critical factor in geohazard, can influence SAR coherence measured using CCD.
- Coherence data using C-band radar can effectively measure soil moisture change only in low to medium vegetation conditions.
- Integration of coherence change detection (CCD) with radar imagery highlighted the role of soil moisture changes in triggering geohazards, providing a new dimension for early detection.

### 7.2 Contribution to Research and Practice

- Introduced a novel monitoring framework that enhances geohazard detection and risk assessment.
- The framework consists of three post-processing methods developed to enhance the monitoring of sites classified as C.
- The post-processing methods use MTInSAR analysis in the "Rolling Stack" approach

- The "Rolling Stack" avoids the loss of deformation scatterers by using multiple stacks of data covering a large time period.
- The three post processing methods are
  - o Thresholding: Filters data to retain high-quality scatterers.
  - Scatterer Accumulation: Aggregates scatterers over time for better continuity.
  - Clustering Timeline: Identifies critical areas prone to geohazard failures
     by analyzing temporal deformation patterns.
- The post processing methods have demonstrated effectiveness in identifying increasing deformation activity and potential triggering events in challenging sites.
- The proposed framework successfully identified geohazard in post event analysis
  of Sandstone, WV, and Wayanad, India, where deformation activity was detected
  before catastrophic events.
- Advanced the field of railway geohazard monitoring by providing a scalable, noninvasive solution applicable across extensive railway corridors.
- Demonstrated the practical benefits of the framework for early hazard detection,
   enabling cost-effective and targeted mitigation strategies for railway operators.
- Established methodologies for integrating multi-temporal radar techniques (PSInSAR, SBAS) with coherence analysis to monitor both mobilization and environmental triggers of hazards.

# 7.3 Limitation of Study

- The framework is developed based on open-access SAR data. Currently, only
  Sentinel-1A is available in this category, limiting the coverage as it restricts the
  geographic properties to one option in site classification.
- The framework depends on auxiliary data, such as weather data, to improve the
  accuracy of measurements. The absence of this data removes the context from the
  deformation patterns.
- Sentinel-1A, a C-band radar used in this research, has low penetration power, restricting its application in soil moisture and deformation measurements.
- Dependence on historical data availability, with some sites lacking sufficient temporal datasets to conduct robust multi-temporal analyses.
- The multi-temporal analysis in "Rolling Stack" utilizes constant Ground Control Points location in all the stacks. A change might induce errors in the deformation measurements, as large deformations in the location of GCP points will generate bad deformation readings throughout the image.
- Currently, the framework is performed manually, which is computationally expensive when large regions are to be monitored.

### 7.4 Future Research Direction

• Several parts of the framework are constant steps that do not change based on the site under investigation, making it ideal for automation.

- Develop and integrate machine learning models to enhance predictive capabilities
   by identifying patterns and triggers for geohazards.
- Explore using higher wavelength radar sensors, such as L-band sensors, to overcome limitations in vegetation-covered areas.
- Future SAR applications in moisture content should be explored using intensity
  data and coherence. Intensity data has fewer factors contributing to the signal loss,
  reducing the ambiguity in the estimation.

#### REFERENCES

- [1] E. Marcus, Multi temporal InSAR in Land-cover and vegetation mapping, Aalto University, 2013.
- [2] Wikipedia, "Ingenheim derailment," 2020. [Online]. Available: https://en.wikipedia.org/wiki/Ingenheim derailment. [Accessed 14 May 2020].
- [3] CSX, "CSX Responds to Derailment in Draffin, KY," 13 February 2020. [Online]. Available: https://www.csx.com/index.cfm/about-us/media/press-releases/csx-responds-to-derailment-in-draffin-ky/. [Accessed 14 May 2020].
- [4] F. C. Dai, C. F. Lee and Y. Y. Ngai, "Landslide risk assessment and management: an overview," *Engineering Geology*, pp. 65-87, 2002.
- [5] D. D. C. Rizos, D. R. L. Mullen and S. V. Byrraju, "Satellite and Aerial Monitoring of Rail Infrastructure A Feasibility Study," in *Center for Connected Multimodal Mobility*, clemson, 2018.
- [6] P. E. Clark and M. L. Rilee, Remote sensing tools for exploration: observing and interpreting the electromagnetic spectrum, Springer Science \& Business Media, 2010.
- [7] M. Sarder, Logistics transportation systems, Elsevier, 2020.
- [8] Association of American Railroads, "Freight Rail's Positive Impact on America," August 2024. [Online]. Available: chrome-extension://efaidnbmnnnibpcajpcglclefindmkaj/https://www.aar.org/wp-content/uploads/2023/06/AAR-Impact-Fact-Sheet.pdf. [Accessed 08 12 2024].
- [9] K. Gholamizadeh, E. Zarei and M. Yazdi, "Railway Transport and Its Role in the Supply Chains: Overview, Concerns, and Future Direction," *The Palgrave Handbook of Supply Chain Management*, pp. 769--796, 2024.

- [10] V. Sadovnichii, G. Osipov, A. Akaev, A. Malkov and S. Shulgin, "Socio-Economic effectiveness of the development of the railway network in Siberia and the Far East: mathematical simulation and forecast," *Ekonomika Regiona*= *Economy of Regions*, p. 758, 2018.
- [11] D. J. Closs, S. B. Keller and D. A. Mollenkopf, "Chemical rail transport: The benefits of reliability," *Transportation Journal*, pp. 17--30, 2003.
- [12] S. Muzira, M. Humphreys and W. Pohl, "Geohazard management in the transport sector," in *World Bank, Washington, DC*, 2010.
- [13] M. Kumar and A. Agarwal, "Supply Chain Management and its Role in Rail Transport," in *E3S Web of Conferences*, 2024.
- [14] U. Haque, P. F. Da Silva, G. Devoli, J. Pilz, B. Zhao, A. Khaloua, W. Wilopo, P. Andersen, P. Lu and J. Lee, "The human cost of global warming: Deadly landslides and their triggers (1995--2014)," *Science of the Total Environment*, vol. 682, pp. 673--684, 2019.
- [15] G. F. Wieczorek and J. B. Snyder, "Historical rock falls in yosemite national park, California," *US Geological Survey Open-File Report*, vol. 3, p. 491, 2004.
- [16] K.-H. Yang, T. Nguyen, H. Rahardjo and D. Lin, "Deformation characteristics of unstable shallow slopes triggered by rainfall infiltration," *Bulletin of Engineering Geology and the Environment*, vol. 80, pp. 317--344, 2020.
- [17] z. yang, Monitoring and predicting railway subsidence using InSAR and time series prediction techniques, 2015.
- [18] M. G. Anderson, T. Glade and M. J. Crozier, Landslide hazard and risk, John Wiley and Sons Ltd, 2005.
- [19] Q. Zheng, H.-M. Lyu, A. Zhou and S.-l. Shen, "Risk assessment of geohazards along Cheng-Kun railway using fuzzy AHP incorporated into GIS," *Geometics, Natural Hazards and Risk,* vol. 12, pp. 1508--1531, 2021.
- [20] F. C. G. Gonzalez, M. d. C. R. Cavacanti, W. N. Ribeiro, M. B. d. Mendonça and A. N. Haddad, "A systematic review on rainfall thresholds for landslides occurrence," heliyon, vol. 10, 2024.
- [21] A. Dhikshit, B. Pradhan and A. M. Alamri, "Pathways and challenges of the application of artificial intelligence to geohazards modelling," *Gondwana Research*, vol. 100, pp. 290--301, 2021.

- [22] E. Monsieurs, O. Dewitte and A. Demoulin, "A susceptibility-based rainfall threshold approach for landslide occurrence," *Natural Hazards and Earth System Sciences*, vol. 19, pp. 775-789, 2019.
- [23] M. Emadi-Tafti and B. Ataie-Ashtiani, "A modeling platform for landslide stability: A hydrological approach," *Water*, vol. 11, p. 2146, 2019.
- [24] N. Bezak, M. Jemec Auflic and M. Mikov, "Application of hydrological modelling for temporal prediction of rainfall-induced shallow landslides," *Landslides*, vol. 16, pp. 1273--1283, 2019.
- [25] A. Innocenti, A. Rosi, V. Tofani, V. Pazzi, E. Gargini, E. B. Masi, S. Segoni, D. Bertolo, M. Paganone and N. Casagli, "Geophysical Surveys for Geotechnical Model Reconstruction and Slope Stability Modelling," *Remote Sensing*, vol. 15, p. 2159, 2023.
- [26] F. Ardizzone, M. Cardinali, M. Galli, F. Guzzetti and P. Reichenbach, "Identification and mapping of recent rainfall-induced landslides using elevation data collected by airborne Lidar," *Natural Hazards and Earth System Sciences*, vol. 7, pp. 637--650, 2007.
- [27] N. S. Chen, T. C. Li and Y. C. Gao, "A great disastrous debris flow on 11 July 2003 in Shuikazi valley, Danba County, western Sichuan, China," *Landslides*, vol. 2, pp. 71--74, 2005.
- [28] A. Machado, T. Munoz, C. Ballesteros, A. Juan, S. Allen and M. Stoffel, "Deforestation controls landlside susceptibility in Far-Western Nepal," *Catena*, vol. 219, p. 106627, 2022.
- [29] H. Rahardjo, A. Satyanaga and E. Leong, "Effects of flux boundary conditions on pore-water pressure distribution in slope," *Engineering Geology*, vol. 165, pp. 133-142, 2013.
- [30] J.-J. Wang, Y.-f. Huang and H. Long, "Water and salt movement in different soil textures under various negative irrigating pressures," *Journal of Integrative Agriculture*, vol. 15, pp. 1874-1882, 2016.
- [31] S. V. Byrraju, D. C. Rizos and Y. Qian, "Satellite radar imagery for detection and monitoring of geohazards," *Transportation Research Record*, pp. 283-292, 2020.
- [32] M. Hurlimann, V. Coviello, C. Bel, X. Guo, M. Berti, C. Graf, J. Hubl, S. Miyata, J. B. Smith and H.-Y. Yin, "Debris-flow monitoring and warning: Review and examples," *Earth-Science Reviews*, p. 102981, 2019.

- [33] L. Gao, L. m. Zhang, H. Chen and P. Shen, "Simulating debris flow mobility in urban settings," *Engineering geology*, vol. 214, pp. 67--78, 2016.
- [34] J. H. Bretz, "Solution cavities in the Joliet limestone of northeastern Illinois," *The Journal of Geology*, vol. 48, pp. 337--384, 1940.
- [35] H. Ali and J.-H. Choi, "Risk prediction of sinkhole occurrence for different subsurface soil profiles due to leakage from underground sewer and water pipelines," *Sustainability*, vol. 12, p. 310, 2019.
- [36] X. Fan, Q. Xu, J. Liu, S. S. Subramanian, C. He, X. Zhu and L. Zhou, "Successful early warning and emergency response of a disastrous rockslide in Guizhou province, China," *Landslides*, vol. 16, pp. 2445--2457, 2019.
- [37] N. Ju, J. Huang, C. He, T. Van Asch, R. Huang, X. Fan, Q. Xu, Y. Xiao and J. Wang, "Landslide early warning, case studies from Southwest China," *Engineering Geology*, vol. 279, p. 105917, 2020.
- [38] A. Mcclymont, E. Ernst, P. Bauman and N. Payne, "Integrating geophysical and geotechnical engineering methods for assessment of pipeline geohazards," *International Pipeline Conference*, vol. 3, p. V003T04A020, 2016.
- [39] h.-h. zhu, B. Shi and C.-C. Zhang, "FBG-based monitoring of geohazards: current status and trends," *Sensors*, vol. 17, p. 452, 2017.
- [40] R. Bell, H. Petschko, M. Rohrs and A. Dix, "Assessment of landslide age, landslide persistence and human impact using airborne laser scanning digital terrain models," *Geografiska Annaler: Series A, Physical Geography*, vol. 94, pp. 135--156, 2012.
- [41] M. V. D. Eeckhaut, J. Poesen, G. Verstraeten, V. Vanaker, J. Nyssen, J. Moeyersons, L. v. Beek and L. Vandekerckhove, "Use of LIDAR-derived images for mapping old landslides under forest," *Earth Surface Processes and Landforms*, vol. 32, pp. 754--769, 2007.
- [42] X. fan, G. Scaringi, Q. Xu, W. Zhan, L. Dai, Y. Li, X. Pei, Q. Yang and R. Huang, "Coseismic landslides triggered by the 8th August 2017 M s 7.0 Jiuzhaigou earthquake (Sichuan, China): factors controlling their spatial distribution and implications for the seismogenic blind fault identification," *Landslides*, vol. 15, pp. 967--983, 2018.
- [43] F. Fiorucci, M. Cardinali, R. Carla, M. Rossi, A. Mondini, L. Santurri, F. Ardizzone and F. Guzzetti, "Seasonal landslide mapping and estimation of landslide mobilization rates using aerial and satellite images," *Geomorphology*, vol. 129, pp. 59-70, 2011.

- [44] R. O. Dubayah and J. B. Drake, "Lidar Remote Sensing for Forestry," *Journal of Forestry*, vol. 98, pp. 44-46, 2000.
- [45] A. Segalini, A. Carri, C. Grignaffini and G. Capparelli, "Formulation of landslide risk scenarios using underground monitoring data and numerical models: conceptual approach, analysis, and evolution of a case study in Southern Italy," *Landslides*, vol. 16, pp. 1043-1053, 2019.
- [46] Y. Yang, Z. Zhao, D. Zhou, Z. Lai, K. Chang, T. Fu and L. Niu, "Identification and Analysis of the Geohazards Located in an Alpine Valley Based on Multi-Source Remote Sensing Data," *sENSORS*, vol. 24, p. 4057, 2024.
- [47] Q. Zheng, H.-M. Lyu, A. Zhou and S.-L. Shen, "Risk assessment of geohazards along Cheng-Kun railway using fuzzy AHP incorporated into GIS," *Geomatics, Natural Hazards and Risk,* vol. 12, pp. 1508--1531, 2021.
- [48] C. Esmersoy, A. Ramirez, S. Teebenny, Y. Liu, C.-C. Shih, C. Sayers, A. Hawthorn and M. Nessim, "A new, fully integrated method for seismic geohazard prediction ahead of the bit while drilling," *The Leading Edge*, vol. 32, pp. 1222-1233, 2013.
- [49] A. Dikshit, B. Pradhan and A. M. Alamri, "Pathways and challenges of the application of artificial intelligence to geohazards modelling," *Gondwana Research*, vol. 100, pp. 290--301, 2021.
- [50] T. Kavzoglu, E. K. Shin and I. Colkesen, "Selecting optimal conditioning factors in shallow translational landslide susceptibility mapping using genetic algorithm," *Engineering Geology*, vol. 192, pp. 101--112, 2015.
- [51] A. Carrara, M. Cardinali, R. Detti, F. Guzzetti, V. Pasqui and P. Reichenbach, "GIS techniques and statistical models in evaluating landslide hazard," *Earth surface processes and landforms*, vol. 16, pp. 427--445, 1991.
- [52] B. T. Pham, I. Prakash, S. K. Singh, A. Shirzadi, H. Shahabi and D. T. Bui, "Landslide susceptibility modeling using Reduced Error Pruning Trees and different ensemble techniques: Hybrid machine learning approaches," *Catena*, vol. 175, pp. 203--218, 2019.
- [53] G. Hughes, "On the mean accuracy of statistical pattern recognizers," *IEEE transactions on information theory*, vol. 14, pp. 55--63, 1968.
- [54] F. Guzzetti, M. Cardinali and P. Reichenbach, "The influence of structural setting and lithology on landslide type and pattern," *Environmental and Engineering Geoscience*, vol. 2, pp. 531--555, 1996.

- [55] A. M.-G. C. P. F. R. Alessandro Ferretti, InSAR Principles: Guidelines for SAR Interferometry Processing and Interpretation, ESA Publications , 2007.
- [56] T. Strozzi, u. Wegmuller, L. Tosi, G. Bitelli and V. Spreckels, "Land subsidence monitoring with differential SAR interferometry," *Photogrammetric engineering and remote sensing*, vol. 67, pp. 1261--1270, 2001.
- [57] P. Desmond, Y. James, E. Jerry, R. Karen, C. Scott and H. Roger, "InSAR applications for Highway Transportation Projects," U.S. Department of Transportation Federal Highway Administration, 2006.
- [58] A. Ferretti, C. Prati and F. Rocca, "Nonlinear subsidence rate estimation using permanent scatterers in differential SAR interferometry," *IEEE Transactions on geoscience and remote sensing*, vol. 38, pp. 2202-2212, 2000.
- [59] A. Ferretti, C. Prati and F. Rocca, "Permanent scatterers in SAR interferometry," *IEEE Transactions on Geoscience and Remote Sensing*, pp. 8-20, 2001.
- [60] P. Berardino, G. Fornaro, R. Lanari and E. Sansosti, "A new algorithm for surface deformation monitoring based on small baseline differential SAR interferograms," *IEEE Transactions on geoscience and remote sensing*, vol. 40, pp. 2375-2383, 2002.
- [61] A. Chaabani and B. Deffontaines, "Application of the SBAS-DInSAR technique for deformation monitoring in Tunis City and Mornag plain," *Geomatics, Natural Hazards and Risk*, vol. 11, pp. 1346--1377, 2020.
- [62] A. Ferretti, Satellite InSAR Data Reservoir Monitoring from space., EAGE Publications, 2014.
- [63] H. A. Zebker and J. Van Zyl, "Imaging radar polarimetry: a review," *Proceedings of the IEEE*, vol. 79, pp. 1583-1606, 1991.
- [64] Y. E. Molan and Z. Lu, "Modeling InSAR Phase and SAR Intensity Changes Induced by Soil Moisture," *IEEE Transactions on Geoscience and Remote Sensing*, pp. 4967-4975, 2020.
- [65] C. Damien and M. Nada, InSAR Coherence and Intensity Changes Detection, 2017.
- [66] S. V. Byrraju, D. Rizos, M. Sutton and N. Li, "Enhancing Railway Safety Through Satellite-Based Monitoring for Rockfall Potential," in *ASME/IEEE Joint Rail Conference*, 2024.

- [67] OSHA, "1926 Subpart P App A Soil Classification," 18 February 2020. [Online]. Available: https://www.osha.gov/laws-regs/regulations/standardnumber/1926/1926SubpartPAppA.
- [68] G. Asrar and D. J. Dokken, "1993 Earth Observing System Reference Handbook," 1993.
- [69] C. Roberto, A. Jailson, M. Hanna, P. Julia and R. A. Wilson, "Applicability of the InSAR technique for slope monitoring," *Soils and Rocks*, 2023.
- [70] A. Flores, Africa Ixmuca, K. E. Herndon, R. B. Thapa and E. Cherrington, "The SAR handbook: comprehensive methodologies for forest monitoring and biomass estimation," 2019.
- [71] S. V. Byrraju, D. Rizos, M. Sutton, N. Li and K. Hughes,"On the Use of InSAR Techniques to Detect Precursors of Shallow Geohazards in Railway Right of Way," in *AREMA Annual Meeting*, 2023.
- [72] S. Esch, Determination of soil moisture and vegetation parameters from spaceborne c-band sar on agricultural areas, 2018.
- [73] P. Marzahn and R. Ludwig, "On the derivation of soil surface roughness from multi parametric PolSAR data and its potential for hydrological modeling," *Hydrology and Earth System Sciences*, vol. 13, pp. 381--394, 2009.
- [74] A. Flores, I. Africa, K. E. Herndon, R. B. Thapa and E. Cherrington, "The SAR handbook: Comprehensive methodologies for forest monitoring and biomass estimation," 2019.
- [75] A. Gaber, F. Soliman, M. Koch and F. El-baz, "Using full-polarimetric SAR data to characterize the surface sediments in desert areas: A case study in El-Gallaba Plain, Egypt," *Remote Sensing of Environment*, vol. 162, pp. 11--28, 2015.
- [76] H. Jack, "Manufacturing Processes. Surfaces," 2013. [Online]. Available: http://engineeronadisk.com/V3/engineeronadisk-67.html.
- [77] R. Prakash and D. Singh, "Modeling of Scattering Response for Retrieval of Soil Parameters with Bistatic Radar," *Mathematics Applied in Information Systems*, vol. 2, pp. 168-196, 2018.
- [78] H. W. Yang, B. Baudet and T. Yao, "Characterization of the surface roughness of sand particles using an advanced fractal approach," *Proceedings of the Royal Society A: Mathematical, Physical and Engineering Sciences*, vol. 472, 2016.

- [79] L. Li, M. A. Nearing, M. H. Nichols, V. O. Polyakov, C. L. Winter and M. L. Cavanauggh, "Temporal and spatial evolution of soil surface roughness on stony plots," *Soil and Tillage Research*, vol. 200, p. 104526, 2020.
- [80] E. Sabrina, Determination of Soil Moisture and Vegetation Parameters from Spaceborne C-Band SAR on Agricultural Areas, 2018.
- [81] M. Nolan and D. R. Fatland, "Penetration depth as a DInSAR observable and proxy for soil moisture," *IEEE Transactions on Geoscience and Remote Sensing*, vol. 41, pp. 532-537, 2003.
- [82] B. Barrett, P. Whelan and E. Dwyer, "The use of C-and L-band repeat-pass interferometric SAR coherence for soil moisture change detection in vegetated areas," *Open Remote Sensing Journal*, vol. 5, pp. 37--53, 2012.
- [83] L. L. Bourgeau-Chavez, Y. M. Lee, M. Battaglia, S. L. Endres, Z. M. Laubach and K. Scarbrough, "Identification of woodland vernal pools with seasonal change PALSAR data for habitat conservation," *Remote Sensing*, vol. 8, p. 490, 2016.
- [84] T. L. Evans, M. Costa, W. Tomas and A. R. Camilo, "A SAR fine and medium spatial resolution approach for mapping the Brazilian Pantanal," *Geografia*, vol. 38, pp. 25-43, 2013.
- [85] National Centers for Environmental Information, "U.S. Climate Reference Network," 3 May 2023. [Online]. Available: https://www.ncei.noaa.gov/access/crn/.
- [86] P. W. Mueller and R. N. Hoffer, "Low-pass spatial filtering of satellite radar data," *Photogrammetric Engineering and Remote Sensing*, vol. 895, p. 887, 1989.
- [87] K. Pepin, H. A. Zebker and W. Ellsworth, "High-Pass Filters to Reduce the Effects of Broad Atmospheric Contributions in Sbas Inversions: A Case Study in the Delaware Basin," in *IGARSS 2020 2020 IEEE International Geoscience and Remote Sensing Symposium*, 2020, pp. 1030-1033.
- [88] R. Palama, M. Crosetto, O. Monserrat, A. Barra, M. Cuevas-González, B. Crippa, J. Rapinski and M. Mróz, "Filtering of the Atmospheric Phase Screen in InSAR Data Using the Nonequispaced Fast Fourier Transform," 2021.
- [89] R. Lanari, O. Mora, M. Manunta, J. J. Mallorqui, P. Berardino and E. Sansosti, "A small-baseline approach for investigating deformations on full-resolution differential SAR interferograms," *IEEE transactions on geoscience and remote sensing*, vol. 42, pp. 1377-1386, 2004.

- [90] S. Fiaschi, E. P. Holohan, M. Sheehy and M. Floris, "PS-InSAR analysis of Sentinel-1 data for detecting ground motion in temperate oceanic climate zones: a case study in the Republic of Ireland," *Remote Sensing*, vol. 11, p. 348, 2019.
- [91] R. Bamler and D. Just, "Phase statistics and decorrelation in SAR interferograms," in *Proceedings of IGARSS'93-IEEE International Geoscience and Remote Sensing Symposium*, 1993, pp. 980--984.
- [92] S. Byrraju and D. C. Rizos, "A Rolling Stack MTInSAR Approach for Critical Areas Detection in Geohazard Monitoring," *Transportation Research Record*, vol. In preparation, 2025.
- [93] K. Dhinesh, "572 mm of rainfall in just 48 hours: a battering that Wayanad did not anticipate," THIRUVANANTHAPURAM, 2024.
- [94] P. Aneesa, S. Soham, K. Wasif, G. Prajna and N. Shruti, "THE DEADLY DELUGE OF WAYANAD," 2024.
- [95] The Weather Channel, "Kerala Weather," Jul 2024. [Online]. Available: https://weather.com/en-IN/weather/monthly/l/76f086affaebf2ff6be9633d47611d1d50e1b655d9c634e906d0 6b4fd1dcd8ac.
- [96] S. V. Byrraju, R. C. Dimitris, A. S. Michael and L. Ning, "A Site Classification System for the Implementation of Multi-Temporal SAR for Geohazard Initiation Potential on the Railway Right of Way," *TRR*, 2024.
- [97] S. Iyer, "Wayanad landslides: ISRO's satellite images show extent of damage; crown of 1550m, debris travelled 8km along," Asianet news, 02 08 2024. [Online]. Available: https://newsable.asianetnews.com/india/wayanad-landslides-isro-s-satellite-image-show-extent-of-damage-crown-of-1550m-debris-travelled-8km-along-snt-shkvt4. [Accessed 12 01 2025].
- [98] U.S. Department of Agriculture, "Soil Survey Geographic (SSURGO) database for Chippewa County, Minnesota," U.S. Department of Agriculture, Natural Resources Conservation Service, Fort Worth, Texas, 2022.
- [99] ESA, "Copernicus Open Access Hub," 28 4 2023. [Online]. Available: https://scihub.copernicus.eu/.
- [10] ASF, "Alaska Satellite Facility Distributed Active Archive Center," 05 4 2023.
- 0] [Online]. Available: https://search.asf.alaska.edu/#/.

- [10 U.S. Department of Agriculture, "Soil Survey Geographic (SSURGO) database for
- 1] Jefferson County, Alabama," U.S. Department of Agriculture, Natural Resources Conservation Service, Fort Worth, Texas, 2021.
- [10 U.S. Department of Agriculture, "Soil Survey Geographic (SSURGO) database for
- 2] Wasco County, Oregon, Northern Part," U.S. Department of Agriculture, Natural Resources Conservation Service, Fort Worth, Texas, 2022.
- [10 U.S. Department of Agriculture, "Soil Survey Geographic (SSURGO) database for
- 3] Dekalb County, Georgia," U.S. Department of Agriculture, Natural Resources Conservation Service, Fort Worth, Texas, 2019.
- [10 SSURGO, "Soil Survey Geographic (SSURGO) database for ward county, North
- 4] Dakota," U.S. Department of Agriculture, Natural Resources Conservation Service, Fort Worth, Texas, 2021.
- [10] Accuweather, "Bulington ND weather," 04 2022. [Online]. Available:
- 5] https://www.accuweather.com/en/us/burlington/58722/aprilweather/2152407?year=2022.
- [10 U.S. Department of Agriculture, "Soil Survey Geographic database for Lavaca
- 6] County, Texas," U.S. Department of Agriculture, Natural Resources Conservation Service, Fort Worth, Texas, 2022.
- [10] U.S Department of Agriculture, "Soil Survey Geogrphic (SSURGO) database for
- 7] Yellowstone National Park, Wyoming-Montana-Idaho," U.S. Department of Agriculture, Natural Resources Conservation Service, Fort Worth, Texas, 2021.
- [10 U.S. Department of Agriculture, "Soil Survey Geographic (SSURGO) database for
- 8] San Diego County, California," U.S. Department of Agriculture, Natural Resources Conservation Service, Fort Worth, Texas, 2022.
- [10 EPA, "Raymond Train Derailment," On-Scene Coordinator EPA, 2023.
- [11 A. a. P. C. a. R. F. Ferretti, "Nonlinear subsidence rate estimation using permanent
- o] scatterers in differential SAR interferometry," *IEEE Transactions on Geoscience and Remote Sensing*, vol. 38, pp. 2202--2212, 2000.
- [11 KKTV11, "kktv," 15 10 2023. [Online]. Available:
- 1] https://www.kktv.com/video/2023/11/02/pueblo-train-derailment-preliminary-report-released/.
- [11 B. Matthieu, "Sentinel-1 Product Definition," European Space Agency, 2016.

- [11 M. Y. Jin, "Optimal Doppler centroid estimation for SAR data from a quasi-
- 3] homogeneous source," *IEEE Transactions on Geoscience and Remote Sensing*, pp. 1022--1025, 1986.
- [11 F. De Zan and A. M. Guarnieri, "TOPSAR: Terrain observation by progressive
- 4] scans," *IEEE Transactions on Geoscience and Remote Sensing*, vol. 44, pp. 2352-2360, 2006.
- [11 C. Lopez-Martinez and E. Pottier, "On the extension of multidimensional speckle
- 5] noise model from single-look to multilook SAR imagery," *IEEE Transactions on Geoscience and Remote Sensing*, vol. 45, pp. 305--320, 2007.
- [11 D. Small and A. Schubert, "Guide to Sentinel-1 geocoding," Remote Sensing Lab.
- 6] Univ. Zurich (RSL), Zurich, Switzerland, Tech. Rep. UZHS1-GC-AD, 2019.
- [11 Z. Li and J. Bethel, "Image coregistration in SAR interferometry," The
- 7] International Archives of the Photogrammetry, Remote Sensing and Spatial Information Sciences, vol. 37, p. 433, 2008.
- [11 D. O. Nitti, R. F. Hanssen, A. Refice, F. Bovenga and R. Nutricato, "Impact of
- 8] DEM-assisted coregistration on high-resolution SAR interferometry," *IEEE Transactions on Geoscience and Remote Sensing*, vol. 49, pp. 1127--1143, 2010.
- [11 J. Fan, G. Li, X. Guo, G. Liu, H. Guo, D. Ge and S. Liu, "Evaluating Interpolation
- 9] Kernels for InSAR Using Scilab," Claude Gomez Hangzhou, Aug. 29, 2006, p. 9.
- [12 K. D. Murray, D. P. Bekaert and R. B. Lohman, "Tropospheric corrections for
- 0] InSAR: Statistical assessments and applications to the Central United States and Mexico," *Remote Sensing of Environment*, vol. 232, p. 111326, 2019.
- [12] W. Xu, L. Xie, Y. Aoki, E. Rivalta and S. Jonsson, "Volcano-wide deformation after
- 1] the 2017 Erta Ale dike intrusion, Ethiopia, observed with radar interferometry," *Journal of Geophysical Research: Solid Earth.*
- [12 Q. Wang, W. Yu, B. Xu and G. Wei, "Assessing the use of GACOS products for
- 2] SBAS-INSAR deformation monitoring: A case in Southern California," *Sensors*, vol. 19, p. 3894, 2019.
- [12] R. Xiao, C. Yu, Z. Li and X. He, "Statistical assessment metrics for InSAR
- 3] atmospheric correction: Applications to generic atmospheric correction online service for InSAR (GACOS) in Eastern China," *International Journal of Applied Earth Observation and Geoinformation*, vol. 96, p. 102289, 2021.
- [12] R. Xiao, C. Yu, Z. Li, C. Song and X. He, "General survey of large-scale land
- 4] subsidence by GACOS-corrected InSAR stacking: Case study in North China

- Plain," *Proceedings of the International Association of Hydrological Sciences*, vol. 382, pp. 231--218, 2020.
- [12] J.-S. Lee, L. Jurkevich, P. Dewaele, p. Wambacq and a. Oosterlinck, "Speckle
- 5] filtering of synthetic aperture radar images: A review," *Remote sensing reviews*, vol. 8, pp. 313--340, 1994.
- [12 Q. Feng, H. Xu, Z. Wu, Y. You, W. Liu and S. Ge, "Improved Goldstein
- 6] interferogram filter based on local fringe frequency estimation," *Sensors*, vol. 16, p. 1976, 2016.
- [12 r. m. goldstein and c. l. werner, "Radar interferogram filtering for geophysical
- 7] applications," *Geophysical research letters*, vol. 25, pp. 4035--4038, 1998.
- [12] I. Baran, M. P. Stewart, B. M. Kampes, Z. Perski and P. Lilly, "A modification to
- 8] the Goldstein radar interferogram filter," *IEEE Transactions on Geoscience and Remote Sensing*, vol. 41, pp. 2114-2118, 2003.
- [12] R. M. Goldstein, H. A. Zebker and C. L. Werner, "Satellite radar interferometry:
- 9] Two-dimensional phase unwrapping," *Radio science*, vol. 23, pp. 713--720, 1988.
- [13] A. Pepe, M. Manunta, L. Euillades, L. Paglia, Y. Yang and R. Lanari, "New
- 0] improvements of the EMCF phase unwrapping algorithm for surface deformation analysis at full spatial resolution scale," 2011.
- [13 J. Huang and Z. Li, "A Delaunay triangulation approach to space information flow,"
- 1] in 2016 IEEE Globecom Workshops (GC Wkshps), 2016.
- [13] F. Casu, M. Manzo and R. Lanari, "A quantitative assessment of the SBAS
- 2] algorithm performance for surface deformation retrieval from DInSAR data," *Remote Sensing of Environment,* vol. 102, pp. 195--210, 2006.
- [13] Y. Yan and Y. Wang, "An Effective Approach to Select Valid and Accurate Ground
- 3] Control Points in SBAS-InSAR Technique," *13th European Conference on Synthetic Aperture Radar*, pp. 1--4, 2021.
- [13] Y. Yan and Y. Wang, "Delineating Reliable Ground Control Points in SBAS-InSAR
- 4] Analysis with Phase Derivative Variance," 2021 IEEE International Geoscience and Remote Sensing Symposium IGARSS, pp. 3360--3363, 2021.

## APPENDIX A: SITE MOBILIZATION MONITORING

### A.1 Lincoln, NE

### A.1.1 Event

On June 25, 2021, a BNSF train carrying coal derailed near Bennet, Nebraska, as depicted in Figure A.1(a). The incident occurred at Saltillo Road and 148th Street intersection, as shown in A.1(b), close to 2 miles from Bennet. This track remained inactive for two decades but was recently reactivated. While the exact cause of the derailment remains unknown, it should be noted that the region had recently encountered heavy rainfall, resulting in approximately 4 inches of precipitation and flash flooding.

#### A.1.2 Site Description

The region under investigation is located in the southeastern part of Nebraska at latitude and longitude (40.70, -96.53). This region is approximately 13 miles from the state capital of Bennet and has a mean annual precipitation of 28 to 40 inches with 158 to 203 frost-free days. The region is classified as prime farmland. The InSAR analysis region can be divided into 2 regions. The first is the track region (7050 Figure A.2) and the area immediately surrounding it, and the second region (7684 Figure A.2) is the farmland beyond, indicated by Figure A.2. The track region has a silt loam soil profile of up to 41 inches of the topsoil layer, with the soil below it being silty clay loam from 41 to



Figure A.1 (a) Shows the derailment; (b) Shows the location where the derailment took place; (c) The coverage of Sentinel-1A covering the area of the accident.



Figure A.2 Shows the soil profile of the region.

79inches of the soil layer. It is moderately well-drained and has the capacity to transmit water in a moderately high range (0.20 to .60 in/hr). This region was occasionally flooded as the region is located in flood plains. The farmland does have a similar soil profile to the track region. Its only difference is that it's not located in the flood plane and has not experienced flooding events. A detailed soil profile of the region can be found in [98].

## A.1.3 Data Availability

The region under investigation is in Nebraska, where Sentinel-1A provided coverage. This region is covered by the satellite once every 12 days and is located in rural areas, suggesting lower coherence due to obstructions from vegetation. The dataset for this study is obtained from the Sentinel constellation, and the satellite images are downloaded from the Sentinel-1 EU data hub (ESA) [99] and Alaska Satellite Facility (ASF) [100]. Figure A.1 (c) shows the path taken by the Sentinel-1A satellite. The analysis employs PSInSAR and CCD techniques using archived satellite radar images spanning 24 months, covering the event's occurrence. To ensure accurate results, the study is divided into two periods, pre-event and post-event. Separation is essential since events such as rockfalls can cause sudden subsidence and significant changes in the DEM, leading to a loss of coherence and persistent scatterers, affecting data quality. The acquisition periods are detailed in Table A.1.

## A.1.4 PSINSAR Analysis

The PSInSAR analysis for site mobilization was conducted using a stack of 20 images, at a minimum. The deformation maps from the Sentinel-1A orbit are

Table A.1 Data Availability of Sentinel-1A covering the city of Lincoln, Nebraska.

Data Set	Sentinel 1-A
Pre-event	10/19/2020 to 6/16/2021
Post-event	6/28/2021 to 5/20/2022

superimposed on an optical image taken on June 21, 2021. The displacement observed is in mm and plotted on the color-coded PS images that show the total displacement over the entire analysis. The negative displacement (blue) indicates subsidence, and the positive displacement (red) denotes height gain about the line of sight of each satellite and orbit.

Pre-Event Analysis: The PSInSAR analysis using the one orbit produced the deformation map shown in Figure A.3(a), the PS over the region covers the time period from October 10, 2020, to June 16, 2021. Figure A.3(a), the red highlighted region, shows where the derailment occurred. Figure A.3(b) shows the PS with the stable PS removed and only the high-displacement PS being shown. Figure A.3(c) shows the region where the derailment took place. The white highlighted region shows the largest subsidence in the observation period. Figure A.3(d) shows the progress of the displacement over the analysis time period. The displacement over time shows consistent subsidence activity with the exception of acquisition on Feb 16, which shows a sudden drop in subsidence. It is unknown if the subsidence in this location led to the derailment of the train.

Post-event analysis: The PSInSAR analysis of the region analyzes the derailment from June 28, 2021, to May 20, 2022. Figure A.4(a) shows the PS analysis, with Figure A.4(b) showing the PS analysis with stable PS removed from the analysis. This analysis shows that the region in the white highlighted box in Figure A.4(b) has consistently high subsidence. This region needs further monitoring to understand the reason for this high subsidence and whether the subsidence is affecting the railway line. The region in the red highlighted box in Figure A.4(b) experienced derailment following the post-event analysis.

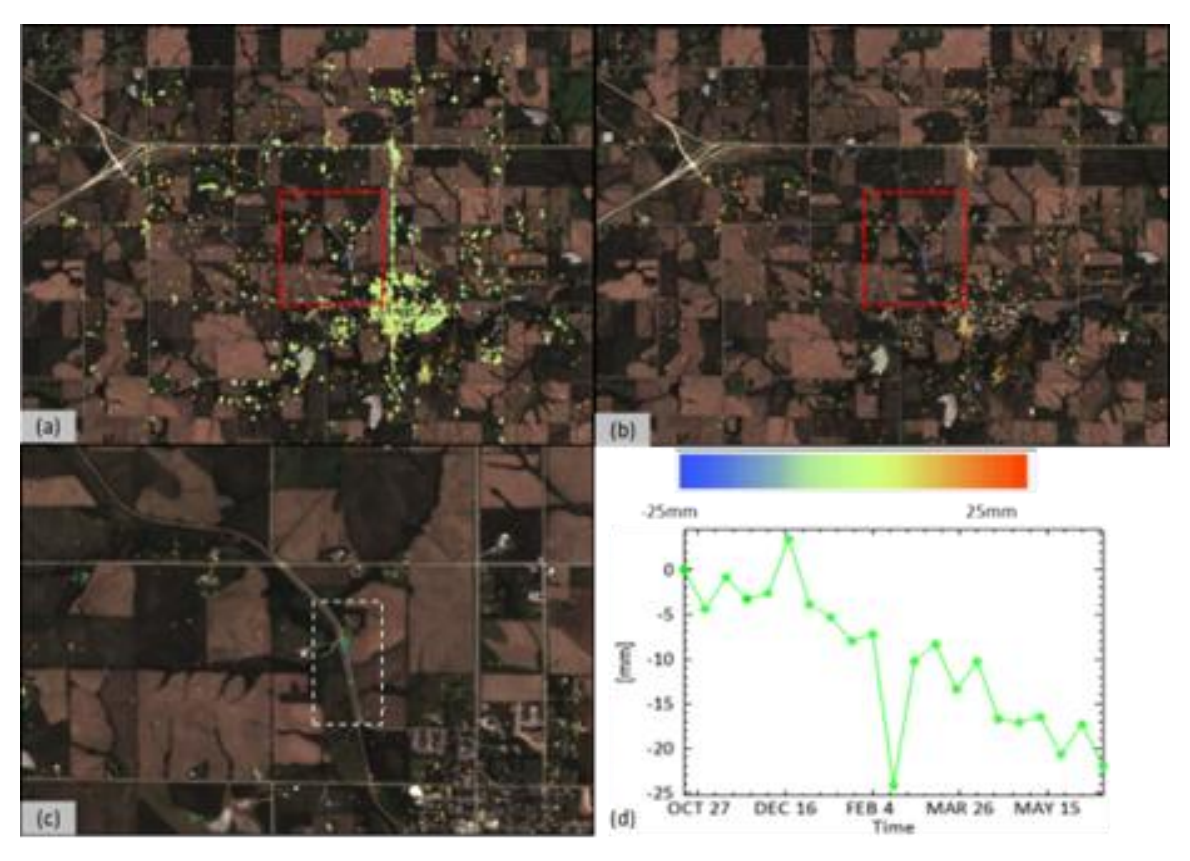


Figure A.3 (a) the displacement map superimposed on the optical image. (b) PS analysis results with high displacement (c) shows the derailment site with high subsidence in the region highlighted (d) Shows the progress of the displacement over time of one PS point.

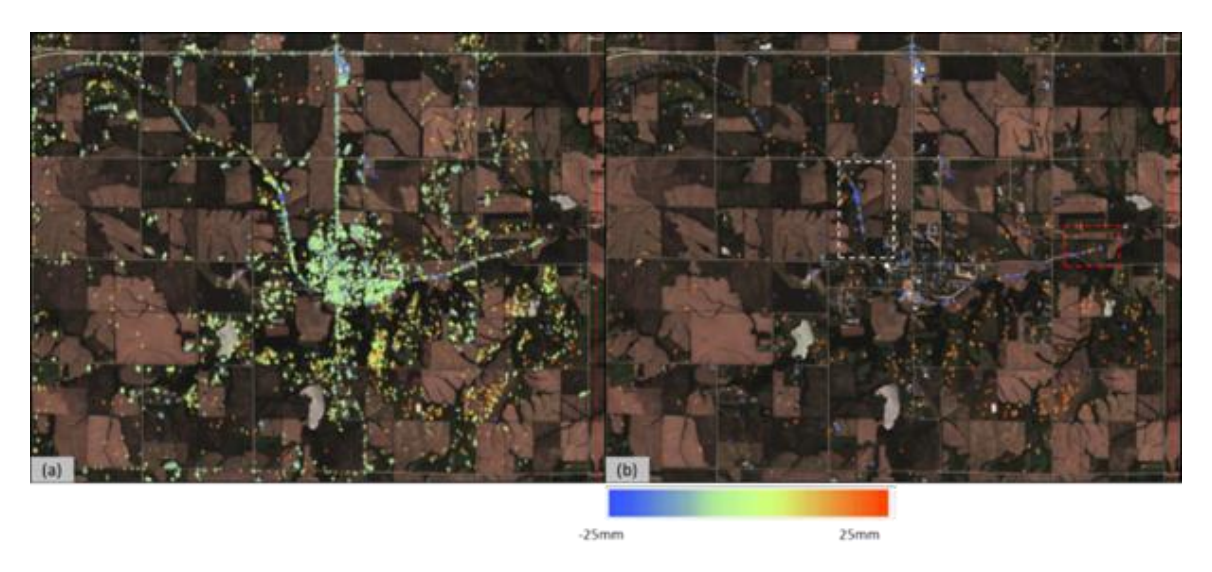


Figure A.4 (a) the post event displacement map superimposed on the optical image. (b) PS analysis results with high displacement with red-highlighted region showing consistently high subsidence and red-highlighted region showing a derailment event which took place 2 months after the analysis.

### A.1.5 CCD Analysis

Pre-event analysis: The CCD timeline analysis produces coherence analysis results over an optical image, and the CCD analysis uses data from the same orbit with 12 days between each acquisition. This particular analysis used data from May 11, 2021, and May 23, 2021, to capture coherence 30 days before the accident. Figure A.5(a) shows moderately high coherence in the region, with some pockets of low coherence indicating low moisture content in the topsoil, with some parts of the track not receiving radar backscatter. The track is visible with high coherence due to its distinct shape.

Figure A.5(b) displays the results of analyzing SAR images from May 23, 2021, and June 04, 2021, which were taken 20 days before the accident. The resulting image shows relatively low coherence throughout the region, with the track barely visible in some areas. This is attributed to rainfall on May 22, 2021.

The coherence image in Figure A.5(c) utilizes SAR images from June 04, 2021, and June 16, 2021, which is the coherence 9 days before the accident. The resulting image shows similar coherence to the coherence image from Figure A.5(b). The region did not experience any rainfall during this period, and the lack of rainfall has not reduced the coherence in the region. Although the coherence is lower than in Figure A.5(a), the track is still visible in this case.

<u>Post-event analysis:</u> Upon conducting a post-event analysis, it has been observed that the railway track has consistently low coherence from June 16 to August 08. This is due to consistently high rainfall in the region during this period, greatly affecting the coherence measurements of the region. Figure A.6(a) shows the coherence from June 16, 2021, and

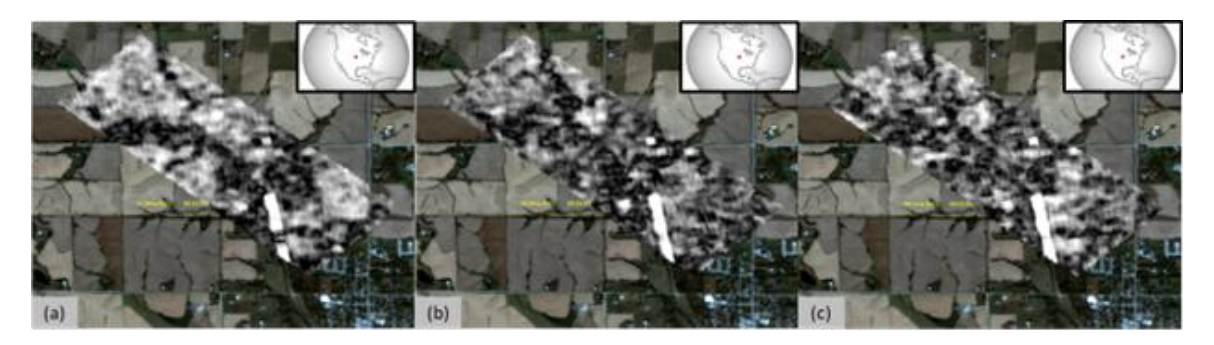


Figure A.5 (a) Coherence from 05/11 to 05/23/2021 (b) Coherence from 05/23 to 06/04/2022 (c) Coherence from 06/04 to 06/16/2022

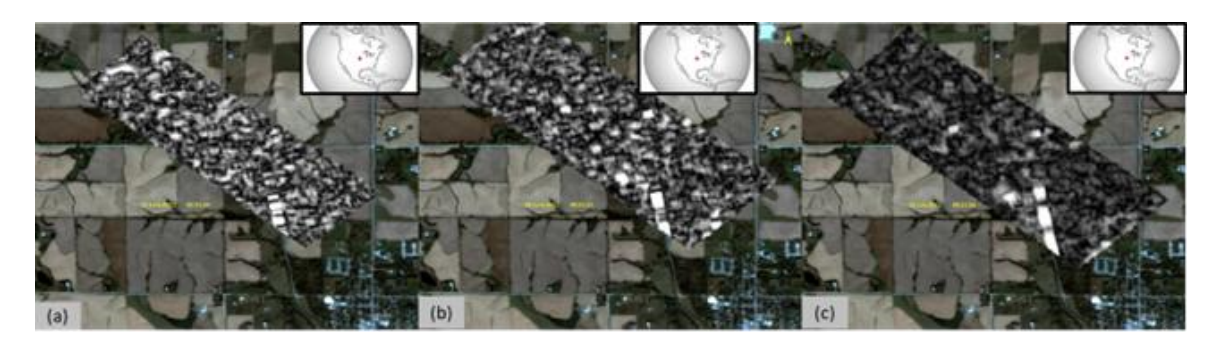


Figure A.6 (a) Coherence from 06/16 to 06/28/2021 (b) Coherence from 06/28 to 07/22/202 (c) Coherence from 07/22 to 08/03/2021

June 28, 2021, covering the derailment, and the effect of the derailment and the rainfall is visible in the coherence image with low coherence throughout the image.

Figure A.6(b) of post-event CCD analysis displays low coherence, with only a few parts of the image having high coherence. This analysis utilizes SAR images captured after the accident on June 28, 2021, and July 22, 2021. The coherence in the region is low due to two reasons: the rainfall affecting the June 28th acquisition and the large time gap between the two acquisitions.

The coherence Figure A.6(c) of post-event CCD analysis reveals low coherence across the area, with the track regaining some coherence compared to the surrounding region. This analysis also utilizes SAR images obtained after the accident on July 22, 2021, and Aug 03, 2022. The weather report during image acquisition indicates high rainfall in the region, which greatly affected the coherence of these acquisitions.

Figure A.7 shows the coherence of the region for images taken on Aug 03, 2021, and Aug 15,2021. This image shows the coherence of the track being visible while the region still shows consistently low coherence. This is due to the rainfall affecting the image on Aug 03, 2021. The high coherence on the track also suggests that it is not affected by the rainfall and is remaining in a stable condition.

#### A.1.6 Discussion

CCD analysis of the region shows the region was susceptible to loss of coherence due to rainfall in the region. The monitored region experienced significant rainfall between the derailment and the last data acquisition. This led to no significant changes to the coherence, as seen in Figure A.3(c). The post-event coherence analysis also had



Figure A.7 Coherence from 08/03 to 08/15/2021

significant rainfall activity, leading to the region's consistently low coherence. Although the surrounding region experienced low coherence in the post-event analysis, the track showed relatively high coherence suggesting the track following the derailment was stable. PSInSAR analysis of the region showed a low density of PS near the derailment site, with the white-highlighted region (Figure A.3 (c)) having consistently high subsidence. It is unknown if this region's subsidence led to the derailment. The postevent region showed high subsidence in the same region as seen in the pre-event analysis. The red-highlighted region in Figure A.4(b) shows high displacement in the region, this region experienced a derailment 3 months after the monitoring period. It is unknown if the displacement observed contributed to the derailment. With the presence of single Sentinel data and low access to the line of sight of the radar sensor, this case study can be categorized in class B. This case suggests the limitations of CCD when the rainfall activity happens after the acquisition date and PSInSAR when the derailment zone is not accessible to radar backscatter. This case also shows that despite the existing limitations, the application of PSInSAR and CCD analysis can have great applications for railway ROW safety applications.

# A.2 Birmingham, AL

## A.2.1 Event

This case didn't experience any event destabilizing it. This region was monitored to observe for any possible case of instability. The railway track passes along the sharp cliff of the Village Creek mine in Birmingham, Alabama, making it susceptible to any unstable activity caused by the mine. Figure A.8(a) shows the cliff where the

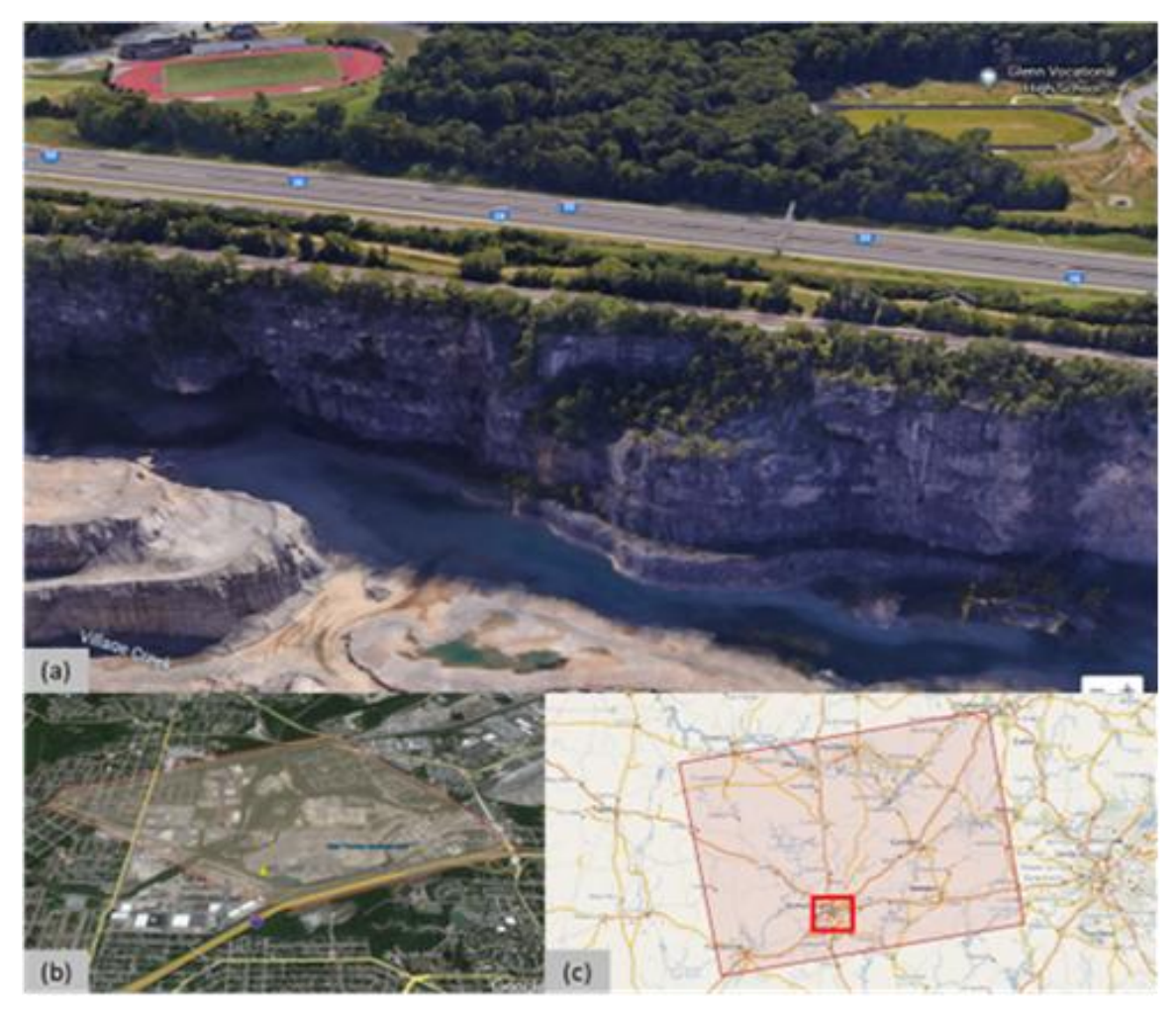


Figure A.8 (a) Shows the location of concern for the instability analysis; (b) Shows the mine region and the area under observation; (c) The coverage of Sentinel-1A covering the city of Birmingham, Alabama.

destabilization concern prompted the monitoring effort. Figure A.8(b)(c) shows the area of analysis.

## A.2.2 Site Description

The region under investigation is located in the city of Birmingham, Alabama, at latitude/longitude (33.52, -86.85). This region has a mean annual precipitation of 48-56 inches, with 180 to 210 frost-free days. This region is 95 percent urban land with hillslopes landform setting. It has a constant soil classification around the city as can be seen in Figure A.9, and a much more in-depth soil profile can be found in [101]

## A.2.3 Data Availability

The region under investigation is located in Alabama and is part of the city of Birmingham. The radar satellite Sentinel-1A covers this region once every 12 days. The region is located in urban areas and, due to proximity to the mine, has a large area exposed to radar backscatter. Since only one satellite covers this area, analysis of the region is restricted to the angle of incidence. The dataset for this study is obtained from the Sentinel constellation, and the satellite images are downloaded from the Sentinel-1 EU datahub (ESA) [99] and Alaska Satellite Facility (ASF) [100]. Figure A.8(c) shows the path taken by the Sentinel1-A satellite. The analysis employs PSInSAR techniques using archived satellite radar images spanning 12 months. The acquisition periods are detailed in Table A.2.

### A.2.4 PSINSAR Analysis

The PSInSAR analysis for site mobilization monitoring was conducted using a stack of 20 images at a minimum. The deformation maps from the Sentinel-1A orbit are



Figure A.9 The soil profile map of the Village Creek mine in Birmingham, Alabama

Table A.2 Satellite Data Acquisition Periods for Birmingham, Alabama

Data Set	Sentinel 1-A (Ascending)
Stability monitoring	02/26/2022 to 10/24/2022

superimposed on an optical image taken on June 21, 2021. The displacement observed is in mm and plotted on the color-coded PS images that show the total displacement over the entire analysis. The negative displacement (blue) indicates subsidence, and the positive displacement (red) denotes height gain about the line of sight of each satellite and orbit.

The PSInSAR analysis uses single orbit data to produce the deformation map in Figure A.10. Figure A.10(a) shows the region's high radar backscatter as seen by the density of PS. Figure A.10(b) shows the displacement in the range of -25 to -14 and 14 to 25 to show the largest deformation in the region without the stationary point. The red dotted square in Figure A.10 (a) and A.10(b) shows the area under observation, with Figure A.10(c) and Figure A.10(d) showing the highlighted region in a zoomed-in manner. Figure A.11(a) shows the high subsidence measured on the tracks on the east side of the analysis area. Figure A.11(b) shows the progress of the displacement highlighted (green and blue highlights) in Figure A.11(a). The displacement is consistent in the region, and since this region is not near the cliff, additional monitoring is required before further action is taken about this subsidence.

Figure A.12(a) shows the high subsidence measured on the tracks near the center of the analysis area. Figure A.12(b) shows the progress of the displacement highlighted (green and blue highlights) in Figure A.12(a). The displacement is consistent in the region. Since this region is near the cliff, these PS points need to be monitored further.

### A.2.5 Discussion

PSInSAR analysis over Birmingham, Alabama, has shown that the region has PS

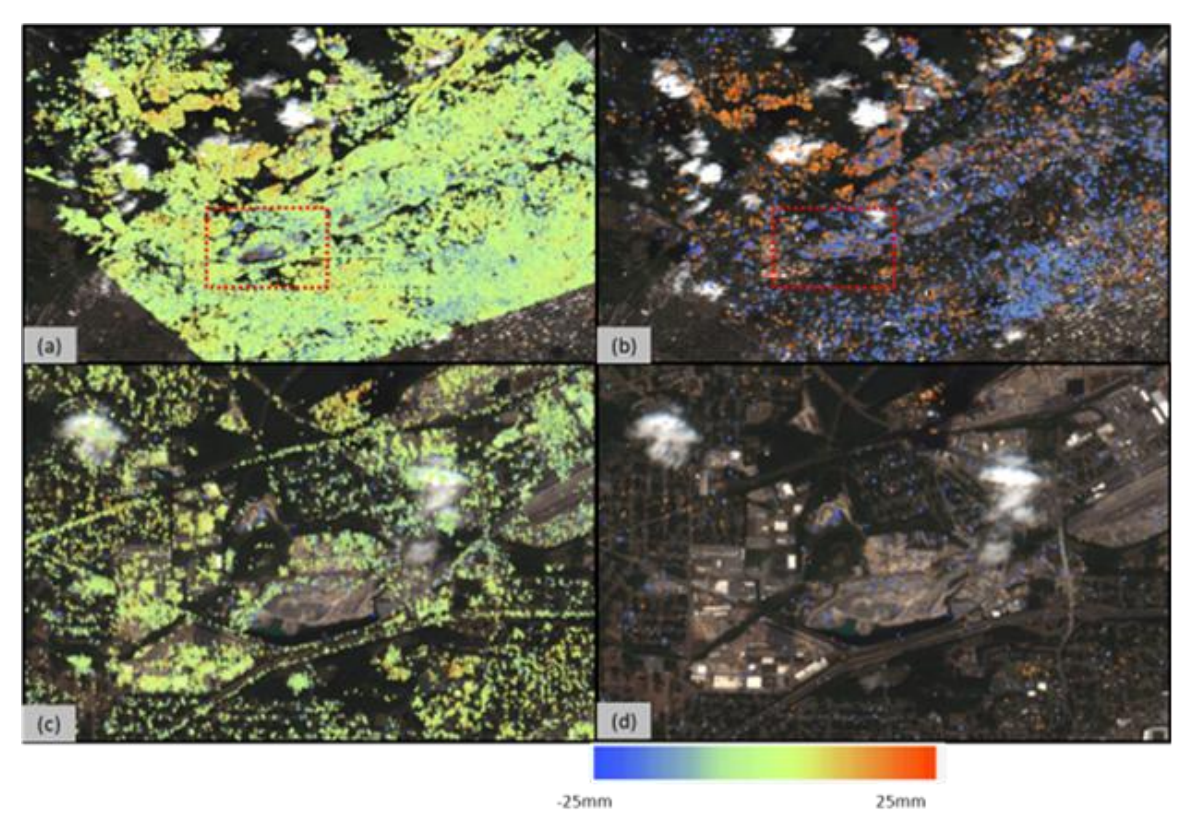


Figure A.10 (a) Shows the total PS in the area under observation. (b) Stable PS has been removed, and high displacement PS are only shown. (c) Shows the total PS in the region of concern (d) Shows only the PS which have experienced high displacement in the region

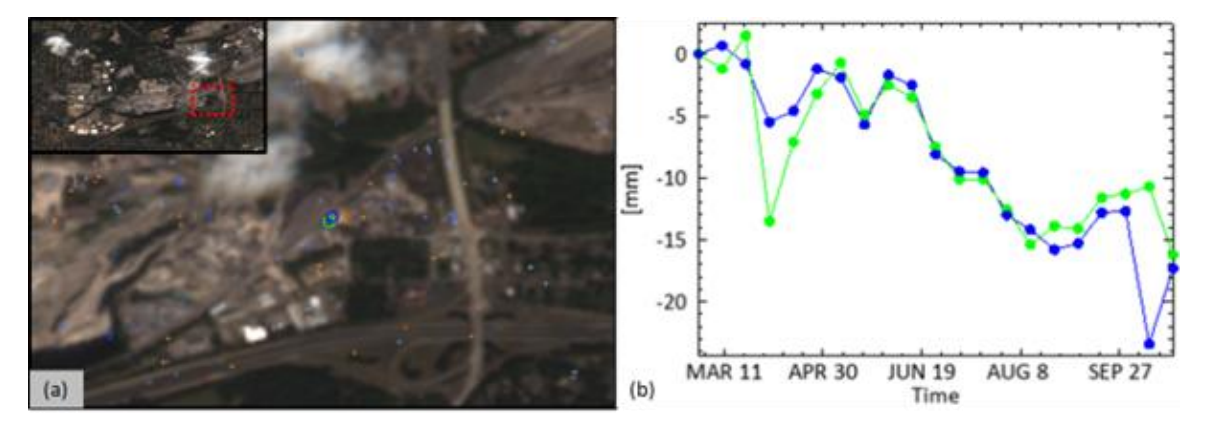


Figure A.11 (a) Shows the high displacement PS on the railway track east of the site. 2 PS are highlighted to observe the progress of displacement. (b) Shows the displacement over time for the highlighted displacement.

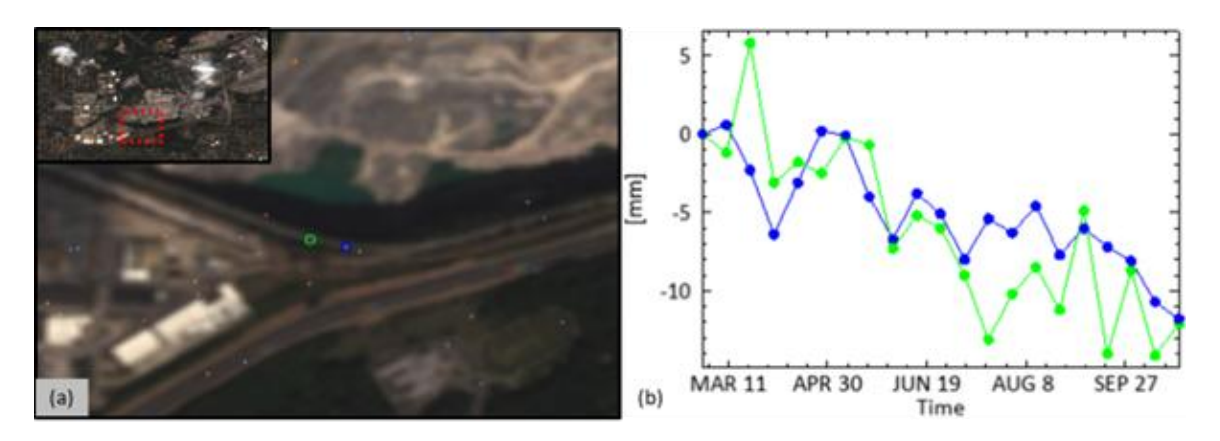


Figure A.12 (a) Shows the high displacement PS on the railway track close to the mine cliff. 2 PS are highlighted to observe the progress of displacement. (b) Shows the displacement over time for the highlighted displacement.

with high displacement surrounding the mine under observation. Most of the high concentrations of PS are not on the track and are believed to be due to the mining activity in the region. However, several PS show high subsidence near the railway track overlooking the cliff. This region can be classified as A due to high radar returns from the area, and further monitoring will provide a better understanding of the subsidence in the region.

# A.3 Maupin, OR

### A.3.1 Event

In the early morning of May 07, 2020, a derailment occurred due to a rockfall near Maupin in Oregon, as shown in Figure A.13(a). The derailment took place approximately 0.71 miles from the city center. This region has a 40 to 70 percent slope and is well drained, as seen in the street view shown in Figure A.13(b). The area of interest encompasses 5.85 mi<sup>2</sup> and is characterized by the top 4 inches of the soil being extremely stony loam, with the bedrock lying 12-20 inches deep [102].

## A.3.2 Data Availability

The study area is on the west coast and benefits from multiple satellite passes, providing access to SAR data from different angles. The site has high radar reflectivity with minimal signal losses. The dataset for this study is obtained from the Sentinel constellation, and the satellite images are downloaded from the Sentinel-1 EU datahub [99] and Alaska Satellite Facility (ASF) [100]. Figure A.13(c) shows the path taken by Sentinel1-B satellites, Figure A.13(d) shows the path of Sentinel1-A satellite. The analysis employs PSInSAR and CCD techniques using archived satellite radar images

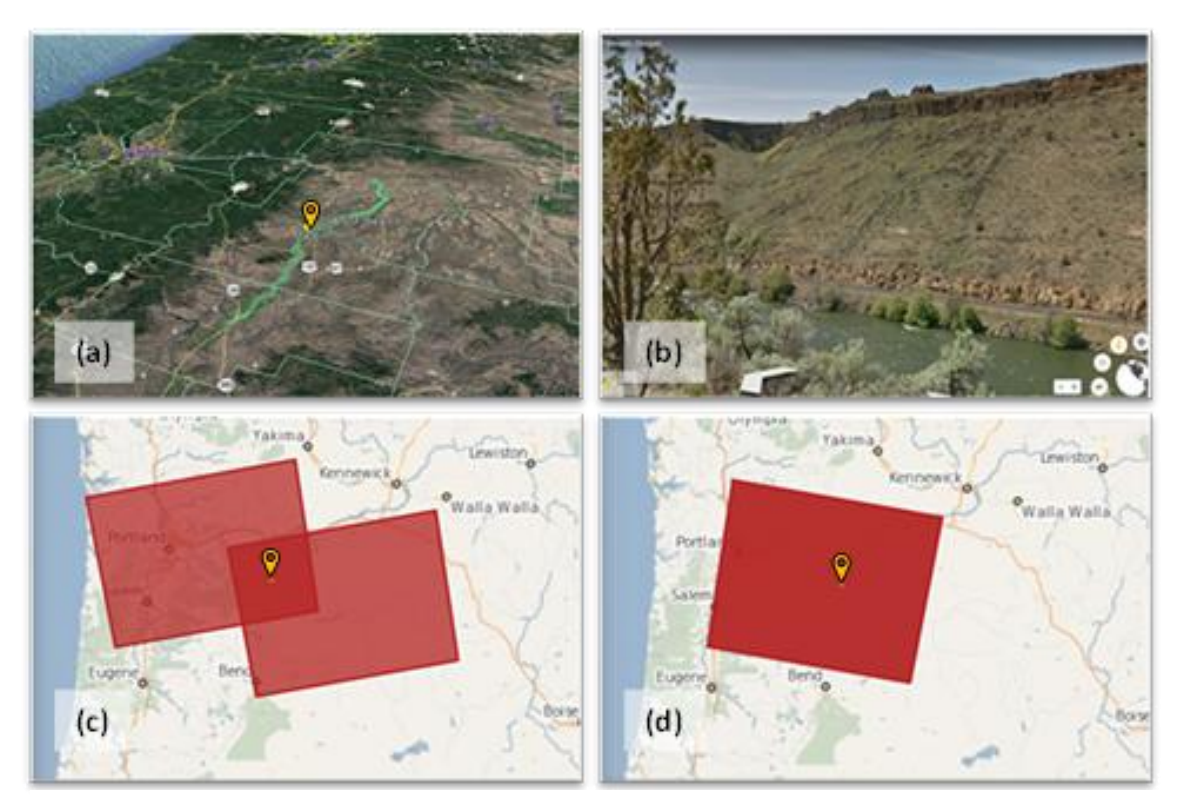


Figure A.13 Oregon Maupin Site: (a) Location on the map; (b) Street view of rockfall site; (c) Sentinel 1-B coverage for primary and alternate orbits; (d) Sentinel 1-A coverage

spanning 24 months, covering the event's occurrence. To ensure accurate results, the study is divided into two periods, pre-event and post-event. Separation is essential since events such as rockfalls can cause sudden subsidence and significant changes in the DEM, leading to a loss of coherence and persistent scatterers, affecting data quality. The acquisition periods are detailed in Table A.3.

## A.3.4 PSInSAR Analysis

The PSInSAR analysis for site mobilization monitoring was conducted using a stack of 20 images, at a minimum. The deformation maps from the three orbits are superimposed on an optical image taken on April 10, 2020. The displacement observed is in mm and plotted on the color-coded PS images that show the total displacement over the entire analysis. The negative displacement (blue) indicates subsidence, and the positive displacement (red) denotes height gain about the line of sight of each satellite and orbit.

Pre-Event Analysis: The PSInSAR analysis using the three orbits produced the deformation map shown in Figure A.14(a), which reveals that a group of points within the white highlighted area had changed position during the monitoring period due to the rockfall. Most of the identified *Persistent Scatterer* (PS) points were stationary. Figure A.14(b) shows only the displacement in the range of -25mm to -10mm and 10mm to 25mm.

This image clearly shows the concentration of high PS points in the area of the accident. Figure A.14(c) displays the change in the position of one PS point with the most substantial displacement over the analysis period. The highlighted area where the rockfall occurred was relatively quiet until the end of September 2019, period T1 in

Table A.3 Satellite Data Acquisition Periods for Maupin OR

Data Set	Sentinel 1-B	Sentinel 1-B	Sentinel 1-A
	Ascending	Descending	
Pre-event	6/1/2019 to	6/21/2019 to	6/16/2019 to 5/5/2020
	5/2/2020	4/28/2020	
Post-event	5/14/2020 to	5/10/2019 to	5/17/2020 to
	1/9/2021	4/6/2021	12/31/2020

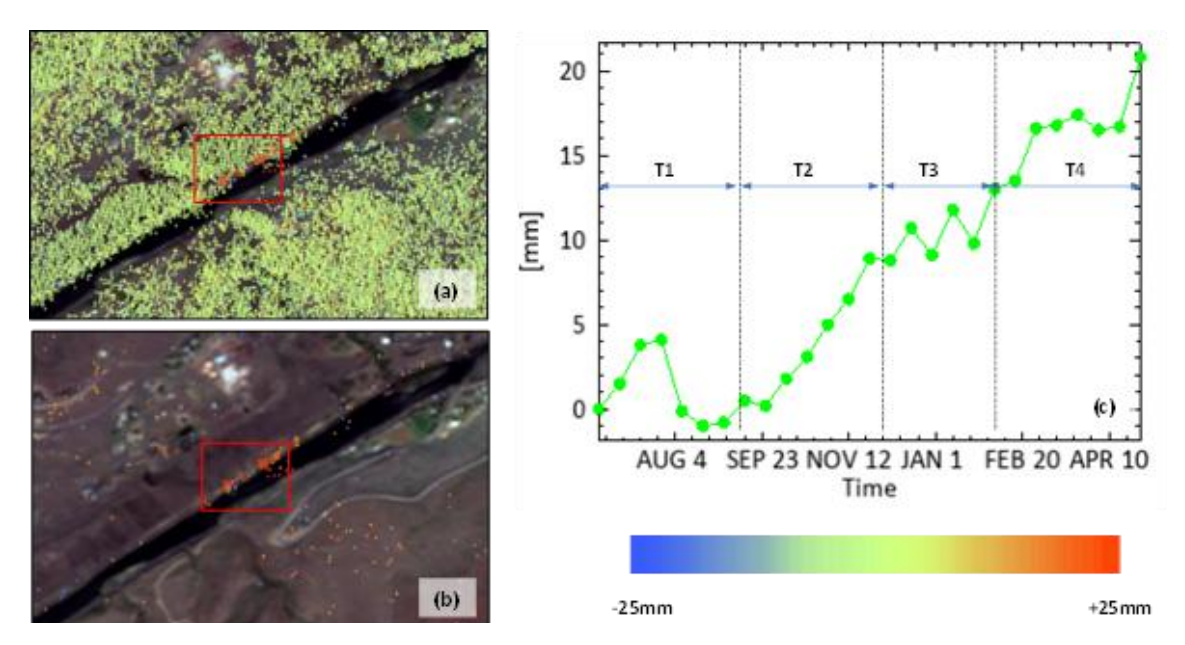


Figure A.14 (a) the displacement map superimposed on the optical image. (b) PS analysis results with displacement (c) Shows the progress of the displacement over time of one PS point.

Figure A.14(c). The region experienced high displacement in the period T2 until the start of December, followed by a brief stable period, T3, before it experienced high displacement leading to the rockfall, T4. This indicates that for at least eight months before the event, the region experienced a change in position, compared to the wider area, with some points subsiding and others moving in the opposite direction to the satellite's line of sight. At the start of the observation period, the deformation changes were due to noise.

<u>Post-Event Analysis:</u> A post-event PSInSAR analysis has been conducted on all three orbits after the event, and the results have been combined to generate the deformation map in Figure A.15. The highlighted area shows no significant displacement, indicating that the region is not undergoing any surface movement and is now in a state of equilibrium. However, the surrounding hills exhibit areas with substantial displacement compared to the PS on the railway right-of-way.

## A.3.5 CCD Monitoring Analysis

The coherence images generated by CCD analysis can provide further insights into the rockfall event. As evidenced in Figure A.16(a), mobilization of the site started after September 2019. The coherence map for the period September 17 to September 29, shown in Figure A.16(b) reveals a low coherence in the region of the rockfall event marked by the red rectangle. Since the site is still "quiet" and no geometry changes are detected, the low coherence over the broader region could be attributed to the other major factor that affects it, i.e., change in soil moisture in the surrounding area. This observation is verified by the rainfall records for the site depicted in Figure A.16(c) for the entire month of September. It is noted that in the period between the two acquisitions,

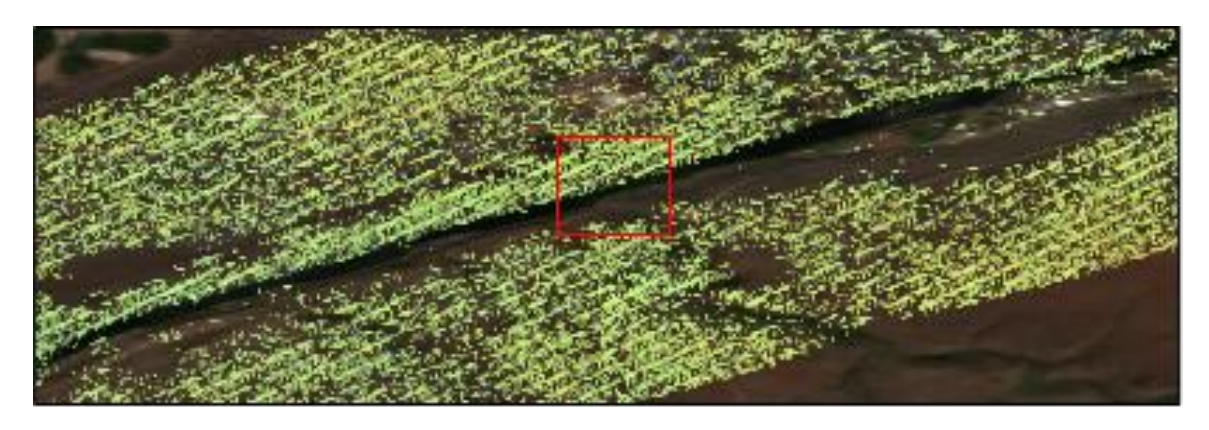


Figure A.15 Post-Event Analysis Total deformation map of Persistent Scatterers. No significant position change noted.

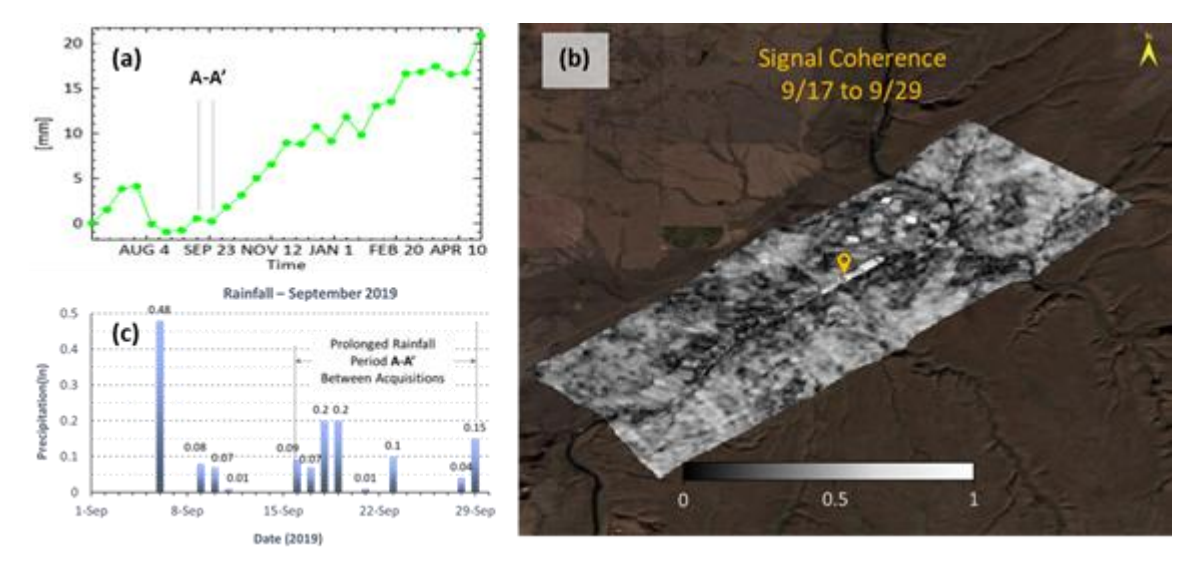


Figure A.16 (a) Coherence from 9/17 to 9/29/2019. (b) Rainfall during September 2019. (c) Displacement progress of a PS point near the rockfall event.

i.e. 9/17-9/29, a moderate and persistent rainfall is recorded, suggesting a correlation between soil moisture change and the signal coherence between the two successive acquisitions and that persistent rainfall has possibly triggered the local mobilization of the site. Further CCD analysis was performed using the pre- and post-event data sets to investigate any coherence loss before the rockfall. Figure A.17(a) exhibits the coherence image from the analysis between an image pair captured on 4/20 and 5/02, demonstrating high coherence in the broader area of the event but noticeable coherence loss in the immediate region of the event, while no rainfall was recorded in the same period, yet an abrupt change in the displacement is noted (Figure A.14(c)). Figure A.17(b) portrays the coherence analysis of the region studied using data from May 02 to May 14, that spans over the May 7<sup>th</sup> event date. The noticeable coherence loss in the immediate area of the event is attributed to the surface changes caused by the rockfall. According to the soil information for the area [102] and shown in Figure A.13(b), the immediate region of the rockfall is a steep, rocky slope where surface runoff is at fast rates, without any ponding or retained water; this is consistent with the high coherence for most of the analysis period in the immediate region. The broader area, however, is relatively flat, and precipitation seeps through the soil changing the soil moisture content; this is consistent with the coherence loss after rain periods. PSInSAR was able to detect the slow mobilization of the slope six to eight months before the rockfall took place. CCD analysis, in this case, shows that sustained rainfall in the area reduced the high coherence of the region one month before the accident. The event analysis of Maupin also suggests a direct relationship between soil moisture content and coherence. The analysis of the other sites considered in this work showed similar conclusions.

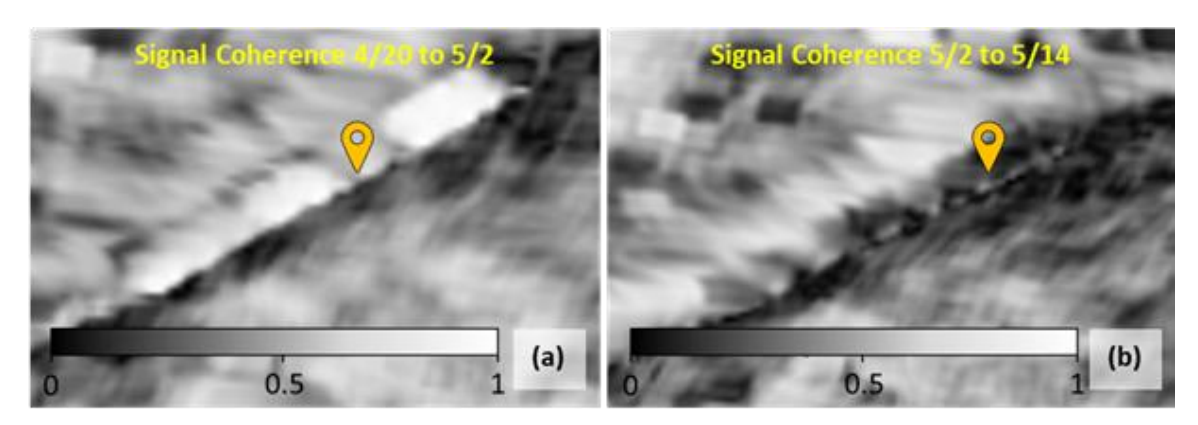


Figure A.17 Coherence maps: (a) 12-day period right before the event; (b) Coherence during the event

## A.4 Atlanta, GA

### A.4.1 Event

According to homeowners in DeKalb County, Georgia, a massive sinkhole has raised concerns regarding their residences' safety, property value, and stability, as reported by FOX 5 Atlanta. The resident discovered cracks in her driveway and around the back of her home approximately in February 2022. Upon investigation, she realized the presence of a sinkhole, steadily growing in size. The sinkhole was reported to DeKalb County in March, but initially, it received low priority. However, with the sinkhole deteriorating rapidly due to heavy rainfall and storms, county officials have taken notice. Investigation into it suggested that leaking drainage pipes could have led to the formation of sinkholes. Figure A.18(a) shows the location of the sinkhole, with Figure A.18(c) showing a closer view of the region, and finally, Figure A.18(d) shows the sinkhole damaging the resident's driveway.

### A.4.2 Site Description

The region under investigation is located in the suburban environment of Atlanta in northern Georgia at latitude/longitude (33.83, -84.30). This region has a mean annual precipitation of 44-60 inches, with 190 to 230 frost-free days. The typical soil profile of Dekalb County consists of the top 5 inches of soil being sandy loam, with soil from 5 to 36 inches being sandy clay loam as seen from soil profile image Figure A.19. Additional properties and qualities of the site include a slope of 10 to 25 percent and a well-drained drainage class. The area does not experience flooding or ponding [103]. Figure A.18(b) shows the path taken by the Sentinel1-A satellite

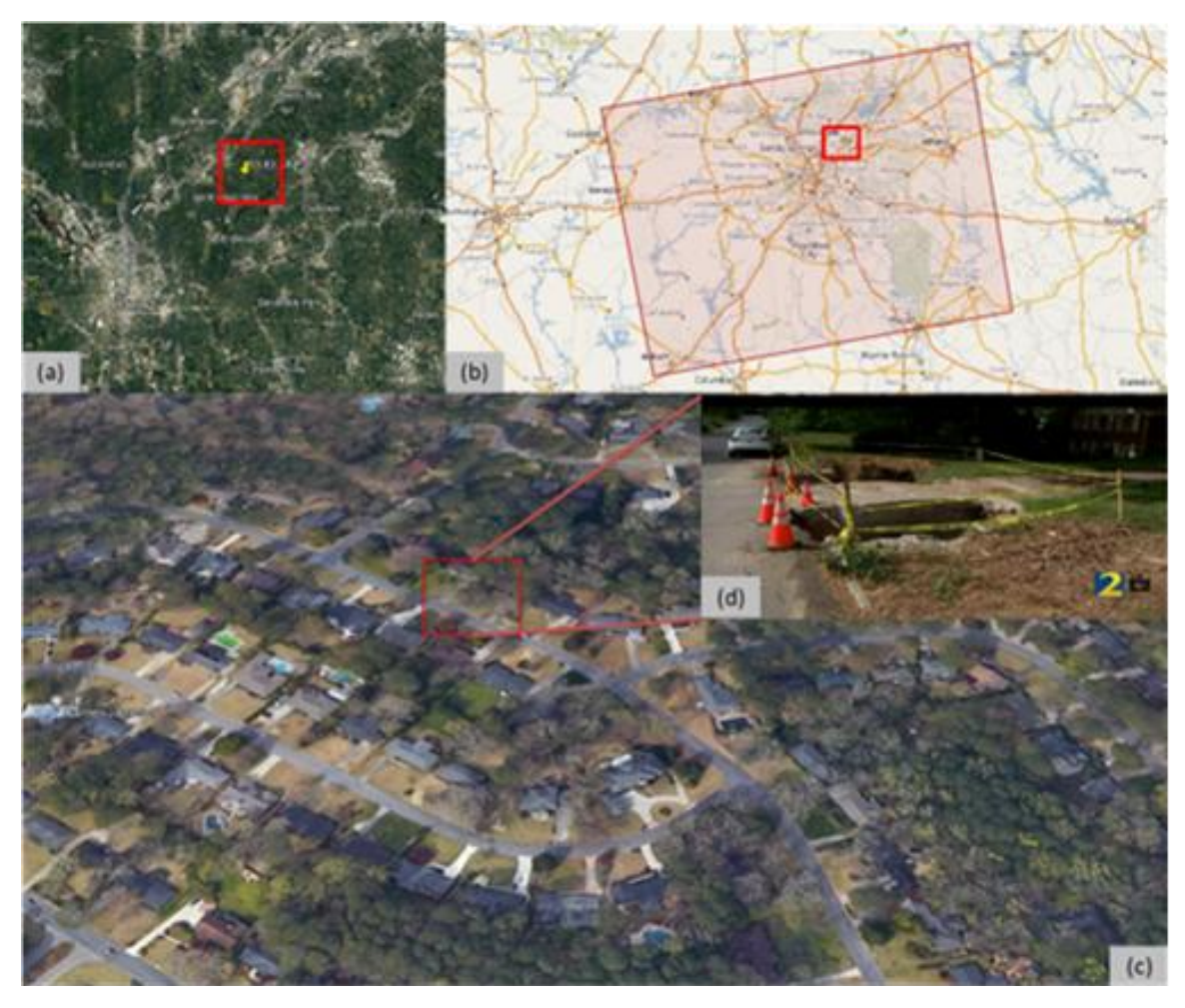


Figure A.18 (a) Shows the location of the sinkhole near Atlanta; (b) Sentinel 1-A coverage of the region; (c) Closer view of the region where the sinkhole took place; (d) The sinkhole affecting the driveway of the resident.



Figure A.19 The soil profile map of the region in Dekalb County

## A.4.3 Data Availability

The radar satellite Sentinel-1A covers this region once every 12 days. The region is located in urban areas, but the area under investigation has significant vegetation cover and the tree canopy reduced the radar visibility in the region. Since only one satellite covers this area, analysis of the region is restricted to the angle of incidence. The dataset for this study is obtained from the Sentinel constellation, and the satellite images are downloaded from the Sentinel-1 EU datahub [99] and Alaska Satellite Facility (ASF) [100]. Figure A.18(b) shows the path taken by the Sentinel1-A satellite. The analysis employs PSInSAR techniques using archived satellite radar images spanning 9 months, covering up to the first appearance of the sinkhole. Table A.4 shows the data used for the analysis

### A.4.4 PSInSAR Analysis

The PSInSAR analysis for site mobilization monitoring was conducted using a stack of 20 images, at a minimum. The deformation maps from the two orbits are superimposed on an optical image taken on April 11, 2022. The displacement observed is in mm and plotted on the color-coded PS images that show the total displacement over the entire analysis. The negative displacement (blue) indicates subsidence, and the positive displacement (red) denotes height gain about the line of sight of each satellite and orbit.

The PSInSAR analysis using Sentinel-1A produced the deformation map shown in Figure A.20(a), which reveals that the region experienced low subsidence during the monitoring period. Figure A.20(b) shows only the persistent scatterers in the range of

Table A.4 Satellite Data Acquisition Periods for Dekalb County, Georgia

Data Set	Sentinel 1-A (Ascending)	
Pre-event	02/04/2021 to 11/06/2021	

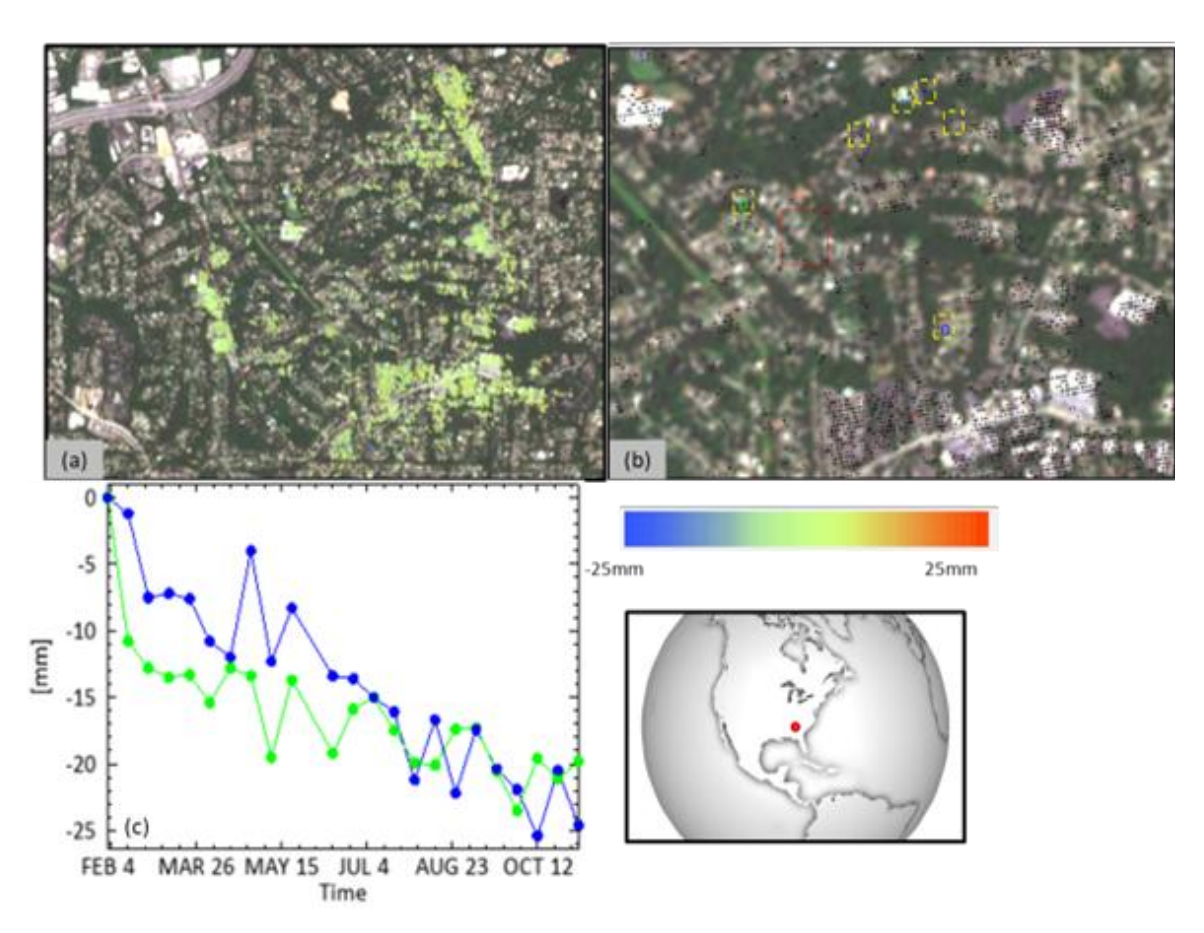


Figure A.20 (a) The displacement map superimposed on the optical image; (b) PS analysis results with high subsidence highlighted;(c) Show the progress of the displacement over time of one PS point.

-25mm to -14mm and 14mm to 25mm near the sinkhole region. Several of these PS are highlighted with yellow boxes with the progress of displacement of two shown in Figure A.20(c). The progress of displacement of these persistent scatters shows they have been experiencing displacement at the same rate as points around the county. These displacements accelerated at the start of March and progressed throughout the observation period.

### A.4.5 Discussion

The region has a large presence of vegetation in the form of trees surrounding the sinkhole. This led to low radar visibility in the region. In the areas where high displacement can be observed, the progress of the displacement suggests they are experiencing subsidence due to similar reasons. The newspaper article following the event suggests that damaged drainpipes were the cause of the initial sinkholes; the same reason could also affect the surrounding regions with high subsidence. Since this region has access to only one satellite path and since this region cannot be observed from alternative angles, we would classify this site as B leaning towards C class. This classification is due to the high presence of vegetation and low radar backscatter. PS points are sparse due to low coherence caused by vegetation, and DS points are unreliable in small-scale subsidence. The restricted satellite line-of-sight prevents cross-validation of displacement signals. These factors significantly limit early-warning capabilities in this region. PSInSAR techniques can be used to detect sinkholes as one indicator for sinkholes is a constant small amount of subsidence before the geohazard, but if the region has no access to satellite visibility, then early detection is difficult, as seen in this case study.

# A.4 Burlington, ND

### A.4.1 Event

According to a report by first responders and the local news station (KFVT TV), a BNSF train en route to Minot, North Dakota, derailed on May 1, 2022, with multiple rail cars catching fire. The derailment occurred near county road 10, between 107th and 128th Avenues Figure A.21(a), approximately 10km away from Minot and 4km from Burlington. The test area has no significant slopes, and the derailment may have been caused by increased moisture content on the railway track, affecting its stability.

## A.4.2 Site Description

The region under investigation is located in northern North Dakota at latitude longitude (48.25, -101.46). This region is closer to the Canadian border and has a mean annual precipitation of 16–23 inches with 110 to 150 frost-free days. The InSAR analysis region can be divided into 2 regions. The first is the track region (F148F) and the area immediately surrounding it, and the second is the farmland beyond (F657B), indicated by Figure A.22. Region A has a loam soil profile of up to 79 inches of soil layer. It is well drained with high runoff classification and a capacity to transmit water at moderately low to moderately high (0.14 to 1.42 in/hr). Region B, on the other hand, has loam soil in the top layer (0 to 8 inch) and clay loam (8 to 35 inch) below it. It is well drained with low runoff classification and can transmit water at a similar rate as Region A. Both regions A and B have never had problems with flooding and ponding. These consistent hydrological and soil characteristics support stable baseline conditions for deformation analysis.



Figure A.21 Burlington, North Dakota (a) Location on the map; (b) Sentinel 1-B coverage for primary and alternate orbits; (c) Sentinel 1-A coverage of the region



Figure A.22: The soil profile map of the region in Burlington, ND

## A.4.3 Data Availability

The region under investigation is in North Dakota, where Sentinel-1B provided coverage until December 2021. The satellite orbited the area twice. However, on December 22, 2021, Sentinel-1B lost contact with mission control for unknown reasons, creating a gap in the data. Sentinel-1A later covered this gap in March 2022. Since the accident zone does not have continuous data access, advanced multi-temporal analysis, such as PSInSAR, cannot be conducted in the region before the accident. Instead, PSInSAR analysis is conducted until the available data in December 2021, followed by CCD analysis using Sentinel-1A data from March 2022. This area exhibits a considerable amount of radar backscatter due to low obstructions. Figure A.21(b) illustrates the satellite data path and data acquired for PSInSAR analysis, and Figure A.21(c) shows the path traveled by satellites used for CCD analysis. The data is downloaded using Sentinel-1 EU datahub [99] and Alaska Satellite Facility (ASF) [100] for the complete analysis period. The investigation is divided into pre-event and post-event periods, and the data used is shown in Table A.5. The PSInSAR analysis is included in the pre-event. This separation is justified because sudden increases in subsidence, such as those occurring during a derailment event, lead to a high loss of coherence and significant changes in DEM, which impact continuous analysis.

## A.4.4 PSInSAR analysis

<u>Pre-event analysis:</u> The PSInSAR analysis for site mobilization monitoring was conducted using a stack of 20 images, at a minimum. The deformation maps from the two orbits are superimposed on an optical image taken on March 22, 2022. The displacement observed is in mm and plotted on the color-coded PS images that show the total

Table A.5 Satellite Data Acquisition Periods for Burlington ND

Data Set	Sentinel 1-A	Sentinel 1-B Ascending	Sentinel 1-B Descending
Pre-event	3/24/2022 to 4/29/2022	03/04/2021 to 12/17/2021	03/11/2021 to 12/12/2021
Post-event	4/29/2022 to 6/5/2021	Unavailable	Unavailable

displacement over the entire analysis. The negative displacement (blue) indicates subsidence, and the positive displacement (red) denotes height gain about the line of sight of each satellite and orbit.

The PSInSAR analysis using the two orbits produced the deformation map shown in Figure A.23(a), which reveals that a group of points within the white highlighted area had changed position during the monitoring period. Most of the identified *Persistent Scatterer* (PS) points were stationary. Figure A.23(b) shows only the displacement in the range of -25mm to -14mm and 14mm to 25mm.

This image clearly shows the concentration of high PS points on the track. Figure A.23 (c) displays the change in the position of one PS point with the most substantial displacement over the analysis period. period T1 in Figure A.23(c) shows the slow displacement in the region. The region experienced relative stability in the period T2 followed by high displacement in the period T3 until the end of the observation period. Site mobilization analysis of the region shows this railway track was experiencing slow sinking activity until December of 2021, after which displacement analysis data is unavailable for this region.

### A.4.5 CCD analysis

<u>Pre-event analysis</u> The CCD timeline analysis produces coherence analysis results over an optical image, and the CCD analysis uses data from the same orbit with 12 days between each acquisition. This particular analysis used data from March 24, 2022, and April 05, 2022, to capture coherence 25 days before the accident. Figure A.24(a) shows moderately high coherence in the region, with some pockets of low coherence indicating

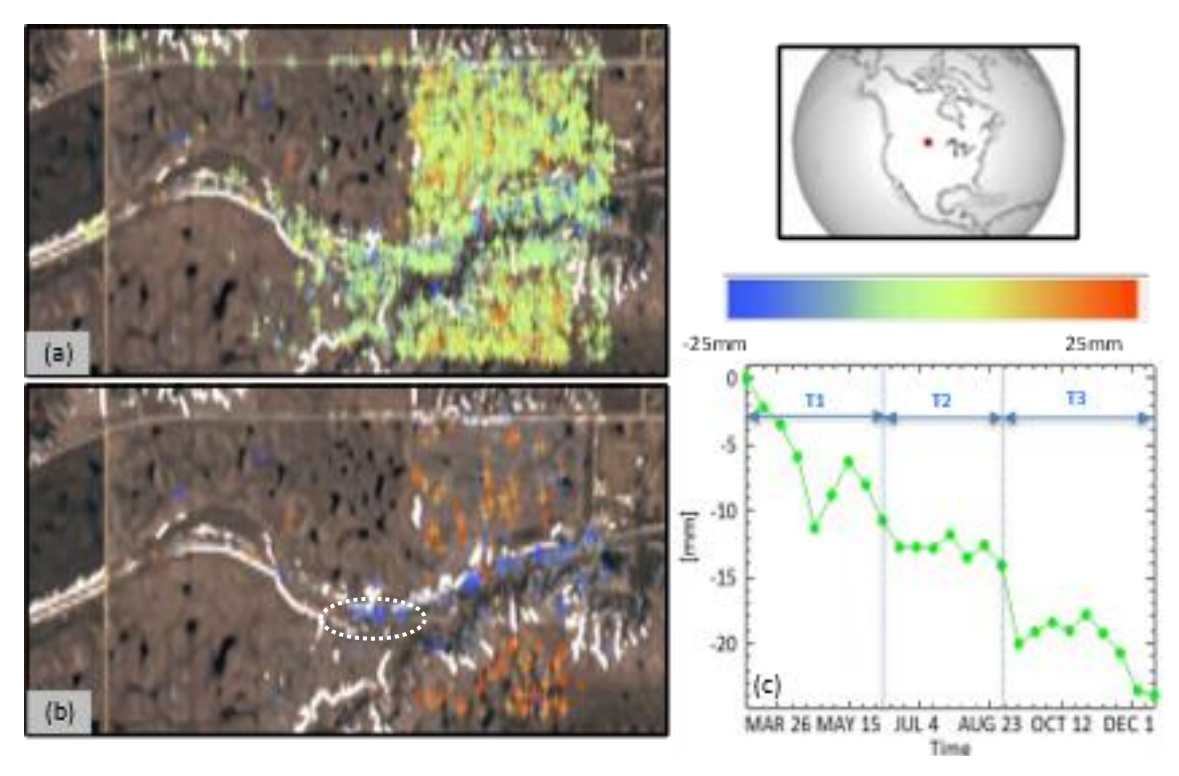


Figure A.23(a) The displacement map superimposed on the optical image; (b) PS analysis results with high displacement; (c) Shows the progress of the displacement over time of one PS point.

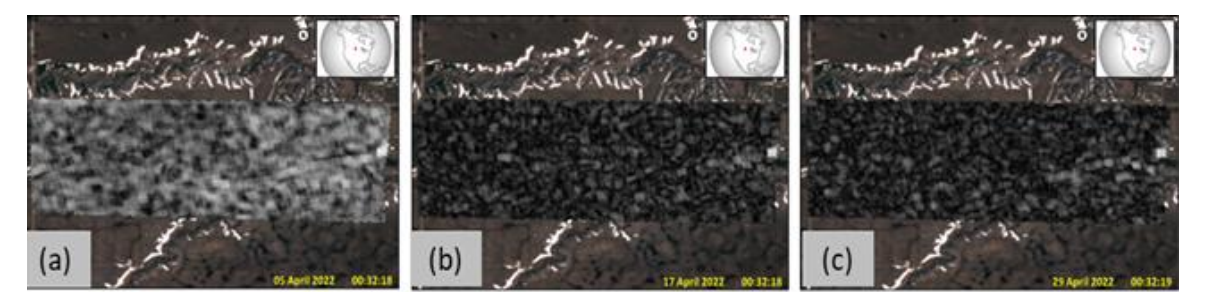


Figure A.24 (a) Coherence from 03/24 to 04/05/2022 (b) Coherence from 04/05 to 04/17/2022 (c) Coherence from 04/17 to 04/29/2022

low moisture content in the topsoil. The track is visible with high coherence due to its distinct shape. However, a weather report [105] suggests that the coherence was affected by rainfall on April 05.

Figure A.24(b) displays the results of analyzing SAR images from April 05, 2022, and April 17, 2022, which were taken 13 days before the accident. The resulting image shows low coherence throughout the region, with the track barely visible in some areas. This is attributed to two weather events: rainfall on April 05 and snowfall on April 14, with continuous low temperatures until April 17, indicating the presence of snow when the image was captured.

The coherence image in Figure A.24(c) utilizes SAR images from April 17, 2022, and April 29, 2022, which is the coherence 2 days before the accident. The resulting image shows low coherence across the area, with the track barely visible in some areas. This is again attributed to snowfall on April 14, with continuous low temperatures until April 17, indicating the presence of snow when the image was captured on the 17th. In addition, low rainfall on April 29 affected the SAR image captured that day.

Post-event analysis: Upon conducting a post-event analysis, it has been observed that the railway track regains coherence even in areas with low coherence, except for Figure A.25(a). The CCD image in analysis Figure A.25(a) utilizes SAR images taken on April 29, 2022, and May 11, 2022, 9 days after the event. The image shows low coherence on the track for two reasons: rainfall that occurred on April 29, 2022, and the change in DEM resulting from the derailment on May 1, 2022.

On the other hand, Figure A.25(b) of post-event CCD analysis displays high

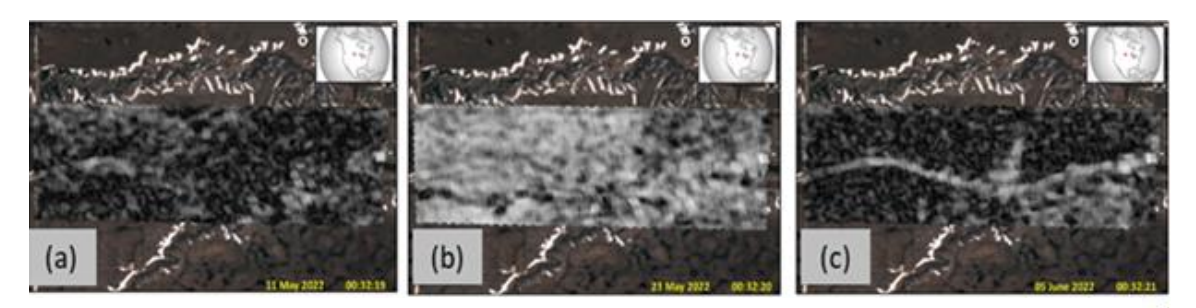


Figure A.25(a) Coherence from 04/29 to 05/11/2022 (b) Coherence from 05/011 to 05/23/2022 (c) Coherence from 05/23 to 06/05/2022

coherence, with only a few parts of the image having low coherence. This analysis utilizes both SAR images captured after the accident on May 11, 2022, and May 23, 2022. The coherence on the track is high, with relatively high coherence compared to the surrounding area. The weather report during image acquisition indicates no significant activity that could have affected the coherence in the region. This analysis should be treated as a baseline for post-event analysis as it uses data after the effect of derailment.

The coherence Figure A.25(c) of post-event CCD analysis reveals low coherence across the area, with the track displaying high coherence. This analysis also utilizes SAR images obtained after the accident on May 23, 2022, and June 05, 2022. The weather report during image acquisition indicates no significant activity that could have affected coherence in the region. The loss of coherence is assumed to be due to vegetation in the area, as additional in-situ information is unavailable. The loss of coherence in this image needs to be further analyzed with in-situ readings to understand the reason better.

### A.4.6 Discussion

This region experienced site mobilization from March 2021 to December 2021. It is unknown if the subsidence experienced on the track continued after that time period or if the subsidence observed on the track caused the derailment later in April 2022. The region's CCD analysis shows a direct relationship between weather activities influencing the track profile. The weather events involving rainfall and snowfall influence the coherence of the given region and the loss of coherence on the track. Following the event, the track showed high coherence even when there was a loss of coherence in the surrounding region Figure A.25(c). This suggests that the loss of coherence observed on Figure A.24(c) indicates precursive events affecting the railway track. With the presence

of multiple Sentinel data and clear access to the line of sight of the radar sensor, this case study can be categorized in class A. Although this region currently has access to only Sentinel-1A due to low obstruction to the radar path, it can still be classified as A. This case suggests that both CCD and PSInSAR have railway ROW safety applications; these techniques can be used for future applications.

## A.5 Shiner, TX

### A.5.1 Event

A train derailment occurred at approximately 7 p.m. on Friday, June 3, 2022, resulting in US Highway 90-A (Avenue E) shutting down for over 20 hours. The incident, which involved a Union Pacific train carrying open-top coal cars, occurred near Avenue E's intersection in Shiner, as shown in Figure A.26(a). Eyewitnesses reported smoke emanating from one of the train's wheels before the axle broke, causing the car to topple, as seen in Figure A.26(b).

## A.5.2 Site Description

The region under investigation is located in southern Texas at latitude/longitude (29.43, -97.18). This region is closer to the Mexican border and has a mean annual precipitation of 32-40 inches, with 260 to 280 frost-free days. The typical soil profile of Shiner consists of the top 8 inches of soil being sandy clay loam with soil from 8 to 36 inches being clay loam. Additional properties and qualities of the site include a slope of 1 to 3 percent and a well-drained drainage class. The runoff class is low, indicating limited water runoff. The region transmits water from moderately high to high (0.20 to 1.98 inches per hour). The depth of the water table exceeds 80 inches, indicating it is well



Figure A.26 (a) Shows the location of the derailment near the center of the town shiner; (b) shows the derailment; (c) the coverage of Sentinel-1A's Ascending orbit; (d) the coverage of Sentinel-1A's descending orbit.

below the soil surface. The area does not experience flooding or ponding. Additional information related to the soil profile can be found in [106] and is shown in Figure A.27.

## A.5.3 Data Availability

The region under investigation is in Texas between San Antonio and Houston, where Sentinel-1A covers the region in multiple orbits observing the area in multiple directions. Since the accident is located in the city, the region exhibits a considerable amount of radar backscatter. Figure A.26(c)(d) illustrates the satellite data path for the analysis. The data is downloaded using Sentinel-1 EU datahub [99] and Alaska Satellite Facility (ASF) [100] for the complete analysis period. The region is investigated for preevent site mobilization using PSInSAR analysis. The post-event analysis is not conducted for this case as it was determined that the region is not susceptible to further site mobilization activities. Table A.6 shows the data used for the analysis.

# A.5.4 PSInSAR Analysis

The PSInSAR analysis for site mobilization monitoring was conducted using a stack of 20 images, at a minimum. The deformation maps from the two orbits are superimposed on an optical image taken on May 21, 2022. The displacement observed is in mm and plotted on the color-coded PS images that show the total displacement over the entire analysis. The negative displacement (blue) indicates subsidence, and the positive displacement (red) denotes height gain about the line of sight of each satellite and orbit. The PSInSAR analysis using the two orbits produced the deformation map shown in Figure A.28(a), which reveals a group of points that had changed position during the monitoring period. Most of the identified *Persistent Scatterer* (PS) points were



Figure A.27 The soil profile map of the region in Shiner Texas

Table A.6 Satellite Data Acquisition Periods for Shiner, Texas

Data Set	Sentinel 1-A Ascending	Sentinel 1-A Descending
Pre-event	07/10/2021 to 5/30/2022	07/08/2021 to 05/28/2022

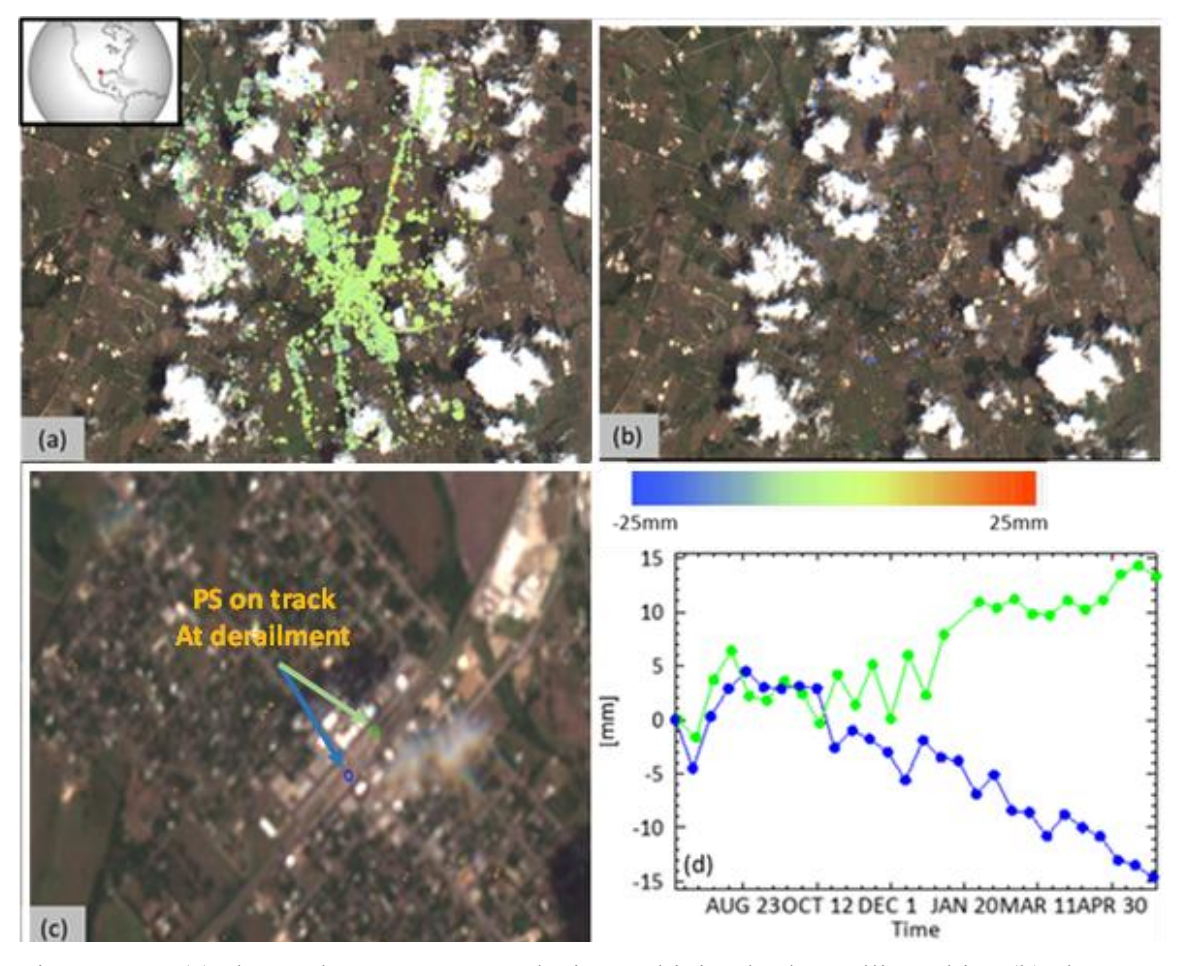


Figure A.28 (a) shows the PSInSAR analysis combining both satellite orbits. (b) shows PS with high displacement. (c) shows the near the great crossing where the train derailment took place. (d) shows the displacement over time of the PS near the great crossing.

stationary. Figure A.28(b) shows only the displacement in the range of -25mm to -12mm and 12mm to 25mm. This image shows the high PS points in the region are close to the track but not on the track. Figure A.28(d) shows the displacement over time for the two PS points on the track where the derailment occurred, highlighted in Figure A.28(c). The progress of the displacement shows major displacement started during the month of October.

### A.5.5 Discussion

PSInSAR analysis over Shiner, Texas, has shown that the region has some PS with high displacement near the railway tracks. Most of the high concentrations of PS are not on the track but in the surrounding region. If this region is near a hilly terrain or the concentration of these high displacement points is near a sloped surface, it would be considered an indicator of landslides being developed in the area. However, subsidence is observed at the identified PS on the track suggesting the possibility of track settlement/movement.

# A.6 Yellowstone, MT

### A.6.1 Event

On the morning of June 13, 2022, Yellowstone National Park experienced an unprecedented 500-year flood event. The northern parts of the park were hit by a combination of heavy rainfall and snowmelt, receiving an astonishing 7.5-9.5 inches of precipitation within a 24-hour period. This deluge resulted in severe damage to infrastructure and disrupted the normal operations of the park. The flood wreaked havoc on transportation routes within the park. Figure A.29(a) shows the regions where large



Figure A.29 (a) Shows the locations where significant damage to infrastructure took place; (b) Shows the flooding event near Gardiner River; (c) the coverage of Sentinel-1A covering Yellowstone Park and cities surrounding it

damage has been done due to the flooding event. Figure A.29(b) shows the flooding event of the Gardiner River near the northern entrance to Yellowstone.

## A.6.2 Site Description

The area under analysis is a large area covering over 200 square miles and is shown in Figure A.30. The soil profiles information of the region is too extensive to summarize, however, details can be obtained from [107]. On average, this region experiences 20 to 31 inches of annual precipitation, with frost-free periods of 35 to 60 days. The average water table is 60 to 80 inches below the soil surface.

## A.6.3 Data Availability

Two regions are considered, a region in the park where multiple landslides occurred, and the BNSF right of way connecting Cody and Ralston.

Yellowstone Park: The first region under investigation is located on the border of Wyoming and Montana. The radar satellite Sentinel-1A covers this region once every 12 days. The region is in a mountainous environment with a large area exposed to radar backscatter. The dataset for this study is obtained from the Sentinel constellation, and the satellite images are downloaded from the Sentinel-1 EU datahub [99] and Alaska Satellite Facility (ASF) [100]. Figure A.29(c) shows the path taken by the Sentinel1-A satellite. The analysis employs PSInSAR techniques using archived satellite radar images spanning 10 months, for the dates shown in Error! Reference source not found..

<u>Cody-Ralston BNSF ROW:</u> The BNSF ROW region is located in Wyoming. The radar satellite Sentinel-1A covers this region once every 12 days. The dataset for this study is obtained from the Sentinel constellation, and the satellite images are downloaded from



Figure A.30: Shows the region under observation.

Table A.7: Shows the Sentinel-1A data used for analysis.

Data Set	Sentinel 1-A Ascending
Stability monitoring	08/07/2021 to 05/22/2022

the Sentinel-1 EU datahub [99] and Alaska Satellite Facility (ASF) [100]. The same data set used for monitoring stability in Yellowstone is used here as it covers both regions.

## A.6.4 Stability Monitoring

Yellowstone Park The PSInSAR analysis for site mobilization monitoring was conducted using a stack of 20 images, at a minimum. The deformation maps from the two orbits are superimposed on an optical image taken on May 15, 2022. The displacement observed is in mm and plotted on the color-coded PS images that show the total displacement over the entire analysis. The negative displacement (blue) indicates subsidence, and the positive displacement (red) denotes height gain about the line of sight of each satellite and orbit. The PSInSAR analysis uses single orbit data to produce the deformation map shown in Figure A.31(a). The region shows high radar backscatter as evidenced by the density of PS. Figure A.31(b) shows the displacement in the range of -25 to -14 and 14 to 25 to show the largest deformation in the region without the stationary points. The PSInSAR analysis in the region shows that the regions experiencing failure were experiencing large displacement patterns before the large rainfall event triggered them.

BNSF ROW Following the site analysis at Yellowstone Park, a mobilization assessment was conducted for the railway right-of-way along the Cody–Ralston line. The analysis focused on the rail corridor and a 250-meter buffer zone surrounding it. This monitoring approach is designed to detect significant ground displacements that could impact the railway infrastructure. However, the analysis was not correlated with any precise location of the slope failure and derailment events. Figure A.32(a) shows the location of the BNSF railway line as compared to the Yellowstone analysis. Figure A.32(b) shows the regional railway lines BNSF uses. The PSInSAR analysis for site mobilization monitoring was

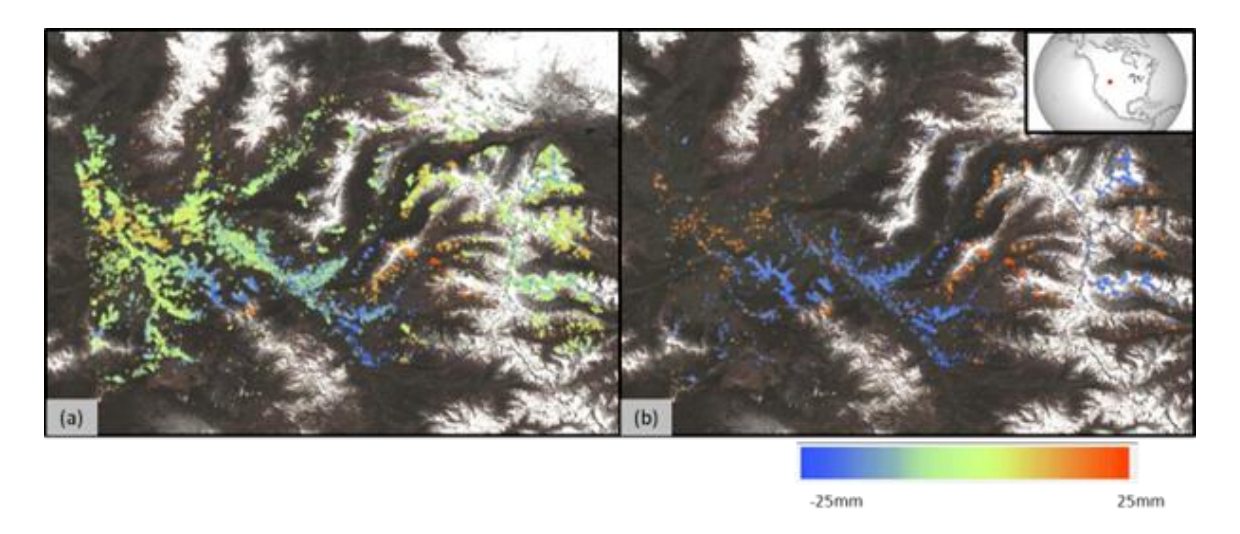


Figure A.31 (a) Shows the PSInSAR deformation points; (b) Shows the area of instability in the area under observation

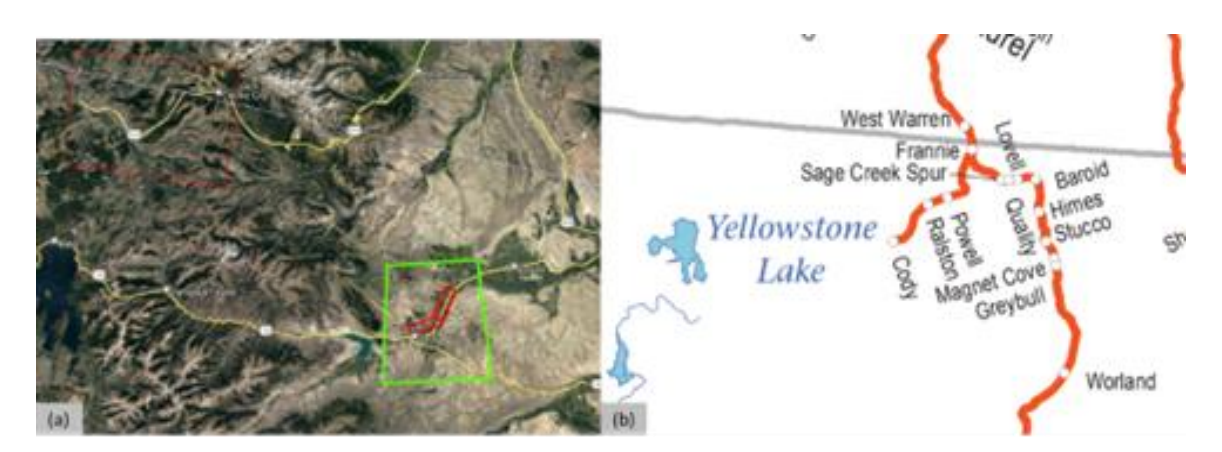


Figure A.32 (a) Shows the Yellowstone monitoring region and the railway track connecting Cody and Ralston; (b) Shows the BNSF rail network in the region.

conducted using a stack of 20 images, at a minimum. The deformation maps from the two orbits are superimposed on an optical image taken on August 10, 2022. The displacement observed is in mm and plotted on the color-coded PS images that show the total displacement over the entire analysis. The negative displacement (blue) indicates subsidence, and the positive displacement (red) denotes height gain about the line of sight of each satellite and orbit.

The PSInSAR analysis uses single orbit data to produce the deformation results shown in Figure A.33. Figure A.33(a) shows the region's high radar backscatter as seen by the density of PS. Figure A.33(b) shows the displacement in the range of -25 to -14 and 14 to 25 to show the largest deformation in the region without the stationary point. Figure A.33(c) shows the high deformation activity affecting the railway right of way outside the city of Cody, with Figure A.33(d) showing the deformation's average progress over the analysis time period.

#### A.6.5 Discussion

PSInSAR analysis over the region showed that several areas were experiencing high mobilization events. This region can be classified as A due to high radar returns from the area. These areas were triggered during the rainfall event leading to slope failure. The displacement measured was detected 20 days before the event took place.

PSInSAR analysis in the region led to an analysis of the BNSF railway line connecting Cody and Ralston in Wyoming. The sponsor (FRA) requested this analysis as this line was experiencing frequent derailment events. PSInSAR analysis over the railway right of way connecting Cody and Ralston has shown that the region was

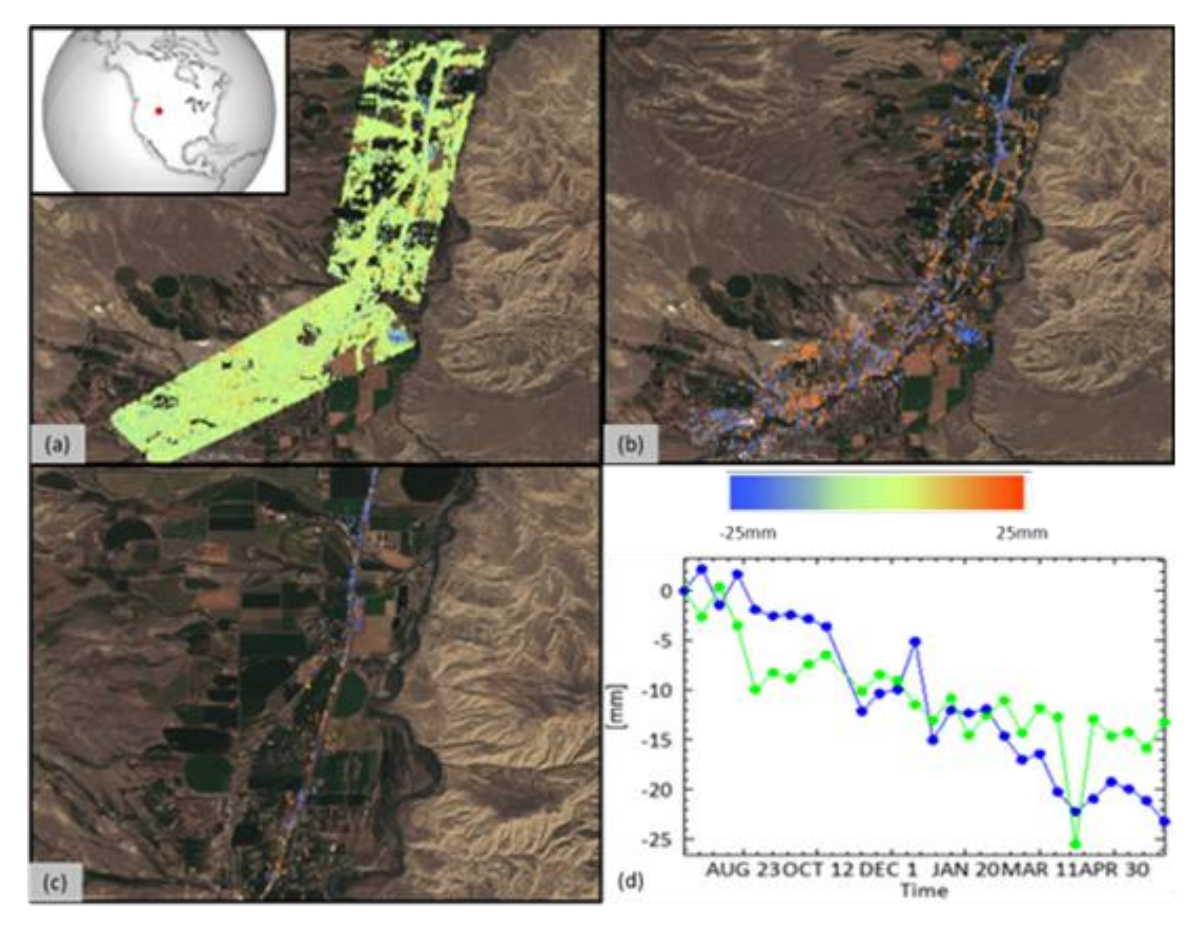


Figure A.33 (a) Shows the results from PSInSAR analysis over the region; (b) Shows the stable points of analysis being removed with only high subsidence PS; (c) Shows the high PS surrounding railway right of way near the railway track connecting the city of Cody and Ralston; (d) Shows the average displacement over time of PS points with high subsidence.

experiencing high subsidence activity. The displacement over time shows that the subsidence rate is constant in the region with some sharp activity. At this time, it is unknown if derailments in the region are due to the subsidence near the track.

# A.7 Santa Clemente, CA

#### A.7.1 Event

In late September 2022, the San Diego to Los Angeles commuter rail experienced disruption near San Clemente. Passengers are required to make a stop in Irvine and continue their journey via buses to the San Diego border, where they transfer to another train. This disruption is due to safety concerns related to shore erosion on one side and an unstable hillside on the other in the San Clemente area. The Orange County

Transportation Authority (OCTA) has initiated emergency work to stabilize the track and slope to ensure passenger safety. These geohazards have previously led to temporary closures and service delays in the region. Figure A.34(a) shows the railway line segment near the ocean in high risk of disruption. Figure A.34(b) shows the area under observation.

## A.7.2 Site Description

The area under observation covers close to 30 miles of coastal beaches and more fertile grounds inland. This region has an annual precipitation of 42 to 48 inches with a frost-free period of 190 to 210 days. The coastal beaches have coarse sand with poor drainage and negligible runoff. The more fertile ground inland has loam on the top 12 inches and clay from 12-55 inches of the soil profile. This region has well drained with high runoff classification. Figure A.35 shows part of the soil map of the region under



Figure A.34 (a) Shows the location of the railway line facing disruption; (b) Shows the area under observation; (c) Shows the Sentinel-1A Ascending orbit with the area under observation being highlighted; (d) Shows the Sentinel-1A Descending orbit with the area under observation being highlighted.



Figure A.35 Soil map of the region

analysis. More in-depth soil data can be obtained from [108]

# A.7.3 Data Availability

The region under investigation is located between San Diego and Los Angeles. The radar satellite Sentinel-1A covers this region twice in ascending and descending orbits. The region is exposed to radar backscatter, and large PS data was available. The dataset for this study is obtained from the Sentinel constellation, and the satellite images are downloaded from the Sentinel-1 EU datahub (ESA, 2023) and Alaska Satellite Facility (ASF) (ASF, 2023). Figure A.34(c) and A.34(d) show the images taken by the two paths of Sentinel1-A satellite in both orbits of observation. The analysis employs PSInSAR techniques using archived satellite radar images spanning 12 months. The data used for analysis is shown in Table A.8

#### A.7.4 Site Mobilization

The PSInSAR analysis for site mobilization monitoring was conducted using a stack of 20 images, at a minimum. The deformation maps from the two orbits are superimposed on an optical image taken on August 11, 2022. The displacement observed is in mm and plotted on the color-coded PS images that show the total displacement over the entire analysis. The negative displacement (blue) indicates subsidence, and the positive displacement (red) denotes height gain about the line of sight of each satellite and orbit.

The PSInSAR analysis using Sentinel-1A ascending orbit produced the deformation map in Figure A.36(a). Figure A.36(b) shows the deformation map using Sentinel-1A descending orbit. The PS in both images shows only persistent scatterers in

Table A.8: Satellite data for acquisition periods for San Clemente, California

Data Set	Sentinel 1-A Ascending	Sentinel 1-A Descending
Stability monitoring	10/21/2021 to 09/22/2022	11/26/2021-09/22/2022



Figure A.36: (a) shows the high displacement PS for the region using Sentinel-1A Ascending orbit; (b) shows the high displacement PS for the region using Sentinel-1A Descending orbit.

the range of -25mm to -14mm and 14mm to 25mm. Figure A.37(a) and 37(b) show the PS near Oceanside, California as obtained from the Sentinel-1A ascending, and descending orbits, respectively.

Figure A.38(a)(c)(e) shows the track region between Santa Clemente and Oceanside for Sentinel-1A ascending, and Figure A.38(b)(d)(f) shows the track region between Santa Clemente and Oceanside for Sentinel-1A descending.

#### A.7.5 Discussion

PSInSAR analysis over the region showed that several areas were experiencing high mobilization events. The regions near the cities of Oceanside and San Clemente experienced positive displacement, while the regions in between show clear subsidence near the railway lines connecting both cities. Several regions showed positive displacement in ascending orbit and negative displacement in the descending orbit, this suggests the area was experiencing slope movement in the region. This region can be classified as A due to high radar returns from the area and multiple orbits being available.

# A.8 Sandstone, WV

#### A.8.1 Event

A freight train near Sandstone, West Virginia, Figure A.39(a), derailed when it hit a rockslide, Figure A.39(b), causing injuries to three crew members and resulting in the release of diesel gasoline into the nearby river, Figure A.39(c). The yellow dotted box in Figure A.39(d) indicates the site of the rockfall incident that occurred in the early hours of Wednesday, March 8, 2023. The collision in the early morning locomotive footage reveals that the debris blocking the railway path caused the derailment. Furthermore,

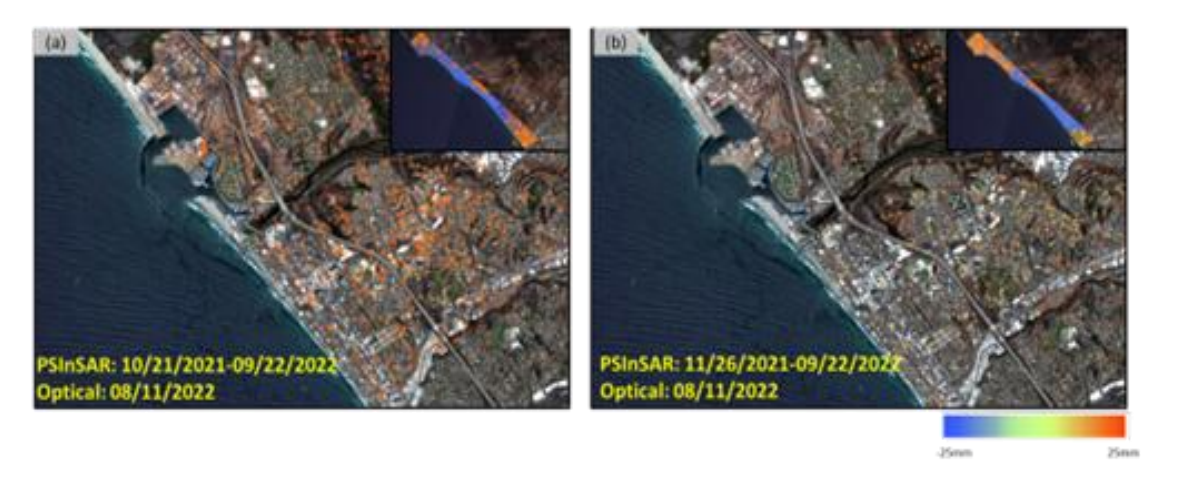


Figure A.37 Show the high displacement PS near Oceanside with (a) showing the Sentinel-1A Ascending orbit and (b) showing the Sentinel-1A Descending orbit

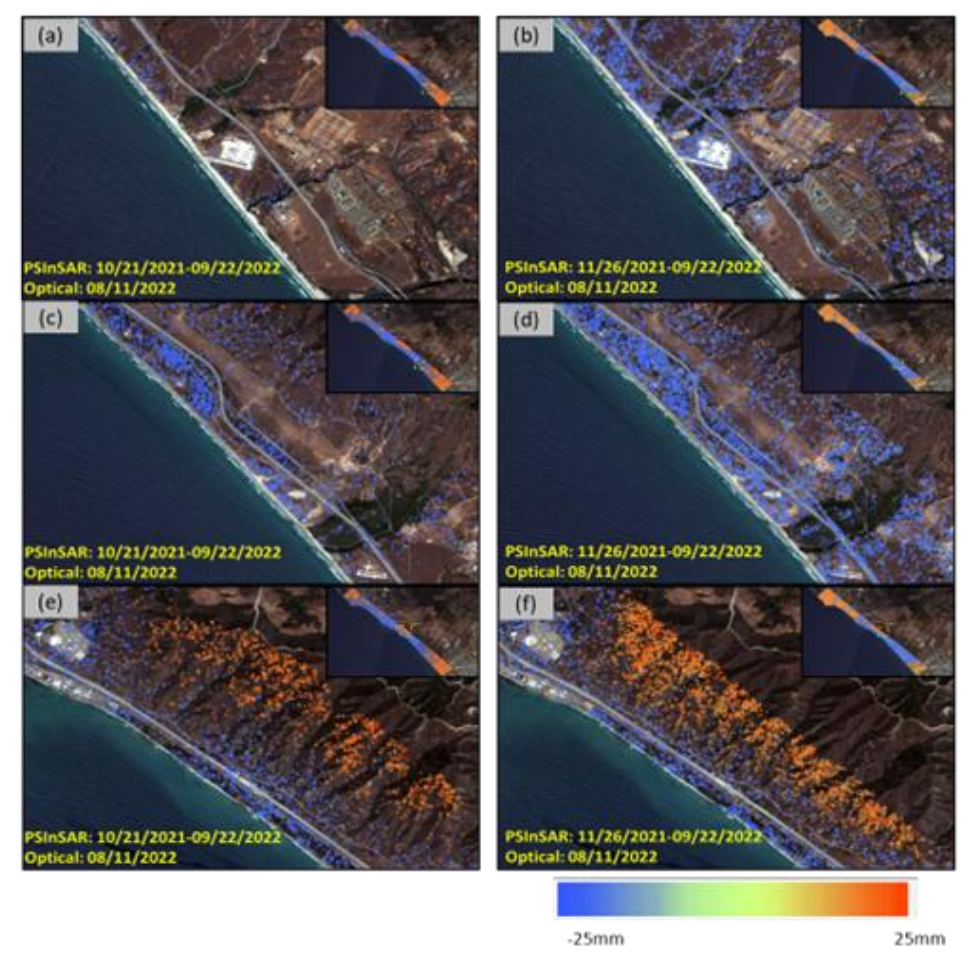


Figure A.38: Shows the high displacement PS between Oceanside and San Clemente (a)(c)(e) shows the PS analysis from Sentinel-1A Ascending orbit (b)(d)(f) shows the PS analysis from Sentinel-1A Descending orbit.

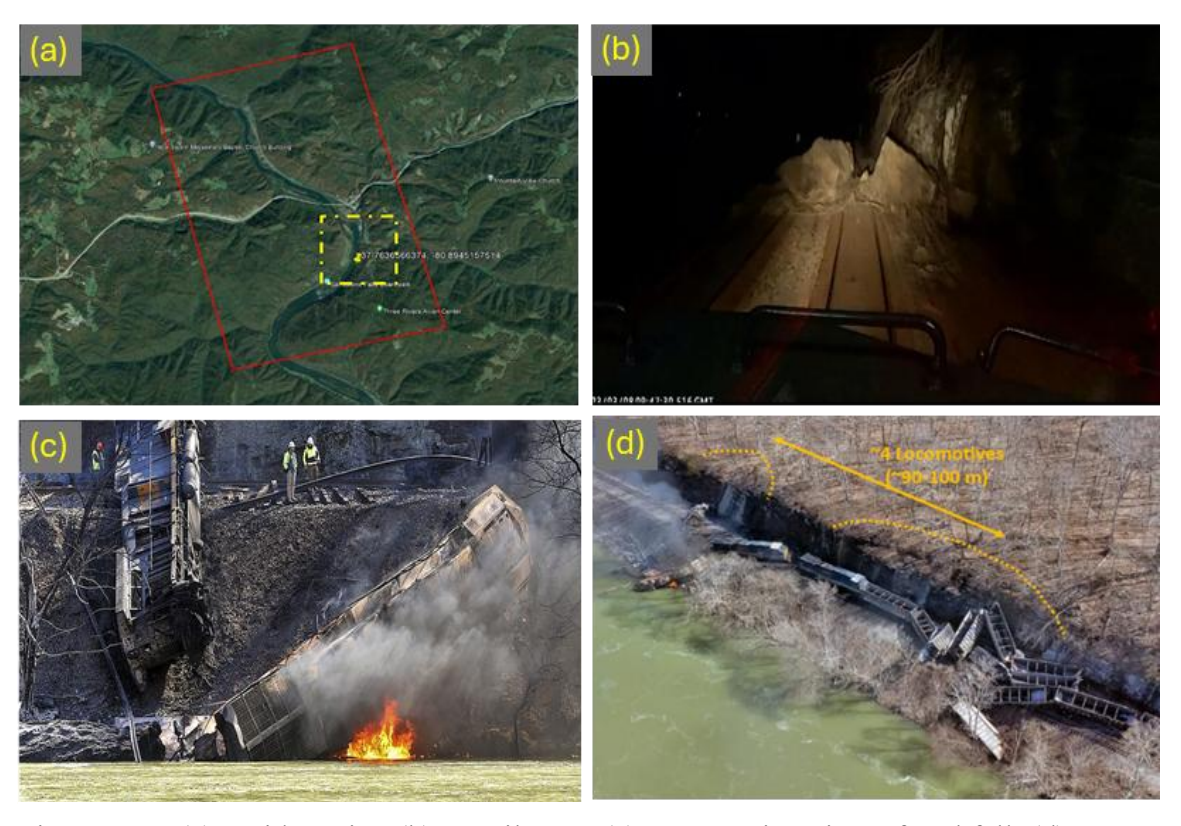


Figure A.39 (a) Incident site; (b) Derailment; (c) Locomotive view of rockfall; (d) Two distinct slope failures  $\sim$ 100 m apart.

upon careful examination of the images reported in the media, it becomes evident that there are two well-defined surface area regions that experienced slope failure, with an approximate distance of 100 meters between them, as evidenced in Figure A.39(d).

The derailment site is about one mile from Sandstone and is located between a cliff on one side and the New River on the other. This region has a 35 to 80 percent slope and is well drained. The area of interest has decaying plant matter and silty clay loam on the top 4 inches with stony silty clay loam underneath. The cliff facing the railway track has a stony profile, with the region above the cliff having dense forest cover. Based on the above factors, the site is classified as B, tending towards C, as indicated in Figure A.40 by the red-highlighted path in the decision tree.

#### A.8.2 Data Availability

The region under investigation is covered by Sentinel-1A, also shown in Figure A.39(a) by the area marked in red, with a frequency of acquisition of 12 days. The region is located in a rural area with radar signals blocked by the cliffs facing away from the satellite path. Due to the geolocation of the incident area, a low number of PS points is expected. The Sentinel dataset for this study is downloaded from the Sentinel-1 EU datahub and Alaska Satellite Facility (ASF). The region also has a high cloud presence, reducing the number of optical images available from Sentinel-2. In view of the relatively low site class, it was decided to employ the RS-SBAS technique with an image stack size of 25. The data acquisition begins on November 14, 2021, and continues until March 2, 2023, a week before the event. A total of 44 acquisitions were obtained for the analysis, yielding seven SBAS analyses for the chosen 25-image rolling stack, as shown in Table A.9.

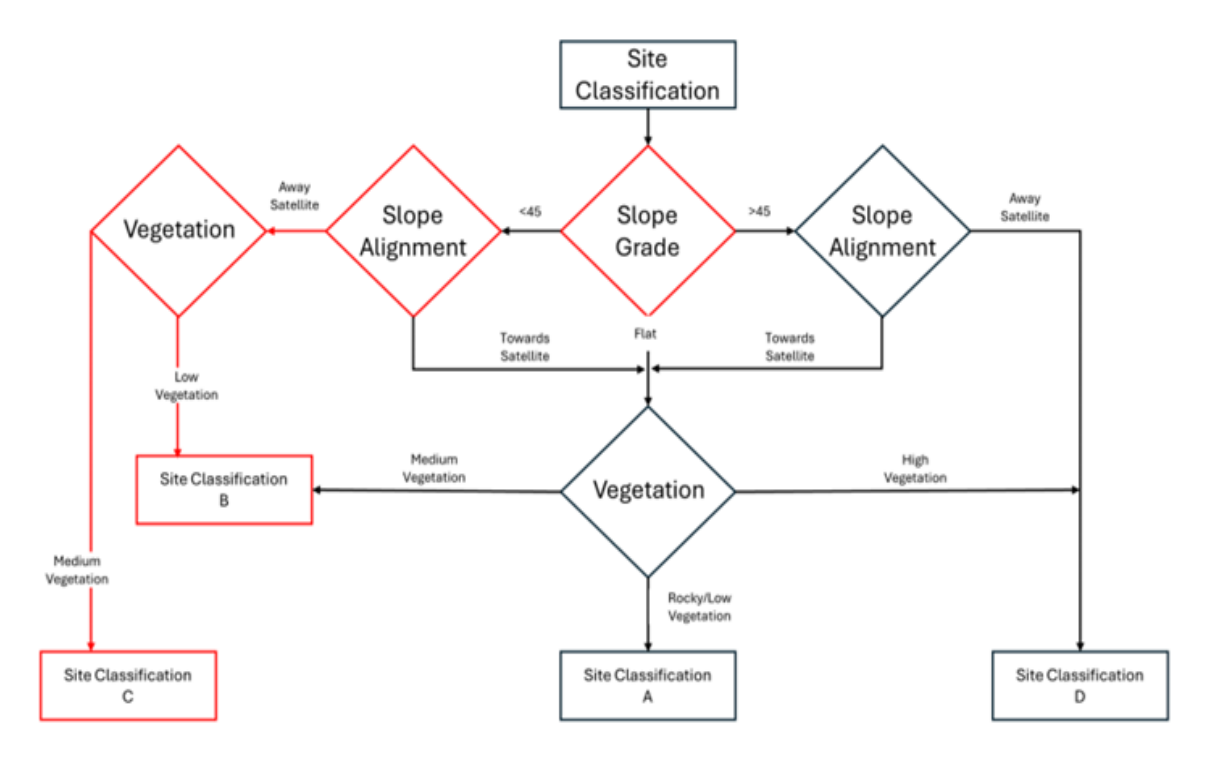


Figure A.40 Shows the site classification for the derailment study.

Table A.9 Sandstone WV Analysis Datasets

Data Set	Sentinel 1-A	
Analysis 1	10/14/2021 to 09/03/2022	
Analysis 2	11/19/2021 to 10/09/2022	
Analysis 3	12/13/2021 to 11/02/2022	
Analysis 4	01/30/2022 to 12/08/2022	
Analysis 5	03/07/2022 to 01/13/2023	
Analysis 6	05/06/2022 to 02/18/2023	
Analysis 7	06/23/2022 to 03/02/2023	

The ground surface deformation is computed in all cases in the satellite LOS.

Each analysis cycles three older images to be replaced by three newer images. Since the acquisitions are 12 days apart, each new analysis is separated by one month.

## A.8.3 Thresholding and Accumulation

SBS analysis showed coherence of 0.3, thus, the threshold limits on the displacement computed at the DS point is set to +/- 20 mm (see Table A.9). The DS accumulation over the entire observation period is shown in Figure A.41 at different times before the event. The location of the event is marked by the yellow dashed circle. DS points are indicated by the white dots that are scarce 7 months before the event in the area of the event, and density increases as the points accumulate over time in potentially critical areas. DS points are detected at the onset of the analysis in other areas of the region of interest. By inspection of the optical image, these DS points correspond to known scatterers, e.g. buildings.

# A.8.4 Clustering and Critical Area Identification

The next step in the process is the identification of the critical areas through detection of clusters. The clustering is observed both through visual inspection, and through the optical image subset approach discussed in Section 4.5. In both cases the identified clusters are marked in Figure A.42 by yellow and red rectangles. In these clusters, the density of the DS points increases with time. The yellow marked areas correspond to areas of known scatterers, such as the structures in the town of Sandstone (cluster A), or agricultural buildings (clusters B and C), or are detected on flat terrain away from the track and are not of immediate interest. However, clusters F and G,



Figure A.41 DS Accumulation at (a) 6 months; (b) 5 months; (c) 4 months; (d) 3 months; (e) 2 months; (f) 1 months; (g) 19 days; and (h) 7 days before the rockfall event and derailment

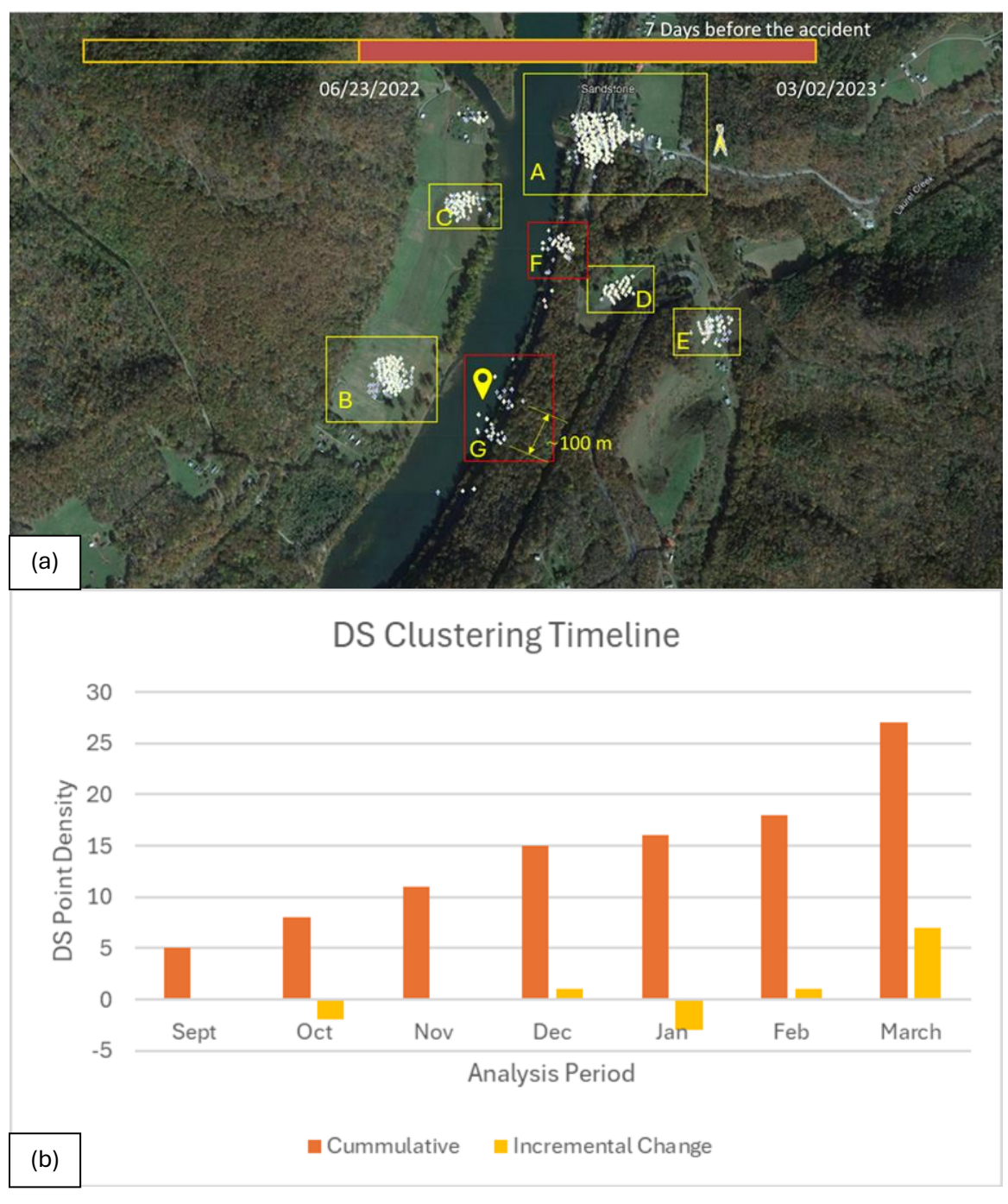


Figure A.42 (a) Clustering and critical area identification; (b) DS Clustering timeline shows the DS cluster density in the critical subset and the timeline of the change

marked by the red rectangles, are deemed the critical ones since they exhibit increasing activity over time and are located on the path of the track on a highly sloped terrain.

Cluster G is located at the derailment site and upon closer investigation the two subclusters within the subset are approximately 100 m apart, which is consistent with the two distinct slope failures identified in Figure A.39d. Cluster F is also identified as a critical area; however, no failure occurred at the time of derailment. It was reported that following the derailment, remedial action was taken on both F and G critical areas.

The DS clustering timeline analysis is shown in Figure A.42b. The graph shows the DS cumulative and incremental cluster density at the different times of the analysis. It is evident in both clustering and timeline analysis that the cluster has become active long before the rockfall event and derailment occurred. Furthermore, the incremental change indicates that the activity has become more pronounced about a week before the slope failure in cluster G. The activity in cluster F also raised concern; however, the issue was addressed by the railroad before an event occurred.

# A.9 Raymond, MN

### A.9.1 Event

On March 30<sup>th,</sup> 2023, a BNSF train carrying highly flammable ethanol derailed and caught fire in Raymond, Minnesota, causing concerns about safety and potential contamination. Out of the 22 derailed cars, four containing ethanol ruptured and ignited Figure A.43(a) leading to a blaze. Other cars carrying ethanol were also at risk of releasing the chemical in the region, with the accident highlighted.

Figure A.43(b) shows the location of the accident on the world map, with Figure

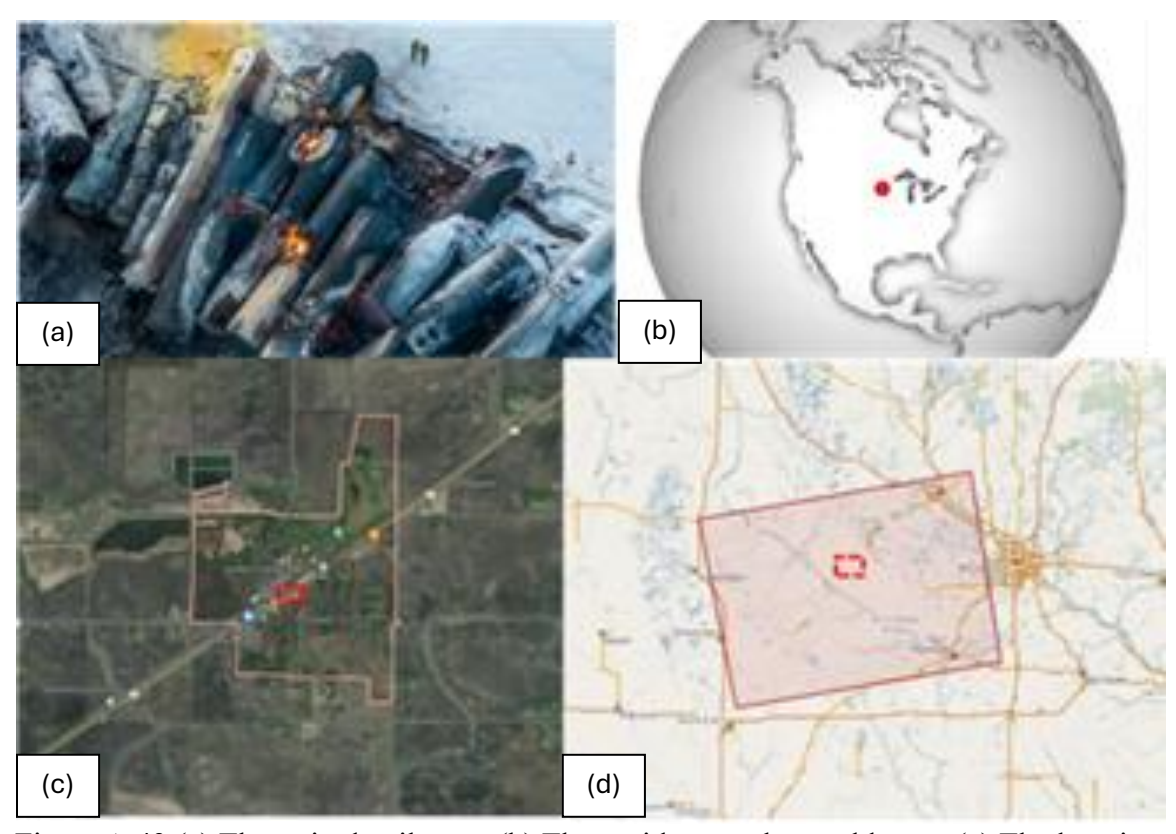


Figure A.43 (a) The train derailment; (b) The accident on the world map; (c) The location of the derailment in the town of Raymond, MN; (d) The data path of Sentinel-1A covering the region with the accident highlighted.

A.43(c) showing the exact location of the derailment in the town of Raymond,
Minnesota. The EPA report of the derailment suggests the cause is due to rupturing two
denatured ethanol tanks, a highly flammable product [109]. This analysis was conducted
before the report was public to see if the cause of the derailment was due to site
mobilization or any other factors that are observable by InSAR analysis.

# A.9.2 Site Description

The region under investigation is located in Minnesota at latitude longitude (48.25, -101.46), about 100 miles from Minneapolis, MN. The region under observation is in a northern state with a mean annual precipitation of 24-37 inches with 140 to 180 frost-free days. The InSAR analysis can be divided into the urban area of Raymond, MN, and the rural farm area surrounding it, as seen in Figure A.44. The Urban area has a soil profile of clay loam in the top 0- 16 inches of the soil layer, with the soil layer from 16 - 79 inches of loam soil. This region is classified as poorly drained, with the depth to the water table being 0 to 8 inches. The rural area has diverse soil classifications, with the largest having silt loam soil in the top layer of 28 inches of soil and loam from 28 to 79 inches below it. The water table in this region is about 47 to 59 inches, with a high capacity to transmit water (0.2 to 2in/hr). Both regions have never had problems with flooding and ponding. Soil profile map is shown in Figure A.44 and complete information related to soil profile can be found in [98]

#### A.9.3 Data Availability

The region under investigation is in Minnesota, at Latitude/longitude 45.01, -95.23. The radar satellite Sentinel-1A covers this region once every 12 days. The



Figure A.44 The soil profile map of the region in Raymond, MN

derailment occurred in the center of the town of Raymond, located in the urban areas with a large area exposed to radar backscatter. The town is surrounded by farmland which has a low radar backscatter. Since only one satellite covers this area, analysis of the region is restricted to the angle of incidence. The dataset for this study is obtained from the Sentinel constellation, and the satellite images are downloaded from the Sentinel-1 EU datahub (ESA, 2023) and Alaska Satellite Facility (ASF) (ASF, 2023). Figure A.43(d) shows the path taken by the Sentinel1-A satellite. The analysis employs PSInSAR techniques using archived satellite radar images spanning 12 months. The analysis has an approximately 3 months gap period between May 2022 to Aug 2022 (Table A.10). The results are overlayed on the optical image acquired by Sentinel-2 on March 11, 2023, for better visualization.

## A.9.4 PSInSAR analysis

The PSInSAR analysis for site mobilization monitoring was conducted using a stack of 20 images, at a minimum. The deformation maps from the two orbits are superimposed on an optical image taken on March 11, 2023. The displacement observed is in mm and plotted on the color-coded PS images that show the total displacement over the entire analysis. The negative displacement (blue) indicates subsidence, and the positive displacement (red) denotes height gain about the line of sight of each satellite and orbit. The PSInSAR analysis uses single orbit data to produce the deformation results shown in Figure A.45. Figure A.45(a) shows that the rural area around Raymond, MN, has a low density of PS, while the highlighted region of Raymond has a high amount of PS. Figure A.45(b) shows the displacement in the range of -25 to -14 and 14 to 25 to show the largest deformation in the region without the stationary point. The town of

Table A.10 Shows the data acquired for conducting PSInSAR from Sentinel-1A.

Data Set	Sentinel 1-A Ascending
Stability monitoring	02/18/2022 to 03/09/2023

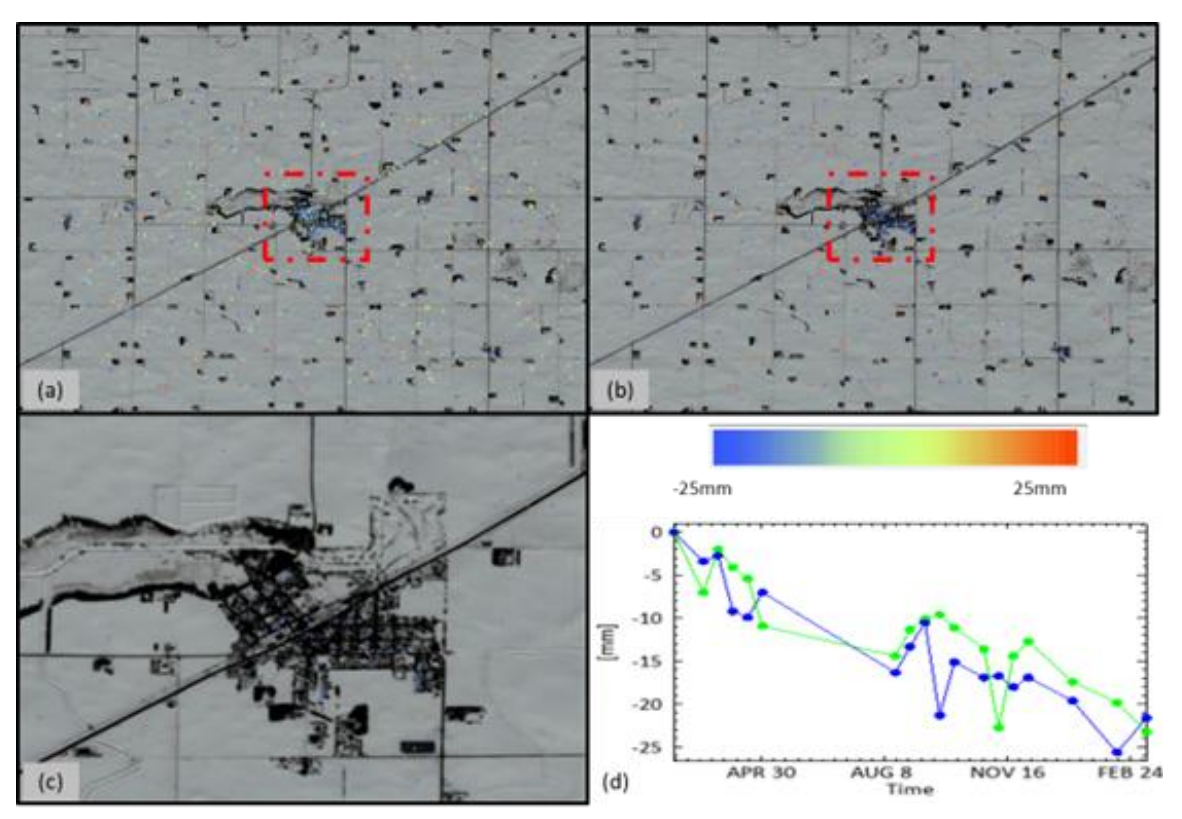


Figure A.45 (a) shows the total PS over the observation area. (b) Shows high displacement PS with stationary points removed. (c) Shows the area where the derailment took place. (d) Shows the average subsidence monitored in the region

Raymond, MN, highlighted in Figure A.45(b), is shown in Figure A.45(c) in a larger scale, with the average displacement of subsidence over time shown in Figure A.45(d).

#### A.9.5 Discussion

PSInSAR analysis over the Raymond, MN, derailment analysis has shown a contrast in the density of PS from the urban environment of Raymond, MN, and the surrounding rural area. The analysis shows the rural regions of Raymond to have positive displacement, while the urban region is experiencing subsidence. By comparing the displacement region with the soil reports, we can see that the water table is relatively high in the case of the urban region (0-8 inches). Similar conditions have been observed in cities where PSInSAR analyses have been conducted [110] [62]. This region can be classified as B due to high radar returns from the area for PS analysis, but lack of multiple angles for better analysis.

## A.10 Quinn's MT

#### A.10.1 Event

On April 2, 2023, a train derailment occurred southeast of Plains, Montana, across the Clark Fork River from Quinn's Hot Springs Resort. The incident, under investigation, involved at least 20 cars derailing, including one carrying hazardous materials in the form of liquefied petroleum gas (butane).

The derailed train cars included boxcars carrying powdered clay and beer brands in cans and bottles. Motorists traveling along Highway 135 could observe approximately 18 partially or fully derailed railcars, while additional boxcars were derailed inside a century-old tunnel near the visible cars. Law enforcement officers were on the highway

to prevent onlookers from blocking the road around blind curves. Figure A.46(a) shows the location of the railway derailment, with Figure A.46(b) showing the derailment leading to the contents being dumped in the river.

## A.10.2 Data Availability

This region was formerly covered by Sentinel-1B, covering it from 3 angles; it could observe the region from multiple angles Figure A.47(a). But since the loss of Sentinel-1B, this region is now in a negative zone not covered by any satellite. Sentinel-1A covers this region nearby, but as Figure A.47(b) shows, there are gaps in the satellite coverage. Due to this reason, InSAR analysis cannot be conducted in this region.

#### A.10.3 Conclusion

This site shows the limitations of SAR analysis and the extent of data availability.

In the future, when new satellites are launched, these limitations can be mitigated.

# A.11 Pueblo, CO

#### A.11.1 Event

On October 15, 2023, in Pueblo, Colorado, a BNSF freight train carrying coal derailed while traveling south on the Pikes Peak Subdivision in the Pueblo West area. The incident occurred within an area of interest covering approximately 4 square miles, located about 8.4 miles from the city center. The derailment caused the collapse of a bridge over Interstate 25, tragically resulting in the death of a truck driver who was passing underneath at the time. Preliminary investigations attributed the derailment to a broken rail and the failure of trackside warning systems, both of which contributed to the



Figure A.46 Quinn's Hot Springs Resort, Montana, Derailment Site: (a) Location; (b) Derailment

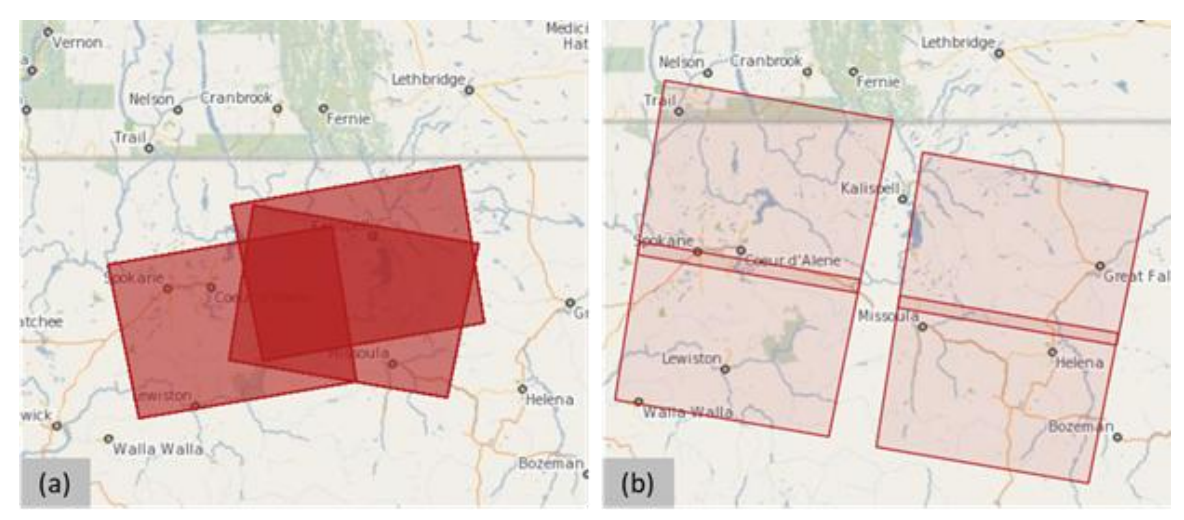


Figure A.47 Data availability for Site: (a) Sentinel-1B original overage; (b) Sentinel-1A inadequate coverage

accident. As a result, a significant portion of I-25—a major transportation corridor used by an estimated 39,000 to 40,000 vehicles per day—was closed, severely disrupting regional traffic and freight movement Figure A.48. The event prompted emergency response actions, federal safety reviews, and infrastructure damage assessments [111].

## A.11.2 Site Description

The region under investigation is located in Pueblo Colorado at latitude/longitude (37.76/-80.89). This region experiences a mean annual precipitation of 11 to 14 inches with 145 to 175 frost-free days. This region is classified as not prime farmland 0 to 2 percent slopes in the area. This region is composed of predominantly channery silty clay loam soil, with the top layer having channery silt loam(0 to 3 inches). The region is well drained with high runoff classification. Additional detailed information related to soil profile can be obtained in [102]

## A.11.3 Data Availability

The region under investigation is in Colorado, where Sentinel-1A provided coverage. This region is covered by Sentinel-1A satellite once every 12 days. T. Due to the geolocation of the incident area, we can expect high PS points. The dataset for this study is obtained from the Sentinel constellation, and the satellite images are downloaded from the Sentinel-1 EU datahub (ESA, 2023) and Alaska Satellite Facility (ASF) (ASF, 2023). The analysis employs PSInSAR and SBAS techniques using archived satellite radar images spanning 12 months, covering the event's occurrence. The analysis uses Sentinel-2 for optical images. Since this is, a recent event post-event analysis is not available at this time.



Figure A.48 Shows the railway derailment taking place

This derailment was monitored post-event to identify conditions that led to the broken rail. The region's site characteristics include flat terrain with slopes of less than 2 percent and uneven terrain. It is dry with low vegetation density and a large presence of shale rocks close to the surface. The region is well-drained and has no history of flooding or ponding. The region is monitored by only one SAR satellite Sentinel-1A, but due to site characteristics, this region falls under site class A. The dataset for this analysis is acquired from the sentinel-1 constellation and is downloaded using the sentinel-1 EU datahub and Alaskan Satellite Facility (ASF). The analysis period covers 10 months using 25 image stacks for PSInSAR analysis. The analysis covers the deformations taking place near the accident site 3 days before the derailment took place.

### A.10.4 PSInSAR Analysis

The PSInSAR analysis was conducted using a 25-image stack. The deformation map is superimposed on an optical image taken on October 15, 2023. The optical image was taken before the derailment event. The displacement observed is in mm and plotted on the color-coded PS images that show the total displacement over the entire analysis. The deformation map in Figure A.49(a) highlights large deformations taking place on the track and on the abutment of the bridge. Figure A.49(b) shows the optical image of the abutment taken in September 2023, a month before the accident. It shows large cracks being formed on the abutment and also on the wing wall in the region where the blue deformation point in Figure A.49(a) was observed. Figure A.49(c) shows the deformation over time of the high deformation PS

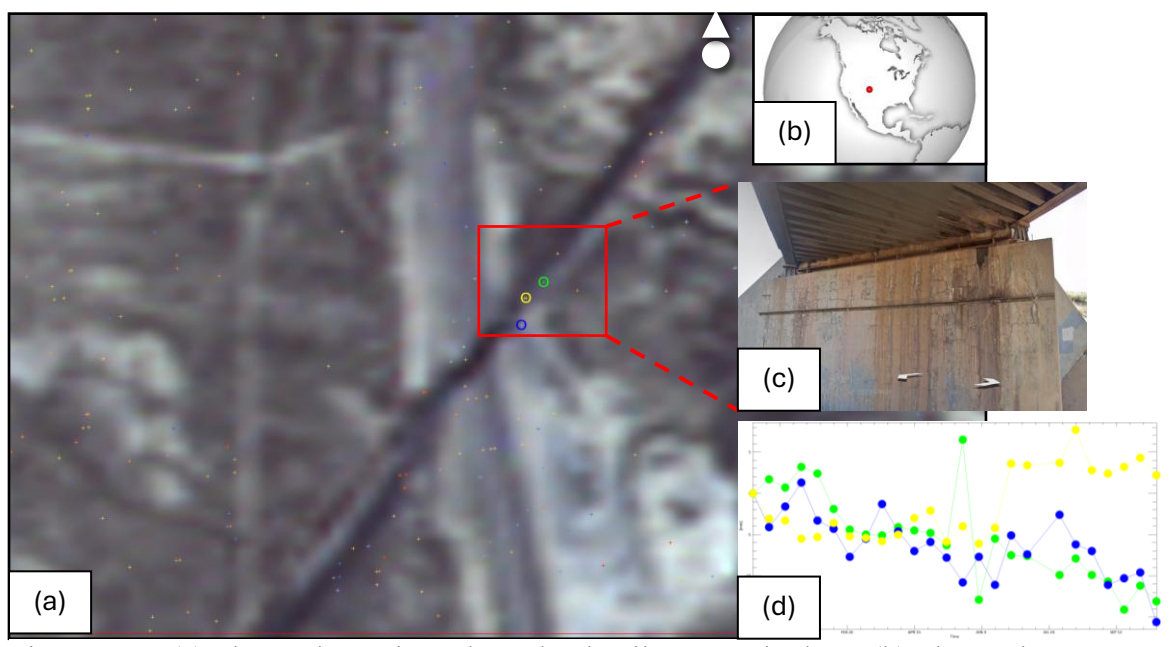


Figure A.49 (a) Shows the region where the derailment took place; (b) Shows the location of the accident; (c) Highlights the optical image of the cracks in the region; (d) Shows the deformation over time of the high PS

#### A.10.5 Discussion

The October 15, 2023, train derailment in Pueblo, Colorado, highlights the importance of integrating geotechnical, structural, and remote sensing data for transportation infrastructure safety. Triggered by a broken rail, the incident caused a bridge collapse over Interstate 25 and resulted in fatalities. A PSInSAR analysis using Sentinel-1A radar data revealed significant ground and structural deformation near the bridge in the days leading up to the event. These deformations, supported by September 2023 optical imagery showing cracks in the abutment and wing wall, suggest that early warning signs were detectable prior to the collapse.

While the study demonstrates the value of InSAR in monitoring infrastructure in semi-arid, low-vegetation areas like Pueblo, limitations remain. The 12-day revisit cycle of Sentinel-1A may miss rapid changes, and the lack of post-event data limits full forensic analysis. Nonetheless, the findings stress the need for enhanced multi-sensor integration, faster data processing, and automated alert systems to support proactive maintenance and prevent similar disasters.

## APPENDIX B: COHERENCE AND SOIL MOISTURE MODEL

# B.1 Blackville, SC

# B.1.1 Site Description

The sensors under investigation are located in southern South Carolina at latitude longitude (33.36, -81.33), roughly 120 miles from the coast and encompassing 1 km<sup>2</sup>. The sensor's location is approximately 0.3 miles from Clemson University Edisto Research Center. The soil is sandy for most of the region, with some regions having seasonal vegetation. The sensor region encompasses an area of approximately 1 km<sup>2</sup>, indicating a significant level of uncertainty compared to the SAR sensor's resolution (15 m<sup>2</sup>). The region experiences roughly 40 to 55 inches of mean annual precipitation with 240 to 285 days of frost-free period. The sensor location and surrounding area are classified as farmland by the state. This site was chosen due to its proximity to the UofSC test center and the availability of the USCRN dataset. The soil profile of the region is further explored in [103].

## B.1.2 Data Availability

The region is located close to east coast and has access to Sentinel-1A data. The data is typically collected with a 12-day interval and analyzed within the same orbit to minimize errors. The datasets for this analysis were obtained from the Sentinel constellation and were downloaded using the Sentinel-1 EU datahub and the Alaska

Satellite Facility (ASF) (ASF, 2023). The study utilizes data from January 3, 2019, to June 18, 2022, with 91 acquisitions taken in the same geometry. The data used for this analysis is shown in Table B.1

#### B.1.3 CCD Analysis

The analysis was based on a large stack of data, and the timeline method was used to perform the CCD analysis. Coherence data from each map was converted to text format, along with the corresponding coordinates. A total number of 90 CCD analyses are conducted in the CCD timeline feature. The soil moisture sensor covered a larger area than the SAR analysis resolution, resulting in numerous data points for each CCD analysis that covered the region based on the sensor coordinates.

The mean and standard deviation of coherence readings were calculated based on the sensor coordinates to obtain a reliable interpretation of coherence over the sensor's coverage area. These readings were tabulated by satellite, orbit direction, and acquisition date and normalized in the range 0 to 1. Similarly, the NOAA sensor's relative humidity, precipitation, and soil moisture content are tabulated by property and acquisition date. Since the C-band sensor has low penetration power, only the top 5cm soil layer data was used for the soil moisture analysis. The soil moisture data represents the average hourly measurements taken throughout the day. The NOAA data have also been normalized, each in the range 0-1. Since coherence represents a change of the signal between two acquisitions, it is necessary to correlate the coherence to the change in moisture content is necessary to correlate the coherence to the change in moisture content in developing the model. Furthermore, both the coherence and soil moisture change values are normalized

Table B.1 Sentinel-1 Data used for Blackville CCD analysis

Data Set	CCD Timeline
Sentinel-1A	01/03/2019 to 05/18/2022

in the range 0 to 1, grouped in increments of 0.1, and the average value in each group is computed.

#### B.1.4 Discussion

The relationship between normalized moisture change to normalized coherence is shown in Figure B.1. The graph shows that the increasing coherence is inversely proportional to moisture change, suggesting a relationship between the two factors.

# B.2 Yosemite, CA

## **B.2.1 Site Description**

The sensors under investigation are located in California at latitude and longitude (37.76, -119.82) and covers 1 km2. It is near the crane flat lookout in Yosemite National Park and roughly 140 miles from the coast. The sensors are located at an altitude approximately 6450 feet from the sea level. The region experiences roughly 33 to 45 inches of mean annual precipitation and 20 to 60 days of free periods. The region is classified as not prime farmland with sandy loam on the top 39 inches of soil. It is well drained and has a large vegetation content.

## B.2.2 Data Availability

The region is located close to the west coast and has access to multiple orbits of Sentinel-1A data. The data is typically collected with a 12-day interval for each orbit and analyzed within the same orbit to minimize errors. The datasets for this analysis were obtained from the Sentinel constellation and were downloaded using the Sentinel-1 EU datahub and the Alaska Satellite Facility (ASF) (ASF, 2023). The study utilizes data from January 4, 2019, until July 29, 2022. The secondary orbit of Sentinel-1A data is available

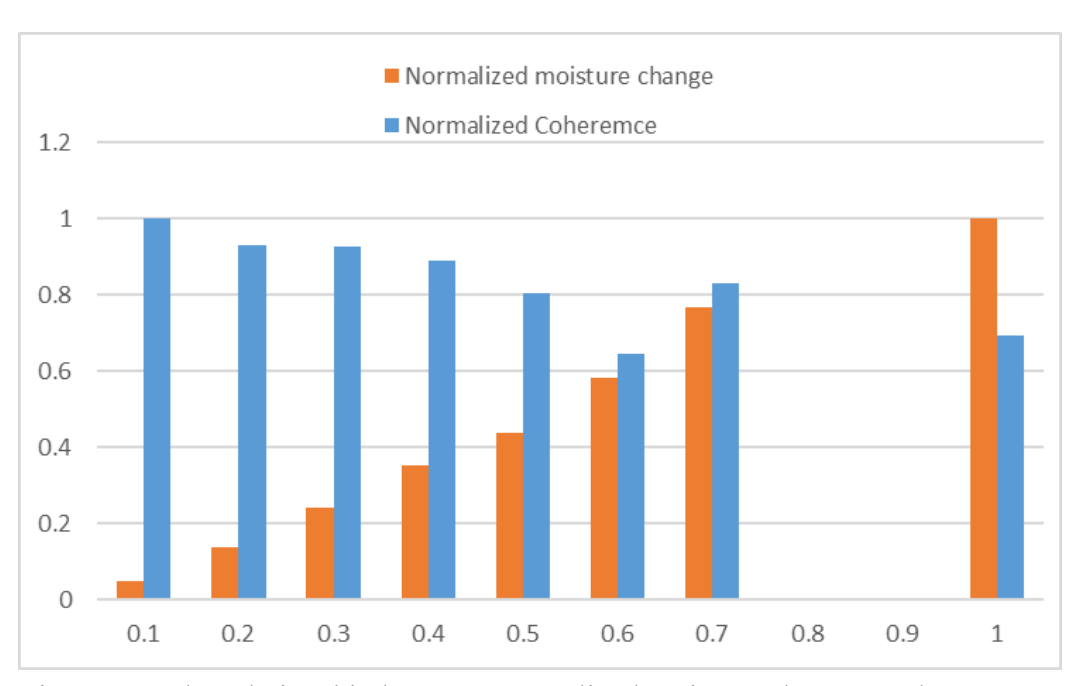


Figure B.1 The relationship between normalized moisture changes and normalized coherence

only till December 2022. Table B.2 shows the data used for the analysis

## B.2.3 CCD Analysis

The analysis was based on a large stack of data, and the timeline method was used to perform the CCD analysis. Coherence data from each map was converted to text format, along with the corresponding coordinates. A total number of 90 CCD analyses are conducted in the CCD timeline feature. The soil moisture sensor covered a larger area than the SAR analysis resolution, resulting in numerous data points for each CCD analysis that covered the region based on the sensor coordinates.

The mean and standard deviation of coherence readings were calculated based on the sensor coordinates to obtain a reliable interpretation of coherence over the sensor's coverage area. These readings were tabulated by satellite, orbit direction, and acquisition date and normalized in the range 0 to 1. Similarly, the NOAA sensor's relative humidity, precipitation, and soil moisture content are tabulated by property and acquisition date. Since the C-band sensor has low penetration power, only the top 5cm soil layer data was used for the soil moisture analysis. The soil moisture data represents the average hourly measurements taken throughout the day. The NOAA data have also been normalized, each in the range 0-1.

Since coherence represents a change of the signal between two acquisitions, it is necessary to correlate the coherence to the change in moisture content in developing the model. Furthermore, both the coherence and soil moisture change values are normalized in the range 0 to 1, grouped in increments of 0.1, and the average value in each group is computed.

Table B.2 Sentinel-1 Data used for Yosemite CCD analysis

Data Set	CCD Timeline
Sentinel-1A Orbit-1	01/10/2019 to 07/29/2022
Sentinel-1A Orbit-2	01/04/2019 to 12/19/2021

#### **B.2.4 Discussion**

The relationship between normalized moisture change, normalized coherence and rainfall is shown in Figure B.2 and Figure B.3. The graphs represent the data from both orbits and show that the rainfall is influencing the soil moisture. The coherence is highest when the rainfall and soil moisture is lowest. This condition is observed in both orbits, suggesting the relationship is directly related and can still be observed in regions with the presence of vegetation.

## B.3 Bodega, CA

### **B.3.1** Site Description

The sensors under investigation are located in southern California at latitude longitude (38.32, -123.07), encompassing 1 km<sup>2</sup>. It is located on the West Coast and has access to both Sentinel-1A and Sentinel-1B, providing access to SAR data from various angles. The soil is sandy for most of the region and is close to the Pacific Ocean. The region experiences roughly 15 to 35 inches of mean annual precipitation with a 300-day frost-free period. The state classifies the sensor location and the surrounding area as Duneland.

## B.3.2 Data Availability

The region is close to the Pacific Ocean and can access Sentinel-1A and 1B data. The data is typically collected within a 12-day interval and analyzed within the same orbit to minimize errors. The datasets for this analysis were obtained from the Sentinel constellation and were downloaded using the Sentinel-1 EU datahub and the Alaska Satellite Facility (ASF) (ASF, 2023). The study utilizes data from January 3, 2019; the

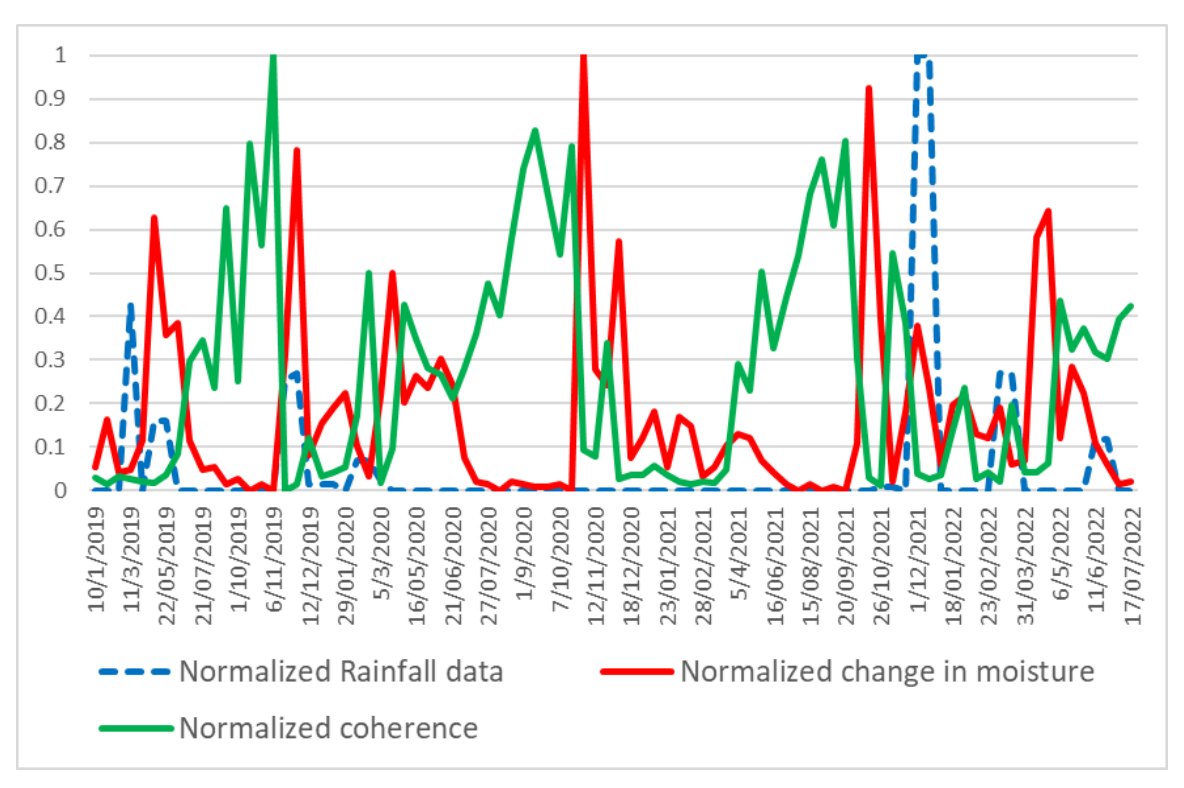


Figure B.2 The relationship between normalized moisture changes, coherence, and rainfall for c Sentinel-1A orbit-1 data.

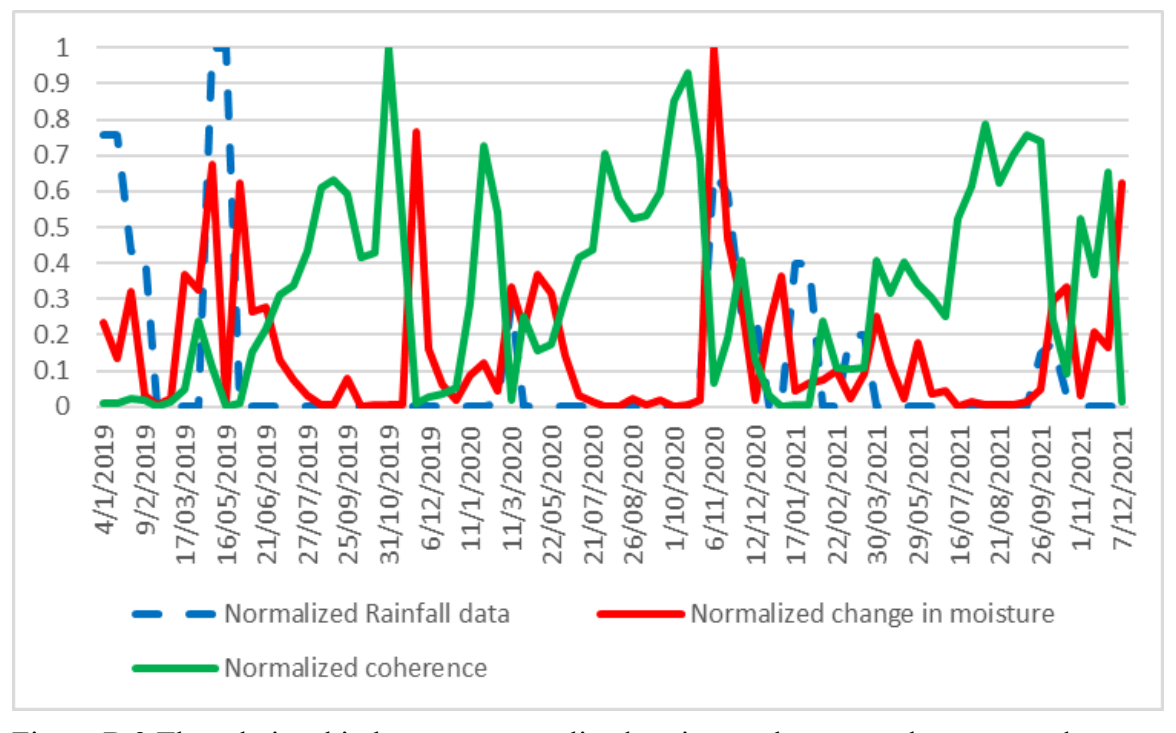


Figure B.3 The relationship between normalized moisture changes, coherence, and rainfall for Yosemite Sentinel-1A orbit-2 data.

last data acquisition was taken on June 18, 2022. Table B.3 shows the data used for the analysis

### B.3.3 CCD analysis

The analysis was based on a large stack of data, and the timeline method was used to perform the CCD analysis. Coherence data from each map was converted to text format, along with the corresponding coordinates. A total number of 90 CCD analyses are conducted in the CCD timeline feature. The soil moisture sensor covered a larger area than the SAR analysis resolution, resulting in numerous data points for each CCD analysis that covered the region based on the sensor coordinates.

The mean and standard deviation of coherence readings were calculated based on the sensor coordinates to obtain a reliable interpretation of coherence over the sensor's coverage area. These readings were tabulated by satellite, orbit direction, and acquisition date and normalized in the range 0 to 1. Similarly, the NOAA sensor's relative humidity, precipitation, and soil moisture content are tabulated by property and acquisition date. Since the C-band sensor has low penetration power, only the top 5cm soil layer data was used for the soil moisture analysis. The soil moisture data represents the average hourly measurements taken throughout the day. The NOAA data have also been normalized, each in the range 0-1.

Since coherence represents signal change between two acquisitions, it is necessary to correlate it with moisture content change in developing the model. Both coherence and soil moisture change values are normalized from 0 to 1, grouped in 0.1 increments, and the average value in each group is computed.

Table B.3 Sentinel-1 Data used for Bodega CCD analysis

Data Set	CCD Timeline
Sentinel-1A Orbit-1	01/03/2019 to 08/15/2022
Sentinel-1A Orbit-2	01/08/2019 to 03/05/2022

#### **B.3.4 Discussion**

The relationship between normalized moisture change, normalized coherence and rainfall is shown in Figure B.4 and Figure B.5. The graphs represent the data from both orbits and show that the rainfall is influencing the soil moisture. The coherence is highest when the rainfall and soil moisture is lowest. This condition is observed in both orbits, suggesting the relationship is directly related and can be observed in regions with low vegetation. The low vegetation in this region shows the relation between these factors more extensively.

## B.4 Santa Barbara, CA

### **B.4.1 Site Description**

The sensors under investigation are located in southern California at latitude longitude (38.32, -119.88), encompassing 1 km<sup>2</sup>. It is located on the West Coast and has access to both Sentinel-1A and Sentinel-1B, providing access to SAR data from various angles. The soil is sandy for most of the region and is close to the Pacific Ocean. The region experiences roughly 19 to 20 inches of mean annual precipitation with 360 to 365 days of frost-free period. The state classifies the sensor location and the surrounding area as Duneland. This region is similar to B.2.3 Bodega CA.

#### B.4.2 Data Availability

The region is close to the Pacific Ocean and can access Sentinel-1A and 1B data.

The data is typically collected within a 12-day interval and analyzed within the same orbit to minimize errors. The datasets for this analysis were obtained from the Sentinel 1 constellation and were downloaded using the Sentinel-1 EU datahub and the Alaska

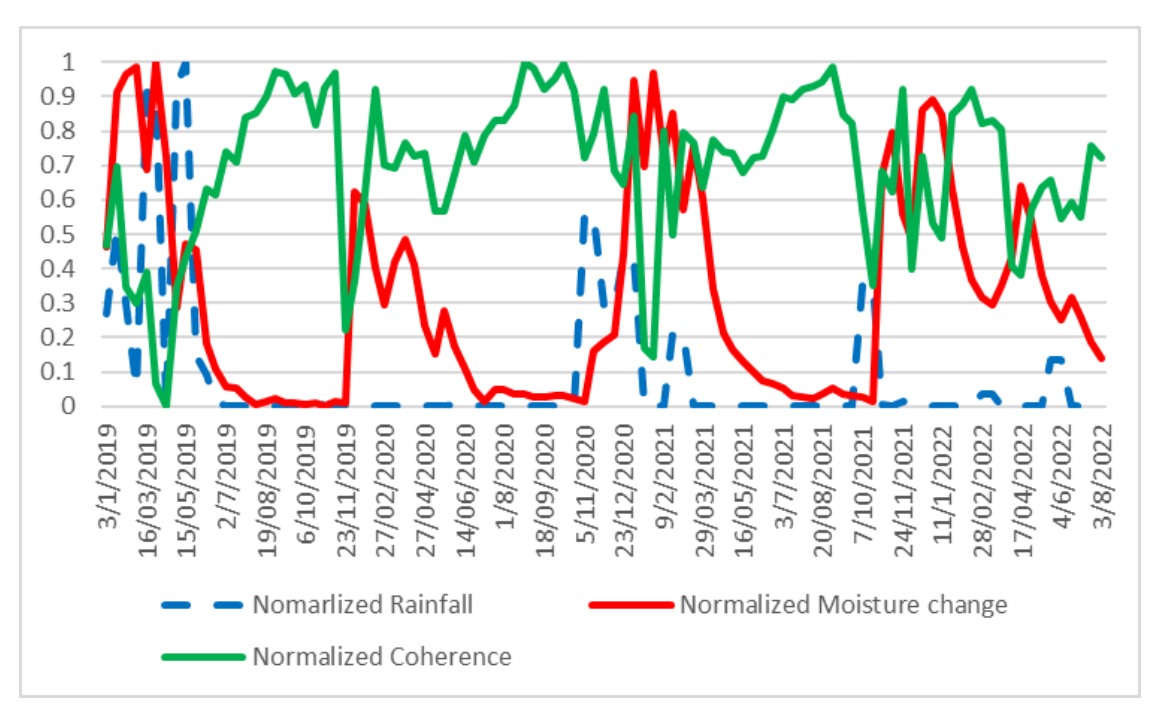


Figure B.4 The relationship between normalized moisture changes, coherence, and rainfall for Bodega Sentinel-1A orbit-1 data.

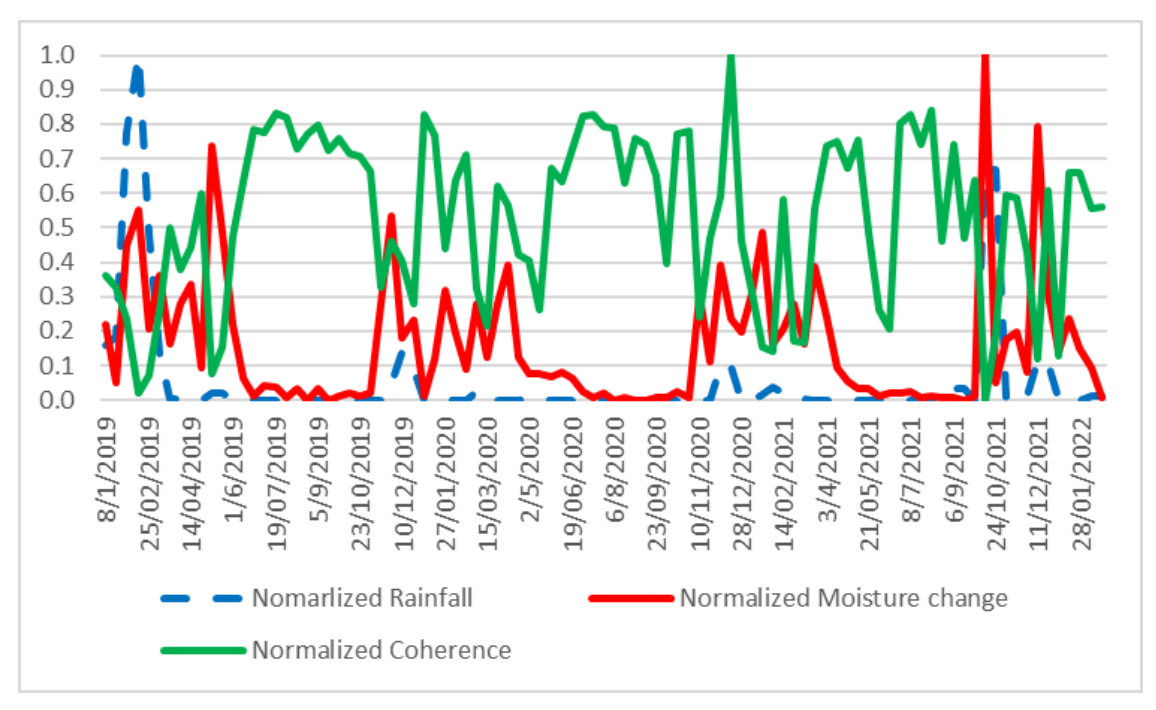


Figure B.5 The relationship between normalized moisture changes, coherence, and rainfall for Bodega Sentinel-1A orbit-2 data.

Satellite Facility (ASF) (ASF, 2023). The study utilizes data from January 1, 2019; the last data acquisition was taken on September 15, 2022. Throughout the analysis period, Sentinel 1-A data is accessible, while Sentinel 1-B data is available until December 2021, after which it becomes unavailable. Table B.4 shows the data used for the analysis

## B.4.3 CCD Analysis

The analysis was based on a large stack of data, and the timeline method was used to perform the CCD analysis. Coherence data from each map was converted to text format, along with the corresponding coordinates. A total number of 90 CCD analyses are conducted in the CCD timeline feature. The soil moisture sensor covered a larger area than the SAR analysis resolution, resulting in numerous data points for each CCD analysis that covered the region based on the sensor coordinates.

The mean and standard deviation of coherence readings were calculated based on the sensor coordinates to obtain a reliable interpretation of coherence over the sensor's coverage area. These readings were tabulated by satellite, orbit direction, and acquisition date and normalized in the range 0 to 1. Similarly, the NOAA sensor's relative humidity, precipitation, and soil moisture content are tabulated by property and acquisition date. Since the C-band sensor has low penetration power, only the top 5cm soil layer data was used for the soil moisture analysis. The soil moisture data represents the average hourly measurements taken throughout the day. The NOAA data have also been normalized, each in the range 0-1.

Since coherence represents a change of the signal between two acquisitions, it is necessary to correlate the coherence to the change in moisture content in developing the

Table B.4 Sentinel-1 Data used for Santa Barbara CCD analysis

Data Set	CCD Timeline
Sentinel-1A Orbit-1	01/10/2019 to 09/15/2022
Sentinel-1A Orbit-2	12/10/2019 to 09/15/2022
Sentinel-1B Orbit-2	01/04/2019 to 12/19/2021
Sentinel-1B Orbit-2	08/20/2019 to 12/19/2021

model. Furthermore, both the coherence and soil moisture change values are normalized in the range 0 to 1, grouped in increments of 0.1, and the average value in each group is computed.

#### B.4.4 Discussion

The results from the analysis are plotted in Figure B.6 The graph is plotted with the X-axis representing the date of acquisition and the Y-axis measuring from 0-1. The results show that coherence is minimum when soil moisture maximizes and vice versa. The graph shows a direct correlation between rainfall and coherence but no apparent correlation between humidity and coherence. It is also noted that the rainfall peaks precede the soil moisture content peaks. The effect of rainfall is essential to developing the model as, in practical cases, the soil moisture data will only be available when determining if loss of coherence will lead to a geohazard. A model has been developed based on data from the normalized coherence using B.3 and B.4 and is discussed in [71]

## B.5 Cortez, CO

## B.5.1 Site Description

The sensors under investigation are located in Colorado at latitude and longitude (37.26, -108.50), encompassing 1 km2. It is in Mesa Verde National Park. The region is mountainous, with an elevation of roughly 7100 feet to 8500 feet. It experiences a mean annual precipitation of 15 to 20 inches and 80 to 100 frost-free days. The region is classified as not prime farmland, with the top 1 to 5 inches of soil having a moderate amount of decomposed plant material and the rest of the soil profile being classified as very stony clay loam. It is well drained and has a large vegetation content.

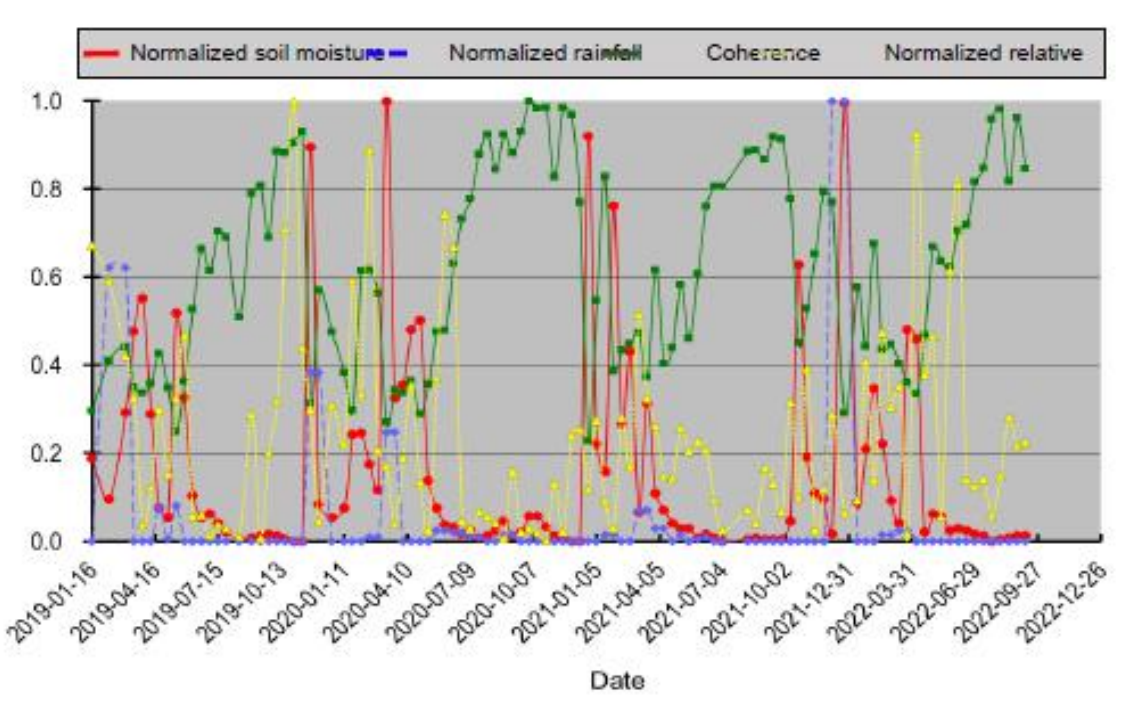


Figure B.6 Santa Barbara site: Normalized soil moisture, rainfall, relative humidity and signal coherence as a function of time

## B.5.2 Data Availability

The region is located in Colorado state and has access to Sentinel-1A and Sentinel-1B data. The data is typically collected with a 12-day interval and analyzed within the same orbit to minimize errors. The datasets for this analysis were obtained from the Sentinel constellation and were downloaded using the Sentinel-1 EU datahub and the Alaska Satellite Facility (ASF) (ASF, 2023). The study utilizes data starting January 9, 2019 and the final acquisition was taken on December 19 2022. Throughout the analysis period, Sentinel 1-A data is accessible, while Sentinel 1-B data is available until December 2021, after which it becomes unavailable. Table B.5 shows the data used for the analysis.

## B.5.3 CCD Analysis

The analysis was based on a large stack of data, and the timeline method was used to perform the CCD analysis. Coherence data from each map was converted to text format, along with the corresponding coordinates. A total number of 90 CCD analyses are conducted in the CCD timeline feature. The soil moisture sensor covered a larger area than the SAR analysis resolution, resulting in numerous data points for each CCD analysis that covered the region based on the sensor coordinates.

The mean and standard deviation of coherence readings were calculated based on the sensor coordinates to obtain a reliable interpretation of coherence over the sensor's coverage area. These readings were tabulated by satellite, orbit direction, and acquisition date and normalized in the range 0 to 1. Similarly, the NOAA sensor's relative humidity, precipitation, and soil moisture content are tabulated by property and acquisition date.

Table B.5 Sentinel-1 Data used for Cortez CCD analysis

Data Set	CCD Timeline
Sentinel-1A Orbit-1	01/09/2019 to 12/31/2022
Sentinel-1B Orbit-2	01/10/2019 to 12/13/2021
Sentinel-1B Orbit-2	05/15/2019 to 12/18/2021

Since the C-band sensor has low penetration power, only the top 5 cm soil layer data was used for the soil moisture analysis. The soil moisture data represents the average hourly measurements taken throughout the day. The NOAA data have also been normalized, each in the range 0-1.

Since coherence represents a change of the signal between two acquisitions, it is necessary to correlate the coherence to the change in moisture content in developing the model. Furthermore, both the coherence and soil moisture change values are normalized in the range 0 to 1, grouped in increments of 0.1, and the average value in each group is computed.

#### B.5.4 Discussion

The relationship between normalized moisture change, normalized coherence and rainfall is shown in Figure B.7, Figure B.8 and Figure B.9. The graphs represent the data from both orbits and show that the rainfall is influencing the soil moisture. The coherence is highest when the rainfall and soil moisture is lowest. This condition is observed in both orbits, suggesting the relationship is directly related and can be observed in regions with low vegetation. Unlike the other site studies there are some periods when this relationship is not observed in this site. This loss of coherence could be due to layovering and shadowing conditions that are influencing the results.

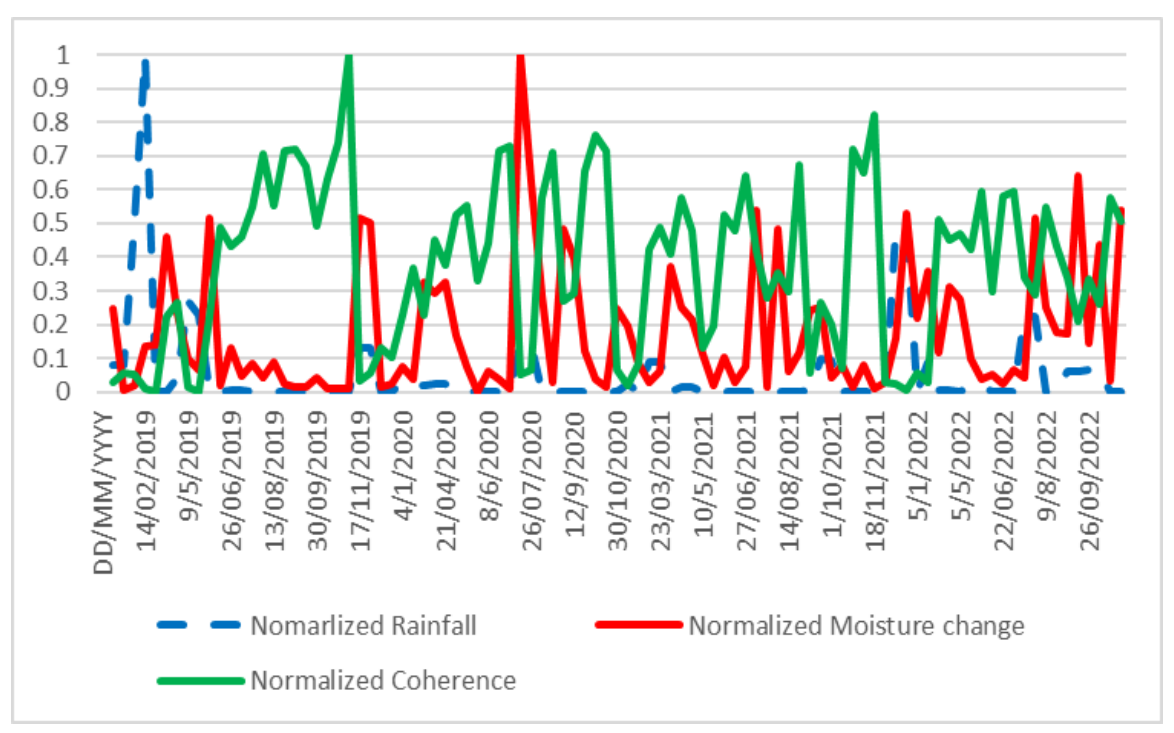


Figure B.7 The relationship between normalized moisture changes, coherence, and rainfall for Cortez Sentinel-1A orbit-1 data.

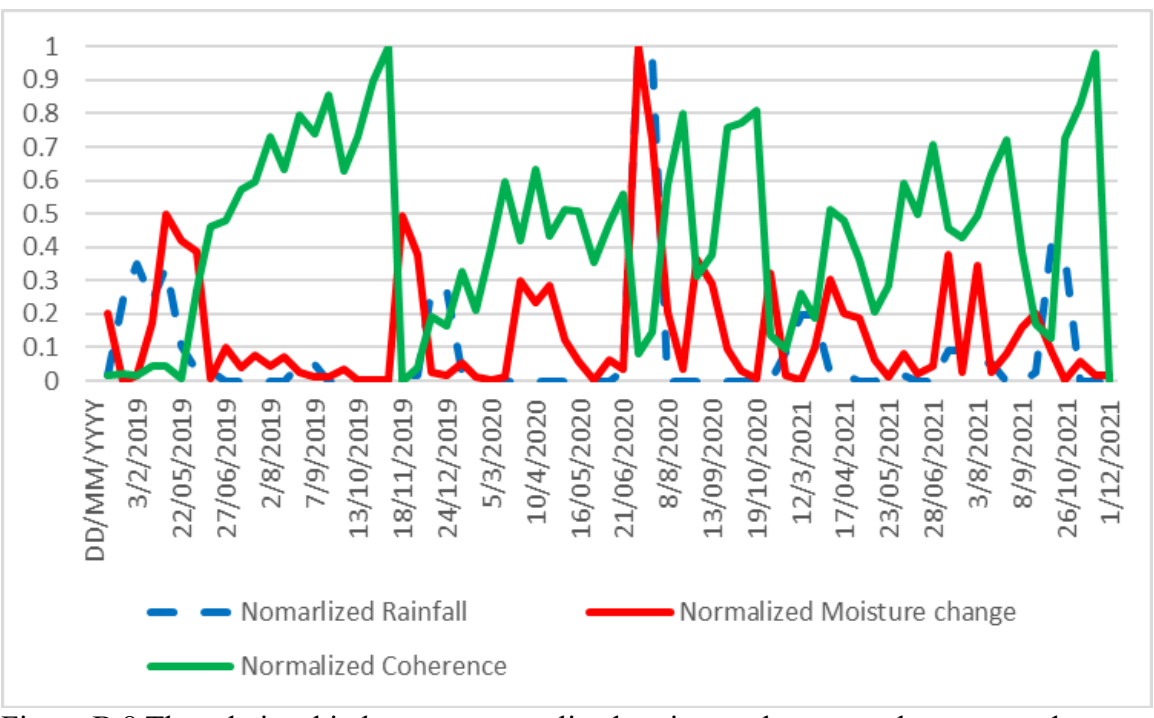


Figure B.8 The relationship between normalized moisture changes, coherence, and rainfall for Cortez Sentinel-1B orbit-1 data.

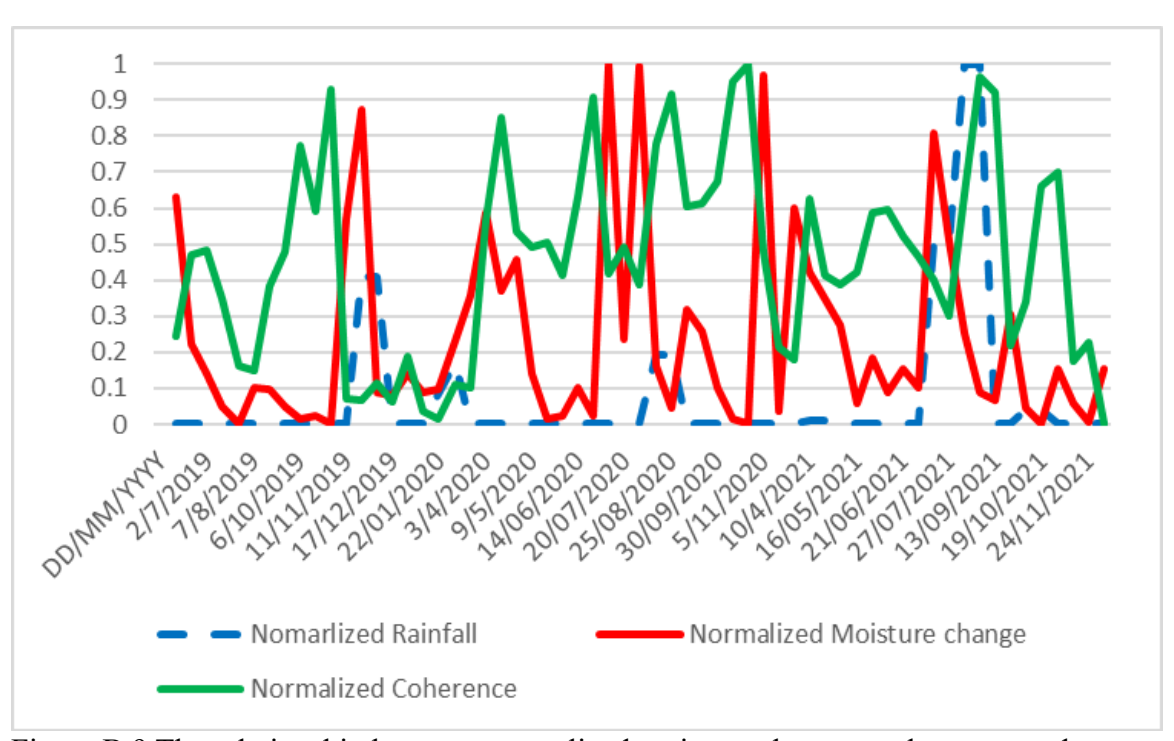


Figure B.9 The relationship between normalized moisture changes, coherence, and rainfall for Cortez Sentinel-1B orbit-2 data.

## B.6 Chatham, MI

## B.6.1 Site Description

The sensors under investigation are located in Northern Michigan at latitude longitude (46.33, -86.92), encompassing 1 km<sup>2</sup>. The sensor's location is approximately 2 miles from the town center. The sensors are located in high-vegetation areas with dense forests surrounding them. The region has the top 2 inches of decomposed plant material and sandy loam underneath it. It experiences an annual precipitation of 28 to 37 inches and frost-free periods of 80 to 160 days. The region is moderately well-drained and falls under the low runoff class.

### B.6.2 Data Availability

The region is close to the Canadian border and has access to Sentinel-1A data. The data is typically collected with a 12-day interval and analyzed within the same orbit to minimize errors. The datasets for this analysis were obtained from the Sentinel constellation and were downloaded using the Sentinel-1 EU datahub and the Alaska Satellite Facility (ASF) (ASF, 2023). The study utilizes data starting January 5, 2019. Throughout the analysis, Sentinel 1-A data is accessible.

#### B.6.3 CCD Analysis

The CCD analysis indicates consistently low coherence and is not attributed to change in moisture levels. This outcome is primarily attributed to the dense vegetation cover surrounding the area, which impedes the Synthetic Aperture Radar (SAR) signal from effectively interacting with the ground surface. As a result, the ability to monitor

ground changes in this region is significantly constrained. Consequently, further research efforts focusing on this region have been suspended due to these limitations.

## B.7 Sandstone, MN

## **B.7.1 Site Description**

The sensors under investigation are located in eastern Minnesota close to the border of Wisconsin at latitude longitude (46.11, -92.99) encompassing 1 km². The sensor's location is approximately 4 miles from the town center. The sensors are located in high-vegetation areas with dense forests surrounding them. The region has the top 11 inches of silt loam with rest of soil profile being fine sandy loam. It experiences an annual precipitation of 27 to 36 inches and frost-free periods of 80 to 150 days. The region is poorly drained and falls under low runoff class. This region is similar to Site B.6 Chatham, MI

## B.7.2 Data Availability

The region is located in the northern United States and has access to Sentinel-1A data. The data is typically collected with a 12-day interval and analyzed within the same orbit to minimize errors. The datasets for this analysis were obtained from the Sentinel constellation and downloaded using the Sentinel-1 EU datahub and the Alaska Satellite Facility (ASF) (ASF, 2023). The study utilizes data starting January 5, 2019. Throughout the analysis, Sentinel 1-A data is accessible.

## B.7.3 CCD analysis

The CCD analysis indicates consistently low coherence and is not attributed to

changes in moisture levels. This outcome is primarily attributed to the dense vegetation surrounding the area, which impedes the Synthetic Aperture Radar (SAR) signal from effectively interacting with the ground surface. As a result, the ability to monitor ground changes in this region is significantly constrained. Consequently, further research efforts focusing on this region have been suspended due to these limitations.

# B.8 Columbia, SC

## **B.8.1 Site Description**

The region under investigation is located in South Carolina at latitude and longitude (33.9359, -81.02877), covering roughly .04 km2. Unlike previous sites that use NOAA's USCRN sensors, the exact location of the sensors used is not uncertain. The region is located 4 miles from the UofSC engineering building and is under the purview of SCDNR. The region experiences roughly 26 to 74 inches of mean annual precipitation and 210 to 2300 days of free periods. The region is located in flood plains and is classified as a floodplain forest protected from flooding during the growing season. The top 10 inches of soil is silt loam, and the region is well-drained and in a low runoff class.

## B.8.2 Data Availability

The region is located in the eastern U.S. and has access to a single orbit of Sentinel-1A data. The data is typically collected with a 12-day interval for each orbit and analyzed within the same orbit to minimize errors. The datasets for this analysis were obtained from the Sentinel constellation and were downloaded using the Sentinel-1 EU datahub and the Alaska Satellite Facility (ASF) (ASF, 2023). The study utilizes data from January 4, 2019, until July 29, 2022. The secondary orbit of Sentinel-1A data is available

only till December 2022.

## B.8.3 Equipment

This analysis employed a comprehensive set of weather monitoring equipment to evaluate the impact of various parameters on SAR coherence. The experimental setup featured a primary sensor functioning as the central hub, complemented by six auxiliary sensors. The primary sensor integrated multiple environmental measurement devices, including a leaf wetness smart sensor, a smart soil moisture sensor, and a Davis anemometer, rain gauge and PAR (photosynthetically active radiation) light sensor. Several of these sensors were multi-functional; for instance, the smart soil moisture sensor measured soil moisture, temperature, and electrical conductivity. Collectively, these sensors monitored key parameters such as leaf wetness, rainfall, wind speed, soil moisture, soil temperature, and PAR. Figure B.10

#### B.8.4 Procedure

The primary and auxiliary sensors were strategically positioned to ensure minimal interference with coherence resolution (15 meters). Each auxiliary sensor was placed at least 60 meters apart. These sensors transmitted their data to the primary sensor, which acted as the data hub. The spatial arrangement of the sensors is depicted in Figure B.11, where the triangle represents the main sensor, and the surrounding black boxes represent the auxiliary sensors. Since the location of the soil moisture content sensor is known, the coordinates' coherence is correlated with the sensor data. Additional factors like the height of the vegetation are also included to develop an efficient model. Since the exact time of satellite pass is known we can use it to the moisture content in the soil at the time



Figure B.10 The equipment deployed in the site (a) Remote Sensing Station (b) Solar panel (c) Leaf wetness smart sensor (d) Repeater (e) Modulator (f) Light Sensor (g) Soil moisture sensor (h) Soil moisture sensor (i) Solar Radiation Shield (j) Runtime Smart Sensor (k) Soil moisture (l) Davis Anemometer (m) Rain Gauge



Figure B.11 The moisture content sensors are denoted by the black boxed numbers, and the middle red triangle represents the main sensor

of passing enabling us to get accurate relationship between radar backscatter and soil moisture.

## B.8.5 CCD Analysis

The analysis was based on a large stack of data, and the timeline method was used to perform the CCD analysis. Coherence data from each map was converted to text format, along with the corresponding coordinates. A total number of 60 CCD analyses are conducted in the CCD timeline feature. The soil moisture sensors cover  $15m^2$  area and are placed in the coordinates shown in Table B.6. These coordinates are based on the SAR analysis resolution, resulting in numerous data points for the sensor coordinates.

The mean and standard deviation of coherence readings were calculated based on the sensor coordinates to obtain a reliable interpretation of coherence over the sensor's coverage area. These readings were tabulated by satellite, orbit direction, and acquisition date and normalized in the range 0 to 1.

#### B.8.6 Discussion

The results from the analysis are shown in Figure B.12. The data shows the relationship between normalized moisture content, coherence, and rainfall for the main sensor. These results are highlights of the study, with the rest of the sensors and model development conducted by other team members. The graph shows a relationship between sensor data and coherence, but the relationship is lost in the final part of the analysis. This is attributed to a change in vegetation, which reduces the backscattering influence.

During the early stages, although vegetation is present in the region, its density is considered low, which changed during the mid time period, affecting data acquisition.

Table B.6 Shows the coordinates of the sensor

Serial number	Location(lat/long)
Main	33.9359/-81.0288
1	33.9354/-81.0292
2	33.9358/-81.0292
3	33.9364/-81.0295
4	33.9364/-81.0290
5	33.9364/-81.0283
6	33.9354/-81.0281

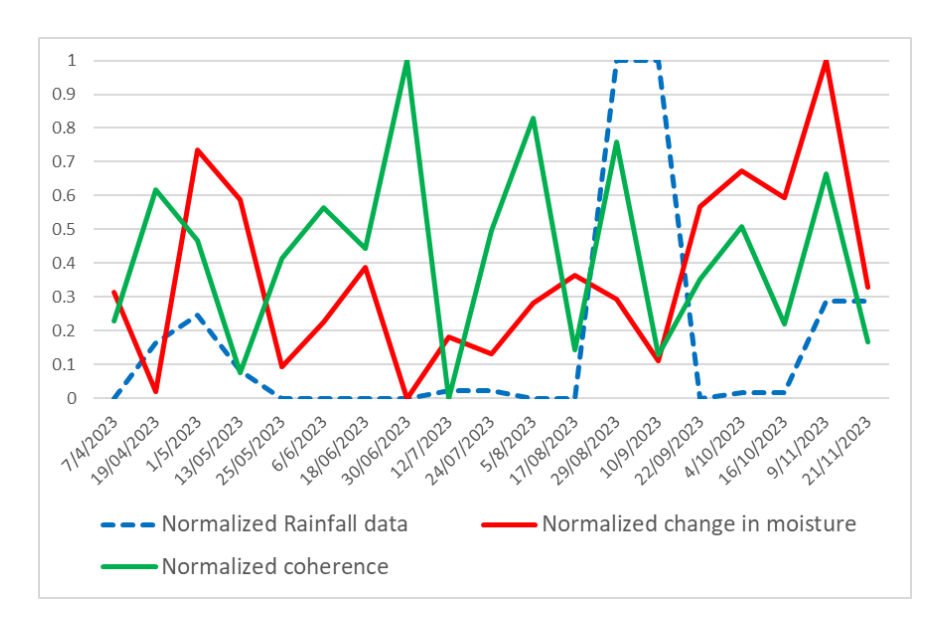


Figure B.12 Shows the relationship between normalized coherence, rainfall and soil moisture.

## APPENDIX C: MATHEMATICAL BACKGROUND

This chapter describes the mathematical background for the SAR methodology in Sections 5.1-5.7 used for geohazard monitoring, as adopted in this work. The post-processing The MTI used for site mobilization identification and soil moisture change measurement have some common steps. These steps are data preparation, interferometric formation, coherence generation, and geocoding. The multi-temporal techniques used for geohazard monitoring utilize DInSAR analysis to generate the displacement phase; for the purpose of this document, we will call DInSAR an InSAR or Interferogram. A DInSAR analysis is an interferogram with the terrain phase removed, but due to the high use of DInSAR analysis over InSAR analysis, the term InSAR became a synonym with DInSAR and replaced it in the lexicon. This document uses the term InSAR when it describes DInSAR procedure.

Unlike conventional InSAR, which utilizes consecutive image pairs, multitemporal techniques pair images based on lower temporal and spatial baselines. This
chapter explains the workflow for the MTI techniques PSInSAR and SBAS analysis.
These two multi-temporal SAR techniques are utilized to overcome the limitations of
deformation analysis from InSAR analysis. Each technique has unique advantages and
disadvantages. PSInSAR effectively measures deformations with large quantities of
coherent or highly reflective surfaces. SBAS can generate displacement trend data based
on distributed scatterers. Two post-processing methods are developed to identify regions

showing progressively increasing activity and sudden increase in activity. Coherence generation is a by-product of InSAR generation, but coherence is needed from consecutive acquisitions for moisture content-model generation. The CCD technique generates coherence in these conditions, and the math behind it is described in this chapter.

# C.1 Data Preparation of Sentinel-1 (TOPS data type)

Sentinel-1 satellite uses Interferometric Wide (IW) swath mode for scanning the surface to acquire data of 250km in length and width with spatial resolution of 3.5m X 22m and pixel spacing of 2.3m X 14.1m [112]. Spatial resolution is the minimum distance at which the radar can distinguish between two closely spaced scatterers with equal-strength responses. The pixel spacing refers to the distance between adjacent pixels in an image measured in meters. IW mode image consists of three sub-swaths acquired using the TOPS or TOPSAR technique. It stands for Terrain Observation by Progressive Scans, where the sensor scans backward to forward in the azimuth direction for each burst, resulting in a near-uniform signal-to-noise ratio (Figure C.1). This method of scanning is an improvement on the conventional ScanSAR [113]. ScanSAR method of acquiring data has limitations due to calibration errors and varying resolution while scanning the target, which is not present in TOPS [114].

Sentinel-1 SAR data from the data hubs can be divided into three levels.

Level-0 SAR products consist of unfocused and compressed SAR raw data. This data includes internal calibration and echo sources and is unusable without additional focusing.

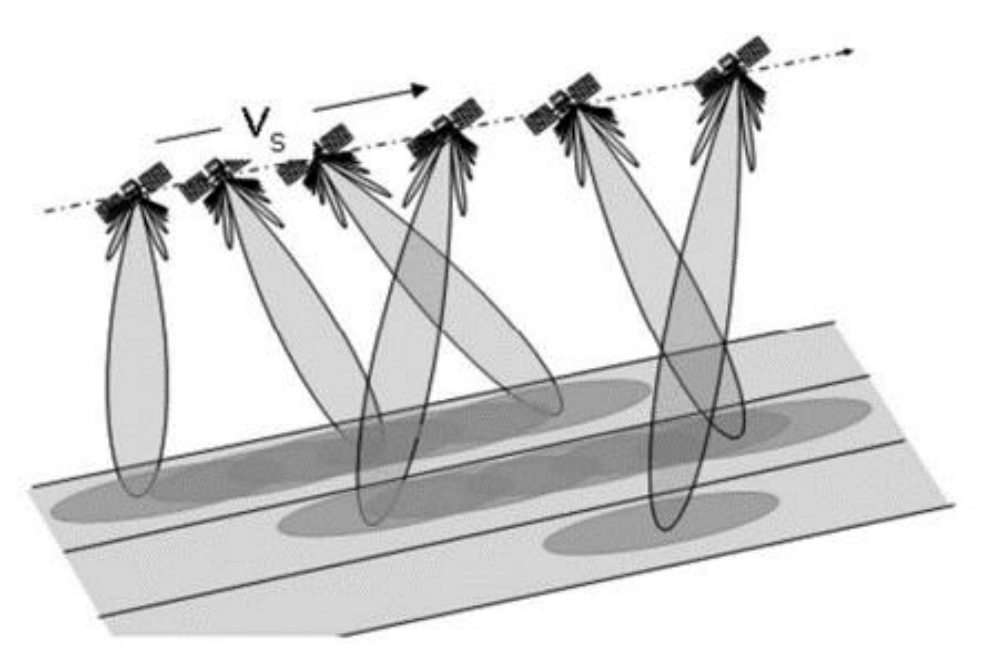


Figure C.1 Show the three sub-swaths in TOPSAR acquisition

<u>Level-1</u> data types are divided into two types: complex images and detected images. The complex data has phase and intensity data, while the detected image uses intensity data for single-image analysis.

<u>Level-2</u> data are derived from level-1 data and are geolocated with specific applications like obtaining ocean wind and wave currents data. These data are derived after being internally processed by the data provider.

Type-1 SAR data are used in this thesis for SAR analysis. Single Look Complex falls into the complex image data type. These images are focused and geo-referenced with full available signal bandwidth and complex samples preserving the phase information. The phase, which is evenly spread out, does not include valuable information about the target. While the phase may appear random, it is a deterministic and repeated assessment of random internal structure within a pixel [1]. The phase is essential in SAR interferometry as it involves the coherent combination of the phase of multiple SAR images. The equation can express each SLC SAR image Z [1].

$$Z(r,a) = A(r,a)e^{-i\phi(r,a)}$$
(12)

Where, "(r, a)" are the image coordinates in range and azimuth; "A" is the amplitude, " $\phi$ " is the phase

Statistically, an SLC image must follow the following conditions.

The measured complex radar reflectivity consists of two components: the real part  $Z_r = A \cos \emptyset$  and the imaginary part  $Z_i = A \sin \emptyset$ . These parts are statistically independent Gaussian random variables with a mean of zero and a variance of  $\sigma/2$ . Where  $\sigma$  is the radar reflectivity. Their combined probability density function (PDF) is:

$$pdf(Z_r Z_i) = \frac{1}{\pi \sigma} e^{-\left(\frac{Z_r^2 + Z_i^2}{\sigma}\right)}$$
(13)

The phase that has been observed is distributed uniformly over the interval  $[0,2\pi]$ .

The other type of level-1 SAR data is detected images. Ground Range Detected falls into the detected image data type. These images are focused and projected onto the ellipsoid of Earth. The phase from a single SAR image is not useful, and GRD image formats remove phase information that is favored for human viewing. These images are created by multiplying a complex image with its conjugate. The intensity image (*I*) formed is of (Equation 14). It is directly proportional to the backscattering signal.

$$I = A^2 \tag{14}$$

For obtaining coherence and displacement level-1 SLC images are used. These images have the phase components to measure the displacement and also the amplitude information to measure the backscattering strength. Each SLC image looks like (Figure C.2). It is an image with a large "salt" and "pepper" look. Additional preparatory steps are performed to accurately measure deformations and to better view the image.

#### C.1.1 Polarization Selection

Sentinel-1 is a dual-polarization sensor that can transmit radar pulses in a single polarization and receive the signal in the same or perpendicular polarization. For the analysis conducted in this thesis, VV polarization has been chosen for its ability to penetrate the surface.

## C.1.2 Multi-looking

Each SAR image looks like (Figure C.3a). These distorted dimensions are due to

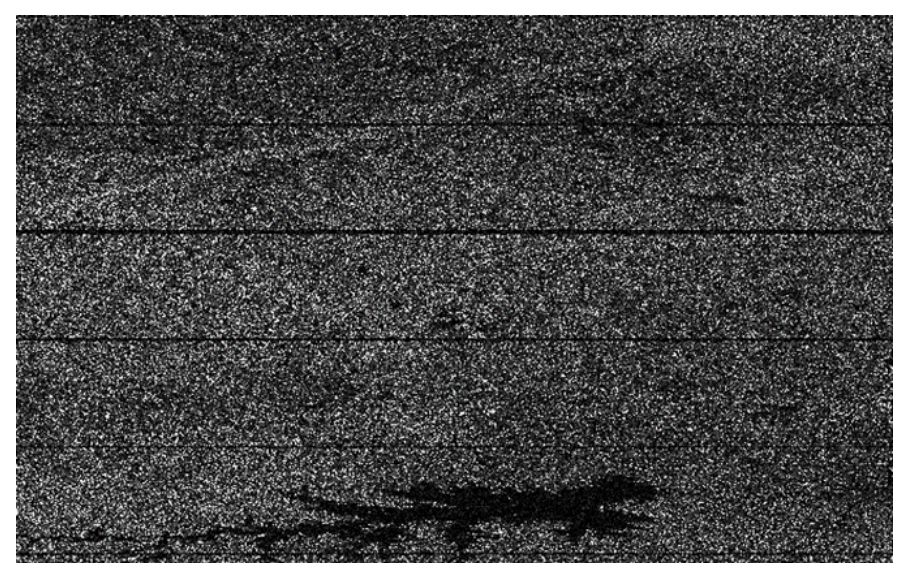


Figure C.2 Shows part of the unprocessed SAR image of the city Columbia, SC. The image shows a distinct salt and pepper look separated by multiple swaths

the side-looking mode of acquisition. The process of converting the image into normal image pixels (Figure C.3b) is called multi-looking [115]. Multilooking is a process that enhances the radiometric accuracy and resolution of SAR data by sacrificing spatial resolution. This can be accomplished during synthetic aperture radar (SAR) processing by partitioning the synthetic aperture into N segments and generating N lower-resolution cells called "looks"; these resolution cells are then averaged incoherently. The underlying assumption is that the separate looks represent the identical underlying radar reflectivity, which is not always accurate in practice. For sentinel-1 images, the range dimension is multi-looked at a factor of 4 for every azimuth multi-looking factor [116]. SAR images can be cut into smaller subsets following the multi-looking process as the complex images are converted to constant-resolution images [1].

#### C.1.3 Data Selection

Some areas of interest have access to data from several orbits (ascending and descending) and satellites (sentinel-1A and Sentinel-1B). The data from multiple orbits should not be used in the same analysis as this would increase the spatial baseline.

Although errors due to spatial baseline can be corrected, the large increase in the special baseline when different satellite orbits are used is beyond the existing capabilities. To prevent errors in the analysis, the data from these orbits and satellites are sorted so that all the SAR images are grouped according to their respective look angle. The sorting is done based on two factors: the first is that each satellite passes over the same region every 12 days, and the second is the look angles.

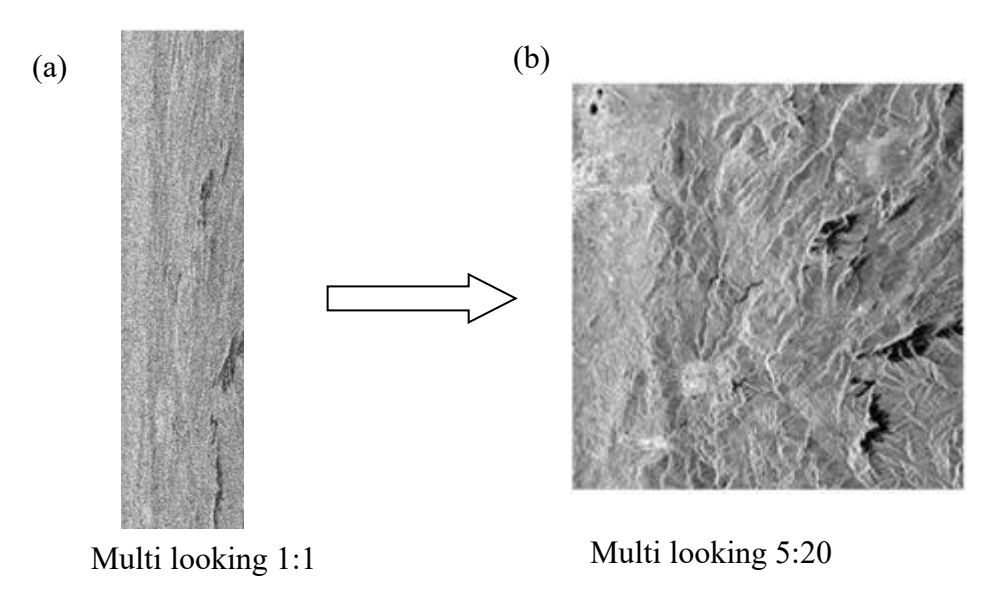


Figure C.3 (a) Shows the SAR image that is not multi-looked. (b) Shows the multilooked image (a) to a factor of 5:20 [1]

# C.2 SAR Interferogram

SAR Interferometry (InSAR) is a method that utilizes the phase differences of at least two SAR images obtained from distinct orbit positions and/or at separate points in time. The obtained interferogram data can quantify many geophysical parameters, including topography, surface deformations, glacier movements, vegetation characteristics, etc. SAR interferometry is widely acknowledged as a highly effective technique for mapping the Earth's terrain, specifically for generating Digital Elevation Models (DEM). The Differential InSAR technique is a distinctive approach used to identify and record surface movements across time and space, with a high accuracy ranging from centimeters to even millimeters [14].

This thesis describes the core InSAR analysis used in multi-temporal analysis and explains the steps required for each analysis. The criteria for an image pair to be able to generate an interferogram depends on the baseline between them. The baseline is the distance or time between two acquisitions. If it is distance, it's called the spatial baseline, and the temporal baseline is time. For an interferogram to be viable, we need to first obtain a critical baseline in a perpendicular direction. In interferometry, there exists a critical baseline over which the generated interferogram will be pure noise.

Interferometry becomes impossible as the difference in viewing angle becomes too great to prevent the overlapping of the imaged ground spectra. This critical baseline is based on the ground resolution cell, the radar frequency, and the sensor-to-target distance. The critical baseline for Sentinel-1 interferometry is approximately 5 Km, as determined by Equation (15). In practice, anything more than 3/4 of the critical baseline produces

significant noise. Interferometry can only be used for point-like targets when the baseline is more significant than this [1].

$$B_{perp}^{crit} = \frac{H.BW_r}{f} \frac{\sin \theta}{\cos^2 \theta} \tag{15}$$

Where,

 $B_{perp}^{crit}$  is the critical baseline in the perpendicular direction; H is the satellite altitude;  $BW_r$  is the range bandwidth or inverse of the duration of the pulse; f is the frequency of the radar.

Once the baseline between two images is within the limit, we can perform the following steps in order to develop an interferogram.

### C.2.1 Coregistration

Co-registration overlays two Synthetic Aperture Radar (SAR) images (master and slave) that share the same orbit and acquisition mode in slant range geometry. This step ensures that the scatterer located on the ground contributes to the relevant pixel in both the master and slave images.

There are two types of co-registration: conventional co-registration and DEM-assisted co-registration.

Conventional co-registration can be divided into two steps. The first step is coarse co-registration. A cross-correlation method matches the corresponding pixels in the picture pair after identifying tie points within the imaged area. Tie points refer to specific characteristics on the ground that correlate to pixels in the image pair (similar to GCP)

points explained in 5.x). A portion of the master image is chosen by selecting a window. The pixels in the master image within this window are compared with the windows of the exact dimensions in the slave image. Thus, the azimuth and ground range offsets of the relevant pixels are acquired. The average azimuth and range offsets of the pixels can be calculated by matching all the pixels within the windows. According to the calculation result, the slave image can be adjusted to align with the position of the master picture. The second stage in the conventional co-registration process is known as fine coregistration. Many pixel pairs that correspond to each other are selected on the master and slave images. A second-order polynomial can be derived from the azimuth and range coordinates of the pixels on the master image and the coarse coordinate offsets of the corresponding pixels on the slave image. This polynomial can then estimate a more accurate coordinate offset for the pixel pair. Consequently, instead of calculating the average azimuth and range offsets between the pixels during coarse co-registration, a mathematical solution is derived to align the SLC image pair during fine co-registration precisely [117].

DEM-assisted co-registration follows a more straightforward approach. This method of co-registration incorporates elevation data obtained from reference DEM to enhance the accuracy of predicting the offset vectors. The offset vectors are calculated pixel-by-pixel by performing geocoding on the master image and then applying inverse geocoding processes on the slave reference geometry to determine the corresponding locations using orbit data [118].

The conventional method of co-registration does not require external input(external DEM), but regions with rough topography and long baselines produce a

higher number of misalignments. Since this thesis works on regions with rough topography DEM assisted co-registration is preferred. The preferred DEM for the co-registration is the Shuttle Radar Topography Mission (SRTM) with a resolution of 90 X 90 m (outside the U.S.) and a height accuracy of 15m. The slave image is resampled onto the master image at the end of the co-registration step using the 4<sup>th</sup> cubic convolution. According to [119] 4<sup>th</sup> cubic convolution produces lower interpolation errors than alternative methods like nearest neighbor and piecewise linear. These parameters of the DEM and resampling method will dictate the spatial resolution of the analysis conducted in this thesis. The grid size of 15m used as the resolution is also generated due to these factors. Additional analytics of the process are discussed further by [118], where both co-registration methods are tested on real-world cases with multiple bands of radar data.

#### C.2.2 Interferometric Formation

Following the process of coregistration and resampling, the pixels in the slave image are now aligned with the corresponding pixels in the master image, sharing the exact coordinates [62]. As each pixel is represented as a complex number, an interferogram can be created by multiplying the complex numbers of the pixels in the master image with the conjugate complex numbers of the corresponding pixels in the slave image [1].

$$Z_{int} = Z_1 Z_2^* = A_1 A_2 e^{i(\phi_1 - \phi_2)} = I_{int} e^{i\phi_{int}}$$
(16)

Where, " $Z_{int}$ " is the complex interferogram; " $\phi_{int}$ " is the interferometric phase; " $I_{int} = A_1 A_2$ " is the interferometric magnitude (Equation 17) describes the

interferometric phase in conditions where the effective baseline is zero and the observed surface is flat.

$$\phi_{int} = \frac{4\pi}{\lambda} (R_1 - R_2) = \frac{4\pi}{\lambda} (\Delta R)$$
 (17)

Where, " $R_n$ " is the slant range distance of acquisition "n"; " $\Delta R$ " is the Range difference.

This demonstrates that variations in the distance between the scatterer and the radar during the time interval between repeat-pass acquisitions significantly impact the interferometric phase. The interferometric phase is highly sensitive to  $\Delta R$ , with a range difference of half the wavelength, causing a  $2\pi$  phase change, resulting in one fringe on the interferogram. The range difference may arise due to two potential causes: the motion of the scatterers during the acquisitions in interferometry, which forms the foundation of Differential InSAR (DInSAR), or the difference in viewing angles resulting from the interferometric baseline [62].

<u>Flat earth correction</u> Due to the curvature of the Earth, objects on the ground at the same elevation would generate a phase difference between the two radar acquisitions. This phase component in the interferogram's phase is called the flat earth phase and the process is called flattening. Estimating the baseline between the two radar antennas is essential to remove the flat earth phase. We can determine the baseline using the precise location of radar antennas obtained through orbit files of both satellite acquisitions. This processing step is called flattening. The flat earth phase can be computed using Equation 18.

$$\phi_{flat\ earth} = \frac{4\pi}{\lambda} \frac{B_{perp} \Delta R}{R_1 t a n \theta}$$
 (18)

Based on (Equations (16)(17)(18)) we can obtain the combined interferometric phase in conditions with an effective baseline as (Equation 19)

$$\phi_{int} = \frac{4\pi}{\lambda} \frac{B_{perp} \Delta R}{R_1 t a n \theta} + \frac{4\pi}{\lambda} \frac{B_{perp} h}{R_1 s i n \theta} + \frac{4\pi}{\lambda} d + \alpha_h + \alpha_t + n$$
(19)

Where, d is the displacement of the observed region in a satellite line of sight; h is the terrain variation element that incorporates the changing height of the area under observation.  $\alpha_h$  is the phase difference in atmospheric components influenced by topography and is caused by atmospheric stratification;  $\alpha_t$  is the phase difference in atmospheric components influenced by turbulence in the troposphere; n is the phase decorrelation due to the geometry of acquisition and time.

All phase contributions in Equation 19 are present and combined together in multi-temporal SAR interferograms. Equation 19 offers a systematic approach to unravel distinct phase contributions and is an important equation related to InSAR [62]. Atmospheric phase delay correction The precision of surface displacements acquired from InSAR can be significantly impacted by the spatiotemporal fluctuations of atmospheric (tropospheric) water vapor( $\alpha_t$ ), leading to errors of a magnitude similar to those caused by crustal deformation. Two atmospheric filtration methods are available to reduce the error due to the tropospheric atmospheric component. MODIS, short for Moderate Resolution Imaging Spectroradiometer, is a crucial device found on both the Terra and Aqua satellites. MODIS sensors capture images of the entire Earth's surface at intervals of 1 to 2 days. They collect data in 36 spectral bands based on different wavelengths. MODIS quantifies the characteristics of aerosols, which are minuscule liquid or solid particles in the atmosphere. MODIS assists scientists in quantifying the quantity of water vapor in the atmosphere and the arrangement of temperature and water vapor at different heights of the atmosphere. These observations are used as a dynamic filter for SAR analysis [120].

GACOS, Short for Generic Atmospheric Correction Online Service, is a comprehensive InSAR atmospheric correction tool that uses the tropospheric decomposition model (ITD) to distinguish between stratified and turbulent signals in tropospheric total delays. The delay maps are created by integrating operational high-resolution European Centre for Medium-Range Weather Forecasts (ECMWF) data and the precise and continuous pointwise measurements obtained from GPS with appropriate weighting. These maps correct InSAR observations that arise due to water vapor delay and are updated every 6 hrs with a resolution in 11.1 km (6.9 miles) based on the available ECMWF sensors data [121].

Several studies [122] [123] [124] into both methods showed GACOS outperformed MODIS in most conditions. The GACOS atmospheric model was used in all the cases in this thesis. The efficiency of each atmospheric model was not tested for this thesis as local on-site data was not available for most of the test cases.

#### C.2.3 Speckle Filtering

Phase filtering has become a critical step in the processing of InSAR data in order

to decrease the complexity of phase unwrapping and increase the precision of the unwrapped phase. The ideal phase filter would reduce phase residues without losing phase fringe information. The produced interferogram undergoes filtering following flattening (flat earth phase removal), topographic phase removal, and atmospheric adjustment to enhance the accuracy and precision of potentially inaccurate pixels.

Various filters, such as the Goldstein, Boxcar, or Adaptive Non-Local filter, are available for speckle reduction [125].

This thesis uses modified Goldstein adaptive filtering for phase filtering because of its noise reduction and quick operation capacity. Goldstein's approach suppresses noise by analyzing usable signals and noise characteristics [126]. The conventional Goldstein filter works by multiplying the Fourier spectrum of an interferometric patch by its smoothed absolute value to the power of the exponent  $\alpha$ . The filter's parameter  $\alpha$  is arbitrarily selected from zero to one, and it significantly influences the filter's performance [127]. An issue arises when applying a high parameter value with the conventional Goldstein radar interferogram filter. Subtracting the filtered interferogram from the unfiltered one reveals a residual systematic phase trend, which suggests a decrease in resolution in the filtered phase. To overcome this problem, the absolute value of  $\alpha$  is replaced with an adaptive filter  $(1 - \bar{\gamma})$  based on the mean coherence value  $(\bar{\gamma})$  of the region [128]. The filtered interferogram using the modified Goldstein approach can be expressed as

$$H(r,a) = S\{|Z(r,a)|\}^{1-\overline{\gamma}}.Z(r,a)$$
 (20)

Where, "H(r, a)" is the filtered interferogram; "(r, a)" represent the spatial frequencies in range and azimuth direction; "Z(r, a)" is the Fourier spectrum of each filtering window in range and azimuth direction. " $S\{.\}$ " is the smoothing operator.

The filter parameter is automatically configured depending on the mean coherence value, requiring no additional input. This adjustment adjusts the Goldstein interferogram filter to avoid excessive filtering in regions with high coherence (less noise), while allowing for stronger filtering in regions with low coherence (high noise). Therefore, the reduction in resolution in the interferogram caused by filtering can be minimized in regions with strong coherence [128].

# C.2.4 Phase Unwrapping

The interferogram's phase of two SAR images can only be measured to a modulo  $2\pi$  value. Phase unwrapping (PU) aims to recover the integer number of cycles n that must be added to the wrapped phase  $\phi$  to obtain the unambiguous phase value  $\Psi$  for each resolution cell in the image.

$$\Psi = \phi + 2\pi . n \tag{21}$$

The phase resets whenever the phase change exceeds  $2\pi$ , and the cycle restarts. The restart is seen in the interferogram as multiple color fringes. Phase unwrapping is the procedure that resolves the ambiguity of a  $2\pi$  cycle. Resolving the ambiguity involves adding or subtracting an integer multiple of  $2\pi$  from the wrapped phase. The accurate phase is determined using numerical analysis or geometric techniques to get the corresponding integer period.

Most PU algorithms assume that the true unwrapped phase field is "smooth" and

"slowly" varying. More specifically, neighboring phase values are assumed to be within a half cycle ( $\pi$  radians). While most image pixels tend to support this idea, discrepancies arise when certain phase discontinuities occur (i.e., absolute phase changes between nearby pixels higher than  $\pi$  radians). Various approaches have been implemented to address phase discontinuities, and distinct algorithms have been devised. In this thesis, Delaunay Minimum Cost Flow (MCF) approach is used for phase unwrapping. Delaunay MCF is further explored in [129] [130] [131] Its advantages, when used for surface deformation, make it preferable to alternatives.

## C.3 CCD

Coherence change detection is a method of generating coherence between two SAR images. Coherence, interferometric coherence, or magnitude of coherence measures the similarity between the two acquired SAR images. It is calculated as the complex correlation coefficient between the two interfering SAR images [62].

To generate a coherence map of the area of interest, CCD analysis follows the following steps on two SAR images with the same polarization and look angle.

Co-registration > Interferometric formation > Coherence generation

The above steps are similar to those used to generate an interferogram, except for the coherence generation step. This is partly because coherence is a byproduct of the process and is used to observe an interferogram's signal-to-noise ratio (SNR). However, coherence has uses beyond the SNR in this thesis.

The Equation (22) can describe the coherence between two SAR images Equation (16) from previously used parameters.

$$\bar{\gamma} = \frac{|\sum Z_1 Z_2^*|}{\sqrt{\sum |Z_1|^2 \sum |Z_2|^2}}$$
(22)

Where,  $\bar{\gamma}$  is the complex interferometric coherence and the magnitude of coherence. In practice, Coherence maps are produced by substituting the spatial average in the equation with the "sampled estimator" and calculating for each image pixel, which is equivalent to Equation 23.

$$|\bar{\gamma}| = \frac{|\sum_{k=1}^{N} Z_{1k} Z_{2k}^*|}{\sqrt{\sum_{k=1}^{N} |Z_{1k}|^2 \sum_{k=1}^{N} |Z_{2k}|^2}}$$
(23)

The summation is extended to a suitable 2D window N. The numerator in the equation is just a complex average of the SAR interferogram, which is why coherence is considered a byproduct of an interferogram.

### C.3.1 Processing Coherence Data for Moisture Content Model Development

The results from the analysis are correlated with normalized data from soil moisture, rainfall data and relative humidity. This data is used for soil moisture and coherence model development not part of this thesis.

#### C.4 Multi-Temporal SAR

DInSAR analysis can detect surface deformation in the satellite line of sight. However, the DInSAR technique is affected by atmospheric conditions and other error sources, as mentioned in 2.7. This thesis uses two multi-temporal SAR techniques to obtain deformation data that negates the limitations of DInSAR. These techniques are further used in post-processing methods to overcome some limitations of using large stacks of data while keeping the advantages of MT-InSAR techniques over DInSAR.

Both MTI techniques follow the workflow mentioned in Figure C.4 However, the criteria differ in the connection graph and 1<sup>st</sup> inversion stages.

## C.4.1 Data Preparation

The Interferometric datasets used for MTInSAR in this thesis were collected from Sentinel-1A and Sentinel-1B, using 25 SAR images in each implementation example. The data are 12 days apart in most cases, with few exceptions due to satellite maintenance and extreme weather affecting satellite acquisitions. Each MTInSAR analysis requires 20 SAR image stacks for deformation recognition. This thesis uses 25 SAR image stacks to reduce the number of false positives. Further, an increase in the number of SAR image stacks will reduce the detection capabilities of MTInSAR as some scatterers stop being coherent targets following an increased time period. Each SAR image used for the MTInSAR stack follows the data preparation from (5.1). It is VV polarized and multi-looked to a 15m grid size, and the data is separated based on the sensor look angle.

#### C.5 PSInSAR

## C.5.1 Connection Graph

The initial stage of the PSINSAR stacking technique involves constructing a connection graph. This step establishes a network connecting the master and slave pairs based on their baseline values, ultimately generating differential interferograms. The images in the network have a common master image based on a minimum temporal baseline for the most extreme pair. The maximum number of possible connections is equal to N-1, where N is the number of acquisitions.

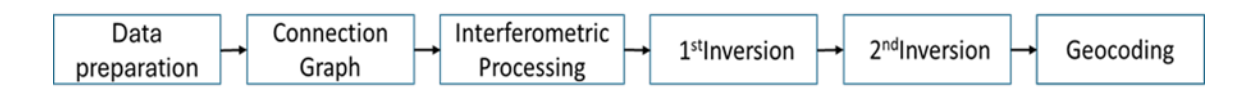


Figure C.4 Shows the workflow of MT-InSAR process

# C.5.2 Interferogram formation

This procedure encompasses essential steps of Interferogram generation as described in C.2. The steps involved are co-registration, interferogram generation, implementation of an adaptive filter, the generation of coherence, and phase unwrapping. The images are paired based on the connection graph. The interferogram formation determines the distance between the ground surface and the radar sensor between the co-registered image data pairs.

#### C.5.3 First Inversion

This stage involves calculating the residual height and the displacement velocity. The PS approach identifies a series of "coherent radar signal reflectors" called Persistent Scatterers. The PS are identified using amplitude dispersion MuSigma. In the time frame under consideration, the amplitude dispersion index is calculated as the ratio of the mean value to the standard deviation  $\sigma A$  of the picture intensity.

$$MuSigma = \frac{mA}{\sigma A} \tag{24}$$

A PS is present when backscattering intensity shows little temporal variability. The amplitude dispersion index calculation enables the selection of candidates for PSC (Permanent Scatterers Candidates) points at the outset without the need for phase coherence analysis. High dispersion index pixels (MuSigma=0.60%), which have comparable values throughout time and relatively high amplitude values in most conditions, make them suitable candidates for persistent scatterers. After identifying these targets, a phase history analysis is conducted to identify potential PS candidates based on their coherence. MuSigma should always be less than the threshold for coherence, as a

larger MuSigma will reduce the number of PS in the identification stage. A threshold of 0.7 coherence is chosen to identify PS targets. A higher threshold for coherence would reduce the number of PS but increase the accuracy of the measured displacement. However, due to a large temporal baseline for a 25-image SAR stack, a 0.7 coherence threshold is preferable; a higher threshold reduces the presence of PS in the active monitoring region. The PS technique employs a linear model exclusively during the first inversion process to obtain residual height and displacement velocity. The linear model can be described by the Equation 25

$$\phi(M) = (H \times K) + (V \times T \times \frac{4\pi}{\lambda})$$
 (25)

Where, " $\phi(M)$ " is the displacement phase for the M<sup>th</sup> interferogram pair; "V" is the mean displacement velocity of the observation time period; "T" is the temporal baseline between the two acquisitions in the interferogram; " $\lambda$ " is the wavelength of the radar signal used; "H" is the residual height error due to the reference DEM used; "K" is the geometric parameter which depends on the baseline and incidence angle

Equation 25 is solved using a brute force approach to obtain the displacement velocity and residual height. The software utilizes a "Brute Force" method to systematically test various velocity values on a date-by-date basis to determine the most accurate fit with the interferogram phases [59].

### C.5.4 Second Inversion

In this step, the atmospheric component is filtered from the displacement rate using the grids developed in the first inversion. This step uses a Low-Pass spatial filter(1200m) and a High-Pass temporal filter(365 days) to get a displacement rate with

the contributions of atmospheric effects reduced. The parameters for the atmospheric filtering in the second inversion step are described further in [86] [87] [88]. Data from the second inversion is processed through geocoding to convert it from satellite coordinates to a datum of our choice.

## C.6 SBAS

#### C.6.1 Connection Graph

The SBAS technique uses multiple master files to develop interferogram data pairs with narrow temporal and spatial baselines. The connection graph specifies the combination of SAR pairs (Masters and Slaves) and the connections network utilized to generate numerous differential interferograms. The pairs to be processed are represented as connections in a network that connects each acquisition to the others. Given N acquisitions, the most significant number of viable connections M between all of the acquisitions is

$$\frac{N+1}{2} \le M \le N(\frac{N+1}{2}) \tag{26}$$

The differential interferograms are generated based on the spatial baseline shorter than 2% of the critical baseline. A critical baseline is the maximum viable baseline for the satellite platform—a temporal baseline in the 90 to 180-day range. An additional criterion based on the maximum connections for each master file is set at 10. Increasing the maximum connections increases the processing time as the number of interferograms increases, but the improvement in accuracy falls significantly after 10. Reducing the number of connections to less than 5 increases the atmospheric errors as the number of redundant interferograms decreases substantially [60].

# C.6.2 Interferogram Formation

This step calculates the interferogram and arranges the deformation data into a matrix form for use in the first inversion stage. The matrix is formed based on the steps described below. The connection graph generates multiple InSAR pairs. Each interferogram formation follows the steps as described in (C.2) and the interferometric phase can be described by the equation

$$\delta\phi_{int}(r,a) = \phi(t_B, r, a) - \phi(t_A, r, a)$$

$$\approx \Delta\phi_{disp} + \Delta\phi_{topo} + \Delta\phi_{atm} + \Delta\phi_{orb} + \Delta\phi_{noise}$$
(27)

Equation 27 represents the DInSAR interferogram where,

" $\phi_{int}(r,a)$ " is the interferometric phase for range (r) and azimuth(a) coordinates, with  $\delta$  denoting the differential interferogram i.e, interferometric phase without the topographic phase component; " $t_A \& t_B$ " represent the time of acquisition of the SAR images with  $t_A < t_B$ ; " $\Delta \phi_{disp}$ " is the deformation phase along the line of sight direction between  $t_A \& t_B$ ; " $\Delta \phi_{topo}$ " is the residual topographic phase caused by DEM inaccuracy; " $\Delta \phi_{atm}$ " is the atmospheric phase error; " $\Delta \phi_{orb}$ " is the phase error caused by the orbit; " $\Delta \phi_{noise}$ " is the random phase noise error;

The set of M differential interferograms from the connection graph can be represented by a system of M equations with N unknowns, which can be defined as

$$A\phi = \delta\phi \tag{28}$$

Where, A is the M X N matrix;  $\phi = (\phi(t_1), \phi(t_1), \phi(t_2), \phi(t_3), \dots, \phi(t_N))^T$  is the deformation phase N X 1 vector; The vector for the differential interferogram phase

 $\delta \phi$  can be expressed as

$$\delta\phi = (\delta\phi(t_1), \delta\phi(t_1), \delta\phi(t_2), \delta\phi(t_3), \dots, \delta\phi(t_N))^T$$
(29)

Based on the Equation 28 the deformation velocity can be described by

$$Bv = \delta \phi \tag{30}$$

Where B is M X N matrix and v is the mean phase velocity and is described as

$$v = [v_1, v_2, v_3, \dots, v_N]^T$$

$$= \left[\frac{\phi_1}{t_1 - t_0}, \frac{\phi_2 - \phi_1}{t_2 - t_1}, \frac{\phi_3 - \phi_2}{t_3 - t_2}, \dots, \frac{\phi_N - \phi_{N-1}}{t_N - t_{N-1}}\right]^T$$
(31)

The least square method can calculate the deformation velocity in conditions where matrix B is M>N. In most conditions where the matrix B is M $\leq$ N, the deformation velocity can be estimated using the singular value decomposition(SVD) method [60].

## C.6.3 First Inversion

The singular value decomposition (SVD) is implemented to calculate the displacement rate over a specific time series. The first inversion of the SBAS method involves flattening the unwrapped interferograms and repeating the orbital refining and phase unwrapping to enhance the quality of the results. The SBAS technique can employ linear, quadratic, and cubic models to calculate acceleration and acceleration variation, as well as height, displacement, and velocity.

This thesis uses linear models for deformation generation.

#### C.6.4 Second Inversion

The second inversion step involves calculating the displacement inside time

series using SBAS first inversion. The second inversion utilizes the ground control points (GCPs) as fixed reference points, assuming that these are stable points on the ground in those specific areas. The ground control points (GCPs) were utilized to reduce the phase constant, so the first inversion was corrected. The outcomes of this procedure are used to compute the velocity rate and the vertical displacement across the regions within a time series [132].

#### C.6.5 Ground Control Points

C.6.6 Geocoding

In the MT-InSAR study, ground control points (GCPs) are utilized for two objectives. They are employed for orbital error and residual phase adjustments. They serve as reference points for calculating surface displacements along the line of sight (LOS) direction. Consequently, the GCPs significantly affect the accuracy of InSAR-derived outcomes.

Ground Control Points (GCPs) can be selected based on field observations. In the absence of in situ data, selections are made at areas where surface deformation is typically not presumed. Consequently, ground control points (GCPs) i) must not be situated at residual topographic features and ii) should be distanced from deformation zones. By visually recognizing regions that meet the interferometric phase consistency requirements for both selection criteria, one may traditionally establish the GCPs [133].

The process of geocoding uses precise information about the imaging geometry and terrain relief in the form of a Digital Elevation Model (DEM) to project the data into a chosen map projection where each imaged terrain feature is located at its correct map

coordinates. This can help reduce the effects of the inherent geometric distortions in SAR imaging.

Geocoding constitutes the final phase in the MT-interferogram generating process. The geocoding process involves resampling the interferogram onto a uniform grid on the reference ellipsoid. In the geocoding process, two equations are combined: a) the Doppler equation (a plane orthogonal to sensor-target velocity in the case of zero-Doppler focusing), which yields a circle in three dimensions, and b) the range distance equation, which is a sphere centered at the sensor site. The precise location of the scatterer is determined by intersecting with the hyperbola derived from the known Digital Elevation Model (DEM). Following this, processing is repeated for every point, until the complete SAR image is calibrated [134].

# C.7 Proposed Post-Processing Methods

One of MTInSAR's key features is its ability to accurately identify small surface changes over a long time. But during the analysis period, if there is a large change (e.g. movement > 30mm) between two acquisitions or the scatterer loses coherence due to other factors, the change cannot be monitored even if the surface is experiencing the deformation. During geohazard monitoring, regions classified as A or B have been identified as good candidates for geohazard monitoring. These regions are characterized by low vegetation and high radar backscatter coverage and, thus, conventional MTInSAR can be applied for monitoring deformations over the period covered by the SAR image stack. However, as the time period of the analysis increases, seasonal vegetation coverage and errors due to larger satellite spatial baseline make the detection of both PS and DS scatterers scarce due to the loss of continuity in the observable scatterers. Therefore,

detection of critical areas through deformation monitoring using conventional MTInSAR is not possible. The proposed approach implements MTInSAR techniques using a "Rolling Stack" (RS) concept to detect the presence scatterers over longer time periods, in conjunction with three post-processing operations, i.e., "Thresholding", "Scatterer Accumulation" and "Clustering Timeline". Details are presented in [66] [71].

## C.7.1 Rolling Stack MTInSAR

The proposed RS-MTInSAR limits the size of the stack of SAR images in the conventional implementation to a number of images that are necessary to preserve accuracy and to control noise, typically between 15 and 25, depending on the site class and the particular MTInSAR method. Subsequently, site monitoring for a period of time that exceeds the time spanned by the stack is achieved by performing a series of MTInSAR analysis. Each analysis uses an updated SAR image stack where the first SAR image is dropped from the head of the stack and a new SAR image is added to the tail of the stack, creating a "rolling stack" effect. Figure C.5 demonstrates the concept assuming a monitoring period of one year, and temporal image acquisition baseline of 12 days yielding a total number of 30 SAR images. Assuming for demonstration purposes only a stack size of 20 SAR images, 12 MTInSAR analyses need to be performed. Each analysis produces the geolocation of the PS, or DS scatterers, within the analysis stack as well as the time history of movement at each point. This information is considered in the post processing steps of the proposed method.

#### C.7.2 Thresholding

MTInSAR methods implement filters to treat temporal and spatial decorrelation of the signals in order to improve the quality of the deformation results, but only to a

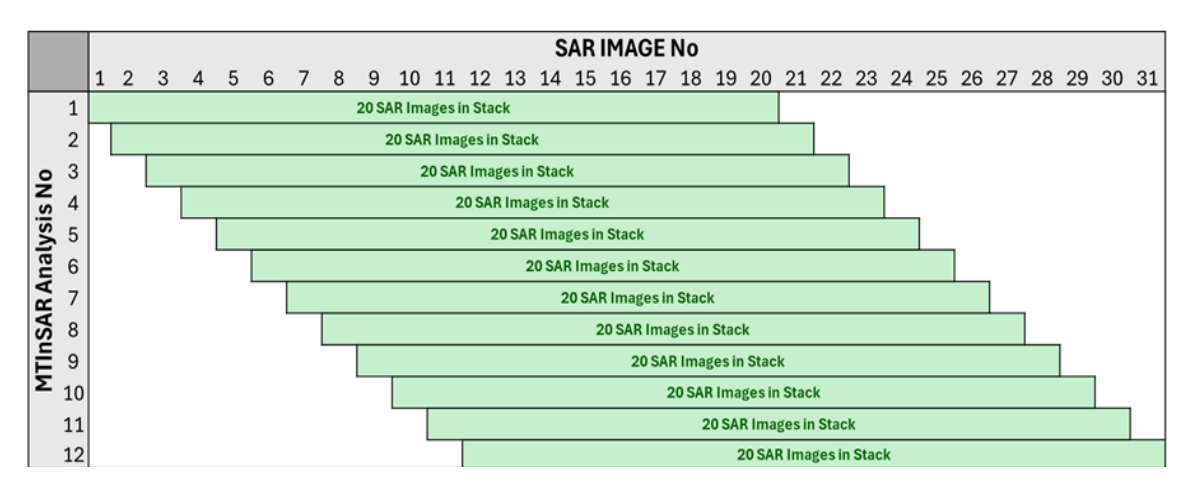


Figure C.5: Rolling Stack MTInSAR analysis concept

certain extent. Loss of coherence due to atmospheric contributions results to higher noise in the deformation measurements derived from the MTInSAR and hinders the detection of critical areas. The proposed *Thresholding* is a post-processing filtering method implemented to all deformation analyses from the proposed RS-MTInSAR. The objective of the proposed filtering is to identify and remove the scatterers from the solutions that are formed by residual coherence losses from decorrelations, or represent points that, although they are properly identified, they exhibit small movement and are of no interest in the identification of the critical areas.

The criterion for the threshold is based on the coherence threshold used in the PS and DS identification process. In the case of PSInSAR, a coherence threshold of 0.7 is used as an indicator of PS, while in the case of SBAS, a coherence threshold of 0.3 is used as an indicator for DS points. The magnitude of the filter is determined by the theoretical precision of SAR deformation data as reported in [90] [91] is based on Equation 32. The precision depends on the wavelength of the SAR sensor and the measured coherence. For example, for a C-band sensor and a scatterer with 0.7 coherence, the theoretical precision is 20 mm and any deformation above the theoretical is considered the true deformation. However, any deformation below the theoretical value may be masked by noise. In the proposed RS-MTInSAR, the theoretical precision should not be used as the threshold criterion because the coherence fluctuates in each SAR image pair in the stack. Thus, to prevent active deformation points from being filtered, conservative threshold values are recommended, as shown in Table C.1.

Table C.1 Recommended Threshold Values

Coherence	Theoretical Precision (mm)	Threshold Value +/- (mm)
0.9	8	6
0.8	14	8
0.7	20	10
0.65	23	11
0.6	26	12
0.55	30	14
0.5	35	16
0.45	41	18
< 0.4	> 50	20

$$\mu = \sqrt{\frac{1 - \gamma}{2\gamma}} \frac{\lambda}{4\pi} \tag{32}$$

#### C.7.3 Scatterer Accumulation

The identification of the critical areas in the region of interest starts with establishing the *Landsat* optical image of the region to geolocate the scatterers. Landsat is publicly available through Google Earth. At the end of each RS-MTInSAR analysis the identified set of scatterers are filtered as discussed in the "Thresholding" section and superimposed on the optical image of the region. For both event investigation and active monitoring, it is recommended that the monitoring period starts at least one year before the date of the event, or before the active monitoring commences. The scatterer accumulation will result in a continuously updated deformation map with the location of all scatterers appearing on the optical image. At this step, the critical locations can be identified by visual inspection, as areas where the density of accumulated scatterers increases over time. The detection of the critical locations, however, is implemented in a structured manner in the last post-processing tool, i.e. Clustering Timeline, discussed next.

## C.7.4 Clustering Timeline

The last step in the proposed process for identifying the critical location within a larger monitoring region pertains to identifying the formation and progression of cluster of scatterers every time a new set of RS-MTInSAR analysis data becomes available. To this end, a grid is overlayed on the optical image with a subset size dependent on a combination of the desired resolution of the critical areas and the average number of the

detected scatterers in the region. Higher risk areas are identified as those subsets, or group of subsets, that exhibit higher density of the clustered scatterers compared to their surrounding subsets. At this stage, although regions with a high potential for geohazard failure are identified, the imminency of the failure is not evident. A timeline analysis showing the rate at which the clusters are formed between any two successive data sets is used as an indication that a geohazard event failure is imminent. The timeline method is based on the geohazard observation that before the triggering event there is a rapid increase in density of the cluster in the geohazard vicinity.